Persistent luminescence mechanism of tantalite phosphors

By

Luyanda Lunga Noto

(M.Sc. Physics)

This thesis is submitted in fulfillment of the requirements for the degree

Doctor of Philosophy

in the

Faculty of Natural and Agricultural Sciences

Department of Physics

Bloemfontein campus

at the

UNIVERSITY OF THE FREE STATE

Promoter: Prof. H.C. Swart

Co – Promoter: Prof. O.M. Ntwaeaborwa

November 2014

"Poverty and life difficulties are never an obstacle enough to stop one from pursuing his goal."

— Nobenza Ruth Noto

"I do not think there is any other quality so essential to success of any kind as the quality of perseverance. It overcomes almost everything, even nature."

— John D. Rockefeller

Acknowledgements

"When we give cheerfully and accept gratefully, everyone is blessed."
— *Maya Angelou*

I have been much honored to be in the midst of several researchers who blessed my life in several ways and shaped my research aptitude. I am sending sincere gratitude to:

1. ***Prof. Hendrik C. Swart*** (promoter) for opening the door for me to enter the world of research, and for his guidance along the length of my postgraduate studies. Thank you for helping me access funding for the studies and leading me with care and patience.

2. ***Prof. Odireleng M. Ntwaeaborwa*** (Co – promoter) for all the valuable inputs in helping me organize my ideas.

3. ***Prof. Roos*** for his valuable advices on X-ray Photoelectron Spectroscopy.

4. ***Dr. SKK Shaat and Dr. MYA Yagoub*** for the lovely collaboration we had.

5. ***Dr. E. Coetzee-Hugo and M.M. Duvenhage*** for the XPS and ToF-SIMS measurements.

6. ***Prof. Makaiko Chithambo*** from the University of Rhodes for his valuable assistance in thermoluminescence spectroscopy.

7. University of Free State Physics department staff and fellow students from both Bloemfontein and Qwaqwa campus, for all the valuable discussions.

8. Thank you to South African National Research Foundation for funding my research work.

9. Most importantly I am sending the deepest gratitude to God, to my late grandmother ***Nobenza Ruth Noto*** (1935 September 25 – 2008 April 22) and the rest of my family for all that I am.

Abstract

Pr^{3+} ion doped $ZnTa_2O_6$, $SrTa_2O_6$, $CaTa_2O_6$ and $ZnTaGaO_5$ phosphors, which display persistent luminescence were prepared by solid state chemical reaction at 1200 ^oC for 4 hours. A $ZnTa_2O_6:Pr^{3+}$ phosphor that resembled an orthorhombic single phase was obtained, as identified by X-ray diffraction (XRD). $ZnTa_2O_6:Pr^{3+}$ displayed both blue and red emission, with the blue emission spectral line observed at 448 nm from the $^3P_0 \rightarrow {}^3H_4$ transition, and the red spectral lines observed at 608, 619 and 639 nm from the $^1D_2 \rightarrow {}^3H_4$, $^3P_0 \rightarrow {}^3H_6$ and $^3P_0 \rightarrow {}^3F_2$ transitions, respectively. For different concentrations of Pr^{3+}, a concentration of 0.4 mol% Pr^{3+} proved suitable to generate a phosphor displaying only red emission with the Commission Internationale de l'Eclairage (CIE) coordinates matching those of an ideal red color. Enhancement of the luminescence intensity of $ZnTa_2O_6:Pr^{3+}$ phosphor was achieved by preparing it in the presence of Li_2SO_4 and Li_2CO_3, which act as flux agents. The strong absorption by the defect levels due to the flux was observed from the diffused reflectance spectra. Pr exists in both Pr^{3+} and Pr^{4+} oxidation states as revealed by the X-ray photoelectron spectroscopy data. The presence of Pr^{3+} increased, while Pr^{4+} decreased in the samples prepared in the presence of a flux. The increased absorption by the defect levels and the reduction of Pr^{4+} in the samples prepared using a flux resulted in the enhancement of the luminescence intensity as observed from the photoluminescence spectra. The lifetime of the persistent luminescence of $ZnTa_2O_6:Pr^{3+}$ prepared in a flux was calculated using a second order exponential decay curve from the measured phosphorescence decay curves. This showed an enhancement in the lifetime of the persistent luminescence of the fluxed sample, which is attributed to the additional electron trapping centres induced by the flux as observed from the thermoluminescence glow curves. Additional means of enhancing the lifetime of the persistent luminescence were achieved by co-doping $ZnTa_2O_6:Pr^{3+}$ with Li^+, Na^+, K^+ or Cs^+ ions, and by also incorporating gallium ions to form a new host $ZnTaGa_5:Pr^{3+}$. The scanning electron microscopy (SEM) images showed that particles were of irregular shape and with different sizes. The preparation with the fluxing material showed and increased particle sizes. The SEM images of $ZnTaGa_5:Pr^{3+}$ showed a surface morphology that is composed of particles with different shapes, including the irregular, rhombus and rod shapes. The distribution of the ions in the material was investigated using the Time of Flight Secondary

Ion Mass Spectroscopy (ToF SIMS) surface maps, which showed that the ions were uniformly distributed throughout the matrix. This showed successful incorporation of the ions. Pr^{3+} exhibits prominent red emission in most oxide phosphors, which comes from the $^1D_2 \rightarrow {}^3H_4$ transition, and greenish-blue emission from $^3P_0 \rightarrow {}^3H_{4,5}$ transitions is normally less intense. However, a greenish-blue emission was observed from the $CaTa_2O_6$:Pr^{3+} oxide phosphor prepared by solid state reaction at 1200 ^oC. A combination of emission coming from $^1D_2$ and $^3P_0$ levels was observed, with the blue emission from the latter much more prominent. Upon investigating the thermoluminescence properties of the phosphor, the glow curves showed the presence of three different types of electron trapping centres. Interesting properties of the trapping centres, such as the competition between the trapping centres, pre-radiation effects and the calculation of the activation energy were studied. The phosphorescence decay curves showed long lasting afterglow. Three $SrTa_2O_6$:Pr^{3+} phosphor samples with persistent emission properties were prepared by solid state reaction at 1200, 1400 and 1500 ^oC. The crystal structure formation improved with an increase in temperature as identified by XRD. The scanning electron microscopy images showed that the particles of the phosphor were agglomerated and co-melting was induced by increasing the synthesis temperature. The ion distribution in the phosphors was determined using the time of flight secondary ion mass spectroscopy. The red emission was obtained from the $^1D_2 \rightarrow {}^3H_4$ and the $^3P_0 \rightarrow {}^3H_6$ transitions at 608 and 619 nm, respectively. The main absorption occurred at 225 nm (5.5 eV), and the band gap (E_g) calculations confirmed that it corresponds to band-to-band excitation. The persistent emission time parameters (260 – 296 s) were calculated from the phosphorescence decay curves using the second order exponential decay equation. The corresponding electron trapping centres were identified using the thermoluminescence spectroscopy, and the activation energy was determined using the initial rise method.

Keywords

Solid State reaction, Persistent luminescence, flux, Photoluminescence, electron trapping centres, Thermoluminescence

Acronyms

IVCT   -   Intervalence charge transfer

XRD   -   X-ray Diffraction

SEM   -   Scanning Electron Microscopy

PL   -   Photoluminescence

TL   -   Thermoluminescence

XPS   -   X-ray Photoelectron Spectroscopy

ToF SIMS   -   Time of Flight Secondary Ion Mass Spectroscopy

ESSCR   -   Electron Stimulated Surface Chemical Reaction

CIE   Commission Internationale de l'Eclairage, which is a mathematical model describing the way colors can be represented

Torr   -   133.32 Pa

273K   -   0 ^{o}C

Long Afterglow   -   Persistent Luminescence

Table of contents

Chapter 1

Introduction

Chapter 2

Luminescence Mechanism

Chapter 3:

Experimental Techniques

Chapter 4

Photoluminescence and thermoluminescence properties of Pr^{3+} doped $ZnTa_2O_6$ phosphor

Chapter 5

Enhancement of the photoluminescence intensity of $ZnTa_2O_6$:Pr^{3+} phosphor

Chapter 6

Enhancement of persistent luminescence of $ZnTa_2O_6$:Pr^{3+} by addition Li^+, Na^+, K^+ and Cs^+ ions

Chapter 7

Enhancement of luminescent intensity and persistent emission of $ZnTa_2O_6$:Pr^{3+} phosphor by adding fluxing agents

Chapter 8

Persistent luminescence study $ZnTaGaO_5$:Pr^{3+}

Chapter 9

The greenish-blue emission and thermoluminescent properties of $CaTa_2O_6:Pr^{3+}$

Chapter 10

Photoluminescence and persistent emission of $SrTa_2O_6:Pr^{3+}$

Chapter 11

Summary and Future work

"How wonderful that we have met with a paradox. Now we have some hope of making progress."

— Niels Bohr

1

Introduction

1.1. The sources of light

Household lighting devices have always been an important component of life and continue to provide us with light beyond sunset. These devices continue to be improved frequently to allow ease of use. There is a great difference in terms of efficiency and ease of use from the earliest documented device by Aime Argand in 1784, the draught oil lamp [1], to the latest and mostly used tungsten electric light bulbs [2]. The pursuit to further develop the lighting devices continues daily in order to develop cheaper and much more efficient devices that rely on renewable energy for operation, like phosphor LEDs, fluorescent tubes and other phosphor based devices continues [3].

The difference between the tungsten electric bulb and the fluorescent tubes lies in the origin of light from the two devices. Tungsten electric light bulbs emit visible electromagnetic waves under the continuous heating of the filament [4]. This phenomenon is referred to as the incandescence or blackbody radiation [4]. On the contrary, fluorescent tubes are manufactured with a powder material (phosphor) that emits electromagnetic waves by re-emitting absorbed external radiation [5]. The absorbed radiation brings about transition of electrons from the valence band to the conduction band, and when the electrons return to their natural ground state in the valence band, they do so by converting their energy to electromagnetic waves [5].

Luminescent materials are often differentiated using the lifetime of their emission. Those with an emission that is only detectable in the presence of the excitation source are referred to as fluorescent. Those with an emission that continues for a considerable period after the excitation source has been removed are referred to as phosphorescent [5,6]. Fluorescence occurs when an electron is excited to a higher state from where it de-excites to ground state

by photon emission, without undergoing much non-radiative relaxation between the vibration states of the excited level. The life time of the excited state in fluorescent materials is less than 10^{-8} sec [6]. The non-radiative relaxation between the vibrational states of the excited level brings about change in the photon energy of the excitation source and the emitted photon energy, and the phenomenon is referred to as Stokes shift. The Stokes shift is also applicable to phosphorescent materials [7].

Phosphorescence on the other hand is an emission that is characterised by an afterglow that lasts approximately for 10^{-3} to 10 secs [6]. Additionally, there is also an emission that lasts for a couple of minutes, up to several hours after the source is removed, and it is called persistent luminescence [8]. The persistent emission was first reported for a bologna stone ($BaSO_4$), and the underlying phenomenon was by then not well understood. Some of the early persistent materials are ZnS doped with Cu or radioactive lanthanides [8].

In the modern times from 1995, there appeared a new generation of persistent luminescence phosphors, such as $Sr_2MgSi_2O_7:Eu^{2+},R^{3+}$ (where R is any rare earth ion) [8], $MAl_2O_4:Eu^{2+},R^{3+}$; M = Ca and Sr [8], $CaTiO_3:Pr^{3+}$ [9], $Zn_3Ga_2Ge_2O_{10}:Cr^{3+}$ [10], etc. These materials are researched in different laboratories for different applications, such as: security signage, emergency route signs, traffic signage, medical diagnostics, luminous paints [10] and airplane cabin floors [8]. The additional interest is to combine the rare earth ions rendering different colour emissions to produce a white glowing persistent phosphor. Such a phosphor would have great use in solid state lighting applications [8].

The mechanisms underlying the mechanism of phosphorescence is not yet clearly understood, and this opens up an opportunity for fundamental researchers to research on the topic. The focus has mainly been on developing new phosphors and hoping that they do meet the requirements of persistent phosphorescence emission. Agreeably is that good phosphorescent materials have been oxide compounds such as listed above [8]. Swart et al [11] present the mechanism of the persistent phosphorescent emission of $SrAl_2O_4:Eu^{2+},Dy^{3+}$, and suggest that it is caused by the trapping of electrons by the oxygen related vacancies, upon exciting the phosphor with an ultraviolet light. These electrons are then ambient thermally bleached back to the 5d level of Eu^{2+}, from where they will radiatively de-excite to the 4f level of Eu^{2+}. According to the mechanism the long route travelled by the electrons from the 5d of Eu^{2+} to the oxygen vacancies and then back to the Eu^{2+} is the main cause of the persistent phosphorescence [11].

1.2.   Problem statement and aim

The persistent luminescence is a subject of interest lately, particularly to the researchers that strongly intend to make contribution to its less understood mechanism. Apart from understanding the mechanism, there are several applications that drive the research of materials that display persistent luminescence. Such materials are set to answer the need for energy conservation. A typical example of such a phosphor would be one that can absorb energy from the sunlight during the day, and continue to glow longer than 12 hrs in the absence of the excitation source. Such a phosphor will lead to cost-effective lighting of street and houses.

The strong persistent luminescence properties have for a long time been associated with silicate and aluminate phosphors. A recent achievement is the research done on $CaTiO_3:Pr^{3+}$ [9] and $Zn_3Ga_2Ge_2O_{10}:Cr^{3+}$ [10], (Y, La or Gd)$TaO_4:Pr^{3+}$ [5] phosphors, which show persistent luminescence from different hosts other than the silicate and aluminate phosphors. The main contribution of the present work is to contribute valuable work that will increase the understanding of the phosphorescence mechanism. The focus is on enhancing the quantity of the electron trapping centres inside the material, and to generate different phosphor with a persistent luminescence using tantalite based phosphors.

1.3.   Objectives of the study

- ➢ To prepare new phosphors by doping $ZnTa_2O_6$, $CaTa_2O_6$, $SrTa_2O_6$ and $ZnTaGaO_5$ with Pr^{3+} via solid state chemical route.
- ➢ Use XRD to identify the phase change and strain in the host, and SEM to identify change in the surface morphology, due to Pr^{3+} incorporation
- ➢ To probe the luminescence properties of the phosphors by using PL, PLE and UV/Vis spectroscopies that arise in the unique crystal field of the new hosts.
- ➢ To map the elements in the material using ToF-SIMS to identify Pr^{3+} distribution in the host.
- ➢ Use the TL spectroscopy to investigate the energy distribution of the electron trapping centres and how they change as a result of Pr^{3+} incorporation.
- ➢ Use XPS to investigate the chemical state of the surface of the host material and the oxidation state of Pr^{3+} when the phosphor is prepared under different environments

- ➢ Enhance the phosphorescence decay time by preparing the sample in the presence of fluxing agents.
- ➢ Enhance phosphorescence decay time by disordering the crystal structure to generate more oxygen vacancies, by adding different alkali metals.

1.4. Organisation of the thesis

1.4.1. Supervision

The work was supervised by Professor Hendrik C. Swart and co-supervised by Professor Odireleng M. Ntwaeaborwa, both from the University of Free State, Bloemfontein Campus in South Africa. Additional contribution to the work was from Professor Makaiko L. Chithambo from the University of Rhodes, South Africa, with the thermoluminescence spectroscopy and analysis of the data.

1.4.2. Collaboration

- The University of Rhodes with the thermal stimulated luminescence measurements for the analysis of the energy distribution of the electron trapping centres.
- The Centre for Microscopy at the University of Free State for the measurements of SEM images.

1.4.3. Additional contributors

- Dr. Elizabeth Coetzee-Hugo for the XPS measurements.
- Prof. Wiets D. Roos for the XPS analysis.
- Dr. Mart-Mari Duvenhage for the TOF-SIMS measurements.
- Dr. Mubarak Y.A. Yagoub for the luminescence mechanism.
- Dr. Samy K.K. Shaat for the mixed phase sample preparation.
- Prof. M. Chithambo for the thermoluminescence.

1.4.4. Layout of the chapters

Chapter 1: The present chapter introduced the concept of persistent emission and its current/future applications, the factors that motivated the study, the factors to be addressed, the collaboration with others scientists, and the layout of the thesis.

Chapter 2: This chapter describes the phenomenon of luminescence by describing the different types of luminescent materials and how they emit light. Additionally, the basic concept of thermoluminescence is introduced.

Chapter 3: Description of the characterization techniques that are used to probe information from the luminescent materials that are investigated.

Chapter 4: Introduces the luminescence and thermoluminescence properties of $ZnTa_2O_6:Pr^{3+}$.

Chapter 5: Enhancement of the photoluminescence intensity of $ZnTa_2O_6:Pr^{3+}$ Phosphor.

Chapter 6: Enhancement of persistent luminescence of $ZnTa_2O_6:Pr^{3+}$ by addition Li^+, Na^+, K^+ and Cs^+ ions.

Chapter 7: Enhancement of luminescent intensity and persistent emission of $ZnTa_2O_6:Pr^{3+}$ phosphor by adding fluxing agents.

Chapter 8: Persistent luminescence study $ZnTaGaO_5:Pr^{3+}$.

Chapter 9: The blue emission and TL properties of $CaTa_2O_6:Pr^{3+}$.

Chapter 10: Photoluminescence and persistent emission of $SrTa_2O_6:Pr^{3+}$.

Chapter 11: Summary, future work, publications and conferences.

1.5. References

1   M. Day, Voices from the world of Jane Austen, 2011, F&W Media International, UK.

2   T. Denton, Automobile electrical and electronic systems, 2004, 3rd edition, Elsevier Butterwoth-Heineman, UK.

3   R. Cross and R. Spencer, Sustainable Gardens, 2009, CSIRO publishers, Australia.

4   D.D. Busch, Nikon D200 digital field guide, 2006, Wiley Publishers, Indiana.

5   L.L. Noto, Red emission of Praseodymium ions, 2011, M.Sc. Thesis, University of The Free State.

6   J.R. Lakowicz, Principles of fluorescence spectroscopy, 2006, 3rd Ed., Springer publishers, USA.

7   K.D. Sattler, Handbook of nano-physics; nanoparticles and quantum dots, 2011, CRC Press, USA.

8   Jorma Holsa, The Electrochemical Society Interface meeting, Winter 2009, http://www.electrochem.org/dl/interface/wtr/wtr09/wtr09_p042-045.pdf [20 October 2013].

9   L.L. Noto, S.S. Pitale, M.A. Gusowski, J.J. Terblans, O.M. Ntwaeaborwa, H.C. Swart, Powder Technol. **237** (2013) 141.

10 Z. Pan, Y.Y. Lu, F Liu, Nature Mater. **11** (2012) 58.

11 H.C. Swart, J.J. Terblans, O.M. Ntwaeaborwa, E. Coetsee, B.M. Mothudi, M.S. Dhlamini, Nucl. Instr. Meth. Phys. Res. B **267** (2009) 2630.

"Men love to wonder, and that is the seed of science."

— Ralph Waldo Emerson

2

Luminescence Mechanism

2.1. Introduction.

Light forms the basis of the human life and it is needed on a daily basis to carry out activities when the sun sets. There are several forms of light, ranging from candles, gas lighting, incandescent lighting, and luminescence based lighting. Luminescence is known as cold emission, and the materials that emit this kind of light are referred to as phosphors. Applications of a phosphor material are in the modern LEDs, Television screens, cell phone screens, lighting watches, emergency route signage, biological imaging, etc. This chapter aims to illustrate the phenomenon of luminescence, ranging from absorption, luminescence dynamics of the activator and the mechanism of persistent emission.

2.2. Luminescence.

A phosphor is a luminescent material that has the ability to absorb energy from external radiation, and re-emit it as electromagnetic waves [1]. The emission is observed due to the electronic transitions between the intrinsic defect level states [2], or the luminescence states from the levels of an extrinsic defect [1]. ZnO is a good example of a material with emission originating from intrinsic defects. This occurs when a radiation is absorbed (Figure 2.1) and electrons are excited to the conduction band [2], from where they are de-excited to the donor level (intrinsic defects with a positive charge), and the holes are attracted by accepter level (intrinsic defects with negative charge). The two opposite charges, electrons and the holes, will exist in a temporary bound state, which is followed by radiative recombination [2,3].

Phosphors that are made by an incorporation of an activator (extrinsic defect) into a host material, the activator acts as the luminescent centre (Figure 2.2) and the host is any alloy compound [1]. Often the lanthanide ions are employed to act as the luminescent centres. The lanthanide ions give rise to discrete energy levels within the host (Figure 2.1), which are the centre from where luminescence emanates. The energy states are positioned within the band gap, such that the electrons de-excited from the higher to the lower states radiatively [1].
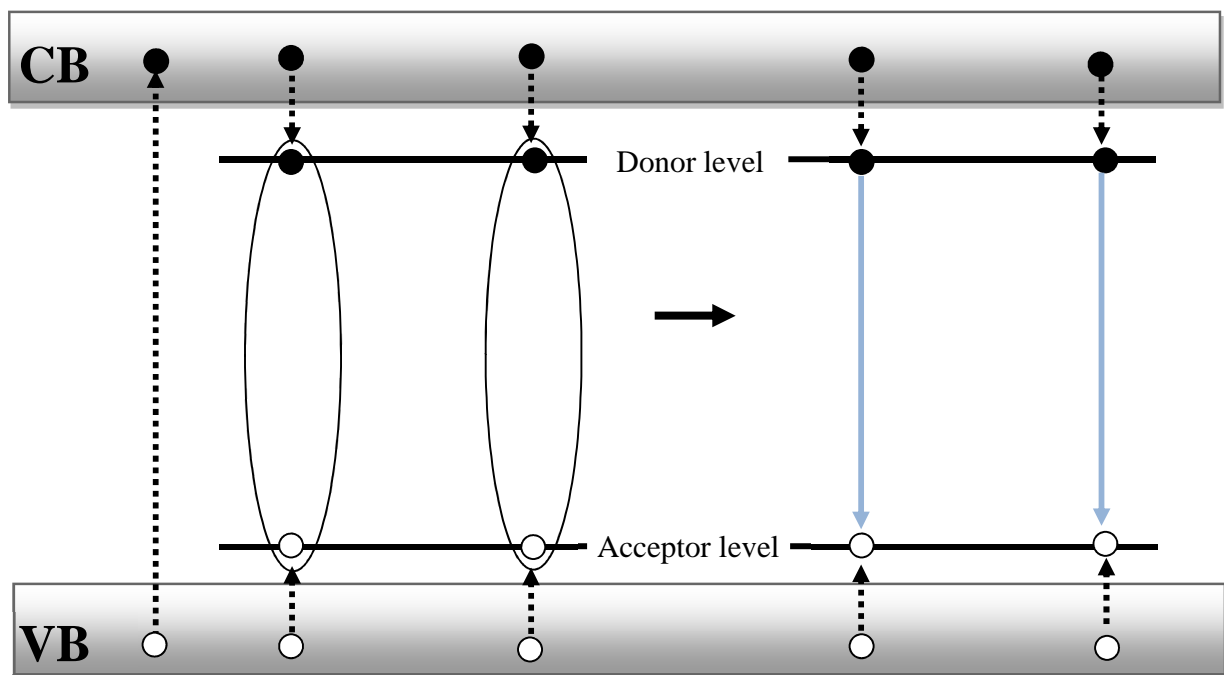

Figure 2.1: Schematic representation of the electronic structure of an intrinsic defect based phosphor.

In the latter type of phosphor, the major energy of the excitation source is absorbed by the host material. This energy is eventually transferred to the luminescent centre, from where the emission will originate. The negatively charged electrons that are excited to the conduction band (CB), when the irradiation is absorbed, leave behind positive charge (holes) in the valence band (VB). The electrons in the conduction band de-excite to the highest state of the activator that is within the band gap (E_g), and the holes are attracted by the lowest state of the activator. The electrons in the luminescent state de-excite from the highest to the lowest by radiatively emitting

light. This is as illustrated in Figure 2.2 by using Pr^{3+} ion activator, where the blue is emission from the $^3P_0 \rightarrow {}^3H_4$ transition and red emission is observed from the $^1D_2 \rightarrow {}^3H_4$, $^3P_0 \rightarrow {}^3H_6$ and $^3P_0 \rightarrow {}^3F_2$ transitions [1,4].
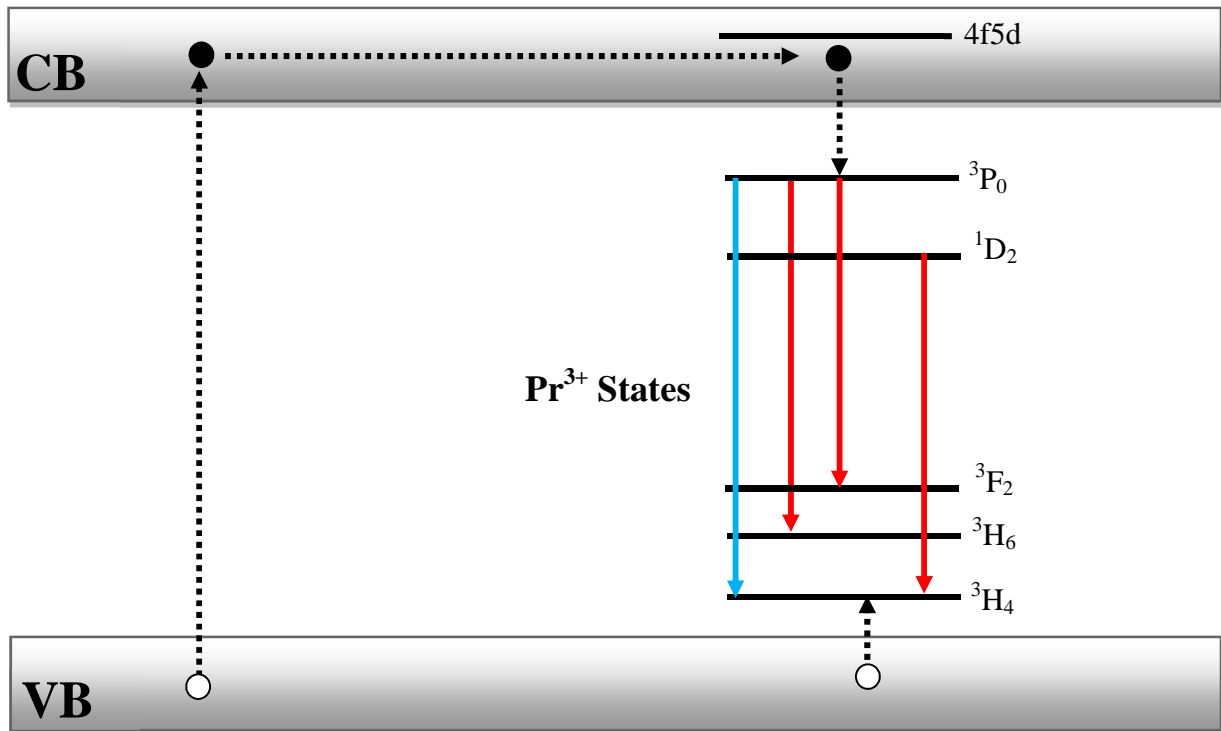

Figure 2.2: Schematic representation of the electronic structure of an extrinsic defect based phosphor.

In a situation where a phosphor has co-doped activators in one host, they will either emit independently or one will transfer energy to another one. In the later phenomenon emission will come only from the ion that receives the energy, and the earlier method is applicable when emission with different wavelengths are required [5,6]. This usually used in generating a phosphor that emits white light [5]. In the latter phosphor, the ion which transfers energy to the other one is referred to as a sensitizer and its role is only to absorb irradiation and transmit it to the other ion (activator). This occurs when the emission position of the sensitizer overlaps with the absorption energy position of the activator ion. This is interesting for enhancement of the luminescence intensity of a phosphor [4,6].

The important processes that are to be discussed next that involve luminescence mechanism are absorption (Section 2.2.1), emission by the lanthanide ions (Section 2.2.2), and the mechanism of persistent emission (2.2.3.). In this chapter, only the mechanism of persistent emission is discussed and later in the experimental chapters better knowledge is established on how persistence emission can be enhanced. Finally, a model that is employed to reveal the defect levels leading to the phosphorescence mechanism will be discussed (Section 2.2.4).

2.2.1. Absorption.

Different types of semiconductor materials are employed in a variety of applications, like: photodiodes, photovoltaic cells and others. When a semiconductor material is directed upon by an energetic radiation, the accompanying energetic particles may be absorbed, reflected or scattered by the heavy nucleus of the atoms. In general, the spectral response of practical devices depends on the energy band gap and the absorption coefficient of the material, and those of higher absorption coefficient absorb more energy compared to those of lower coefficient [7]. Focus is directed on the absorption of photons.

Optical absorption in semiconductor materials is mainly a mechanism that brings about the electronic transition from the valence band states to the states in the conduction band. In such kind of absorption, the wavelength of the incident electromagnetic radiation plays a big role in the absorption coefficient. As the energy of the excitation source increases, more electrons become excited to the states in the valence band, and therefore bring about increased photon absorption [7]. Equation 2.1 explains the relation between the absorption coefficient and the wavelength of the material.

$$\boldsymbol{\alpha = 4\pi k/\lambda} \qquad [\mathbf{2.1}]$$

where $\boldsymbol{\alpha}$ is the absorption coefficient, $\boldsymbol{\lambda}$ is the wavelength of the incoming electromagnetic radiation, and $\boldsymbol{k}$ is the extinction coefficient, which is a factor that determines how much light of a particular wavelength a material can absorb [7,8]. Absorption may change the luminescent properties of a material enormously depending on the number of impurities that may be introduced into it, and also the size of the particles used to enhance luminescence.
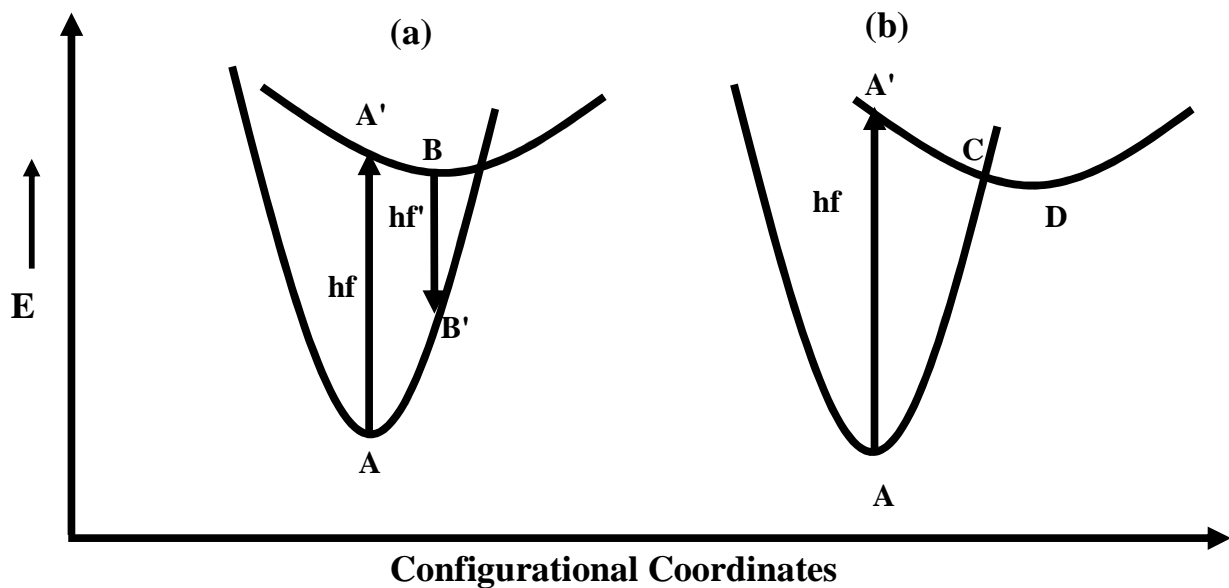
Figure 2.3: Luminescence condition for absorbed radiation energy: (a) potential curves to explain light emission, (b) potential curves used to explain quenching.

The energy absorbed from incident radiation by a luminescent material may be dissipated by an emission of light or may even be quenched (i.e. non-radiative transition as a result of losing energy to heat). The condition for luminescence is explained using potential energy curves of both the ground and excited state that have minima. Thus a stable energy position can be attained. At or near room temperature, the minima of the excited and ground state do not occur at the same configuration coordinate, because of thermal vibrations that increase interactions between the luminescent centre and its environment [9].

Figure 2.3a; absorption of an incident radiation brings about transition from point **A** → **A'**. Since the latter position is not stable, the carriers make a non-radiative transition to a stable configuration (point **B**). When de-excitation takes place, the system undergoes a transition from **B** → **B'** by an emission of electromagnetic radiation (photons). The system then again attains a stable configuration in the ground state (point **A**) from an unstable one (point **B'**) by undergoing non-radiative transition [9].

Figure 2.3b; as a result of increased thermal vibrations, the minimum of the excited state is positioned completely beyond the interaction with ground state potential curve. After the

transition **A** → **A'**, system tends to shift towards a stable configuration (point **D**). However, before this is achieved, most energy is quenched as result of the non-radiatively transition from **C** → **A** due to the strong coupling of the two potential curves [9].

However the miss alignment of the potential of the excited state and that of the ground state is not the only factor that may suppress luminescence of phosphor materials. Luminescence may be suppressed by the excess amount of atoms doped into the host (concentration quenching) [10].

2.2.2. Optical properties of the lanthanide ions.

The phosphor presented in this thesis involves emission from the 4f – 4f electron transitions of the excited lanthanide group induced luminescent centres. These transitions are possible because the ground state configuration of the lanthanides is always half filled [11]. Initially the phosphor is excited using photons, electrons, voltage, or any other source [1,11]. The excitation is either to the host material or the lanthanide, depending on the energy of the excitation source. However, direct excitation to the lanthanide does not result in effective absorption as the host material does, and eventually leading to emission with much less intensity as compared the host absorption [1]. The energy absorbed by the host material is eventually transferred to the luminescence centre non-radiatively [1,11].

The emission of the lanthanide ions originates either from the 4f – 4f transitions or from the 5d – 4f transitions. Lanthanides with an emission originating from 5d – 4f transition have an emission wavelength that changes from one host to another [12,13,14], because such transitions are symmetry dependent [12]. This effect is attributed to the stronger interaction of the 5d orbitals with the ligands of the host than the 4f orbitals, which leads the splitting of the 5d state into several energy levels [12]. The stronger the crystal field, the wider the split of these 5d levels, and the smaller the energy difference between the lowest 5d state and the 4f level [15]. Thus different crystal field strength will result emissions with different wavelengths [15].
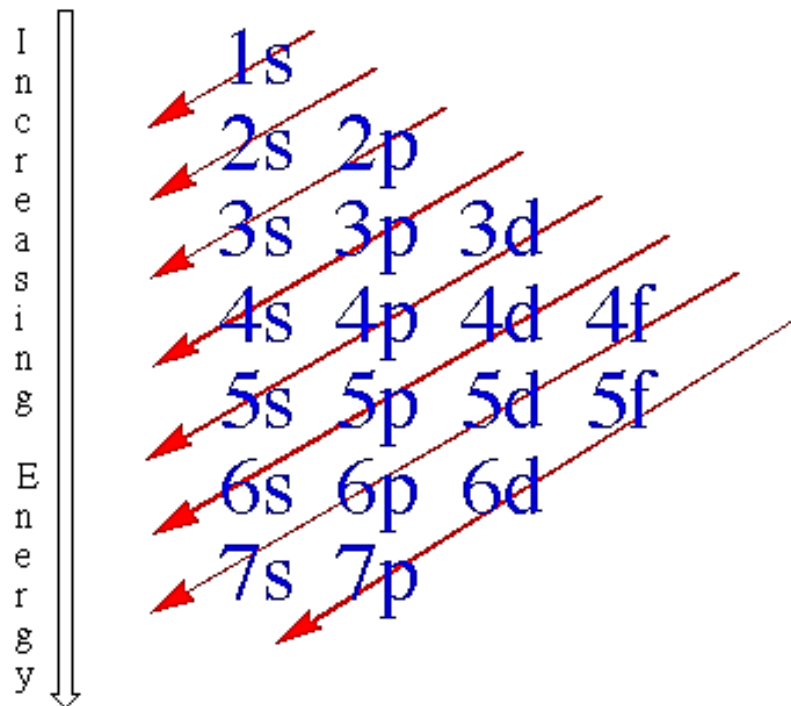
Figure 2.4: Electron configuration schematic diagram [18].

Such transitions have a spectrum with a broad peak caused by electron phonon coupling induced by the interaction of the 5d orbitals with the host material [16]. Additionally, these transitions are very fast because of the strong electron–phonon coupling interaction, which forces internal relaxation with the 5d configuration to be high [17]. This effect leads to the population of electrons accumulating fast on the 5d edge, from where they will immediately de-excite to the the 4f level [17]. Such transitions are responsible for the fluorescence emission [17].

The 4f – 4f transitions are identical in different host materials. If there is a change, then it is very slight, because such transitions are not symmetry dependent [11]. This effect is attributed to the shielding of the electrons in the 4f shell by the outer 5s, 5d and 6s shells (Figure2.4), which are completely filled [11]. The electrons of the 4f shell are not influenced by the outer environment, which leads to electrons de-exciting from one state to another without losing energy to the environment. This leads to them having spectra with sharp peaks [17].

$$\text{I} \qquad \text{II} \qquad \text{III}$$

$$^{2S+1}L_J(\mu)$$

$$^{2S+1}L_J$$

$$^{2S+1}L$$

$$\sim 10^2 \text{ cm}^{-1}$$

$$\sim 10^3 \text{ cm}^{-1}$$
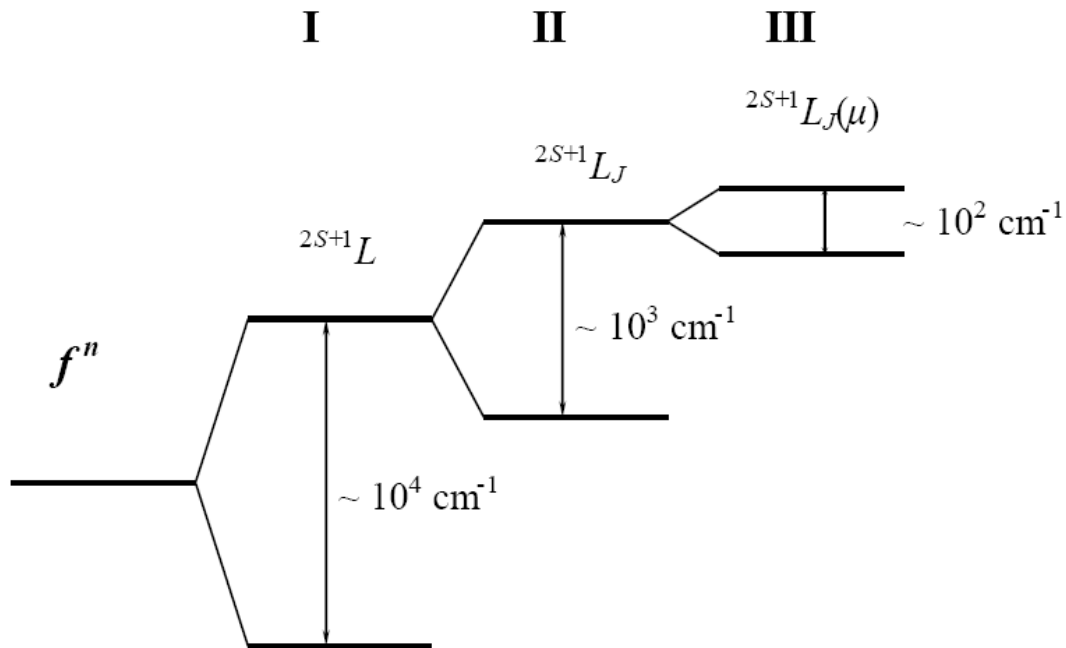
$$f^n$$

$$\sim 10^4 \text{ cm}^{-1}$$

Figure 2.5: Splitting of energy levels of $4f^n$ electronic configuration due to: I – Coulomb interaction; II – spin-orbit interaction; III – crystal-field interaction.

The variety of states of the 4f levels that spread across the band gap of a material (Figure 2.2) is caused by the splitting of the $4f^n$ to ^{2s+1}L because of the columbic interactions from the repulsive forces that exists between the electrons in the 4f shell. S and L are the quantum numbers associated with the total spin and the total orbital angular momentum of the electrons. Furthermore, the electromagnetic interaction between the electron spin and the magnetic field created by the electron's motion causes further splitting to each of the ^{2s+1}L levels into $^{2s+1}L_J$ states that are $(2J + 1)$ in quantity. J is the quantum number associated with total angular momentum. Finally, the slight interaction of the 4f electrons with the crystal field causes a split of each of the $^{2s+1}L_J$ states into $^{2s+1}L_{J(\mu)}$ manifolds that are $(2J + 1)$ in quantity [11].

The above mentioned states can be related for Pr^{3+} ions as; ^{2s+1}L energy levels denoted as S, P, I, D, G, F and H states (Figure 2.6). The $^{2s+1}L_J$ states are denoted as the $^3H_4$, $^3H_5$, and $^3H_6$, which are all split into $^{2s+1}L_{J(\mu)}$ manifolds denoted as $^3H_{4(1)}$, $^3H_{4(2), ...}$, and $^3H_{4(9)}$. Typical sharp emission lines of Pr^{3+} are observed from the $^1D_2$ to $^3H_4$ and $^3P_0$ to $^3H_4$ transitions with wavelengths fixed at

349 ± 3 and 613 ± 3 nm, respectively [1]. These are fixed because of the strong shield of the 4f shell by the outer 5s, 5d and 6s shells [11].
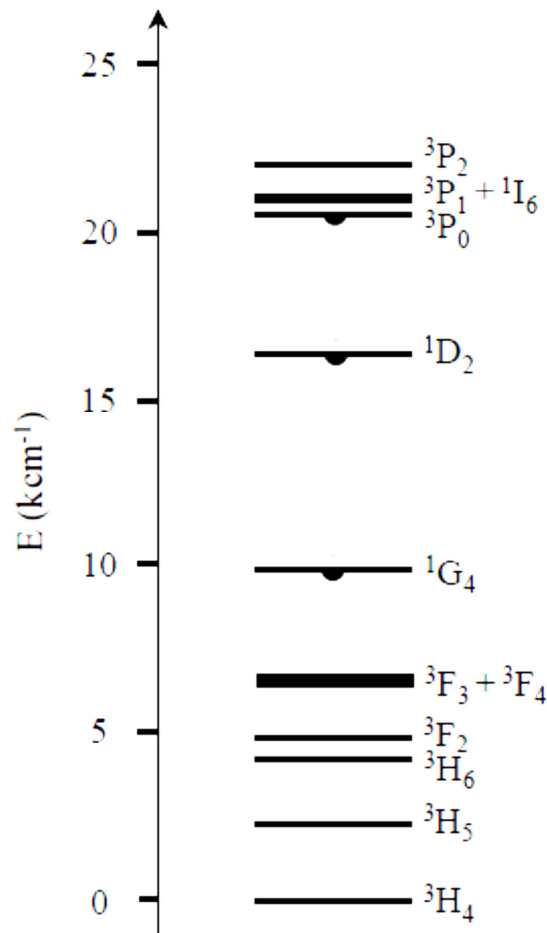

Figure 2.6: The energy level Scheme of Pr^{3+} ions.

The role of the host material above is limited to the crystal, field which determines the nature of the emission of the lanthanide ion. In this section, we extend the role of the host material to effects of the intrinsic defect levels, particularly the oxygen vacancies, which have a role of attracting the electrons and releasing them gradually, leading to persistent emission [1].

2.2.3. The mechanism of persistent luminescence.
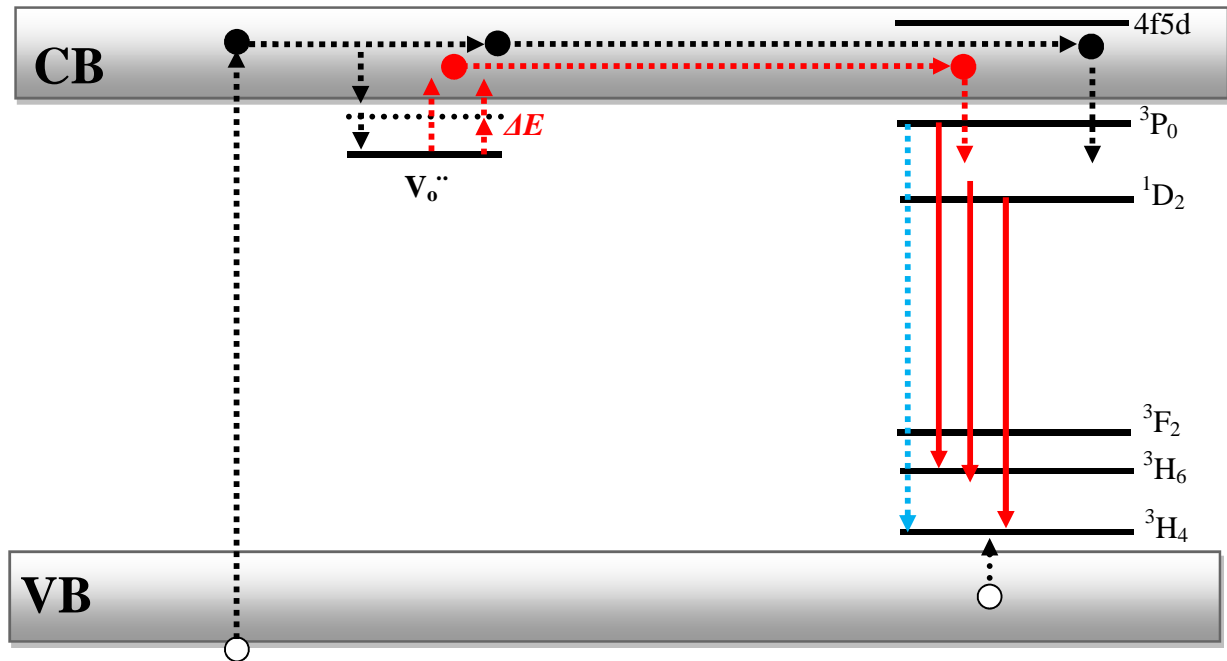
Figure 2.7: Schematic diagram to illustrate the phenomenon of persistent emission.

Oxide materials have oxygen vacancies, which have energy states that overlap with the energy of the band gap (Figure 2.7). These states are positioned at the donor level and are written as the $V_o^{..}$ or $V_o^{.}$ centres, with the former denoting double positive charge and the latter a single positive charge. Their positive charge exerts a coulombic force to the electrons in the conduction band and attracts them to donor level [1]. The persistent luminescence will only be supported by the traps that are shallow enough to have the trapped electrons, excited back to the conduction band by thermal energy that is equal to room temperature. From the conduction band they will then de-excite to the luminescent centres from where emission will emanate [18].

The phenomenon of persistent emission is enhanced when the density of the shallow electron trapping centres is increased [19]. The electrons that are trapped within deeper electron trapping centres, require temperatures higher than room temperature in order to stimulate the electrons back to the conduction band. Thermal bleaching the electron trapping centres using higher temperature is significant in quantifying the electron trapping centres present in a particular

material. This phenomenon, which is known as thermoluminescence is discussed in the following section (2.2.4).

2.2.4. Thermoluminescence mechanism

Thermoluminescence is the thermally stimulated emission of light from an insulator or a semiconductor following the previous absorption of energy from ionizing radiation. Upon radiating a material with ionizing radiation such as UV, alpha, beta & gamma particles, the electrons that are excited from the valence band may be trapped by the electron traps and some are trapped when they de-excite from the conduction band. The electrons that are trapped within the trap centres will remain in the traps until they are supplied with sufficient energy to stimulate and release them from traps. The electrons stimulated to the conduction band, then recombine at the recombination centres which are point defects and give luminescence (as illustrated in Figure 2.7) [20,21,22,23].

The energy (activation energy) required to excite the electrons from the traps to the conduction band, is used to trace the energy distribution (depth of the traps) of the trap centres. There are several methods that have been adopted to approximate the depth of the electron traps, such as [23,24]:

1. Initial rise method
2. Chen's peak shape method
3. Variable heating rate method
4. Glow curve deconvolution methods

Along with these methods; an important aspect that allows us to choose which method to use in evaluating these traps depends on the nature of kinetics which are followed by the electrons when they are detrapped. Possible kinetics are [23,24]:

1. First order Kinetics
2. Second order Kinetics
3. General order kinetics which can be both First and second order Kinetics or none of the two.

The first order (monomolecular) kinetics assume no interaction between the trapping centres and the second order (bimolecular) kinetics assume interaction of trapping centres, which leads to electron retrapping [25,26]. As mentioned above, there are several methods by which a glow curve can be analyzed to obtain the activation energy and the detrapping kinetics. This section focuses more on the theoretical background of the initial rise (IR), Chen's peak shape method and the variable heating rate method.

2.2.4.1. Initial rise method

For any typical experiment of thermally stimulated luminescence, the sample is heated inside the system at a linear heating rate ($\beta = dT/dt$). The electrons that radiatively recombine with the holes at the recombination centres give light with an intensity that is equal to the rate of recombination, which is given by (Eq. 2.2):

$$I(t) = -\frac{dn_e}{dt} \qquad [2.2]$$

where n_e corresponds to the number of the trapped electrons [24]. According to the Randal-Wilkins model [24], the thermoluminescence intensity can also be expressed by Eq. 2.3 for the first order kinetics.

$$I(t) = -\frac{dn_e}{dt} = nse^{-E/kT} \qquad [2.3]$$

E is the activation energy of the electrons within the trap centres, s is the pre exponential factor, which is constant and k is Boltzmann constant [24]. Garlick and Gibson [24] extended this concept further by supplying an expression (Eq. 2.4) for the thermoluminescence emission for the low temperature interval of the glow curve, which is independent of the kinetic order.

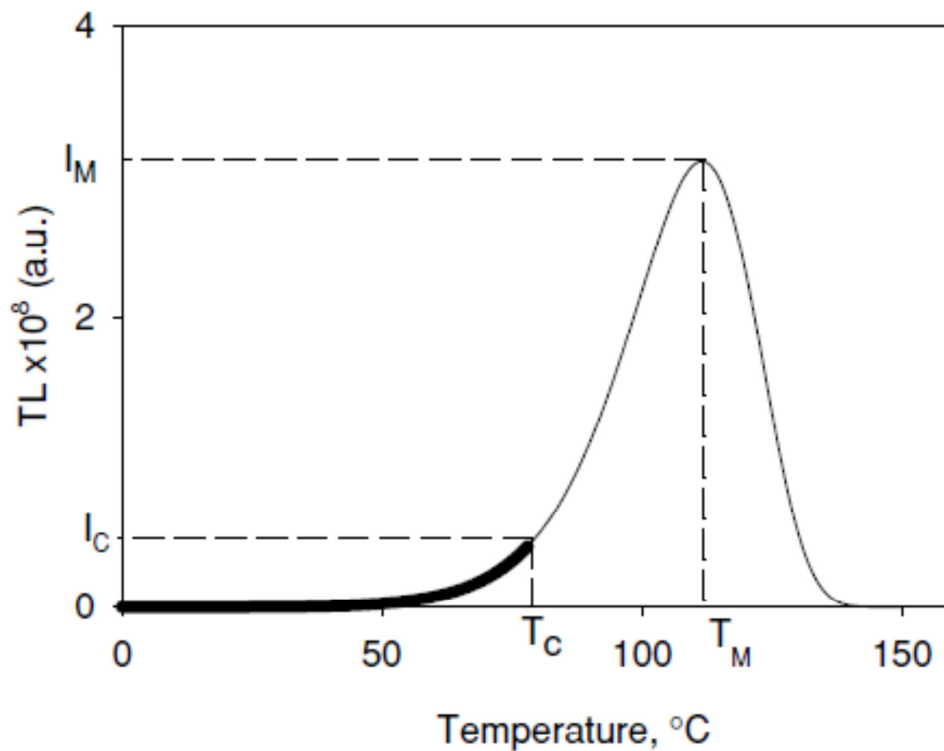$$I(t) \propto e^{-E/kT} \qquad [2.4]$$

Figure 2.8: A figure illustrating the region of the initial rise method

The expression is valid under the condition that $n(T)$ is constant at low temperature of the glow curve, since it is not dependent on T in that region. This assumption is valid upto a temperature (T_c) corresponding to TL intensity (I_c) below 15% of the maximum intensity (I_M) as illustrated in Figure 2.8 [24].

This allows us to obtain the activation energy from the slope of the linear curve obtained by plotting $\ln(I)$ vs $1/kT$, whose slope is $-E$ [21]. The model of analysis is then called initial rise method.

2.2.4.2. Chen's peak shape method

The peak shape method can be used to determine the activation energy and the nature of kinetics based on the geometrical factor ($\mu = \delta/\omega = (T_2 - T_M)/(T_2 - T_1)$) parameters obtained from a glow

curve (Figure 2.9). Along with the geometrical factor, the monotonic factor (b) can be determined, which provides us with the information about the order of kinetics [24].

The activation energy (Eq 2.5) can be approximated from the geometric factors either working with the FWHM (ω), lower temperature parameter (τ) or the upper temperature parameter (δ) from Eq. 2.5 [20,24]:
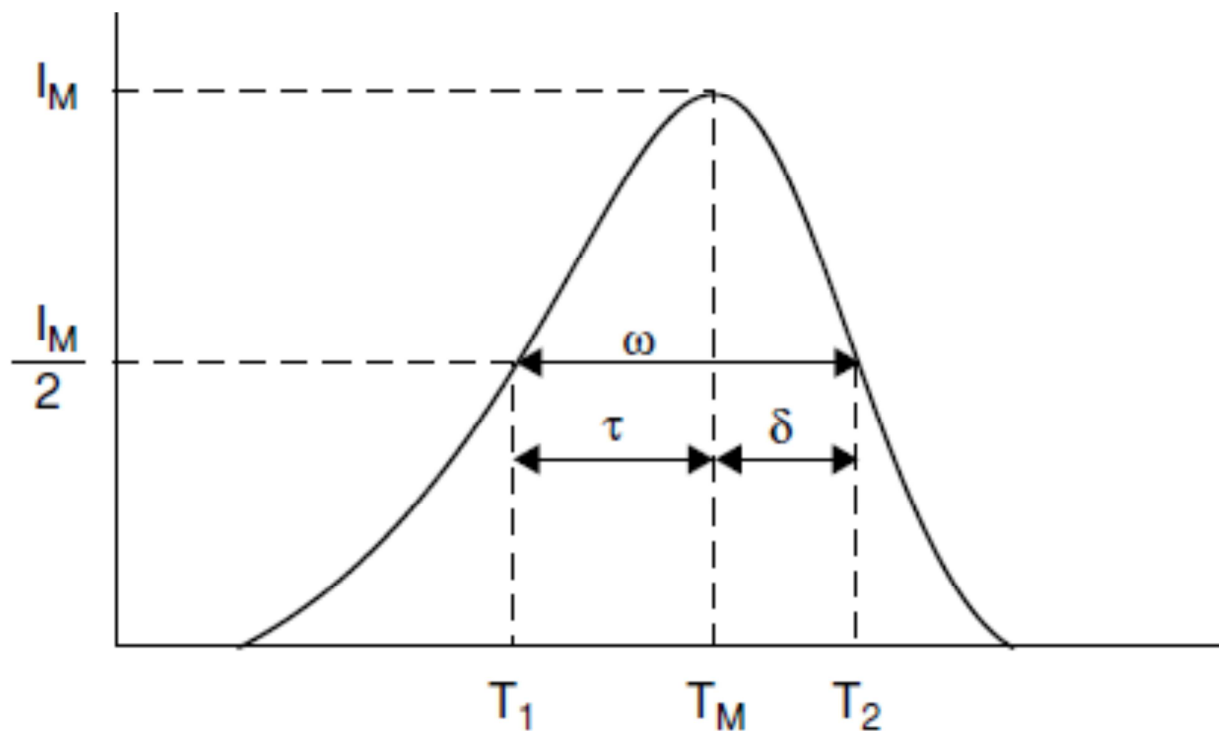
Figure 2.9: Figure showing the geometrical plots using Chen's peak shape method

$$E_\alpha = A_\alpha \left(\frac{kT_m^2}{\alpha}\right) - 2b_\alpha kT_m \qquad [2.5]$$

The geometric parameters that are used in the above equation are incorporated in Chen's general equation of the activation energy (Eq. 2.5) using A_α and b_α asconstants where α can either be τ, ω or δ to give the following assumptions [20,24]:

$A_\tau = 1.51 + 3\ (\mu - 0.42)$ accompanied by $b_\tau = 1.58 + 4.2\ (\mu - 0.42)$

$A_\delta = 0.976 + 7.3\ (\mu - 0.42)$ accompanied by $b_\delta = 0$

$A_\omega = 2.52 + 10.2\ (\mu - 0.42)$ accompanied by $b_\omega = 1$

2.2.4.3. Variable heating rate

The variable heating rate (β) method allows the approximation of the activation energy (E) by considering the temperature (T_M) at maximum intensity position shift when the heating rate changes by which the sample is heated. Various models have been reported upon working with this model by Mckeever [24], beginning from the one suitable for first order kinetics by Christodoulides and Ettinger going to the one modified by Chen and Winer for general order. The latter requires prior knowledge of the order of kinetics before computing for the activation energy. Hoogenstraten showed that the activation energy can be obtained from the plot of $\ln\left(\frac{T_M^2}{\beta}\right)$ vs $1/{kT_M}$, from which the slope is E [20,24].

2.3. Synthesis Method.

The samples used in the process were prepared by solid state chemical reaction, and a short description about is given in this section. Solids exhibit the most condense phase that is unified into a crystal structure that is often crowded by impurities. The molecular behaviour of the different phases of matter is different in that gases have molecules that randomly wander in space. When energy is removed from such molecules they condense to a liquid phase, and similarly liquids condense to solids when their energy is removed. Solids have their atoms closely packed into a rigid structure that may be a regular geometric lattice (*crystalline solid*) or an irregular geometric lattice (*amorphous solid*) [27].

Solid state reaction is the fabrication of solid materials either by direct transformation of a single solid material from one phase to another one through decomposition, or by directly mixing a solid material with other substances (*gases, liquids or other solids*) through ion interdiffusion to create multi component solid materials, at very high temperature. The solid state reaction may be prepared in the presence of the a fluxing agent that acts in facilitating crystal structure formation and also helps in achieving doping processes at very low temperature. The fluxing component has an additional ability of improving the surface morphology of the crystals. Solid state reactions are known to fabricate complete products of a single phase due their high temperature [27, 28].

2.4. References

1. L.L. Noto, Red emission of Praseodymium ions, 2011, M.Sc. Thesis, university of South Africa, South Africa.

2. Y. R. Jong, K.H. Yoo, S.M. Park, J. Korean Phys. Soc. **53** (2008) 110.

3. V. Kumar, H.C. Swart, O.M. Ntwaeaborwa, R.E. Kroon, J.J. Terblans, S.K.K. Shaat, A. Yousif, M.M. Duvenhage, Mater. Lett. **101** (2013) 57.

4. Angiuli Fabio, Energy transfer and charge transfer processes in luminescent materials, 2013, Ph.D. Thesis, Universita Degli Studi Di Parma, Italy.

5. M.A. Mickens, Z. Assefa, J. Lumin. **145** (2014) 498.

6. H.A.A. Seed Ahmed, O.M. Ntwaeaborwa, R.E. Kroon, Curr. Appl. Phys. **13** (2013) 1264.

7. B.G. Yacobi, ***Semeconductor materials – An introduction to basic principles***, 2003, Kluwer Publishers, New York, p183.

8. A. Kitai, ***Luminescent materials and applications***, 2008, John Wiley & sons, England, p264.

9. G.F.J. Garlick, ***Luminescent materials***, 1949, Oxford university press, London, p3.

10. M.S. Dhlamini, ***Luminescent properties of synthesized PBS nanoparticle phosphors***, 2008, [Thesis], University of Free State, South Africa.

11. Isabelle Etchart, Metal oxides for efficeinet infrared to visible upconversion, 2010, Ph.D. Thesis. University of Cambridge, United Kingdom.

12. M.F. Reid, Electronic Structure and Transition Intensities in Rare-Earth Materials, 2013, University of Canterbury, New Zealand.

    a. http://www2.phys.canterbury.ac.nz/~mfr24/electronicstructure/00electronic.pdf

13. M. Marius, E.J. Popovici, L. Barbu-Tudoran,E. Indrea, A. Mesaros, Ceram. Int. http://dx.doi.org/10.1016/j.ceramint.2013.11.079.

14. J. Jiang, X Zhang, W. He, M. Zhang, J. Liu, X. Zhang, Opt. Commun. **285** (2012) 465.

15. P.A. Rodnyi, P. Dorenbos, G.B. Stryganyuk, A.S. Voloshinovskii, A.S. Potapov, C.W.E. van Eijk, J. Phys.: Condens. Matter. **15** (2003) 719.

16. Z. Pan, Y.Y. Lu, F. Liu, nat. mater. 20 Nov. 2011, DOI:10.1038/NMAT3173.

17. E. Sarantopoulou, Z. Kollia, A.C. Cefalas, V.V. Semashko, R.Y. Abdulsabirov, A.K. Naumov, S.L. Korableva, T. Szczurek, S. Kobe, P.J. McGuiness, Opt. Commun. **208** (2002) 345.

18. H.C. Swart, J.J. Terblans, O.M. Ntwaeaborwa, E. Coetsee, B.M. Mothudi, M.S. Dhlamini, Nucl. Instr. Meth. Phys. Res. B **267** (2009) 2630.

19. L.L. Noto, S.S. Pitale, M.A. Gusowki, J.J. Terblans, O.M. Ntwaeaborwa, H.C. Swart, Powder. Technol. **237** (2013) 141.

20. McKeever SWS, *Thermoluminescence of Solids*, 1985, Cambridge University Press, New York.

21. Kirsh Y, *Kinetic Analysis of Thermoluminescence: Theoretical and practical aspects*, phys. Stat. sol. (a) **129** (1992) 15.

22. Veronese I, *The thermoluminescence peaks of quarts at intermediate temperatures and their use in dating and dose reconstruction* [**Thesis**], 2005, UniversitaDegliStudi Milano.

23. Furetta C, *Handbook of Thermoluminescence*, 2003, world scientific publishing, Singapore.

24. Pagonis V, Kitis G, Furetta C, *Numerical and practical exercises in thermoluminescence*, 2006, Springer and business Media Inc. USA.

25. W. Liwei, X Zheng, T. Feng, J. Weiwei. Z Fujun, M. Lijian, J. Rare Earths **23** (6) (2005) 672.

26. H.F. Brito, J. Hassinen, J. Holsa, H. Jungner, T. Lamanen, M.H. Lastusaari, M. Malkanmaki, J. Niittykoski, P. Novak, L.C.V. Rodriguess, J. Therm. Anal. Calorim. **105** (2) (2011) 657.

27. C.H. Bamford and C.H.Tipper, *Comprehensive chemical kinetics,* Vol 22, 1980, Elsevier Scientific publishers, New York, p41.

28. A.S. Wadhwa and H.S.Dhaliwal Er., *A Texbook of Engineering Material and Metallurgy*, 2008, University Science press, India, p115.

"All I have seen teaches me to trust the creator for all I have not seen."

— Ralph Waldo Emerson

3

Experimental Techniques

The phosphors were prepared by solid state reaction, and their luminescence dynamics were probed using spectroscopic techniques to yield luminescence information. Several experimental techniques were used to achieve this goal, such as X-ray diffraction, Scanning electron microscopy, Photoluminescence spectroscopy, Thermoluminescence spectroscopy, Ultraviolet-visible absorption spectroscopy, X-ray photoelectron Spectroscopy and the Time of flight secondary ion mass spectroscopy. The aim of this chapter is to provide better understanding of these techniques.

3.1.   X-ray Diffraction

X-ray diffraction is an analytical technique primarily used for phase identification of crystalline compounds, and it can also be used to provide information of the unit cell dimensions. Information provided by this technique is based on constructive interference of monochromatic X-rays that are generated within an X-ray tube and a crystalline sample that is mounted on the sample holder (figure 3.1). The waves of the x-rays incident to the crystal compound create an oscillating electric field that interacts with electrons of the compound atoms. The electrons coherently scatter the incoming electromagnetic radiation. Diffraction occurs when the atoms arranged in a periodic array scatter radiation at specific angles [1]. The rays that interact to produce constructive interference consequently result in Bragg peaks observed on the pattern. The X-rays are produced inside an X-ray tube (X-ray source in figure 3.1) that contains a copper block that is cooled down using water. A metal is attached to the copper, which forms an anode,

and a cathode made of tungsten filament is placed opposite to the anode. The tungsten filament is heated up and a potential difference is applied between the anode the tungsten cathode to accelerate electrons from the warm tungsten filament to the anode. The K_β and K_α Cu X-rays with 1.39 and 1.54 Å wavelengths, respectively, are produced when the electrons strike the anode. A Nickel filament, which absorbs wavelengths below 1.5 Å is used filter the K_β radiation. The K_α X-rays are finally used to characterise the sample. The detector produces an electrical signal when exposed to radiation, which is converted into a pattern [2,3].
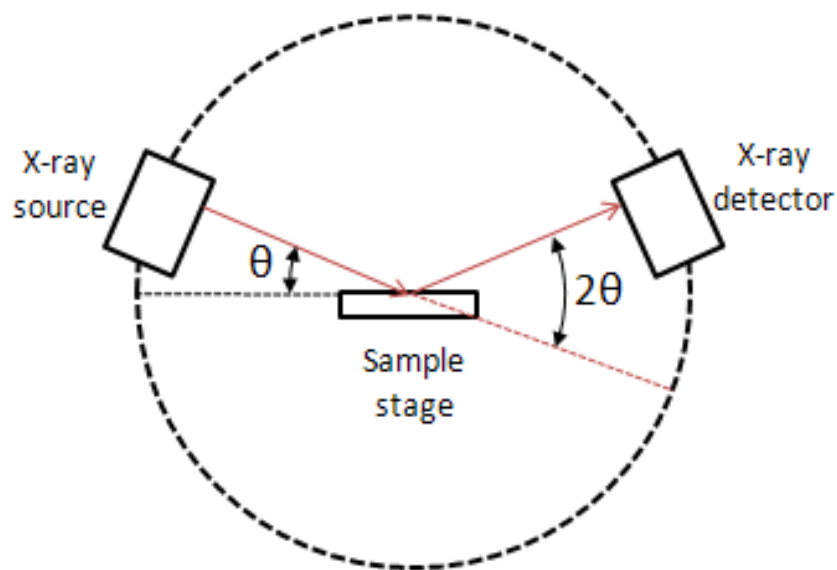
Figure 3.1: The X-ray diffraction system: D8 Advance Bruker [2]

3.2.   Scanning Electron Microscopy

Scanning electron microscopy is a surface technique that is essentially designed to capture images of three dimensional objects on specimen surfaces. Secondary and backscattered electrons emerge from the specimen surface, when it is probed by a primary electron beam with energy between 5 – 30 keV from the electron gun. The primary electrons are focused into a fine spot using the condenser and objective lenses (figure 3.2), which is then scanned across a certain area, from where the secondary electrons are collected. When secondary electrons arrive at the secondary electron detector, they converted into an image is formed. The secondary electrons are

used to extract topographic contrast, and backscattered electron images are used to extract compositional differences on the surface [4]. The secondary electron images are of importance in this study to identify possible particle agglomeration.
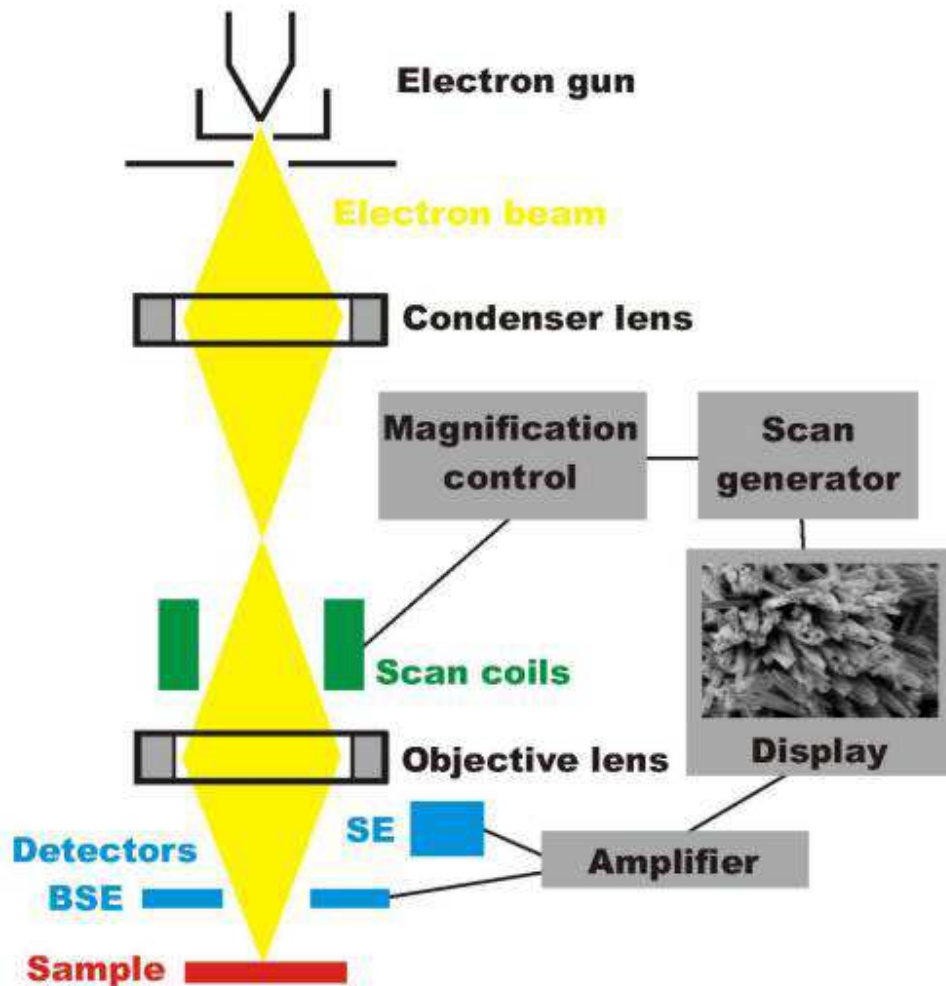
Figure 3.2: Schematic diagram showing the electron beam column in Secondary Electron Microscopy [5].

3.3. Photoluminescence Spectroscopy

Photoluminescence is a resulting optical transition when a material (e.g. phosphor) absorbs electromagnetic waves of sufficient energy to excite electrons from the valence band to the conduction band. These electrons will de-excite to the luminescence centres, from where the electron de-excite radiatively from higher states to lower states to recombine with the holes. A

technique used to characterize such properties is referred to as photoluminescence (PL) spectroscopy.
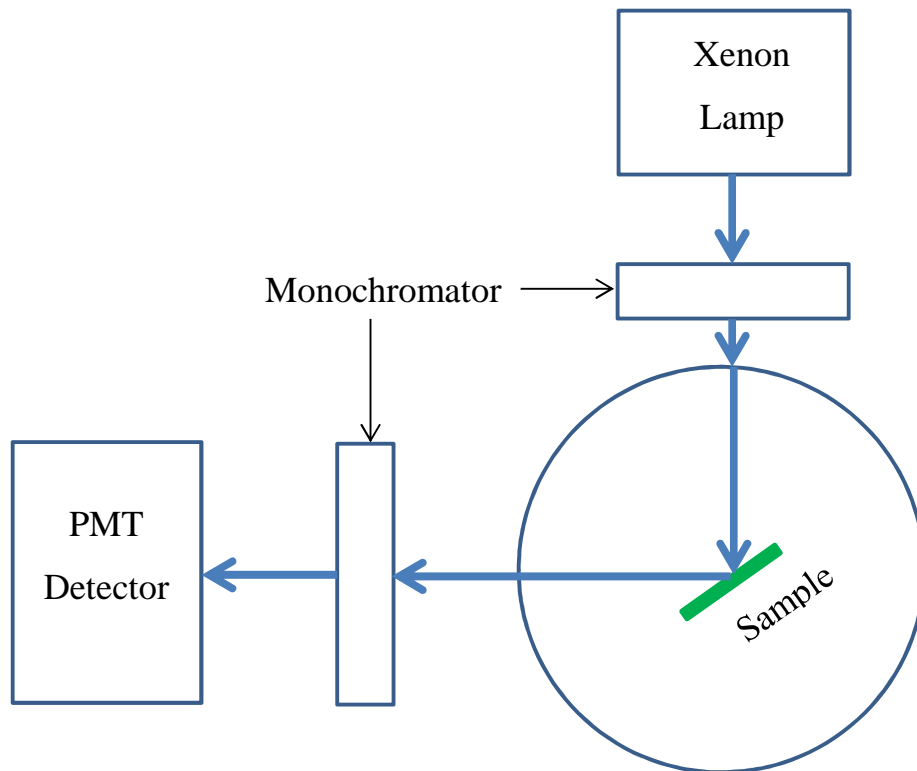
Figure 3.3: Varian Carry-Eclipse spectroscoflourometer setup schematic [8].

Such a system can be achieved using a laser, a xenon lamp or synchrotron radiation to generate the electron hole pairs in the electron structure of a sample, and a photon detector to analyze the light from the sample. The output spectrum of the detected emission is displayed as PL intensity as a function of the emitted light wavelength. Most advanced PL spectroscopy techniques can be used to measure photoluminescence, photoluminescence excitation centres and phosphorescent lifetimes. Amongst such techniques is the Varian-Carry Eclipse system (Figure 3.3), which uses a xenon lamp as a source of excitation [6,7], and photomultiplier tube (PMT) to detect the emission from the sample .

3.4. Thermoluminescence Spectroscopy
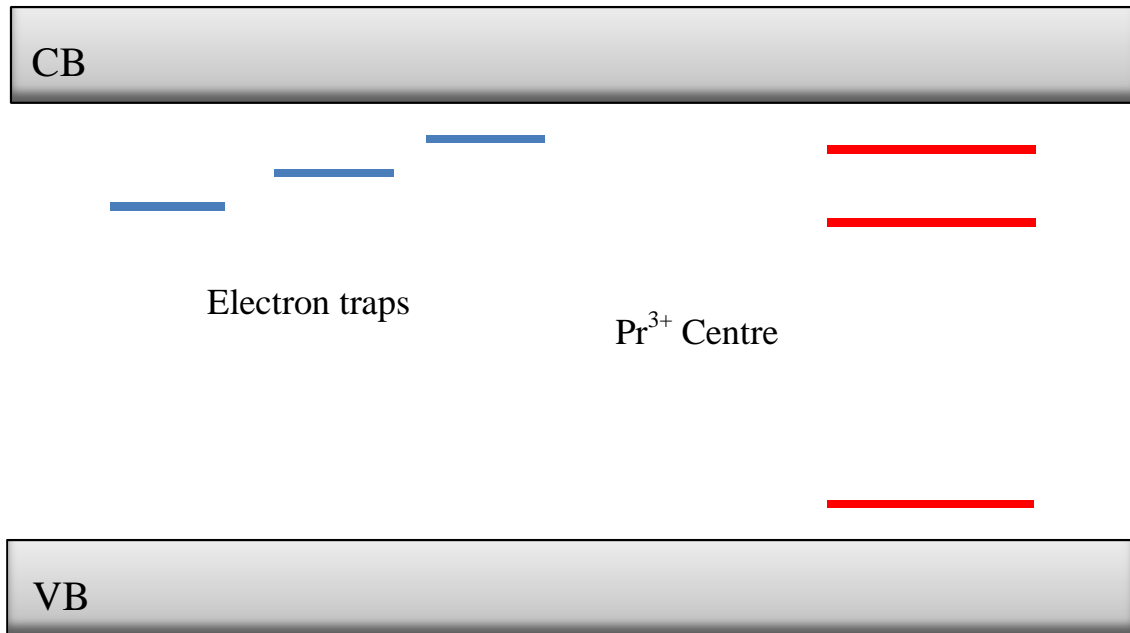
Figure 3.4: Mechanism behind thermoluminescence.

It is a natural ability of materials fabricated at high temperatures, especially the oxides to have defects in their lattice structure. These defects generate localized energy levels positioned within the forbidden band gap of a material and they act as traps of both the holes and electrons upon excitation (Figure 3.4). When the material is heated after it had been irradiated, the trapped carriers accumulate sufficient energy to jump out of the trap sites. These released carriers will then eventually reach the luminescence centre [9,10]. The resulting luminescence is used to approximate the depth of the trap levels within the forbidden region, and thermoluminescence spectroscopy is used to reveal such information. Such information is extracted from the glow curve which is the resulting thermoluminescence emission as function of temperature [9,10].
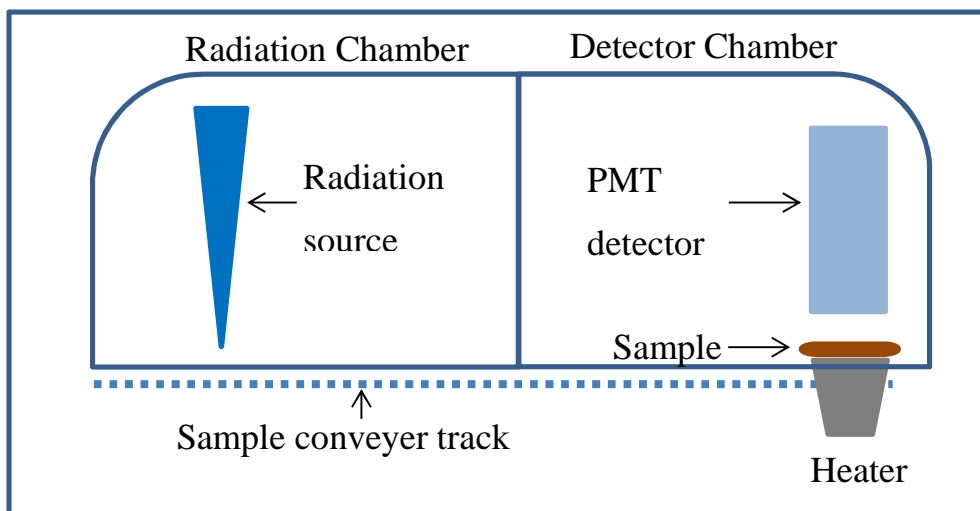
Figure 3.5: Schematic representation of the TL system components.

The thermoluminescence spectroscopy systems which were used in this study were the Riso - TL/OSL-DA-20 that is equipped with a beta particles from ^{90}Sr beta radiation source with a dose rate of 0.1028 Gy/s. The luminescence detection for the TL/OSL system consists of a photomultiplier tube (PMT) with a U340 Schott filter that is effective in the 340–380 nm wavelengths. The system had a heater, which could heat up to 700 ^{o}C. The chamber, which housed the PMT was cooled to almost 0 ^{o}C using a chilled nitrogen gas. A typical setup of the Riso - TL/OSL-DA-20 is illustrated in Figure 3.5. The other system was a TL 10091, NUCLEONIX spectroscopy, which used a 254 nm UV lamp and had a heater that heated upto 600 ^{o}C.

When the electromagnetic radiation in a certain medium is projected towards a solid material, the light waves are reflected, absorbed or transmitted. If the waves are incident on a metallic material, they are specular (Figure 3.6) reflected backwards upon arrival at the surface. Non – metallic materials may simultaneously absorb and reflect or absorb, reflect and transmit the incoming waves. The latter applies to materials that are sufficiently transparent to allow a certain portion of the light waves to pass through their structure. The ability of materials to absorb and reflect is an important parameter that is used by the UV/Vis spectroscopy to identify how phosphor materials respond to electromagnetic radiation. Light reflection by solids occurs in

several ways. However of importance in the context is diffuse reflectance (Figure 3.6), which occurs when light is projected onto rough surfaces like that of powder materials [11,12].

3.5. Ultraviolet-Visible absorption Spectroscopy

Diffuse Reflection

Incident Light

Specular Reflection
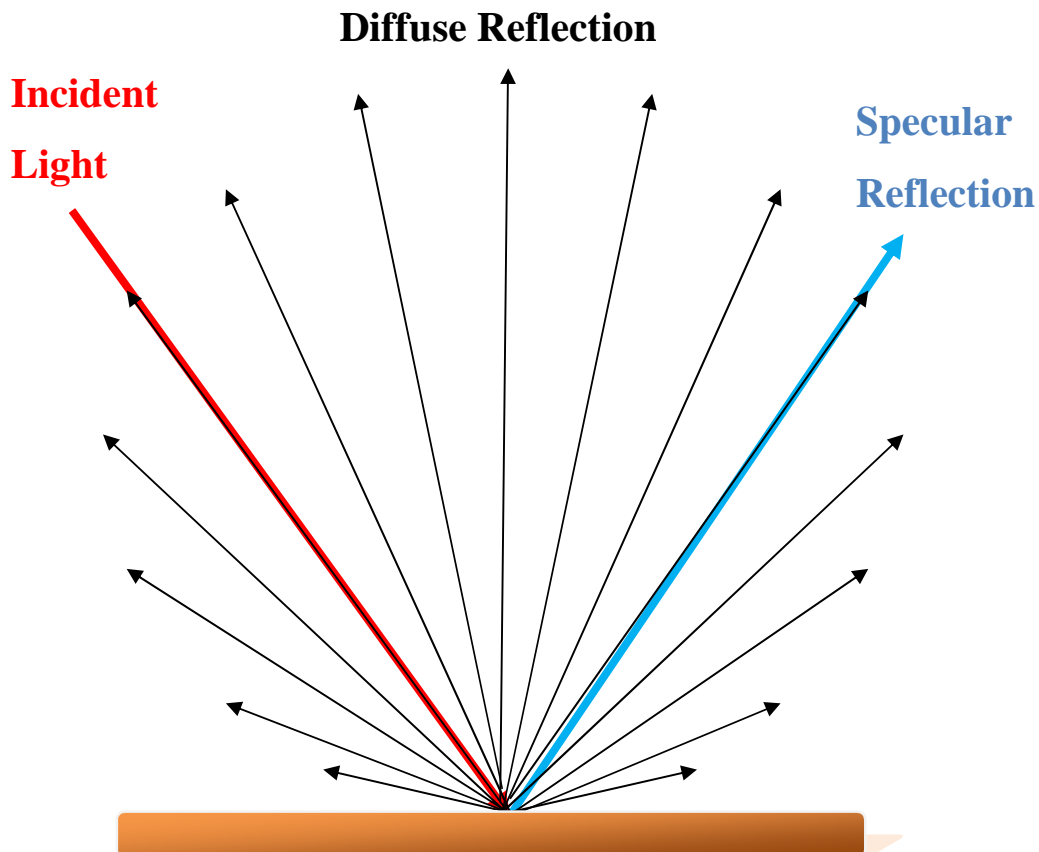
Figure 3.6: Incident light reflection on the surface on a solid material.

The UV/Visible spectroscopy is equipped with two source lamps: Deuterium (from about 10 nm to 330 nm) and Tungsten lamps (300 nm to wavelength greater than 3000 nm). The lamps are used to irradiate the sample, with the Deuterium used from 200 nm up to 319 and then shift to Tungsten up to 1000 nm. Upon irradiating the sample, the source beam is split into two beams. One beam is directed to the sample and the other is sent to the detector as a reference. The sample is positioned inside an integrating sphere (Figure 3.7) that collects the diffusely scattered light (Figure 3.6), by the sample. Some of the incident light is absorbed by sample. The collected

light eventually falls onto the detector, which subtracts the collected light from the source light to determine the amount that has been absorbed. The detectors used in this system are the PbS and PMT which measuring the near infrared region, and Ultraviolet and visible region, respectively. This technique allows determination of the absorbance characteristics of phosphor materials [13].
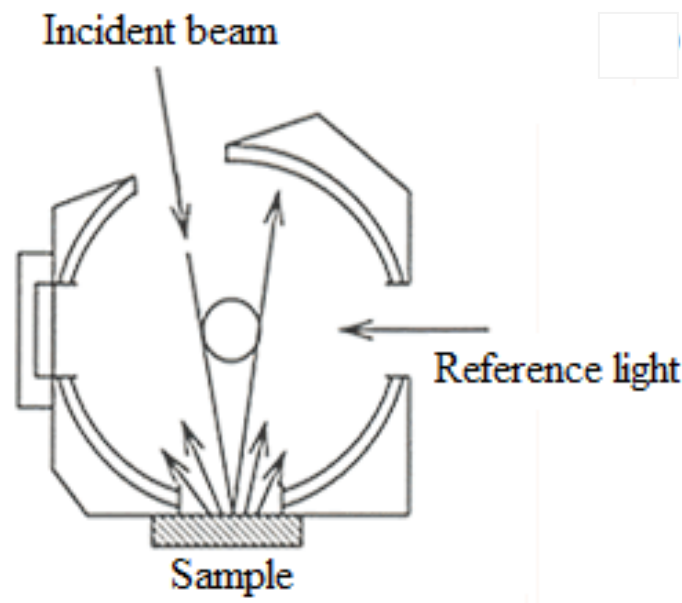
Figure 3.7: Schematic of the integrating sphere interior.

3.6. X-ray Photoelectron Spectroscopy

The X-ray photoelectron spectroscopy (XPS) is a technique used to probe elemental composition and the chemical state on the surface of a specimen [14]. XPS PHI 5000 versaprobe using 100 μm, 25 W and 15 kV Al monochromatic x-ray beam (Figure 3.8) was used to probe such information in the present study. During an analysis, an Aluminum X-ray beam is irradiated on the surface of the specimen, and it ionized the photoelectron, which is knocked off the surface and into the vacuum (Figure 3.9). This electron is then attracted to the detector of the system using potential difference and accelerated along the hemispherical analyser from where its kinetic energy will be used to determine the binding energy of the surface of the specimen. Such is obtained using equation 3.5 [15,16]
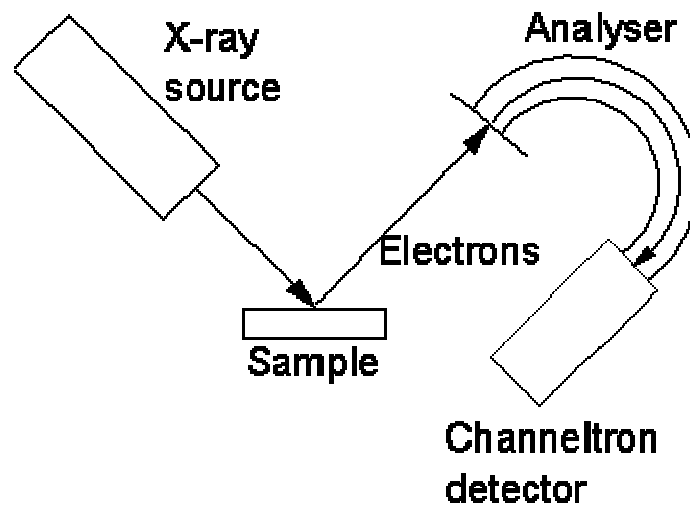
Figure 3.8: Schematic showing the photo electron path from specimen to the detector [17].

$$E_{binding} = E_{photon} - E_{kinetic} - \emptyset \qquad \textbf{[3.1]}$$

where the binding energy is that of an electron emitted as result of electron configuration within the atom, the photon energy being that of the X-ray used, kinetic energy is that of the photoelectron and $\emptyset$ is the work function of the detector [16]. The binding energy of each atom is unique; hence the energy peaks of different atoms have different heights.

XPS earned its popularity by its high ability of chemical analysis. It is a surface sensitive in that it analysis at 2nm depth, and its lateral resolution is greater than 150 μm. However it is limited in elemental composition in that it cannot detect H_2 and He, because their electrons come from the valence band. This causes them not to have unique energy peaks [15,18].
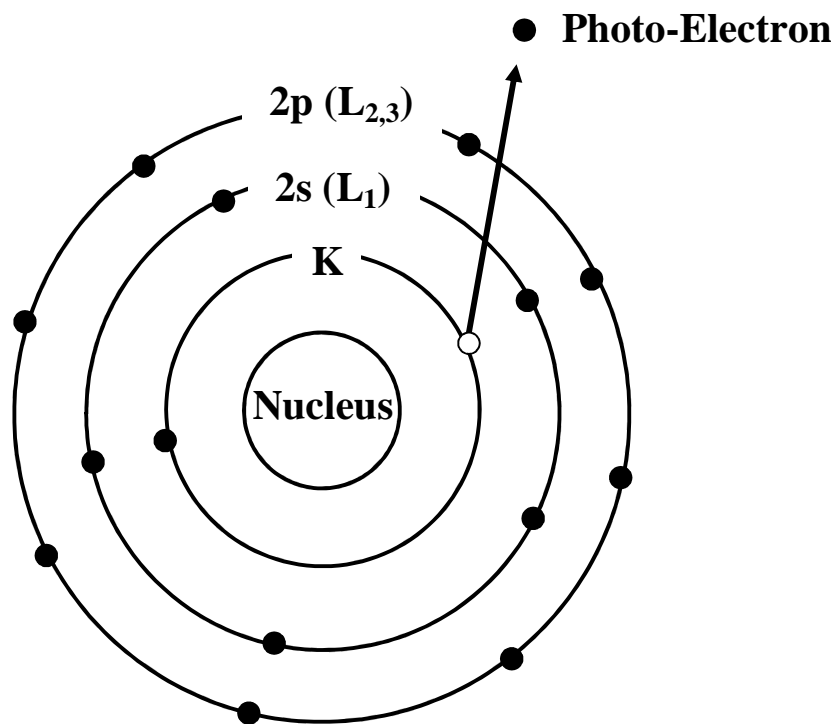
Figure 3.9: Mechanism behind the operation of XPS.

3.7. Time of Flight Secondary Ion Mass Spectroscopy

The Time of Flight Secondary Ion Mass Spectroscopy (ToF – SIMS) shown in Figure 3.10 is a surface technique that is used to identify elements on the surface, do elemental mapping and depth profiling. Bi^+ ion beam is used as the primary source to probe the surface of a sample, from an ion gun that is operated at 30 000V with a beam size of 200 nm in the imaging mode and 5µm in the spectroscopy mode. During an analysis a pulsed (less than one nanosecond) Bi^+ ion beam is irradiated onto the surface of the sample, where it dissociates the outermost surface layer (0.3 – 1 nm) of the sample. This leads to the removal of the ions (secondary ions) forming the outer layer on the surface, which are then accelerated into a column where they fly a distance that is approximately two meters to get to the detector.
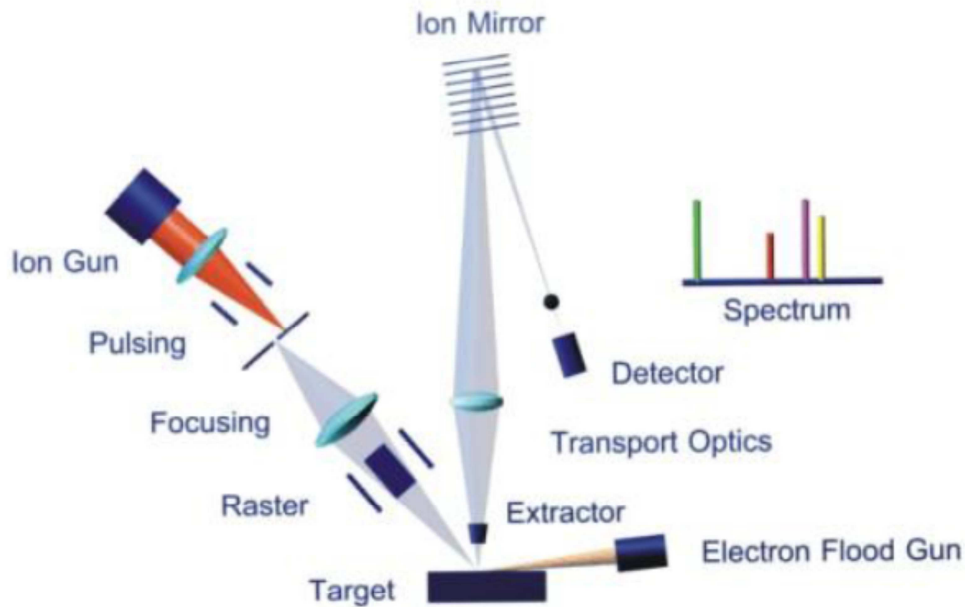
Figure 3.10: ToF-SIMS schematic from IONTOF [25].

Ions of different elements have different masses, and therefore have different times of flight. The difference in the time of flight allows the detector to identify the elements present on the surface. The analysis is carried out over an area of 100×100 µm area, where the ion beam is rastered to produce the map of the elements on the defined area. The maps are obtained by rastering the ion beam over a certain area from where the secondary ions are mapped to form an image representing the distribution of ions in the sample. The ability of the system to focus its beam into a fine spot allows it to have a very high later resolution such that it can resolve particles with a distance of 60 nm [19,20].

3.8. References

1.   M.A. Prelas, G. Popouci, L.K. Bigelow, *Handbook of industrial diamonds and diamond films*, 1998, CRC Press.

2.   http://chemwiki.ucdavis.edu/Analalytical_Chemistry/Instrumental_Analysis/Diffraction/ [14 June 2014].

3.   D.M. Moore, R.C. Reynolds (Jr.), *X-ray diffraction and the identification and analysis of clay minerals*, 1989, Oxford Press, New York.

4.   S.J.B. Reed, *Electron Microprobe analysis and scanning electron microscopy in geology*, 2005, 2nd edition, Cambridge Press, New York.

5.   http://www.microscopy.ethz.ch/sem.htm [14 June 2014].

6.   A.M. Fox, *Optical properties of solids*, 2nd Ed., 2010, Oxford University Press, New York, p120-130.

7.   G.V. Bordo, H.G. Rubahn, *Optics and spectroscopy at surfaces and interfaces*, 2005, Wiley-VCH, p120-122.

8.   http://www.chem.agilent.com/Library/brochures/Cary-Eclipse_FLR-brochure.pdf [16 June 2014].

9.   M.J. O'Brien, R.L. Lyman, *Seriation, stratigraphy, and index fossils: the backbone of archaeological dating*, 2002, Kluwer Academic Publishers, New York.

10.   J. Mike, C. Walker, *Quaternary dating methods*, 2005, John Wiley and sons, England.

11.   D.R. Stille, *Manipulating light: reflection, refraction, and absorption*, 2006, Compass Point Books, USA.

12.   W. A. Wooster, *Diffuse X-ray reflection from crystals*, 1997, Dover Publications, Inc. USA.

13.   R.J. Anderson, D.J. Bendell, P.W. Groundwater, *Organic spectroscopic analysis,*2004, The royal society of chemistry, Great Britain.

14.   H.C. Swart, J.S. Sebastian, T.A. Trottier, S.L. Jones and P.H. Holloway, J. Vac. Sci. Technol. **14** (3), (1996) 169.

15.   D. Briggs and M.P. Seah, ***Practical Surface Analysis by Auger and X-ray Photoelectron Spectroscopy***, 1993, John Wiley & Sons Ltd.

16.   C.D. Wagner, W.D. Riggs, L.E. Davis, *et al,* ***Handbook of X-ray Photoelectron Spectroscopy*** Perkin-Elmer Corp., 1979, Eden Prairie, MN, USA.

17.   http://www.chm.bris.ac.uk/pt/diamond/jamespthesis/chapter2.htm [10 June 2014].

18.   N.M.K. Lamba, A.K. Woodhouse, S.L. Cooper, ***Polyurethanes in Biomedical Applications***, 1997, CRC Press, page 101.

19.   http://serc.carleton.edu/research_education/geochemsheets/techniques/ToFSIMS.html [30 April 2014].

20.   http://iontof.com/technique-sims-IONTOF-TOF-SIMS-TIME-OF-FLIGHT-SURFACE-ANALYSIS.htm [30 April 2014].

"Do your duty and a little more and the future will take care of itself."

— Andrew Carnegie

4

Photoluminescence and thermoluminescence properties of Pr^{3+} doped ZnTa$_2$O$_6$ phosphor

4.1. Introduction

Zinc tantalite is a compound that exhibits excellent microwave dielectric properties, such as high quality factor and high dielectric constant [1]. The compound is mainly developed for applications in microwave frequency devices such as resonators and mobile communication systems [2]. It has been prepared using several chemical routes to establish lower preparation temperatures to make it economically viable for practical applications and ease of preparation [1,3]. The chemical stability of the tantalite group of compounds makes the phosphor suitable for future practical applications [4]. The interest in oxide materials aroused because of their excellent long afterglow properties as reported for MAl$_2$O$_4$:Eu, Dy (M = Ca, Sr, Ba) [5] and CaTiO$_3$[6]. The oxide materials have the ability to generate many positively charged oxygen vacancies residing in the forbidden region of the band structure [7]. These oxygen vacancies that are generated during the synthesis process are the major contributors to the phosphorescence behavior of many oxide-based phosphors [7,8]. The Pr^{3+} ion is an important ion for generating red light because it has shown an emission with colour coordinates (x = 0.68, y = 0.31), which are close to those of an ideal red light when incorporated in CaTiO$_3$ host [9]. The single red emission of Pr^{3+} ion in CaTiO$_3$ host material is attributed to the virtual charge transfer from the lower lying intervalence charge transfer. The virtual charge exchange between $^3P_0$ and $^1D_2$ states via the intervalence charge transfer leads to a complete depopulation of the $^3P_0$ state by transferring all its charge to the $^1D_2$ state [10]. In this study we present a new red phosphor that is

prepared by solid state chemical reaction. We present luminescence properties and the transitions leading to the observable emission wavelengths, we calculated the band width of $ZnTa_2O_6$ and we determined the phosphorescence lifetime and the electron traps responsible for the long afterglow of the phosphor.

4.2.   Experimental

$ZnTa_2O_6$ doped with 1 mol Pr^{3+} phosphor was prepared by solid state reaction method by mixing stochiometric amounts of Ta_2O_5, ZnO and $PrCl_3$ into a slurry mixture using ethanol. The mixture was dried at 100 ^{o}C for 10 hrs and was then fired at 1200 ^{o}C for 4hrs, resulting in a white powder. The photoluminescence emission (PL) and excitation (PLE) of the powder were measured using the Varian Carry-Eclipse fluorescence spectrometer. Phosphorescence lifetime measurements were achieved by irradiating the sample for 5 minutes using a UV lamp, and immediately after switching the lamp off, a PMT was allowed to measure the phosphorescence signal at room temperature, with an approximated delay time of 1 second. A PerkinElmer Lambda 950 UV/VIS spectrometer was used to record the diffuse reflectance spectra. The phase and surface morphology were identified using a Bruker AXS D8 Advance X-ray diffractometer (XRD) and Scanning electron microscopy (SEM) (Shimadzu SSX-550, Kyoto, Japan), respectively. The glow curves were acquired by thermoluminescence spectroscopy (Riso TL/OSL reader – model TL/OSL-DA-20), after irradiating the phosphor using beta particles from ^{90}Sr beta radiation source at a dose rate of 0.1028 Gy/s. The luminescence detection for the TL/OSL system consists of a photomultiplier (PMT) with a U340 Schott filter that is effective in the 340 – 380 nm wavelengths.

4.3.   Results and Discussion

The SEM micrograph of $ZnTa_2O_6$:Pr^{3+} is presented in figure 4.1 and it shows an agglomeration of small spherical particles, which is a unique trace of particles prepared at very high temperatures [11]. The XRD pattern of $ZnTa_2O_6$:Pr^{3+} that matches that of a standard pattern of orthorombic $ZnTa_2O_6$ referenced in ISCD card number 36289 [12] are shown in figure 2. This suggests that a single phase was crystallized. The crystallite sizes were approximated to be 270 nm using the diffraction peaks measured and Scherrer's equation (Eq. 4.1) [13]:
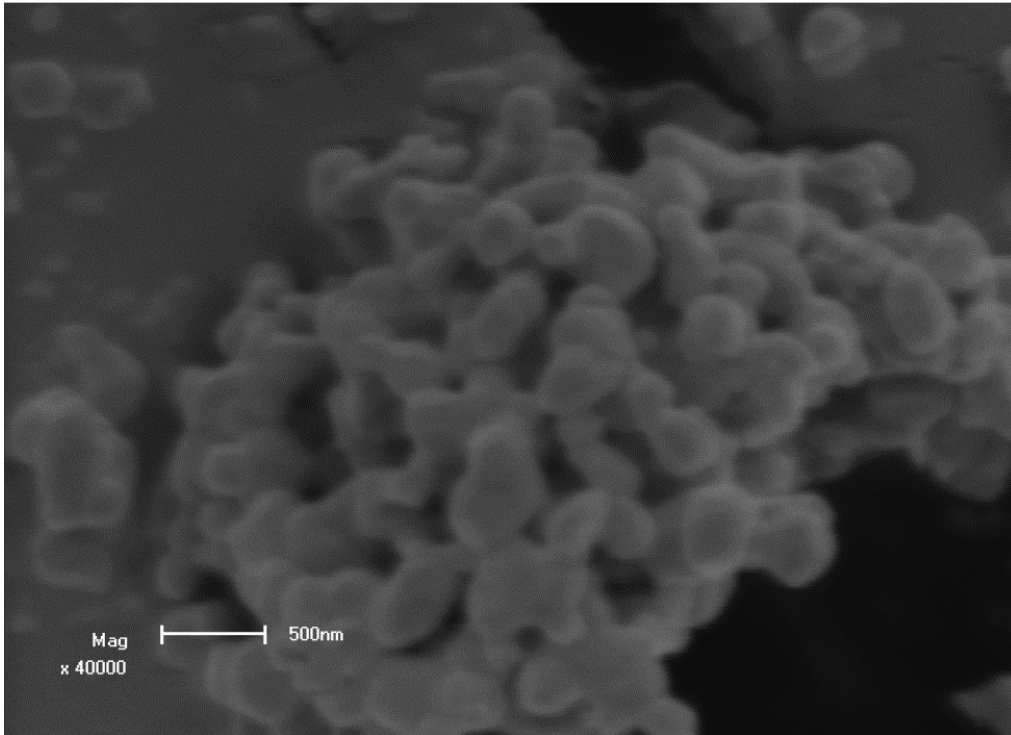
Figure 4.1: The SEM micrograph with 500 nm field view.
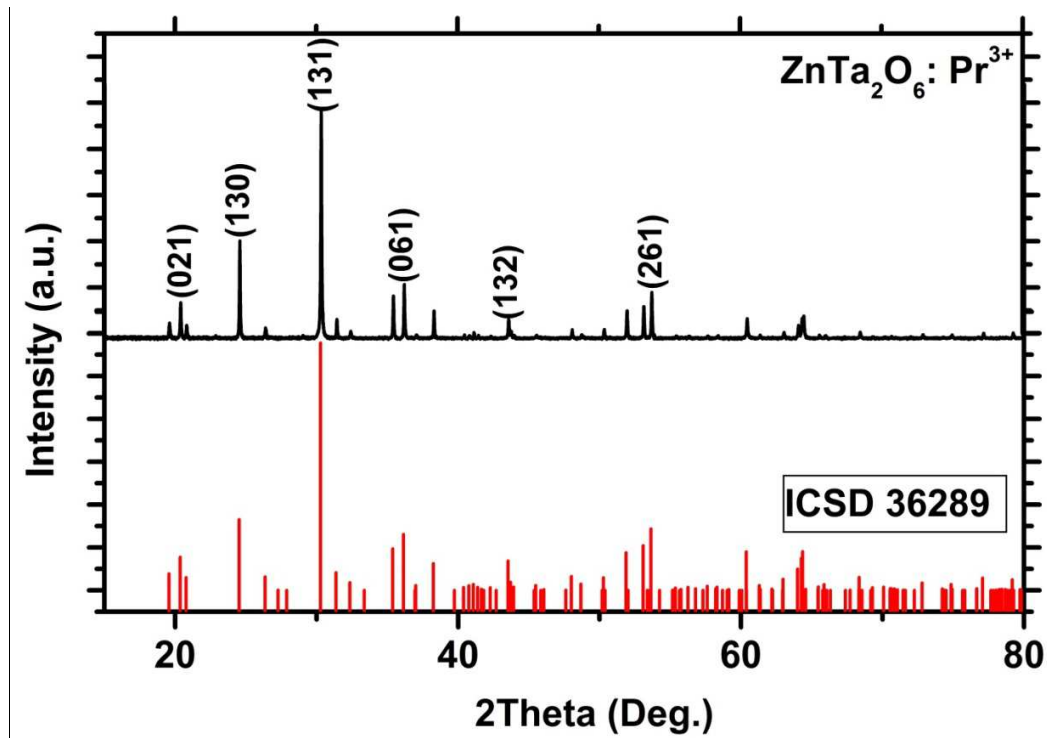
Figure 4.2: The XRD patterns of $ZnTa_2O_6$:Pr^{3+}.

$$s = \frac{k\lambda}{\beta \, cos\theta} \, ,\qquad\qquad [\mathbf{4.1}]$$

where s is the average crystallite size of the $ZnTa_2O_6$, β (5.4×10^{-4} rad.) is the full-width-at-half-maximum of the diffraction at angle θ(0.262 rad.), k is the shape factor that is approximately 0.89 and λ (1.54 nm) is the wavelength of the X-rays used to characterise the compounds [13].
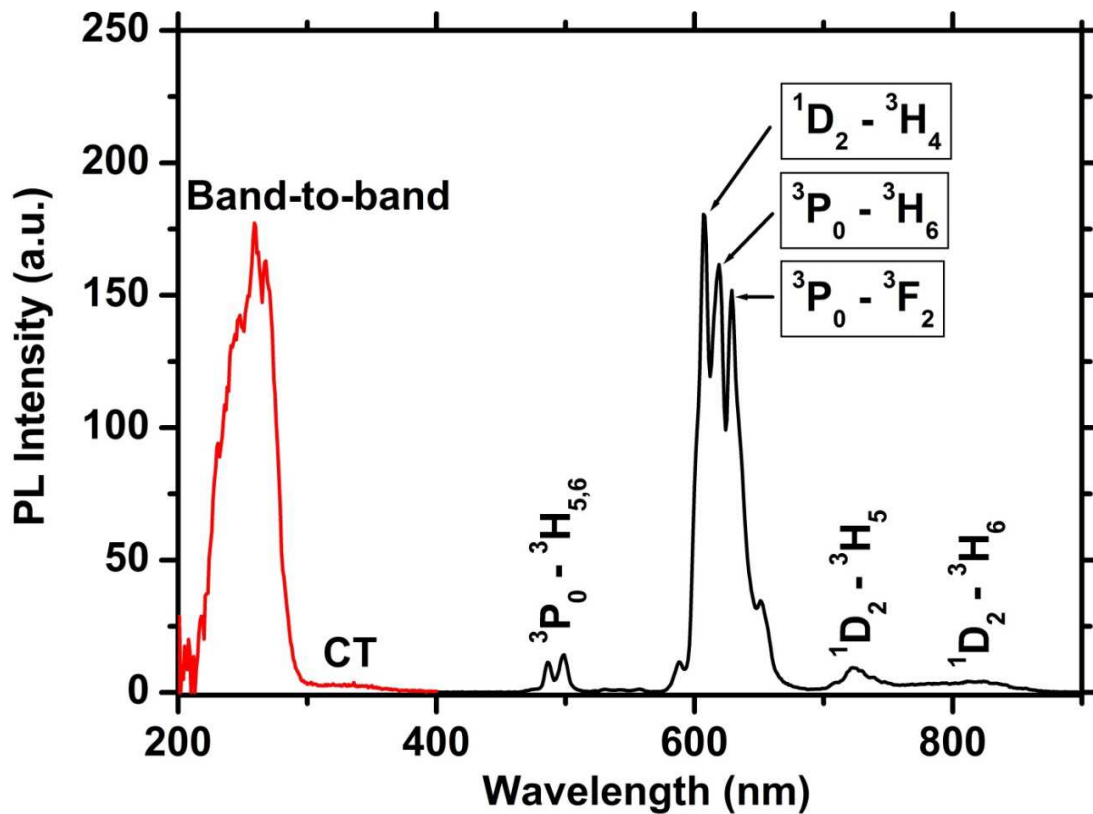
Figure 4.3: PLE and PL spectra of $ZnTa_2O_6$:Pr^{3+} phosphor.

The photoluminescence emission spectrum (Figure 4.3) of $ZnTa_2O_6$:Pr^{3+} phosphor shows blue and red emission lines from Pr^{3+} upon exciting with 259 nm ultraviolet light source. The blue emission attributed to $^3P_0 \rightarrow {}^3H_4$ transition is positioned at 447 – 449 nm, and the red emission lines attributed to $^1D_2 \rightarrow {}^3H_4$, $^3P_0 \rightarrow {}^3H_6$ and $^3P_0 \rightarrow {}^3F_2$ transitions are positioned at 608, 119 and 639 nm, respectively [14]. There are two more minor emission lines attributed to $^1D_2 \rightarrow {}^3H_{5,6}$ transitions positioned at 721 and 820, respectively [14]. The PLE spectrum was acquired to evaluate the position of the excitation bands, and the most prominent absorption band is situated

at 259 nm and was used to excite the phosphor. There is also an additional absorption band at 330 nm that may correspond to the intrinsic defect absorption or the virtual charge transfer reported by Boutinaud et al. [10] for Pr^{3+} ions. The photoluminescence behavior of Pr^{3+} may be affected by the distance between Pr^{3+} to O^{2-} ions, and this factor may be the one leading to the more prominent red emission from D states than the blue emission from the P states as it is expected from orthorhombic and cubic phase, as it is observed to completely quench P state emission in $CaTiO_3$ [15,16].
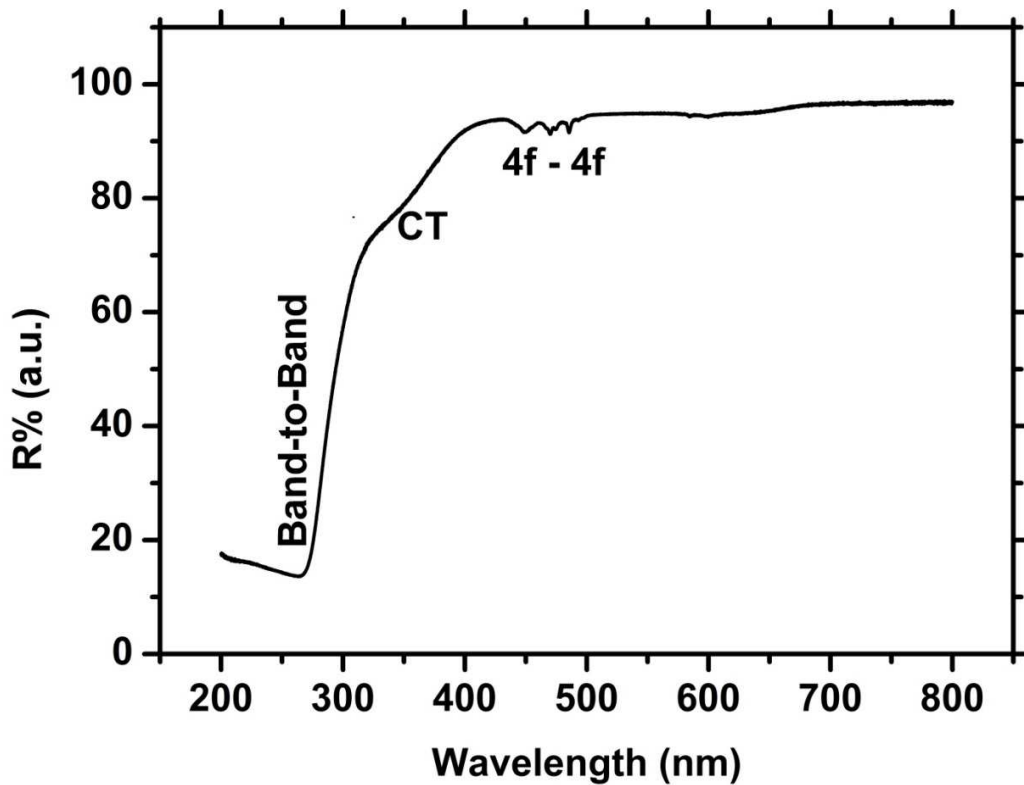
Figure 4.4: Diffuse reflectance spectrum of $ZnTa_2O_6$: Pr^{3+}.

The diffuse reflectance spectrum (Figure 4.4) shows absorption at 260 nm and at lower wavelengths, at 330 nm and in the 450 – 500 nm region of the spectrum, upon exciting the material with 259 nm wavelength source. The strong absorption bands with wavelengths lower than 260 nm may be due to band to band transition or those within the conduction band upon exciting the material [17]. The broad absorption at 330 nm, which is consistent with that observed in the PLE spectrum (Figure 4.3) may be due to intrinsic defect absorption or virtual

charge transfer [10]. The weaker absorption peaks at 450 to 500 nm correspond to f – f transitions of Pr^{3+} [18].
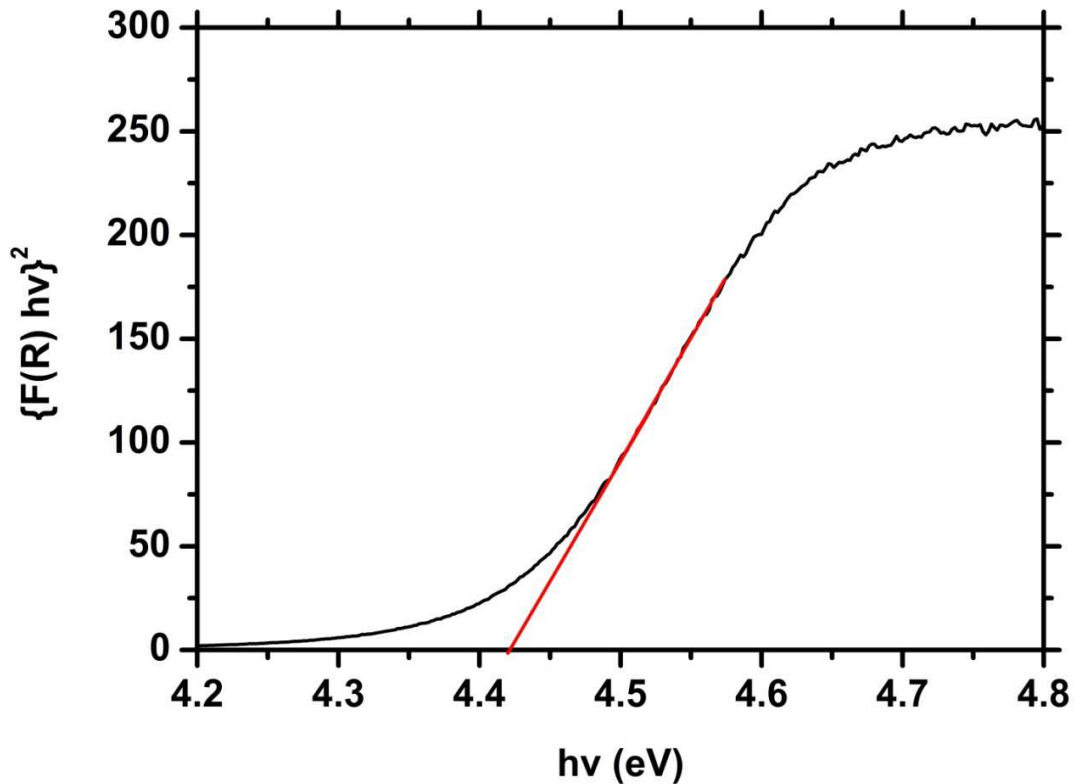
Figure 4.5: Energy band estimation from diffuse reflectance.

The prominent absorption band observed at 259 nm in the PLE spectrum possibly emanates from intrinsic defect levels close enough to the conduction band or it may be from band to band transition as demonstrated below [18]. Figure 4.5 shows the energy band emission from the diffused reflectance spectrum (Figure 4.4) of $ZnTa_2O_6:Pr^{3+}$, transformed by the Kubelka–Munk function (Eq. 4.2):

$$F(R) = \frac{(1-R)^2}{2R},\qquad\qquad [4.2]$$

where $F(R)$ is the reflectance factor that is transformed according to the Kubelka – Munk from the reflectance R. the value of R is obtained by subtracting the system's background obtained using Ba_2SO_4 standard, from the reflectance of the sample [19]. Tauc's relation is then

reconstructed using the Kubelka – Munk relation to obtain (Eq. 4.3) from which the energy band gap (E_g) of the material can be obtained [19]:

$$(F(R)\, hv\,)^2 = C(hv - E_g)\,, \qquad\qquad [4.3]$$

where the hv is the photon energy and C is a proportionality constant [19]. From the relation given by Eq. 4.3, a curve of $(F(R)\, hv\,)^2$ *vs* hv is then constructed, from which a tangent line is fitted at its point of inflection. The point at which the tangent line intersects with the hv is equivalent to the energy band gap of the material [20]. The E_g of $ZnTa_2O_6{:}Pr^{3+}$ of is then approximated to 4.43 ± 0.02 eV according to the point at which the tangent line intersects the hv axis. The value obtained for E_g (4.43 eV) is equivalent to the major absorption (Figure 4.2) at 4.6 eV, this is a verification that the major absorption comes from band to band excitation of the material.
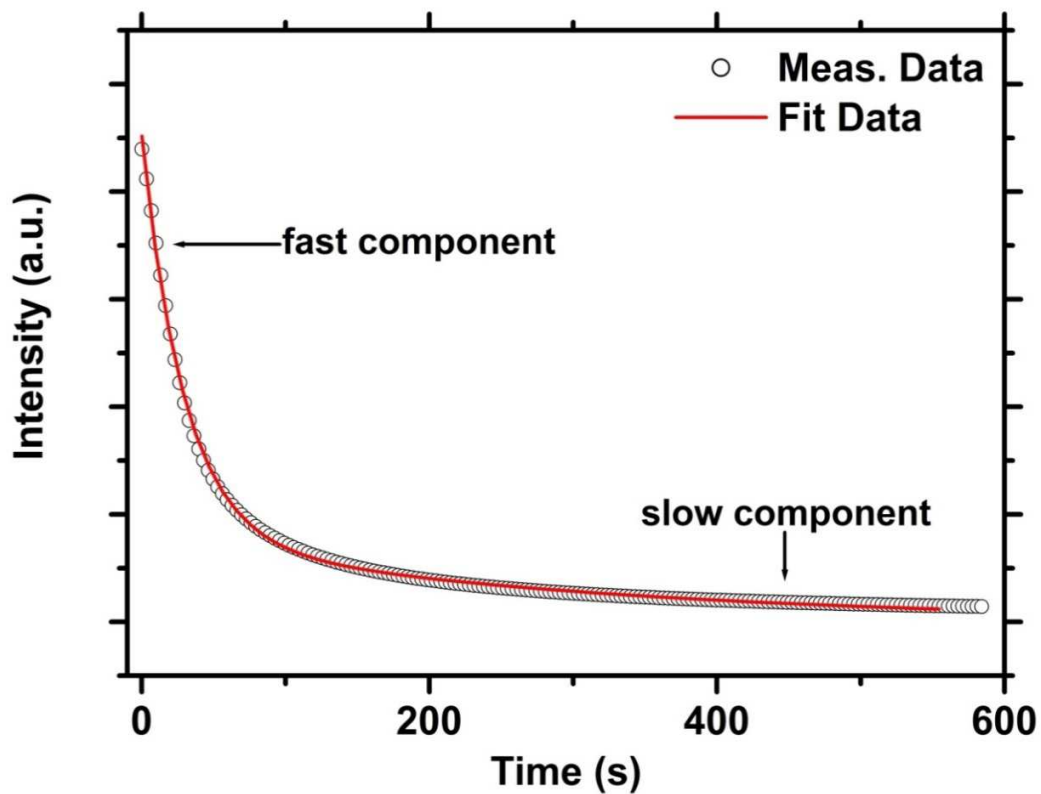
Figure 4.6: Phosphorescence decay curve of $ZnTa_2O_6{:}Pr^{3+}$.

The phosphorescence lifetime of the $ZnTa_2O_6$: Pr^{3+} was investigated by exciting the phosphor for five minutes, followed by measuring the emission intensity after removing the UV excitation source 2 seconds later. The decay profile is presented in figure 4.6 and it is made up of two components; namely the fast and the slow components which correspond to the lifetime coming from Pr^{3+} emission and trapped electrons within oxygen vacancies, respectively [9,21]. The time it takes for each component to decay was extracted by fitting the profile using the second order decaying exponential curve (Eq. 4.4) [22]:

$$I(t) = Ae^{-t/\tau_1} + Be^{-t/\tau_2} , \qquad [4.4]$$

where I is the luminescence intensity, A & B are constants, t is the phosphorescence time, τ_1 and τ_2 are the decay times of the first and the second components, respectively [22].

The phosphorescence decay times were determined to be 56.9 ± 0.6 µs and 570 ± 15 secs for τ_1 and τ_2, respectively. The oxygen vacancies have been reported as the major source for the long afterglow that is observed in most materials [21]. These centres capture electrons and gradually release them to luminescent centres [9] and when they recombine with electrons centres then is the long afterglow luminescence is observed [23]. The depth of the traps centres determines how long the afterglow emission lasts, and the deeper the traps the longer the phenomena will last [23][21].

Thermoluminescence anaylsis was used to investigate the electron trap distribution within the material, from which the energy required to thermally stimulate the electrons from an electron traps is used to determine the depth of the electron traps [24]. The glow curves were measured by varying the heating rate by which the samples are heated from 0.5, 1, 2, 3, 4 and 5 ^{o}C/s for the $ZnTa_2O_6$:Pr^{3+} sample exposed to 370 Gy. The glow curves (Figure 4.7a) show that as the heating rate increases, the TL intensity of the peaks decreases with T_M shifting to higher temperatures. The earlier effect is attributed to thermal quenching [25], and the latter is attributed the recombination that is slowing down [26]. The activation energy can be approximated using Eq. 4.5 [25]:

$$E = \ln\left(\frac{T_M^2}{\beta}\right) kT_M \qquad [4.5]$$
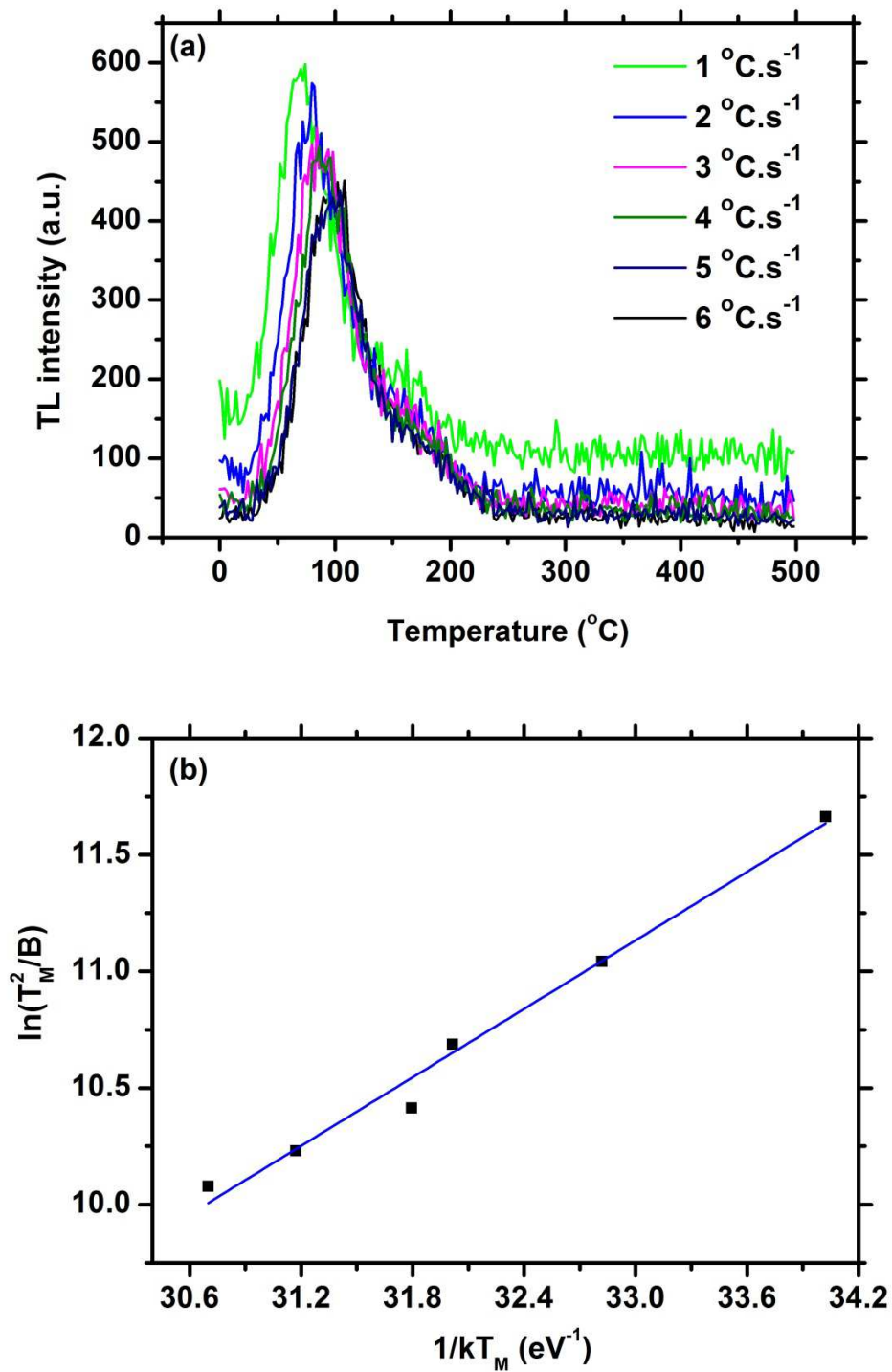
Figure 4.7: (a) shows the glow curves of the variable heating rates, and (b) the slope for activation energy approximation.

where E is the activation energy, T_M is temperature at the maximum intensity of the glow curve, β is the heating rate, and k is Boltzmann's constant. The activation energy is then extracted directly from the slope of $ln\left(\frac{T_M^2}{\beta}\right)$ vs $1/_{kT_M}$ [25] as shown in Figure 4.7b, from which the corresponding activation energy was found to be 0.48 ± 0.03 eV.

4.4. Conclusion

A new red long afterglow phosphor was prepared by doping $ZnTa_2O_6$ with 1 mol% Pr^{3+}. It was observed that the orthorhombic $ZnTa_2O_6$ host promotes red emission from Pr^{3+} ions, with spectral lines at 608, 119 and 639 nm from $^1D_2 \rightarrow {}^3H_4$, $^3P_0 \rightarrow {}^3H_6$ and $^3P_0 \rightarrow {}^3F_2$ transitions, respectively. The phosphor mostly absorbs the ionizing radiation by band to band excitation, as confirmed by calculations of the energy band gap. The phosphorescence was measured and the decay times were approximated to be 56.9 ± 0.6 µs and 570 ± 15 secs for the fast and slow components, respectively. The depth of the electron trapping centres that lead to phosphorescence was approximated to be 0.48 ± 0.03 eV.

4.5.   References

1. Y.C. Zhanga, B. J. Fua , X. Wang, J. Alloys and Compd. **478** (2009) 498.
2. C.R. Ferrari, A.C. Hernandes, J. European Ceramic Society **22** (2002) 2101.
3. A. Kan, H. Ogawa, H. Ohsato, J. Alloys Compd. **337** (2002) 303.
4. S.S. Pitale, L.L. Noto, I.M. Nagpure, O.M. Ntwaeaborwa, J.J. Terblans, H.C. Swart, Advance Materials Research, **306-307** (2011) 251.
5. Y. Lin, Z. Zhang, Z. Tang, J. Zhang, Z. Zheng, X. Lu, Materials Chemistry and Physics **70** (2001) 156–159.
6. E.H. Otal, A.E. Maegli, N. Vogel-Schäuble, B. Walfort, H. Hagemann, S. Yoon, A. Zeller, A Weidenkaff, Opt. Mat. Epress **2** (4), (2012) 405.
7. S. Yang, L.E. Halliburton, A. Manivannan, P.H. Bunton, D. B. Baker, M. Klemm, S. Horn, A. Fujishima, Appl. Phys. Lett. **94** (2009) 162114.
8. I. Tanaka, F. Oba, K. Tatsumi, M. Kunisu, M. Nakano, H. Adachi, Mater Trans **43** (7), (2002) 1426.
9. S. Yin, D. Chen, W. Tang, *J.Alloy and Compd.*, **441** (2007) 327.
10. P. Boutinaud, E. Pinel, M. Dubois, A.P. Vink, R. Mahiou, *J. Lumin.*, **111** (2005) 69.
11. X.C. Jiang, W.M. Chen, C.Y. Chen, S.X. Xiong, A.B. Yu, Nanoscale Res Lett **6** (2011) 32.
12. M. Waburg, H. Muller-Buschbaum, Zeitschrift fuer Anorganische und Allgemeine Chemie **508** (1984) 55.
13. P.S. Khiew, S. Radiman, N.M. Huang, Md. Soot Ahmad, *J.Cryst. Growth*, **254** (2003) 239.
14. C. De Mello Donega, A Meijerink, G. Blasse, J. Phys. Chem. Solids **56** (5), (1995) 673.
15. P. Boutinaud, R. Mahiou, E. Cavalli, M. Bettinelli, Chem, Phys. Lett **418** (2006) 185.
16. E. Pinel, P Boutinaud, R. Mahiou, J. Alloys Compd. **374** (2004) 165.
17. X. Zhang, J. Zhang, Z. Nie, M. Wang, X Ren, Appl. phys. Lett. **90** (2007) 151911.
18. L.L. Noto, S.S. Pitale, M.A. Gusowski, J.J. Terblans, O.M. Ntwaeaborwa, H.C. Swart, 10.1016/j.powtec.2013.01.029.
19. A.E. Morales, E.S. Mora, U. Pal, Rev. Mex. Fis. S **53** (5), (2007) 18
20. E. A. Davis and N. F. Mott, Philos. Mag., **22** (1970) 903

21. H.F. Brito, J. Hassinen, J. Holsa, H. Jungner, T. Lamanen, M.H. Lastusaari, M. Malkanmaki, J. Niittykoski, P. Novak, L.C.V. Rodriguess, J. Therm. Anal. Calorim. **105** (2), (2011) 657.

22. Y. Pan, Q. Su, H. Xu, T. Chen, W. Ge, C. Yang, M. Wu, J. Sol. Stat. Chem. **174** (2003) 69.

23. B.M. Mothudi, O.M. Ntwaeaborwa, J.R. Botha, H.C. Swart, Physica B **404** (2009) 4440.

24. McKeever SWS, *Thermoluminescence of Solids*, 1985, Cambridge University Press, New York.

25. P.R. Gonzales, C. Furetta, E. Cruz-Zaragoza, J. Azorin, Mod. Phys. Lett. B **4** (8) (2010) 717.

26. I. Veronese, *The thermoluminescence peaks of quarts at intermediate temperatures and their use in dating and dose reconstruction* [**Thesis**], 2005, UniversitaDegliStudi Milano.

"If you hear a voice within you saying "you cannot paint," then by all means paint and that voice will be silenced."

–Vincent Van Gogh

5

Enhancement of the photoluminescent intensity of $ZnTa_2O_6$:Pr^{3+} phosphor

5.1.   Introduction

Until today, commercially available red glowing phosphors are limited, whereas the blue and green phosphors have been much more commercialized [1]. This is attributed to red glowing phosphors lacking the application quality [1], because of their inefficient luminescence intensity and long afterglow [2]. Research to enhance luminescence intensity is currently approached in several ways, such as varying the concentration of the dopant ion in the host material [1], adding charge compensators [3] and using different synthesis methods [4]. Another strong emphasis of research on red glowing phosphors is to achieve a phosphor that glows with a pure red emission. In the display technology, Y_2O_3:Eu^{3+} is presently adopted as a red phosphor, because of its sharp intensity from the $^5D_0 \rightarrow {}^7F_2$ transition of the Eu^{3+} ion. In true sense, the emission coming from this phosphor is not entirely red, but close to orange [5]. For application purposes, the emission of Y_2O_3:Eu^{3+} undergoes an expensive process of filtering to change its color index from (0.65, 0.35) [5,6] that is close to orange, to (0.67, 0.33) [4] that resemble the color of an ideal red light as defined using the Commission Internationale de l'Eclairage (CIE) chromaticity coordinates [5]. Red phosphors have attracted attention for applications in medical imaging, self-lit emergency signs, soft illumination and several other applications [8,9]. Pr^{3+} ions have emerged as suitable candidates to assist in generating a phosphor that glows with an almost certainly red emission [9]. This is as observed from the single red emission of $CaTiO_3$:Pr^{3+} phosphor with

colour coordinates (0.68, 0.31) [4]. Pr^{3+} is reported to emit efficiently in the blue and the red regions of the electromagnetic spectrum, depending on their concentration and also the host material in which it is doped [10]. In $CaTiO_3$, it glows with a single red emission that is attributed to the electron population cross-over from the $^3P_0$ level to the $^1D_2$ level as a result of the virtual charge transfer mechanism (IVCT) between the Pr^{3+} and Ti^{4+} ions [8]. This leads to complete quenching of the blue emission from the $^3P_0 \rightarrow ^3H_4$ transition, and leading to a single red emission from the $^1D_2 \rightarrow ^3H_4$ transition [8]. This non radiative process has proven to be of great importance in that it reveals the capability of Pr^{3+} to be used as a standard dopant to prepare red phosphor for commercial purposes in future. In general non radiative processes are desirable for the research on phonon-electron coupling strength and relaxation rates of different optical transitions of a rare-earth ion [11]. These processes also have drawbacks in that they can limit the luminescence intensity by reducing the efficiency of the radiative transitions [11]. In this work, we present the optimisation of the luminescent intensity of the $ZnTa_2O_6$:Pr^{3+} phosphor by varying the concentration of Pr^{3+} ions from 0.1, 0.2, 0.4 to 1.2 mol%. We also investigate the photoluminescent properties of the phosphor and the homegeous distribution of the dopant ion as the concentration is varied.

5.2. Experimental

$ZnTa_2O_6$: Pr^{3+} phosphor was prepared by solid state reaction, at 1200 ^{o}C for 4 hrs, and the Pr^{3+} ion concentration were varied from 0.1 to 1.2 mol%. The crystalline phase was identified by a Bruker AXS D8 Advance X-Ray diffractometer using Cu *Kα* radiation. The scanning electron microscopy (SEM) images were captured using the Shimadzu SSX-550 SEM from Kyoto, Japan. The photoluminescence (PL) emission and excitation (PLE) properties of the phosphor were probed using the Varian Carry-Eclipse fluorescence spectrophotometer. The distribution of Pr^{3+} ions in the phosphors was checked from the surface maps obtained from the ION-TOF SIMS 5 model. The Bi^+ ion gun with 1 pA beam current was used to probe the surface.

5.3. Results and Discussion

The measured X-ray diffraction (XRD) patterns of the $ZnTa_2O_6$:Pr^{3+} (Figure 5.1a) matches that of the standard orthorhombic $ZnTa_2O_6$ phase referenced in the ICSD card number 36289 [12]. This suggests that we have crystallized a single orthorhombic phase of $ZnTa_2O_6$. The phase

purity was not affected by Pr^{3+} doping. The SEM image (Figure 5.1b) shows the particles that are agglomerated together with isolated particles generally appearing circular, implying a spherical shape.
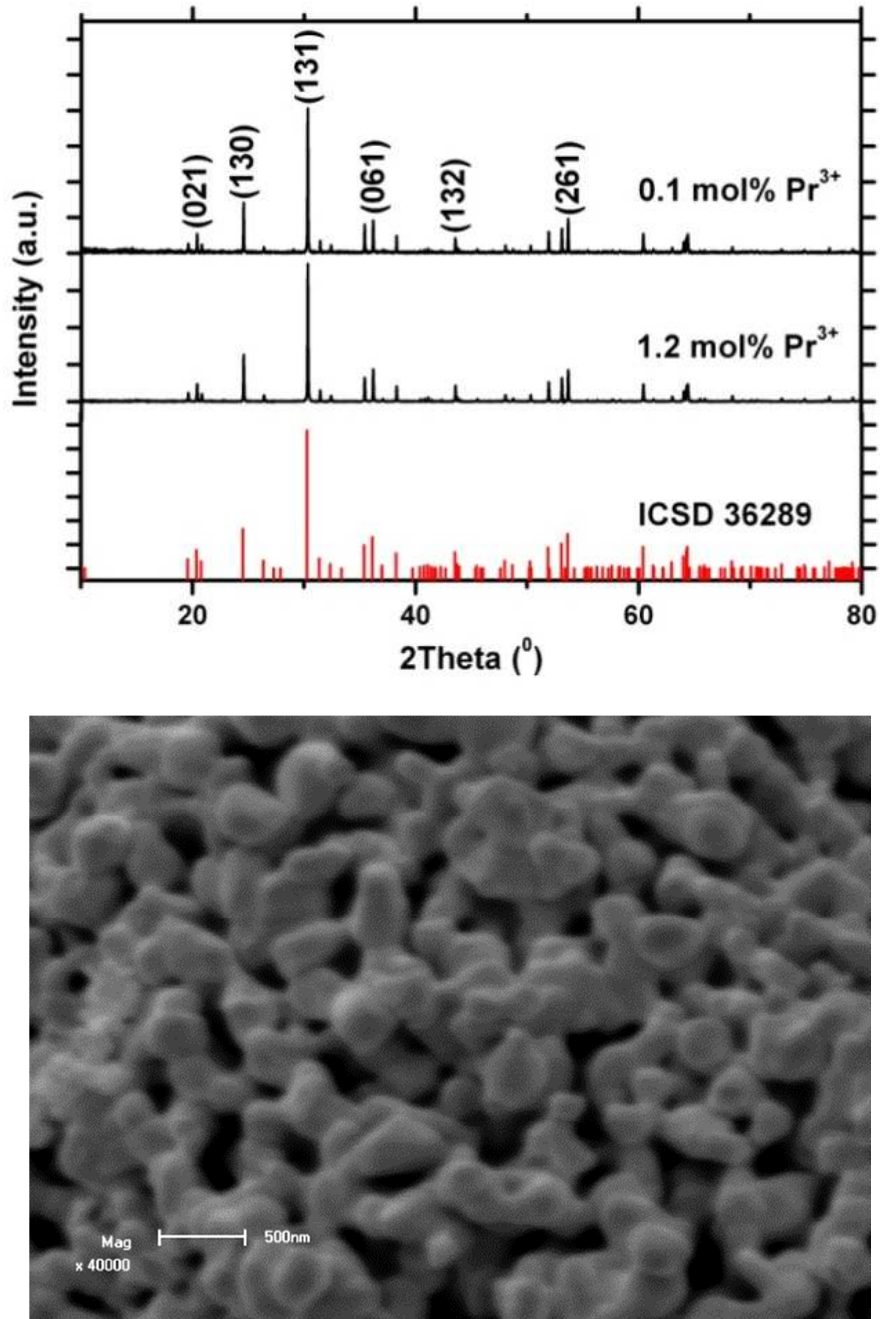
Figure 5.1: (a) XRD patterns of $ZnTa_2O_6$ with different Pr^{3+} ion concentration, (b) SEM image of $ZnTa_2O_6:Pr^{3+}$.
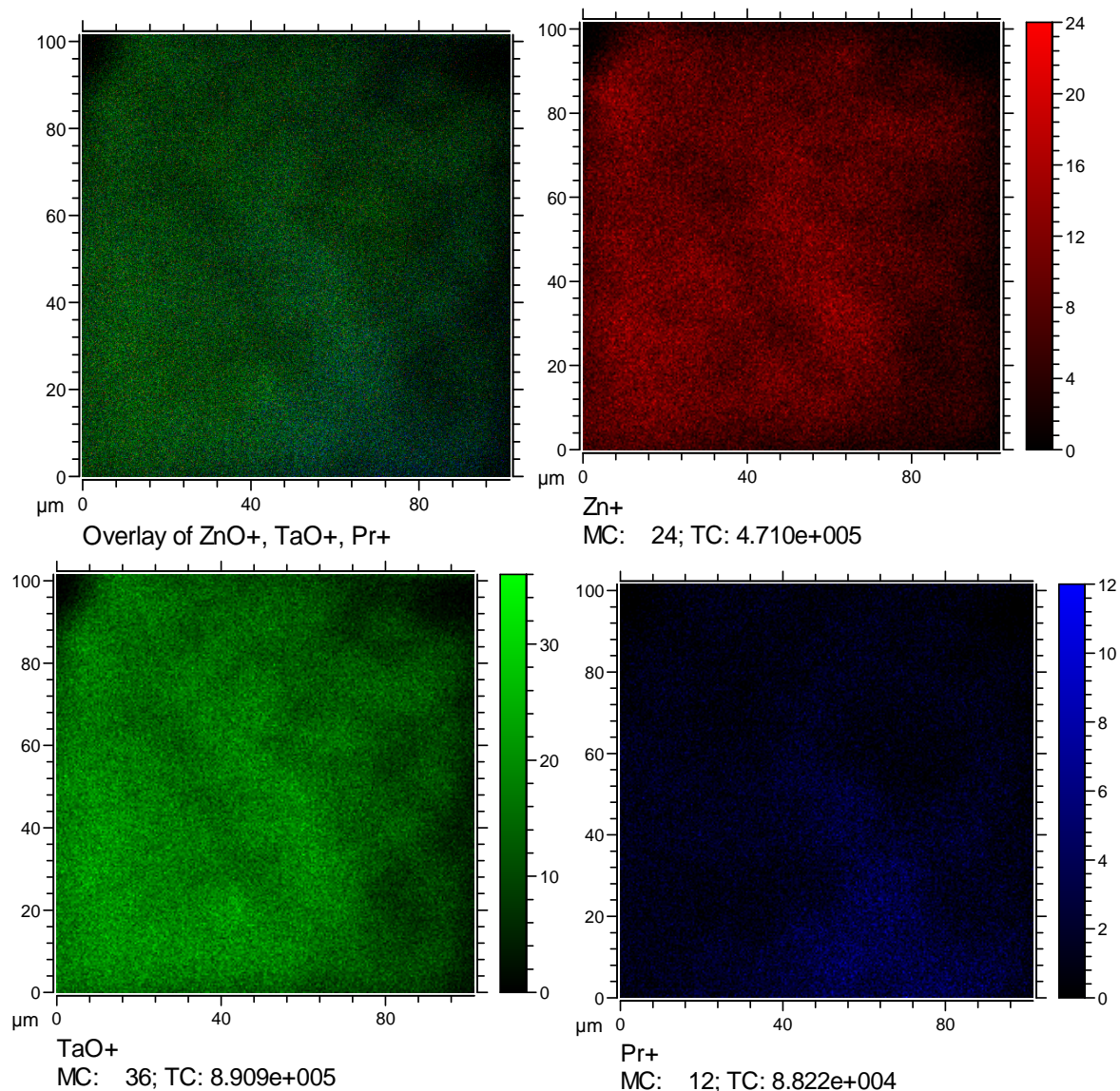
Figure 5.2: A three colour overlay chemical image of 0.1 mol% Pr^{3+} in $ZnTa_2O_6$.

The SIMS-TOF analysis was done to investigate the distribution of the Pr^{3+} ions inside the phosphor. The compositional identification was achieved from the mass spectra (not shown) that were acquired at the surface of the phosphor from which Pr^+, Zn^+ and TaO^+ peaks were used to obtain the maps. The chemical imaging of the three ions was correlated by colour overlay plots to investigate the distribution of Pr^{3+} ions inside the phosphor (Figure 5.2 & 5.3). The 100 µm × 100 µm images of Pr^+ (blue), Zn^+ (red) and TaO^+ (green) were taken and overlaid on each other. Figure 5.2 and 5.3 show the image overlay of 0.1 and 1.2 mol% of the Pr^{3+} ions in $ZnTa_2O_6$,

respectively. In both images a homogeneous distribution of the Pr^{3+} is evident, as revealed by Chakraborty et al [14]. When comparing the two Pr SIMS images, it is clear that there are less Pr^{3+} ions for 0.1 mol% Pr^{3+} concentration (Figure 5.2) than in 1.2 mol% Pr^{3+} concentration (Figure 5.3) as expected. The high concentration in the latter phosphor leads to shortened distances between Pr^{3+} ions as reported by De Mello Donega et al [11].

Overlay of Zn+, TaO+, Pr+

Zn+
MC: 26; TC: 4.363e+005

TaO+
MC: 31; TC: 6.846e+005

Pr+
MC: 13; TC: 1.865e+005
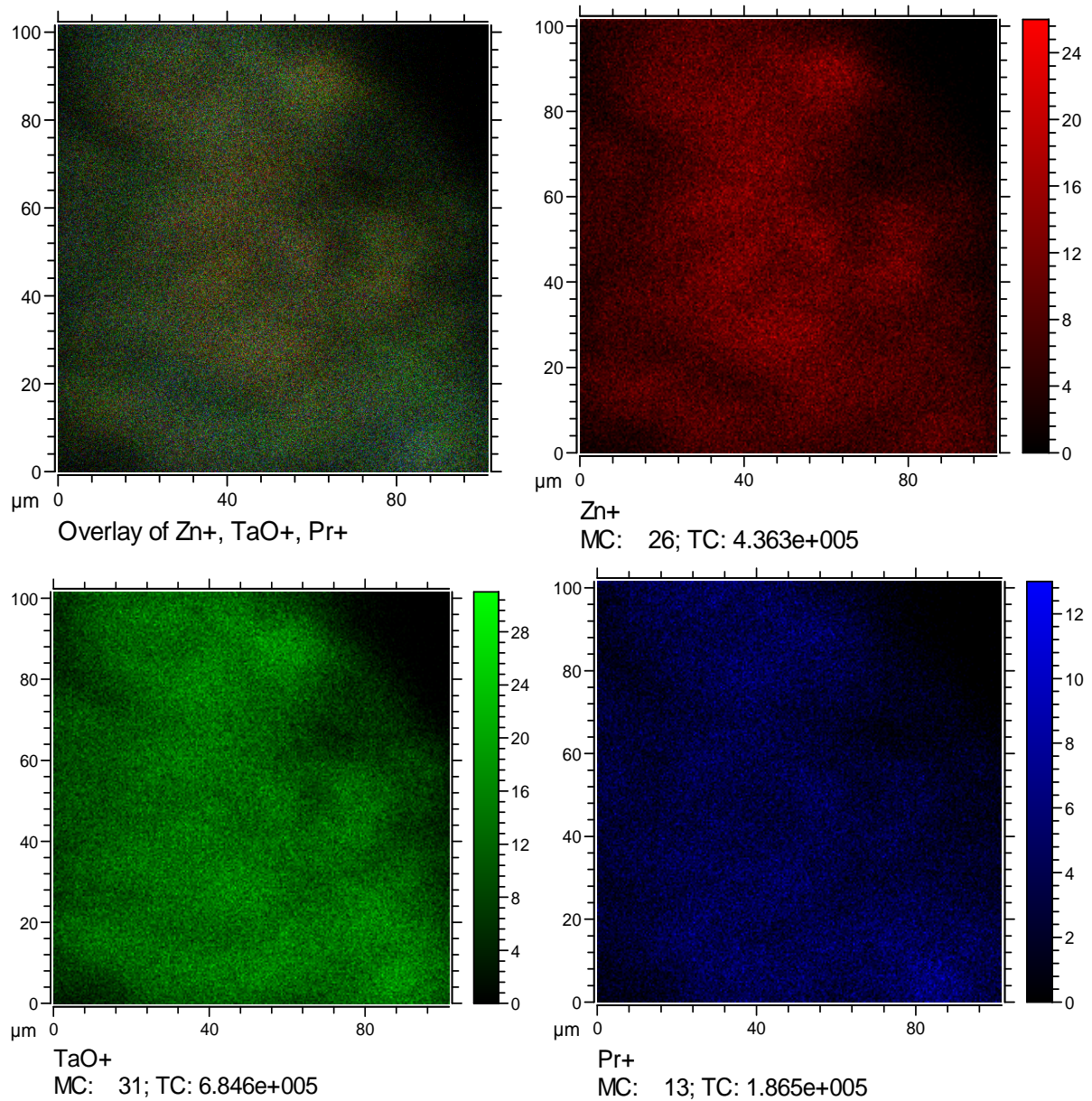
Figure 5.3: A three colour overlay chemical image of 1.2 mol % Pr^{3+} in $ZnTa_2O_6$.

The absorption characteristics of the phosphor are presented in Figure 5.4 and 5.5. Figure 5.4 shows the PLE of the $ZnTa_2O_6$:Pr^{3+} phosphor at different concentrations of Pr^{3+}. The PLE intensity changed with concentration and it was the highest for the 0.4 mol% Pr^{3+} doping. For all the bands obtained at different Pr^{3+} concentrations, the major absorption band was at 259 nm. This band corresponds to the lowest reflectance percentage in the diffused reflectance spectrum of the phosphor (Figure 5.5).
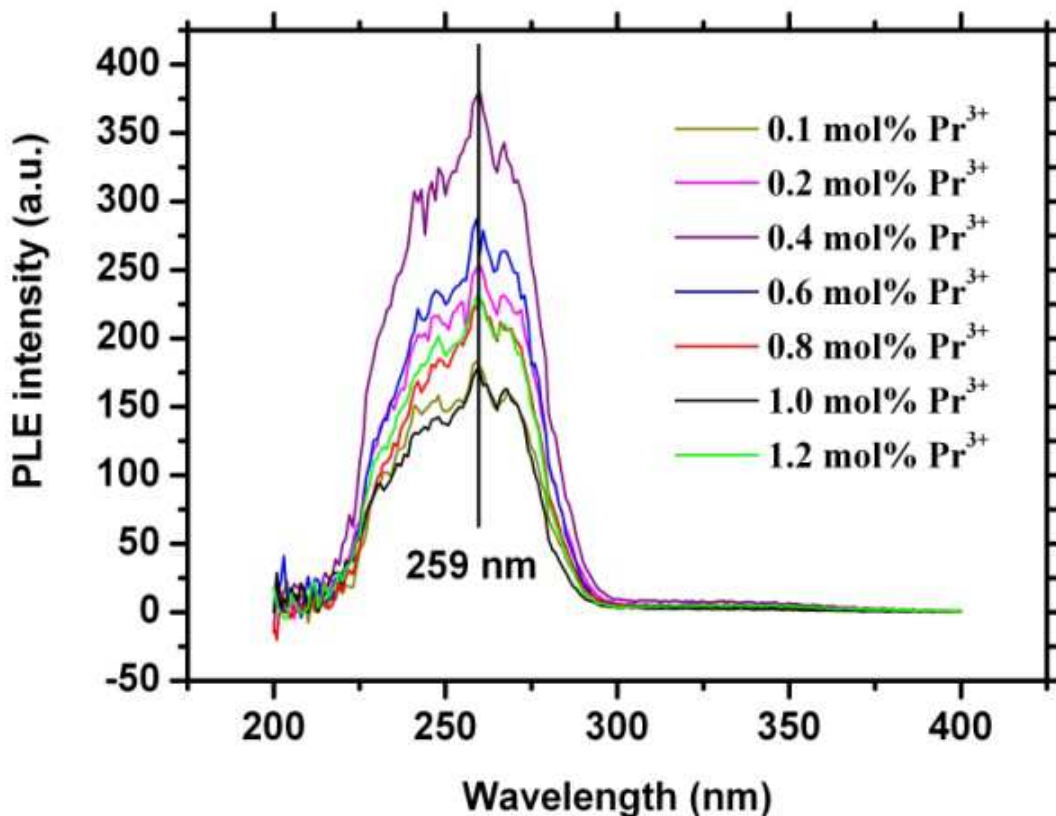
Figure 5.4: PLE spectrum for $ZnTa_2O_6$:Pr^{3+} phosphor with different concentrations of Pr^{3+}.

Figure 5.5 shows the diffuse reflectance of $ZnTa_2O_6$:$0.4Pr^{3+}$ with absorption bands at 430 nm to 500 nm that correspond to the 4f – 4f ($^3H_4 \rightarrow {}^3P_0$, $^1I_6$, $^3P_1$, $^3P_2$) levels of Pr^{3+} [3]. The major absorption is positioned at 259 nm and corresponds to that of the PLE spectra (Figure 5.4.). The band is positioned in a region that has been assigned to band – band excitation [3,4,10].
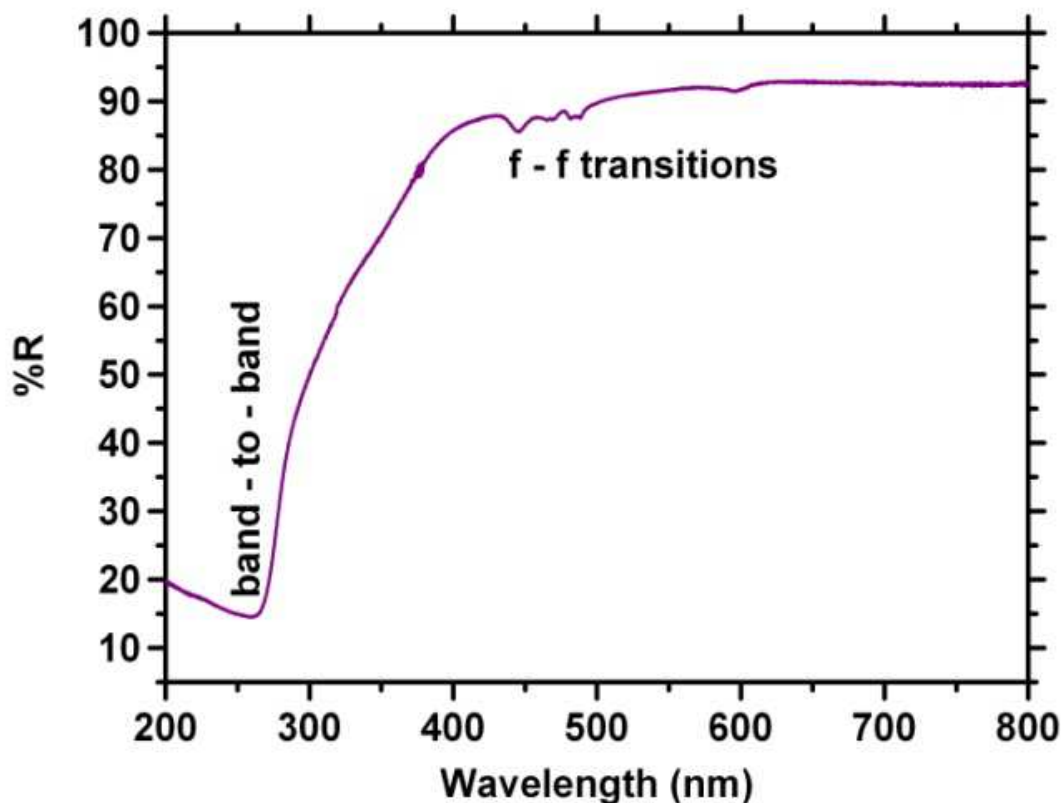
Figure 5.5: Diffused reflectance spectrum for $ZnTa_2O_6:0.4Pr^{3+}$ phosphor.

The PL spectra of $ZnTa_2O_6:Pr^{3+}$ measured at different Pr^{3+} concentrations are presented in Figure 5.6a. The variation of PL intensity with Pr^{3+} concentration is presented in Figure 5.6b. Both blue and red emissions were obtained from the $ZnTa_2O_6:Pr^{3+}$ phosphor, with red emission more prominent than the blue emission. The blue spectral line from the $^3P_0 \rightarrow {}^3H_4$ transition was observed at 448 nm and the more prominent red spectral lines were observed at 608, 619 and 639 nm from the $^1D_2 \rightarrow {}^3H_4$, $^3P_0 \rightarrow {}^3H_6$ and $^3P_0 \rightarrow {}^3F_2$ transitions, respectively [11].

The PL intensity of the red emission increased from 0.1 mol% to 0.4 mol% Pr^{3+}, from where it began to decrease systematically as the Pr^{3+} concentration increased to 1.2 mol% (Figure 5.6b). The increase of the Pr^{3+} ions in the host reduced the distance between adjacent ions, and this lead to cross relaxations between the Pr^{3+} ions. This eventually led to reduction of luminescence intensity as a result of the concentration quenching from the cross relaxation process [11].
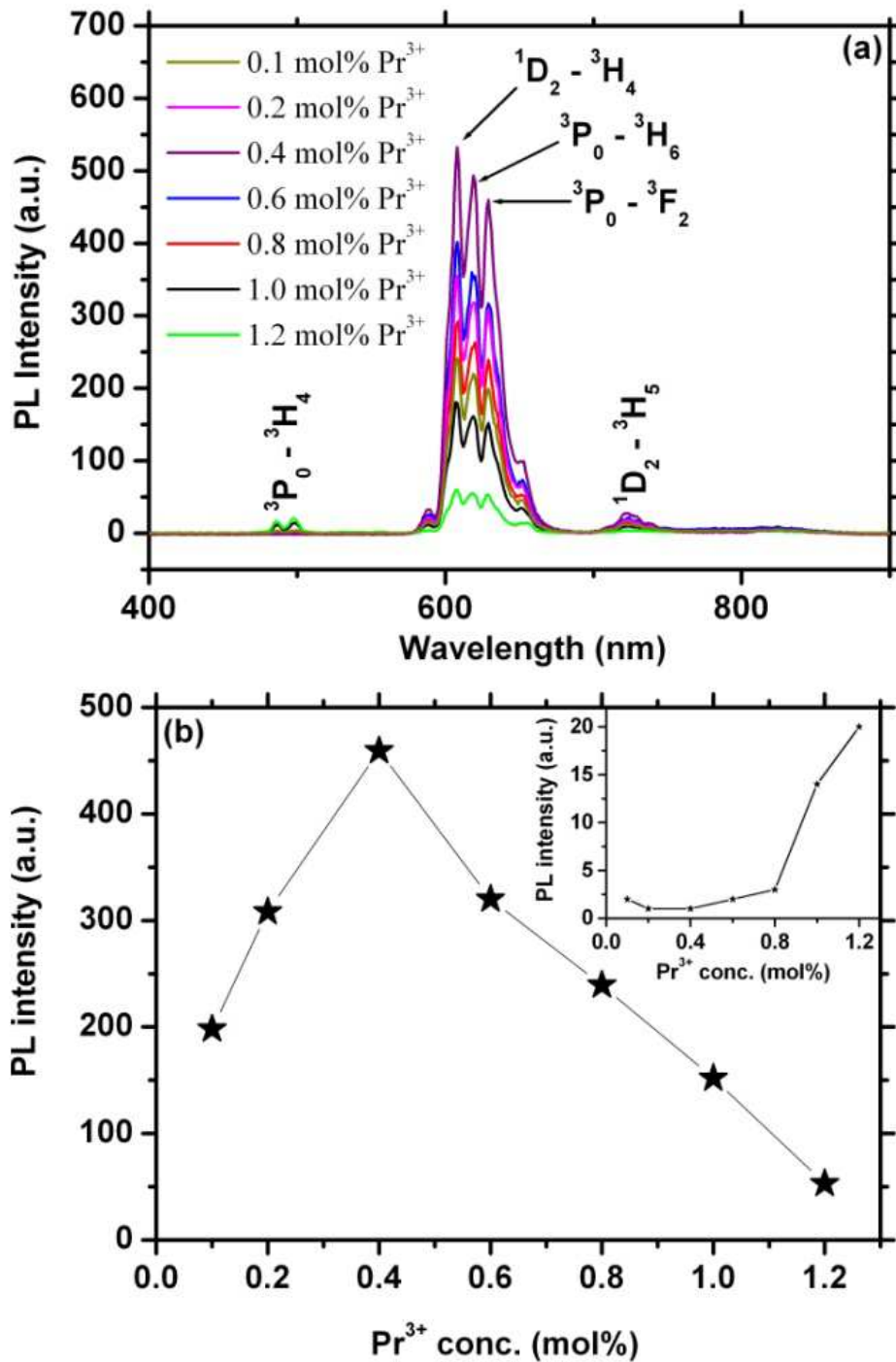
Figure 5.6: (a) PL spectrum for $ZnTa_2O_6:Pr^{3+}$ phosphor with different concentrations of Pr^{3+}. (b) PL intensity of the red emission changes with different Pr^{3+} concentrations and the insert shows the blue emission increment with the increment of the Pr^{3+} concentration.

An interesting observation is the increase of the blue emission at 448 nm with the increase in Pr^{3+} concentration (inset of Figure 5.6b), even when the red emission intensity decreased for 0.6 to 1.2 mol% Pr^{3+}. As reported by De Mello Donega et al. [11], cross relaxation is more efficient in quenching the $^1D_2$ level than the $^3P_0$ level. As the quenching increased for the $^1D_2$ state, energy was transferred to the $^3P_0$ level to support the $^3P_0 \rightarrow ^3H_4$ transition. This is evident in the inset of Figure 5.6b, which shows a rapid increase of the blue emission from 0.8 to 1.2 mol% Pr^{3+}. This is also illustrated in the schematic energy level diagrams of Pr^{3+} (Figure 5.7).
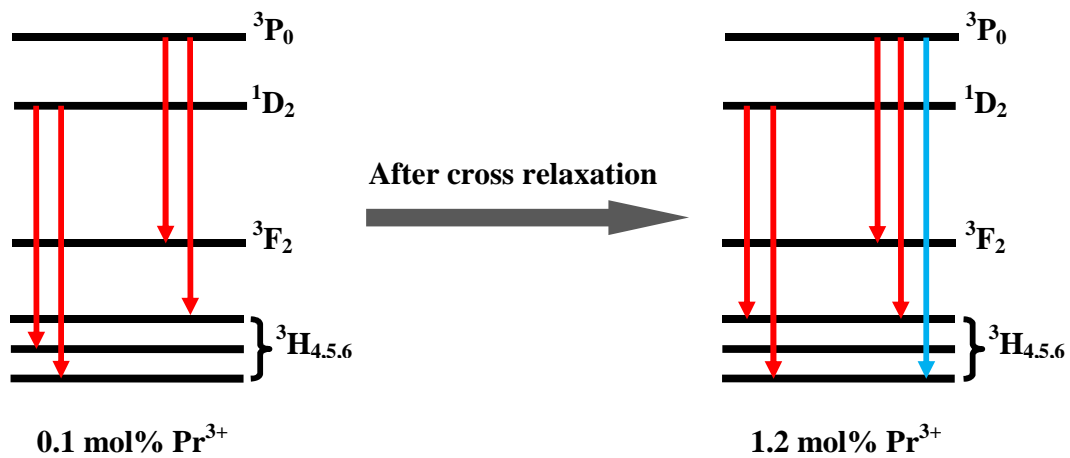
Figure 5.7: Schematic energy level diagrams showing allowed transitions at 0.1 and 1.2 mol% Pr^{3+} concentrations.

Figure 5.8 shows the CIE coordinates plot for the $ZnTa_2O_6:Pr^{3+}$ phosphor with 0.4 and 1.2 mol% of the dopant ion, which are at (0.67, 0.33) and (0.61, 0.35), respectively. The CIE coordinates were obtained using the software by Broadbent [13]. Similar plots were obtained for 0.1, 0.2, 0.6, 0.8 and 1.0 mol% of Pr^{3+}, and the corresponding coordinates were (0.64, 0.33), (0.68, 0.33), (0.67, 0.33), (0.67, 0.33) and (0.65, 0.34), respectively. The coordinates for 0.4, 0.6 and 0.8 mol% correspond to those of an ideal red emission as reported by Lu et al [4]. The ideal nature of the red emission is removed by the presence of the blue emission when the concentration of Pr^{3+} increases.

Figure 5.9 and 5.10 show the phosphorescence decay curves of $ZnTa_2O_6$ doped with different concentrations of Pr^{3+} and $ZnTa_2O_6:Pr^{3+}$ (0.4 mol %) fitted by a second order decay curve, respectively. The phosphorescence decay curves show that there are two components responsible

for the luminescence; the fast and the slow component. The fast component is attributed to the luminescence of the f – f transitions of the Pr^{3+} ion [3], which occurs within the first few seconds. The slow component is attributed to the delayed emission (persistent luminescence) due to the trapping and detrapping of the carriers by the oxygen vacancies [3]. The phosphorescence decay curves of the $ZnTa_2O_6:Pr^{3+}$ phosphor were fitted with the second order decay exponential decay function (Eq. 5.1) to extract the time parameters as presented in table 5.1.
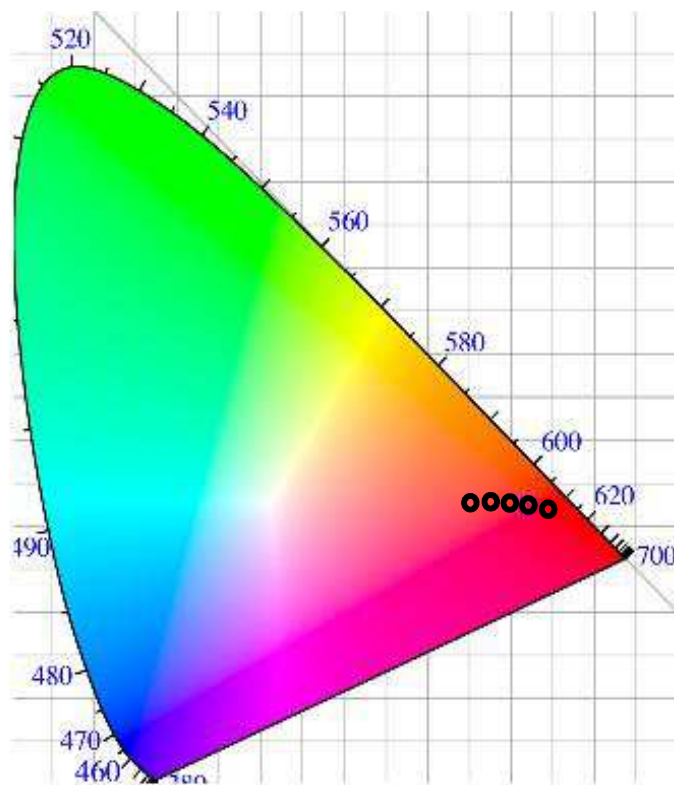
Figure 5.8: CIE coordinates plot for $ZnTa_2O_6:Pr^{3+}$ phosphor with 0.4 (left) and 1.2 (right) mol% Pr^{3+}.

$$I(t) = Ae^{-t/\tau_1} + Be^{-t/\tau_2} \qquad [5.1]$$

I(t) is the luminescence intensity, *A* and *B* are constants and *t* is the time. The first term on the right side of the equation describes the decay of luminescence from the Pr^{3+} ion, and whose lifetime is presented by τ_1 (Table 1). The second term describes the decay of the persistent luminescence, and its lifetime is represented by τ_2 (Table 5.1) [3,10].
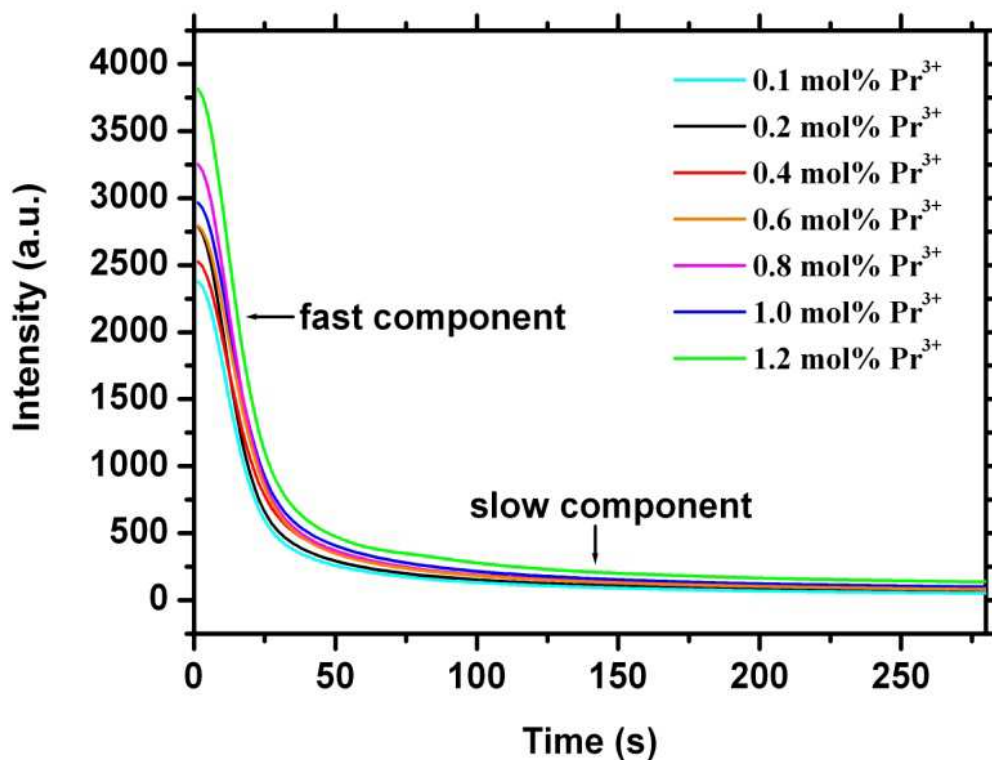
Figure 5.9: Phosphorescence decay curves of $ZnTa_2O_6$ doped with different concentrations of Pr^{3+}.

The decay time corresponding to the trapping and detrapping of carriers (τ_2) by oxygen vacancies, increased with an increase in the Pr^{3+} concentration (table 5.1). This is attributed to more oxygen vacancy probably formed with the increase of Pr^{3+} ions inside the host [3].

Table 5.1: Decay times (τ_1 and τ_2) of $ZnTa_2O_6$ dope with different Pr^{3+} concentrations.

Pr^{3+} Conc.	τ_1	τ_2
mol%	(μs)	(s)
0.1	31.2 ± 0.2	523 ± 10
0.2	29.4 ± 0.1	529 ± 13
0.4	32.1 ± 0.1	540 ± 11

0.6	31.2 ± 0.1	552 ± 15
0.8	33.4 ± 0.2	561 ± 19
1.0	32.0 ± 0.3	570 ± 26
1.2	14.8 ± 0.2	216 ± 13
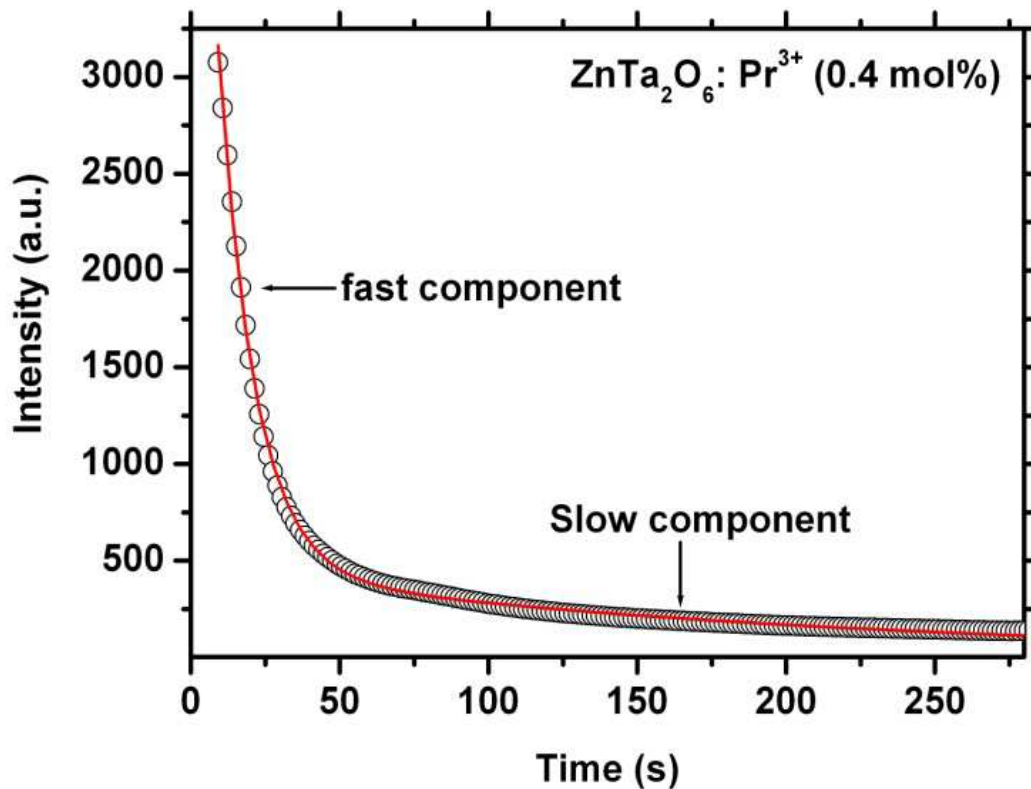
Figure 5.10: Phosphorescence decay curve of $ZnTa_2O_6:Pr^{3+}$ (0.4 mol %) fitted with a second order decay curve.

5.4. Conclusion

A red emitting $ZnTa_2O_6:Pr^{3+}$ phosphor was prepared at 1200 ^{o}C for 4 hours by solid state reaction with different concentrations of Pr^{3+} ions. The main structure was not affected by the incorporation of Pr^{3+} as confirmed by the X-ray diffraction. The f – f transitions were observed from direct Pr^{3+} excitation at 420 to 500 nm, and the major absorption was at 259 nm from band

to band excitation. The blue emission from $^3P_0 \rightarrow {}^3H_4$ transition was absent for 0.1 to 0.8 mol% Pr^{3+} and was detected at 1.0 and 1.2 mol% of Pr^{3+} and this is attributed to cross relaxation between $^1D_2$ and $^3P_0$ states of Pr^{3+} ions. The clustering of Pr^{3+} ions at higher concentrations was confirmed by TOF–SIMS imaging. The absence of the blue emission lead to pure red emission calculated using the CIE coordinate plots. The phosphorescence decay times were calculated from the corresponding decay curves, and it was revealed that they increase with an increase in Pr^{3+} concentration in the matrix.

5.5. References

1. S. Li, X. Liang, Preparation and luminescent properties of $CaTiO_3:Pr^{3+},Al^{3+}$ persistent phosphors by nitrate-citric acid combustion method, J. Mater. Sci: Mater. Electron **19** (2008) 1147.

2. W. Tang, D. Chen, Enhanced red emission in $CaTiO^3:Pr^{3+}$, Bi^{3+}, B^{3+} phosphors, Phys. Status Solidi A **206** (2), (2009) 229.

3. L.L. Noto, S.S. Pitale, M.A. Gusowki, J.J. Terblans, O.M. Ntwaeaborwa, H.C. Swart, Afterglow enhancement with In^{3+} codoping in $CaTiO_3:Pr^{3+}$ red phosphor, Powder Technol. **237** (2013) 141

4. Y. Pan, Q. Su, H. Xu, T. Chen, W. Ge, C. Yang, M. Wu, Synthesis and red luminescence of Pr^{3+} doped $CaTiO_3$ nano-phosphor from polymer precursor, J. Solid Stat. Chem. **174** (2003) 69

5. C. Gheorghies, P. Boutinaud, M. Loic, V.O. Atanasiu, Results on nanosized $CaTiO_3:Pr^{3+}$ phosphor, J. Optoelectron. Adv. Mater. **11** (5), (2009) 583.

6. L. Tian, S. Mho, B.Y. Yu and H. L. Park, Luminescence and VUV Excitation Characteristics of Eu^{3+} - or Tb^{3+} - Activated $Ca_4YO(BO_3)_3$, J. Korean Phys. Soc.47 (6), (2005) 1070

7. Z. Lu, L. Zhang, L. Wang, and Q. Zhang, The concentration dependence of luminescent properties for Sr2TiO4:Eu3+ red phosphor and its charge compensation, J. Nanomater. (2012) doi:10.1155/2012/698434

8. P. Boutinaud, L. Sarakha, E. Cavalli, M. Bettinelli, P. Dorenbos, R. Mahiou, About red afterglow in Pr^{3+} doped titanate perovskites, J. Phys. D: Appl. Phys. **42** (2009) 045106.

9. P. Boutinaud, E. Pinel, M. Dubois, A.P. Vink, R. Mahiou, UV-to-red relaxation pathways in $CaTiO_3:Pr^{3+}$, J. of Lumin. **111** (2005) 69.

10. P.T. Diallo, P. Boutinaud, R. Mahiou, J. Cousseins, Red luminescence in Pr^{3+} doped calcium titanates, Phys. Stat. Sol. (a) **160** (1997) 255

11. C. De Mello Donega, A. Meijerink, G. Blasse, Non-radiative relaxation processes of the Pr^{3+} ion in solids, J. Phys. Chem. Solids **56** (5), (1995) 673

12. M. Waburg, H. Muller-Buschbaum, $ZnTa_2O_6$ ein neuer Vertreter des tri-α-PbO_2-Typs (mit ergänzenden Daten über $ZnNb_2O_6$), Zeitschrift fuer Anorganische und Allgemeine Chemie **508** (1984) 55

13. A.D. Broadbent, A critical review of the development of the CIE1931 RGB color matching functions, Color Res. Appl. **29** (4), (2004) 267.

14. B.R. Chakraborty, D. Haranath, H. Chander, S. Hellweg, D. Dambach, H.F. Arlinghaus, TOF-SIMS and laser-SNMS investigations of dopant distribution in nanophosphors, Nanotechnol. **16** (2005) 1006.

"Some of the best ideas come out of the blue, and you have to keep an open mind to see their virtue"

— Richard Branson

6

Enhancement of persistent luminescence of $ZnTa_2O_6$:Pr^{3+} by adding Li^+, Na^+, K^+, Cs^+ ions

6.1. Introduction

The persistent luminescence is a subject of interest lately, particularly to the researchers that strongly intend to make contribution to its less understood mechanism. Apart from understanding the mechanism, there are several applications that drive the research of materials that display persistent luminescence. Such materials are set to answer the need for energy conservation. A typical example of such a phosphor would be one that can absorb energy from the sunlight during the day, and continue to glow longer than 12 hrs in the absence of the excitation source. Such a phosphor will lead to cost-effective lighting of street and houses. The additional applications for such materials involve phosphors for medical diagnosis, self-lit emergency and security signs [1]. Until today the true mechanism underlying the persistent emission is yet not clearly understood [2]. By definition, the phosphorescence emission is generally referred to as the emission lasting from one millisecond to ten seconds at room temperature after the excitation source has been removed [3]. It is attributed to the intersystem crossing due to vibrational coupling between the excited singlet and triplet state. This process brings about delayed fluorescence emission, which is referred to as phosphorescence [3]. When luminescence persists longer than the defined phosphorescence, it is then referred to as persistent luminescence or rather long afterglow [1,2]. Such luminescence prolongs to minutes and may extend to several hours in other phosphors as reported for $SrAl_2O_4$:Eu^{2+}, Dy^{3+} [2], $CaTiO_3$:Pr^{3+}, In^{3+} [4] and $Zn_3Ga_2Ge_2O_{10}$: Cr^{3+} [1]. The persistent emission is so far understood to be associated with the presence of electron trapping centres inside a material, which originate from the existence of

oxygen vacancies. The trapping and release of the electrons delays the electrons temporarily before they reach the luminescence centre [4]. Though the mechanism is not yet fully understood, there are several methods that have been used to try and enhance the lifetime of the persistence luminescence. Noto et al [4], co-doped In^{3+} ions in $CaTiO_3:Pr^{3+}$ as charge compensators, to suppress the quenching centres and increase the quantity of the electron trapping centres. The resulting effect was enhanced luminescence intensity and enhanced lifetime of the persistent emission. Swart et al [5] report on the persistent luminescence of $SrAl_2O_4:Eu^{2+}$, Dy^{3+}, and attributed it to the delay of electrons by electron trapping centres associated with oxygen vacancies, before they reach the 5d state of Eu^{2+}, from where luminescence emanates. Lin et al [6], suggests that the persistent emission from $SrAl_2O_4:Eu^{2+}$, Dy^{3+} is due to the increased quantity of electron trapping centres generated by co-doping with Dy^{3+} ions.

In this work, we investigate the effects of ionic disordering to the host by co-doping $ZnTa_2O_6:Pr^{3+}$ phosphor with alkali metal ions of different ionic radius. The Li^+, Na^+, K^+ or Cs^+ ions with the ionic radii of 0.073, 0.113, 0.151 and 0.184 nm, respectively [7], were used as co-dopants.

6.2. Experimental

$ZnTa_2O_6$: Pr^{3+} (0.4 mol%) phosphor co-doped with 0.4 mol% of Li^+, Na^+, K^+ or Cs^+ ions, was prepared by solid state reaction. The samples were prepared by mixing ZnO, Ta_2O_5 and $PrCl_3$ in stoichiometric amounts. Additionally, Li_2CO_3, $NaNO_3$, K_2CO_3 or CsF were added in stochiometric amounts to give 0.4 mol% as a co-dopant. The reagents were mixed into a slurry using methol, which was pre-heated at 100 ^oC for 10 hrs and later sintered at 1200 ^oC for 4 hrs. The product was allowed to cool down to room temperature and was ground into powder. The crystalline phase was identified by a Bruker AXS D8 Advance X-Ray diffractometer (XRD) using Cu $K\alpha$ radiation. The photoluminescence (PL) emission and excitation (PLE) properties of the phosphor were probed using the Varian Carry-Eclipse fluorescence spectrophotometer. The scanning electron microscopy (SEM) image was obtained using the Shimadzu SSX-550 SEM from Kyoto, Japan. The surface maps showing the distribution of the ions, were obtained using the time of flight secondary ion mass spectroscopy (ToF – SIMS 5). The Bi^+ ion gun with 1 pA beam current was used to probe the surface of the phosphor, and was operated in the imaging

mode. The phosphorescence decay curves for the measurement of the persistent emission lifetime were measured by exciting the phosphor with an ultraviolet source for 5 minutes, then measuring the time it takes for the emission to decay using a photomultiplier tube (PMT). The glow curves were measured using a 254 nm ultraviolet source for excitation and the TL were measured using a TL 10091, NUCLEONIX spectrometer.

6.3. Results and Discussion

The measured XRD patterns (Figure 6.1(a)) show that pure phase and crystalline particles of $ZnTa_2O_6$:Pr^{3+} were prepared, even in the presence of the co-dopant ions. The pattern is consistent with the standard orthorhombic $ZnTa_2O_6$ phase referenced in the ICSD card number 36289 [8]. However, the XRD peaks of the samples with the co-dopant show a shift to the higher angles (Figure 6.1(b)), and this may be an indication that the co-dopants introduce strain within the material [9].
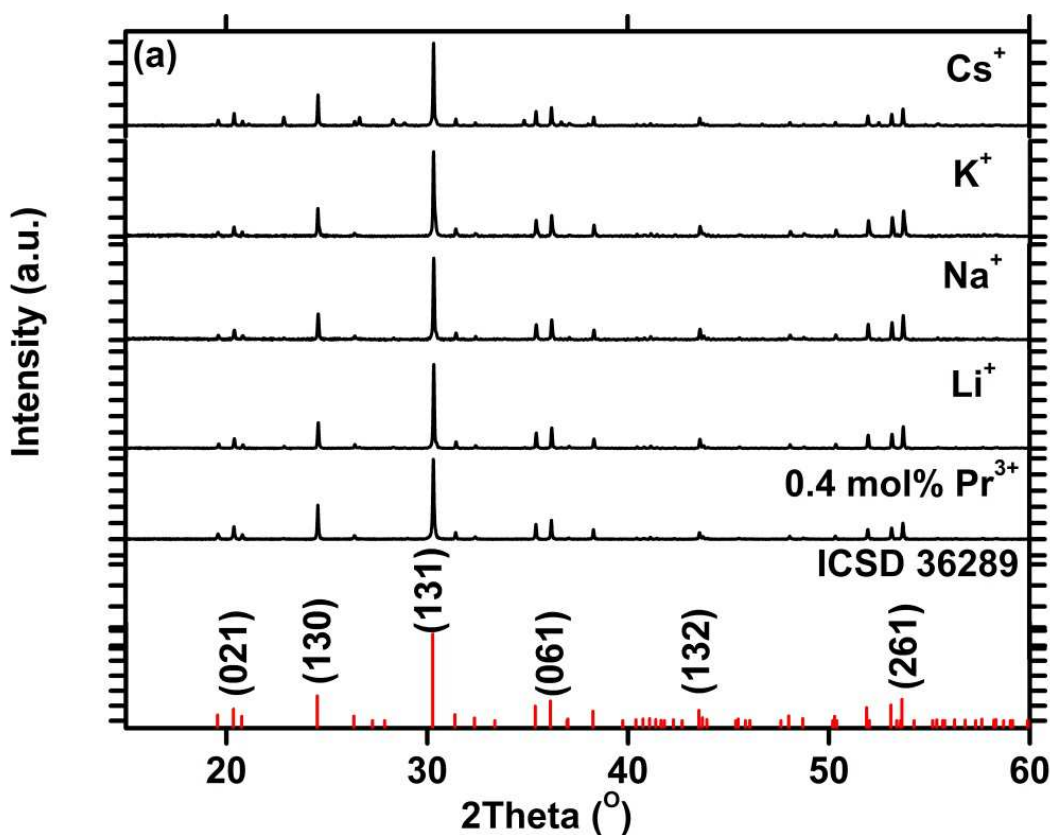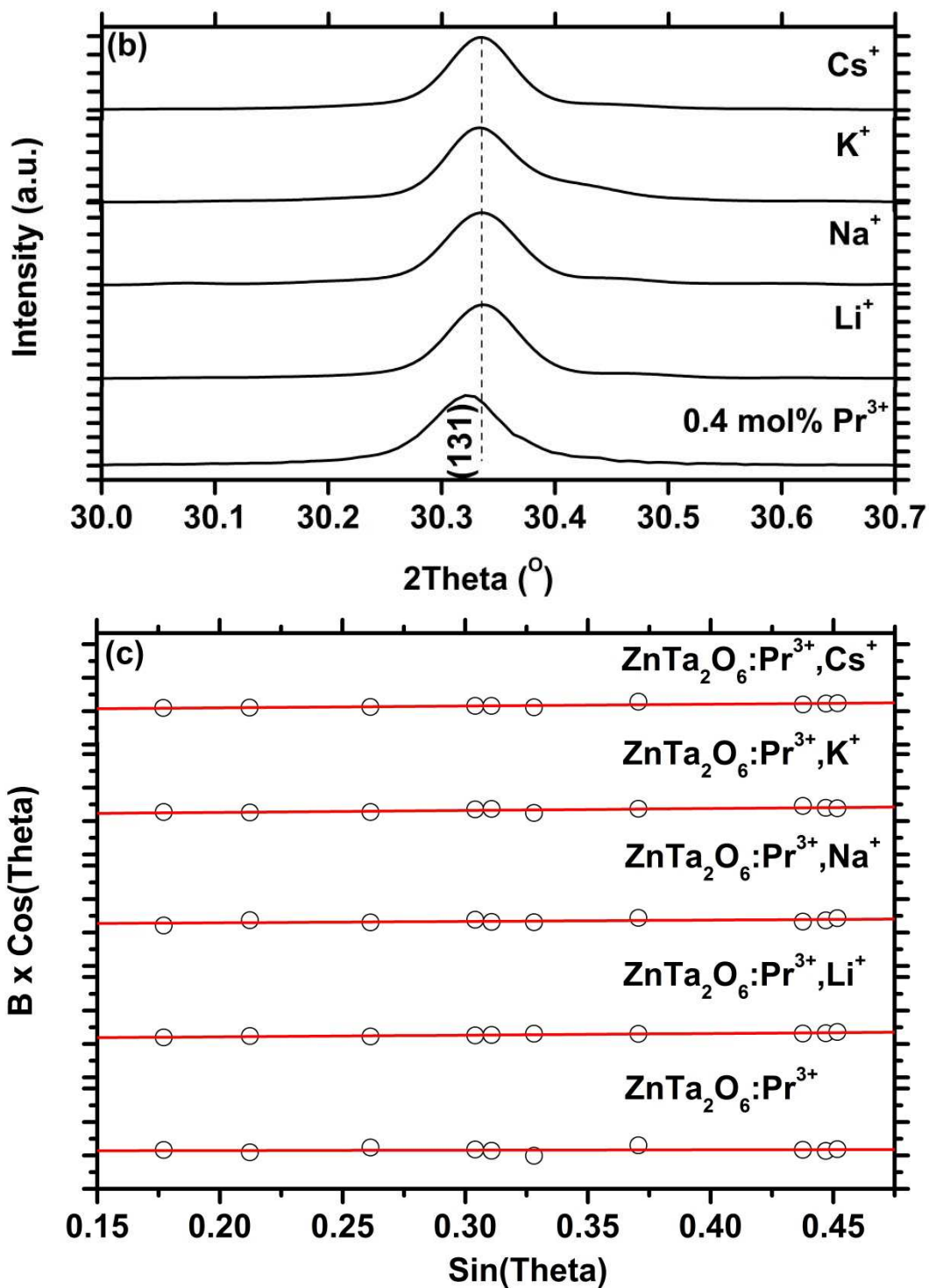
Figure 6.1: (a) Comparison of the XRD pattern of $ZnTa_2O_6$:Pr^{3+} with that of co-doped samples. (b) Shows the shifting of the (131) XRD peak of the co-doped samples. (c) Hall-Williamson plot for microstrain analysis.

Table 6.1: Strain comparison

Sample	Ion	Co-dopant ionic radius nm	Normalised Strain
$ZnTa_2O_6:Pr^{3+}$			0.024 ± 0.001
$ZnTa_2O_6:Pr^{3+},Li^+$	Li^+	0.073	0.029 ± 0.003
$ZnTa_2O_6:Pr^{3+},Na^+$	Na^+	0.113	0.031 ± 0.009
$ZnTa_2O_6:Pr^{3+},K^+$	K^+	0.151	0.035 ± 0.008
$ZnTa_2O_6:Pr^{3+},Cs^+$	Cs^+	0.184	0.041 ± 0.005

The microstrain experienced by the material and the particle sizes were approximated using the Hall–Williamsons' equation (Eq. 6.1):

$$\frac{\beta Cos(\theta)}{\lambda} = \frac{1}{D} + \frac{\varepsilon Sin(\theta)}{\lambda}$$

$$[6.1]$$

where β (Corrected as B in figure 6.1(c)) is the Full width at half maximum, θ angle of the diffraction peak in degrees, λ (1.54 Å) is the wavelength of the corresponding X-rays, D is the crystalline size, and ε is the percentage of the strain in the material [10]. The corresponding strain values as a result of the co-dopant, which is obtained as a slope of the fit in the data plotted in Figure 6.1(c) are listed in Table 6.1. According to the calculations, the strain on the material systematically increases with an increase in the ionic radii of the co-dopant ion.

Figure 6.2 shows the crystal structure of $ZnTa_2O_6$ drawn using the Diamond 3.0 software package [11]. The ionic radii of Zn^{2+} and Ta^{5+} are 0.074 and 0.078 nm, respectively, and the bigger ionic radii of Na^+ (0.113 nm), K^+ (0.151 nm) and Cs^+ (0.184 nm) are likely to substitute in the site of a bigger ion (Ta^{5+}) within the octahedron cage of $ZnTa_2O_6$ (Figure 6.3) [7]. On the contrary, the ions of Li^+ (0.073 nm) have an ionic radius that is smaller than that of both the Zn^{2+} and Ta^{5+} ions [7]. It can therefore substitute both in the site of the Ta^{5+} ions within the octahedron cage or the Zn^{2+} site within the pyramid cage. The strain picked up by the sample upon incorporating the co-dopant ion may be due to the bigger ions substituting in the smaller

sites in the case of Na^+, K^+, Cs^+, and due to the collapse of the cages when the smaller Li^+ substitutes for either Zn^{2+} or Ta^{5+}.
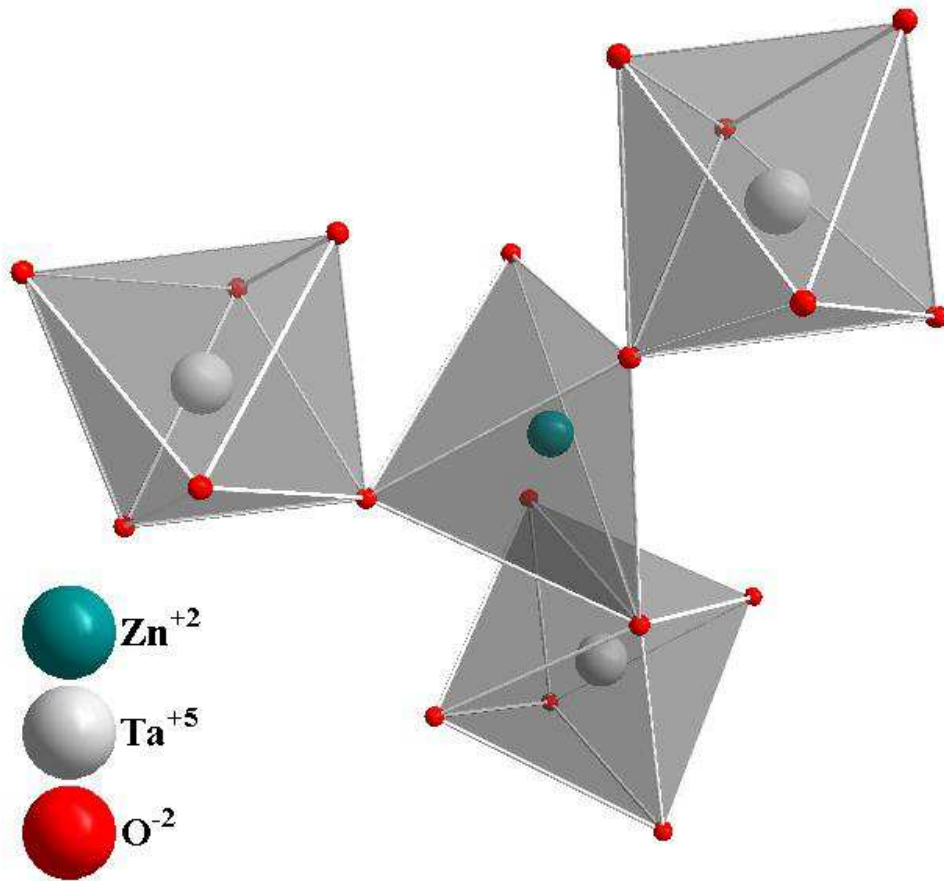
Figure 6.2: $ZnTa_2O_6$ structure drawn with the Diamond crystal structure program.

The intercept value ((λ/D) according to Eq. 6.1) was obtained approximately as 0.006 for all samples from the fit, and was used to calculate the crystallite sizes, which were approximated to be around 257 nm. Figure 6.3 shows the SEM of $ZnTa_2O_6$:Pr^{3+} phosphor from a 5 µm field of view image. The particles show different irregular shapes and sizes, and mostly are agglomerated due to the high preparation temperature [4,10].
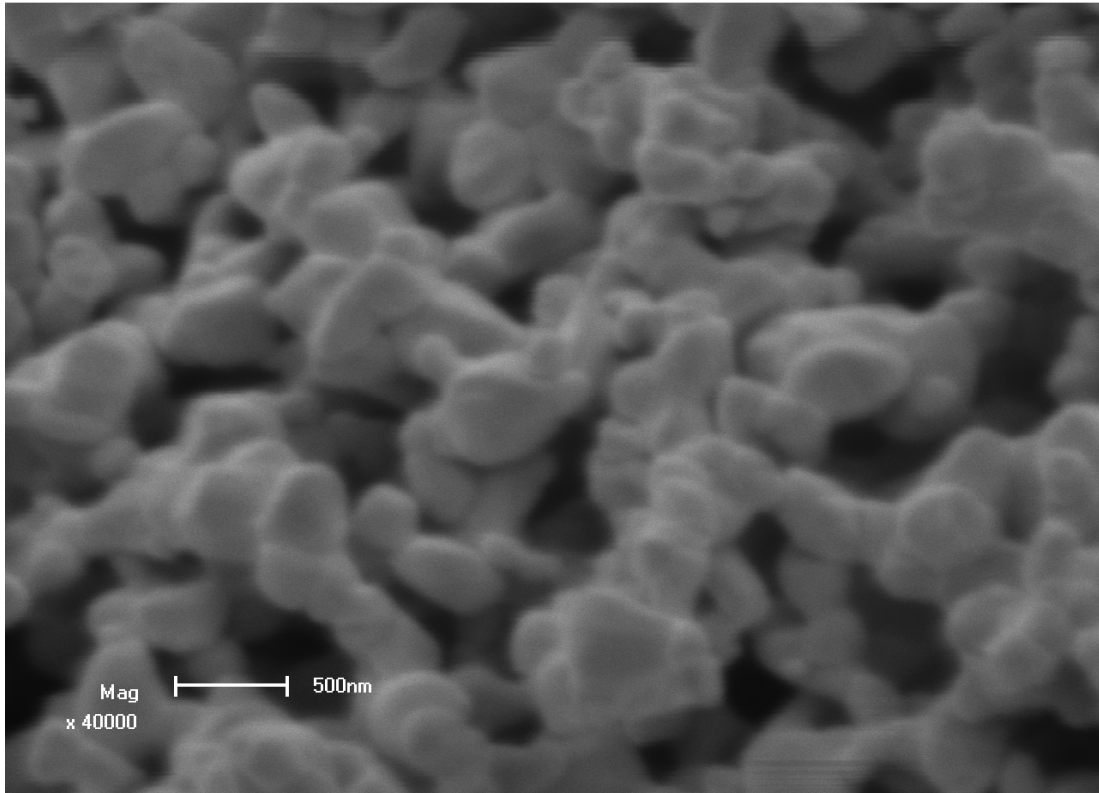
Figure 6.3: SEM image of $ZnTa_2O_6$:Pr^{3+} showing in a 5 µm field of view.

ToF-SIMS images were obtained for the samples co-doped with Li^+, Na^+, K^+ and Cs^+, and are shown in Figure 6.4 (a), (b), (c) and (d). The ion distribution on the surface is shown using a red colour for $ZnOH^+$ ions, a green colour for TaO^+ ions and a blue colour for either PrO^+ or (LiO^+, NaO^+, KO^+, or CsO^+). The mapping was obtained over an area of 100 µm $\times$ 100 µm on the surface of the samples. The $ZnOH^+$, TaO^+, PrO^+ and LiO^+, NaO^+, KO^+ and CsO^+ ions obtained upon probing the sample are used to reflect the distribution of the corresponding Zinc, Tantalum, Oxygen, Praseodymium, Lithium, Sodium, Potassium and Caesium ions inside the phosphor samples, respectively. The overlay mapping shows the distribution of the ions in the samples. In all samples, the Praseodymium ions appear to be uniformly distributed, and this is an indication of its successful incorporation in the host lattice. On the contrary, Lithium ions appear to have clustered in smaller areas as observed in the overlay $ZnTa_2O_6$: Pr^{3+},Li^+ sample (Figure 6.3(a)). Na^+, K^+, Cs^+ions are uniformly distributed in their corresponding samples as observed in Figure 6.4 (b), (c) and (d), respectively.
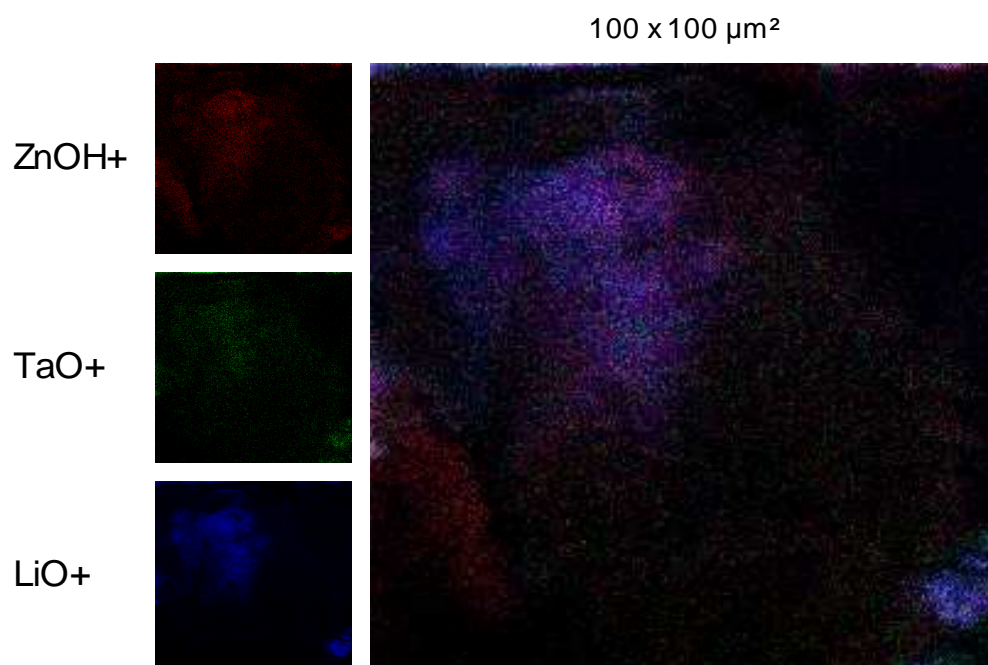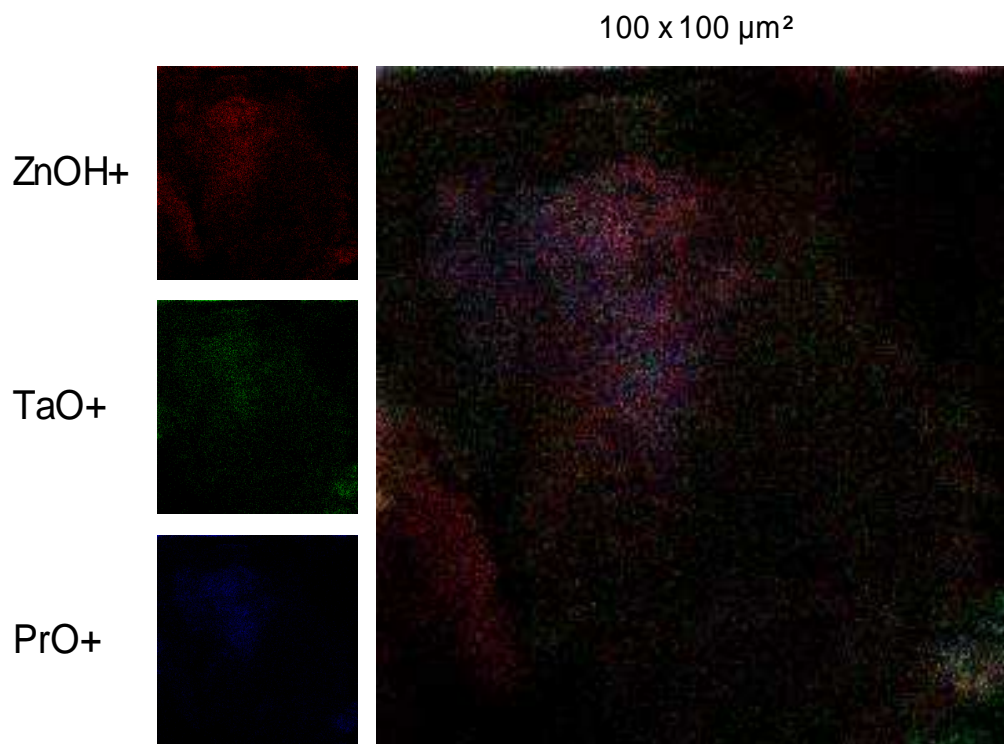
Figure 6.4 (a): ToF – SIMS surface mapping of $ZnTa_2O_6$:Pr^{3+}, Li^+.

ZnOH+

TaO+

PrO+

ZnOH+

TaO+

NaO+
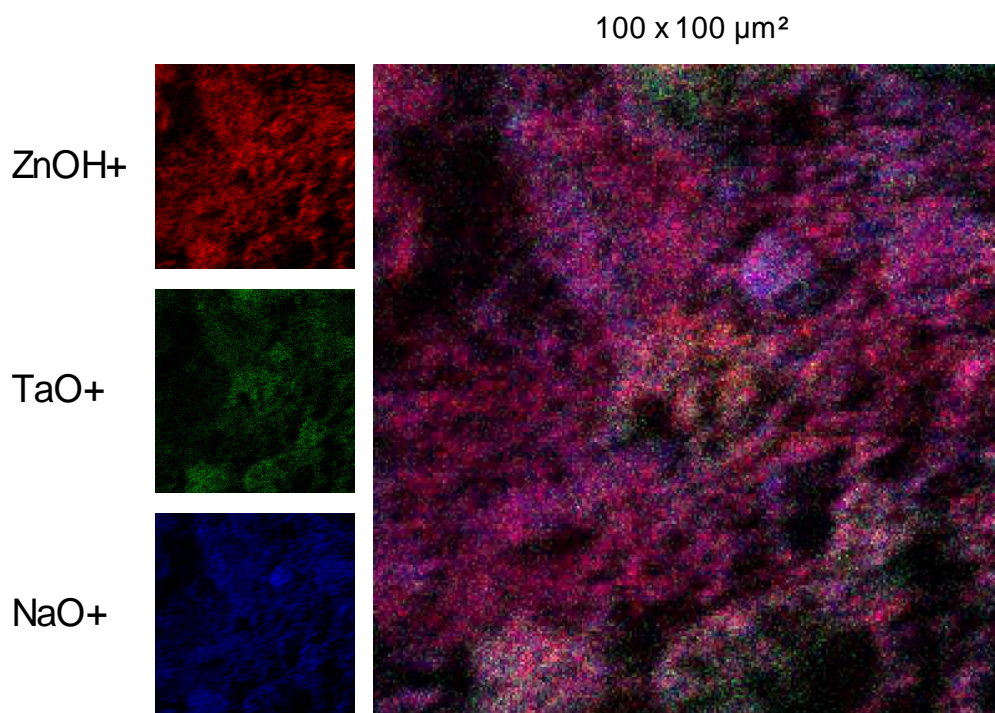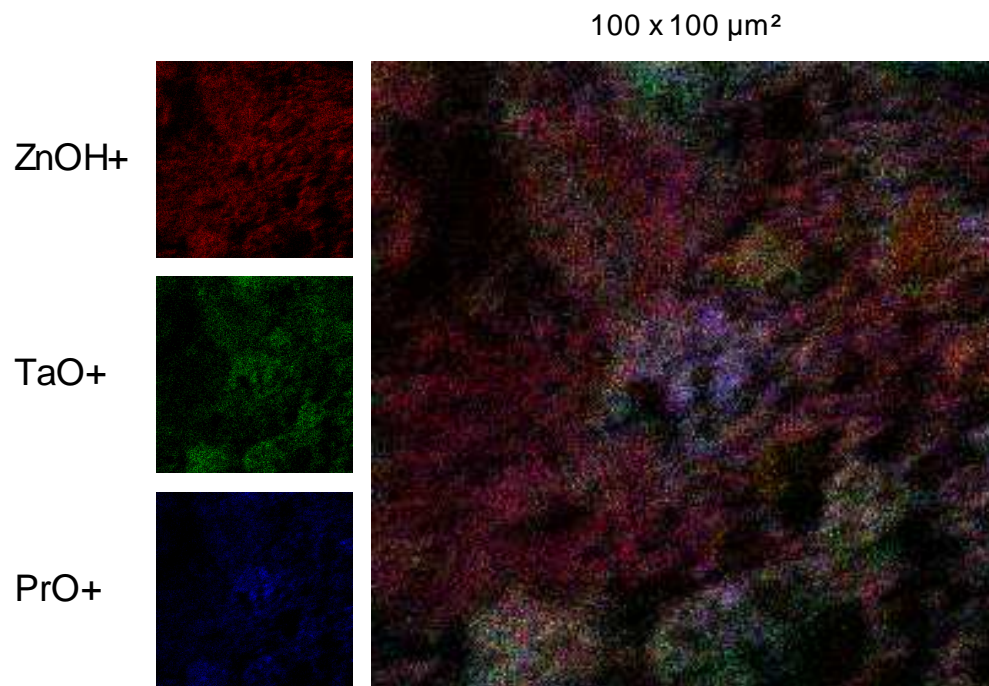
Figure 6.4 (b): ToF – SIMS surface mapping of $ZnTa_2O_6:Pr^{3+}, Na^+$.
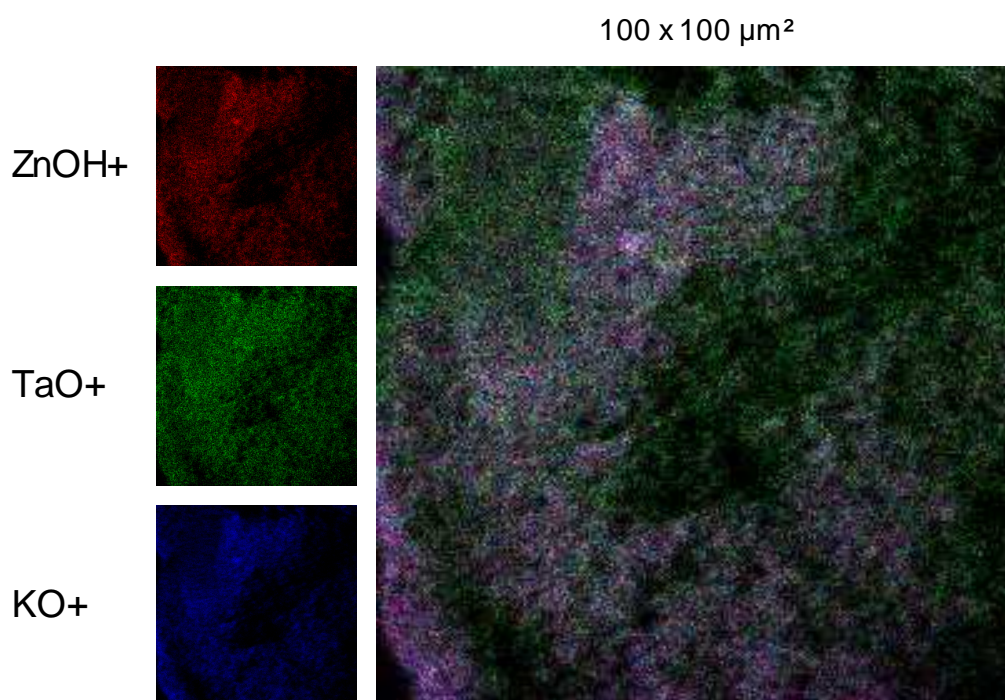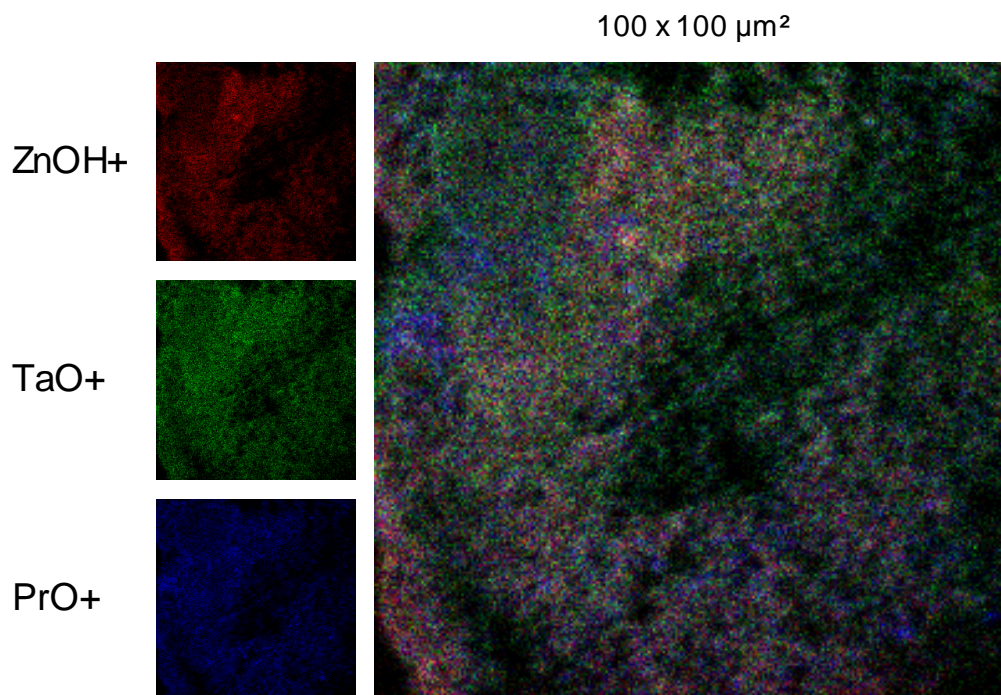
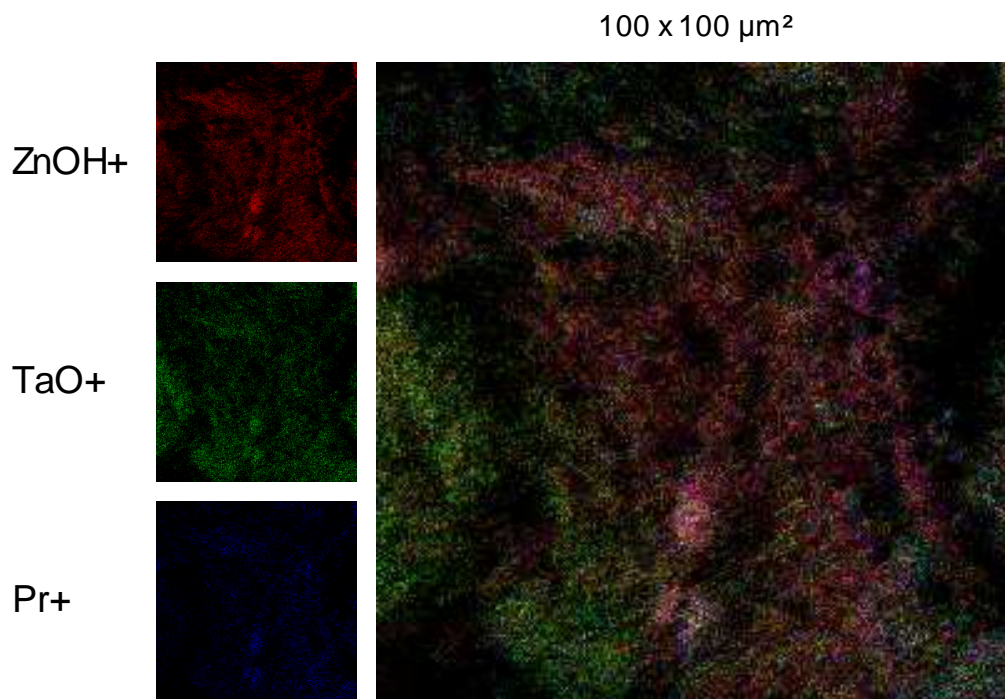Figure 6.4 (c): ToF – SIMS surface mapping of $ZnTa_2O_6:Pr^{3+}, K^+$.

ZnOH+

TaO+

Pr+

ZnOH+

TaO+

CsO+
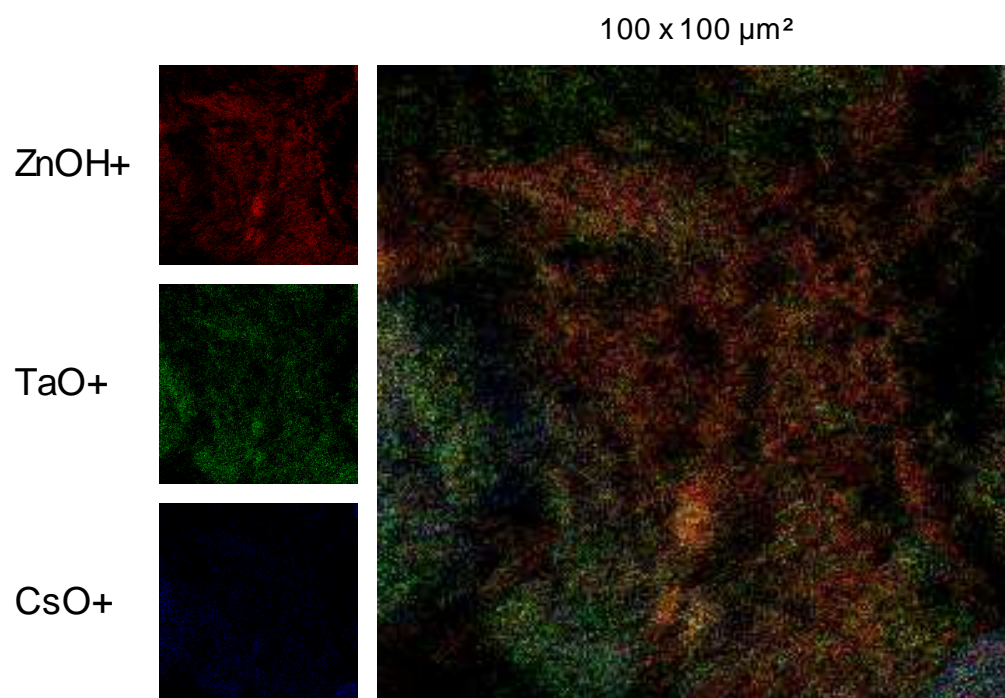
Figure 6.4 (d): ToF – SIMS surface mapping of $ZnTa_2O_6$:Pr^{3+}, Cs^+.
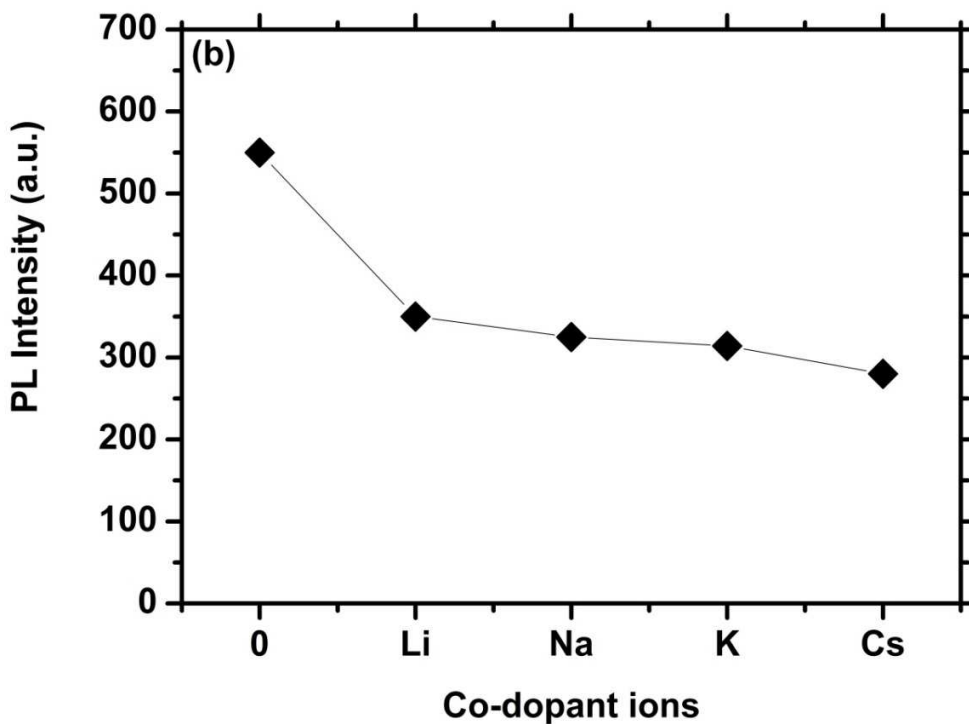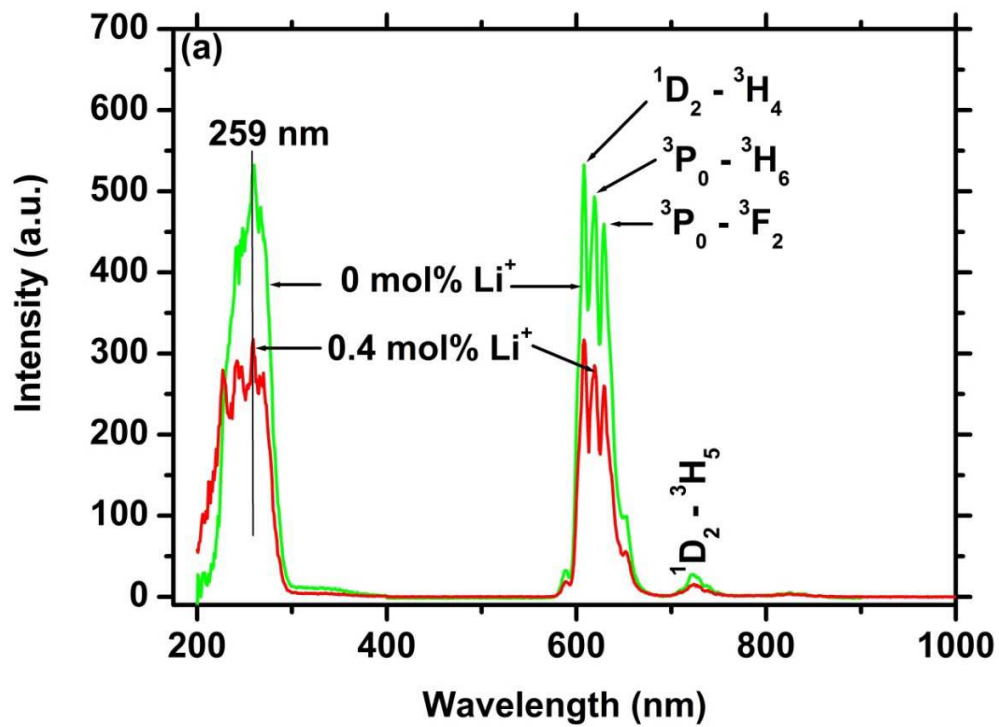
Figure 6.5: (a) PL and PLE of $ZnTa_2O_6:Pr^{3+}$ and $ZnTa_2O_6:Pr^{3+}$, Li^+ phosphor samples. (b) Maximum luminescence intensity comparison for the different co-doped ions.

The photoluminescence emission spectrum (Figure 6.5(a)) of $ZnTa_2O_6:Pr^{3+}$ (0.4 mol%) phosphor shows only red emission lines from Pr^{3+} upon exciting with 259 nm ultraviolet light source. The red emission lines attributed to $^1D_2 \rightarrow {}^3H_4$, $^3P_0 \rightarrow {}^3H_6$ and $^3P_0 \rightarrow {}^3F_2$ transitions are at 608, 619 and 639 nm, respectively [11]. There is additionally a minor emission line at 720 nm, which is attributed to $^1D_2 \rightarrow {}^3H_5$ transition [4,12]. The PLE spectrum was acquired to evaluate the position of the excitation bands, and the most prominent absorption band is situated at 259, which corresponds to band to band excitation [12]. The incorporation of the Lithium ions into $ZnTa_2O_6:Pr^{3+}$ partly hinders the luminescence intensity, as shown in Figure 6.4. Similarly, the incorporation of Na^+, K^+, Cs^+ ions into the phosphor result in a decrease in luminescence intensity (Figure 6.5(b)). This may be an indication that the addition of the co-dopants introduces the defect centres that act as quenching centres of luminescence.
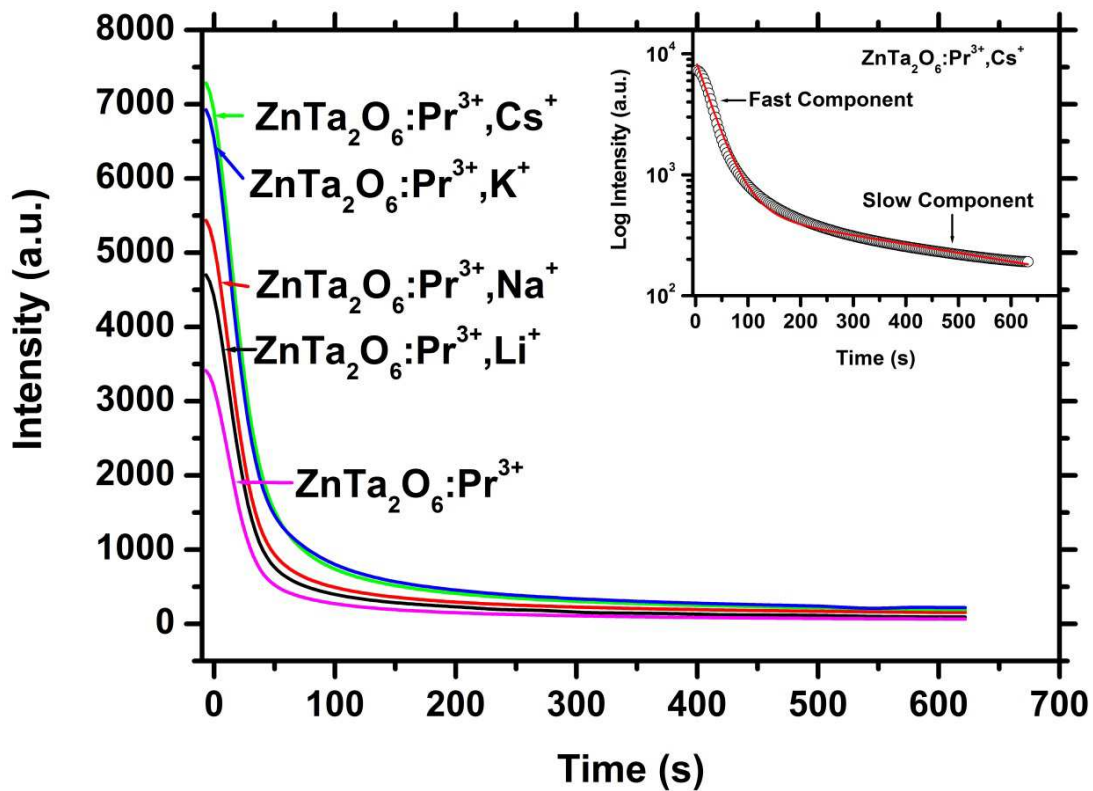

Figure 6.6: Phosphorescence decay curve of $ZnTa_2O_6:Pr^{3+}$ co-doped with Li^+, Na^+, K^+ and Cs^+.

Table 6.2: The decay time parameters; τ_1 and τ_2.

Sample	τ_1 (s)	τ_2 (s)
$ZnTa_2O_6:Pr^{3+}$	29.0 ± 0.6	540 ± 31
$ZnTa_2O_6:Pr^{3+},Li^+$	30.1 ± 0.5	589 ± 21
$ZnTa_2O_6:Pr^{3+},Na^+$	29.5 ± 0.7	619 ± 23
$ZnTa_2O_6:Pr^{3+},K^+$	30.6 ± 0.6	650 ± 19
$ZnTa_2O_6:Pr^{3+},Cs^+$	31.9 ± 0.6	679 ± 25

The phosphorescence decay curves were measured for the 5 samples in order to determine lifetime of the persistent emission. All samples were excited for five minutes with an ultraviolet lamp of 254 nm wavelength, followed by monitoring the emission intensity with a photomultiplier tube after removing the excitation source. The decay profiles are presented in Figure 6.6 and the corresponding time parameters are presented in Table 6.2. The profiles are presented in a linear scale for ease of comparison, and the inset (Figure 6.6 inset) shows the decay profile of $ZnTa_2O_6: Pr^{3+},Cs^+$ in the log scale to show the number of decay components. The profile appears to have two components; namely the fast and the slow components which correspond to the lifetime coming from Pr^{3+} emission and trapped electrons within oxygen vacancies, respectively [4,10]. The time it takes for each component to decay was extracted by fitting the profile using the second order decaying exponential curve (Eq. 6.2) [4]:

$$I(t) = Ae^{-t/\tau_1} + Be^{-t/\tau_2}, \qquad [6.2]$$

where I is the luminescence intensity, A & B are constants, t is the phosphorescence time, τ_1 and τ_2 are the decay times of the first and the second components, respectively [4]. The persistent emission (τ_2) lifetime increases with the incorporation of the co-dopant ions, compared to that of a phosphor without a co-dopant (570 ± 15 secs) as reported by Noto et. al. [12]. The increase continues with an increase in the ionic radius of the co-dopant ion. The electron trapping centres are reported as the main source for the persistent emission [4,10,12], and the increase of the

persistent emission lifetime with the ionic radius, may be an indication that the bigger co-dopant ions promote more formation of the electron trapping centres.
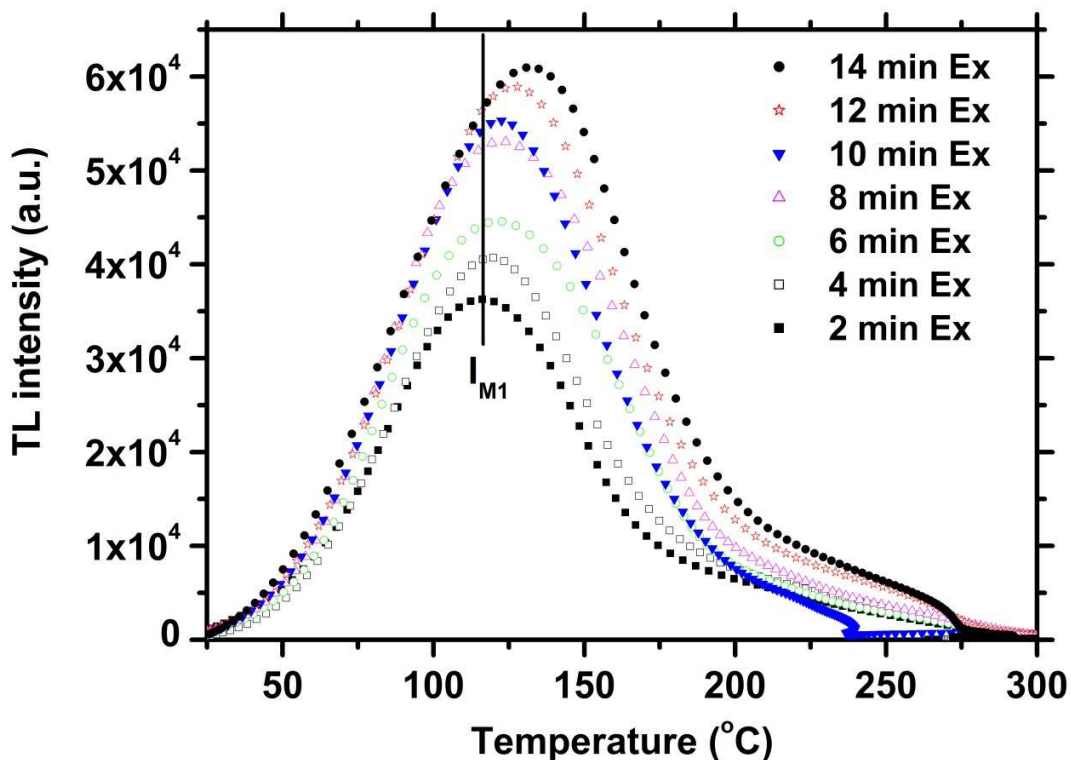

Figure 6.7: Glow curves of $ZnTa_2O_6$:Pr^{3+} obtained after exposing the material to different dose times.

The increase of the electron trapping centres with the increase in the ionic radius of the co-dopant was further investigated with the thermoluminescence spectroscopy. The TL glow curves (Figure 6.7) for $ZnTa_2O_6$: Pr^{3+} exposed to different amounts of UV radiation dosage were measured. The glow curves were measured using a heating rate of 2 K/sec, and the irradiation period was 2 minutes for each sample. A systematic shift to higher temperature of the peak maximum is observed with an increase in the exposure time from the plotted curves (Figure 6.7). The increase to higher temperatures is an indication of kinetics which are neither first nor second order, but of general order [10]. The kinetics of the samples co-doped with Li^+, Na^+, K^+ and Cs^+ were also treated as the general order.
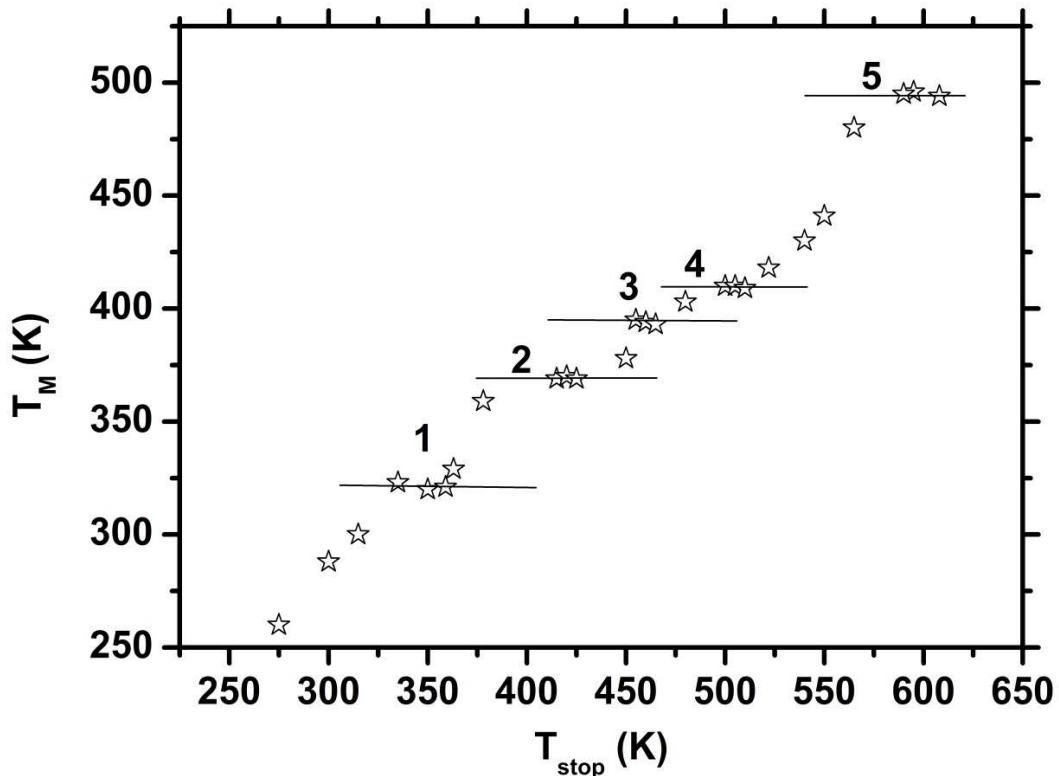
Figure 6.8: $T_m - T_{stop}$ measurements for $ZnTa_2O_6:Pr^{3+}$.

The corresponding number of the electron trapping centres was revealed from the T_m-T_{stop} measurements (Figure 6.8), which suggested the presence of five prominent electron trapping centres. The measurement of the T_m-T_{stop}, involved irradiating the sample for 2 minutes, then heating it until a certain temperature T_{stop} and then recording the temperature (T_m) corresponding to the maximum intensity. The same procedure is repeated by shifting the T_{stop} to higher temperatures, until the whole glow curve is recorded.

The glow curves of all samples were deconvoluted into 5 thermal peaks (Figure 6.9), which correspond to the quasi continuous distribution of electron trapping centres that have a very close energy distribution within the forbidden region [13,14]. The deconvolution was performed by the computerised glow curve deconvolution (CGCD) from a software package (TLAnal) developed by Chung et al [15]. The general order kinetics related functions were used to compute for the activation energy (Eq. 6.3), frequency factor (Eq. 6.4) and the concentration of the electrons trapped within electron trapping centres (Eq. 6.5).
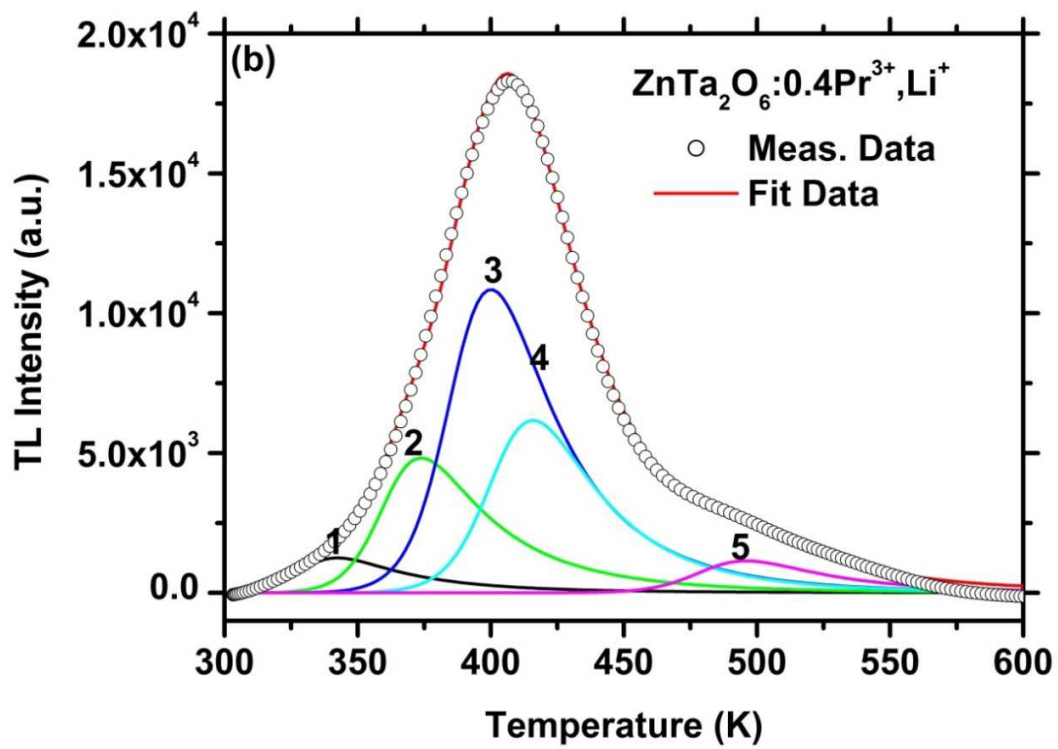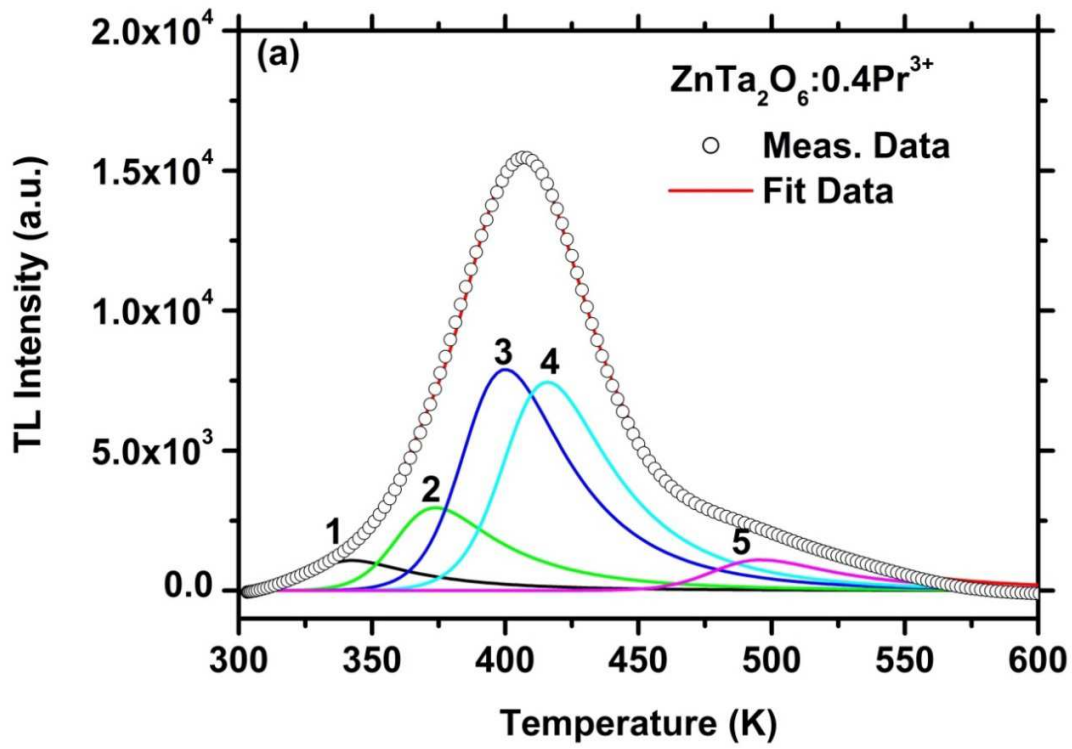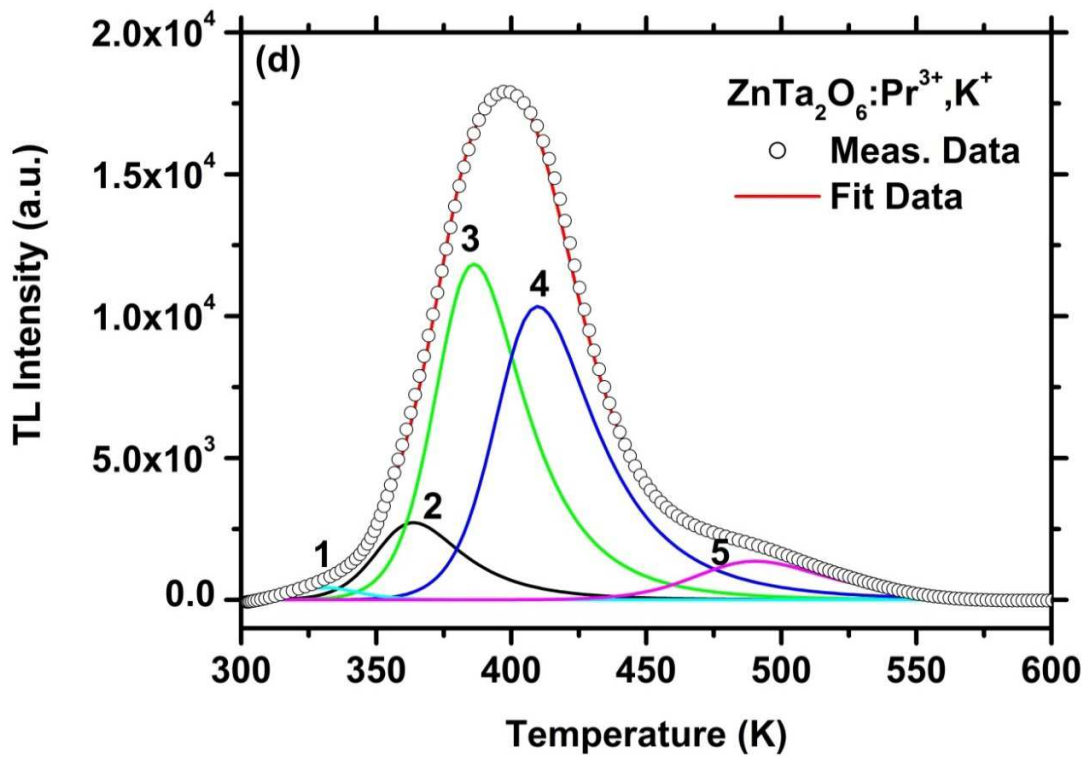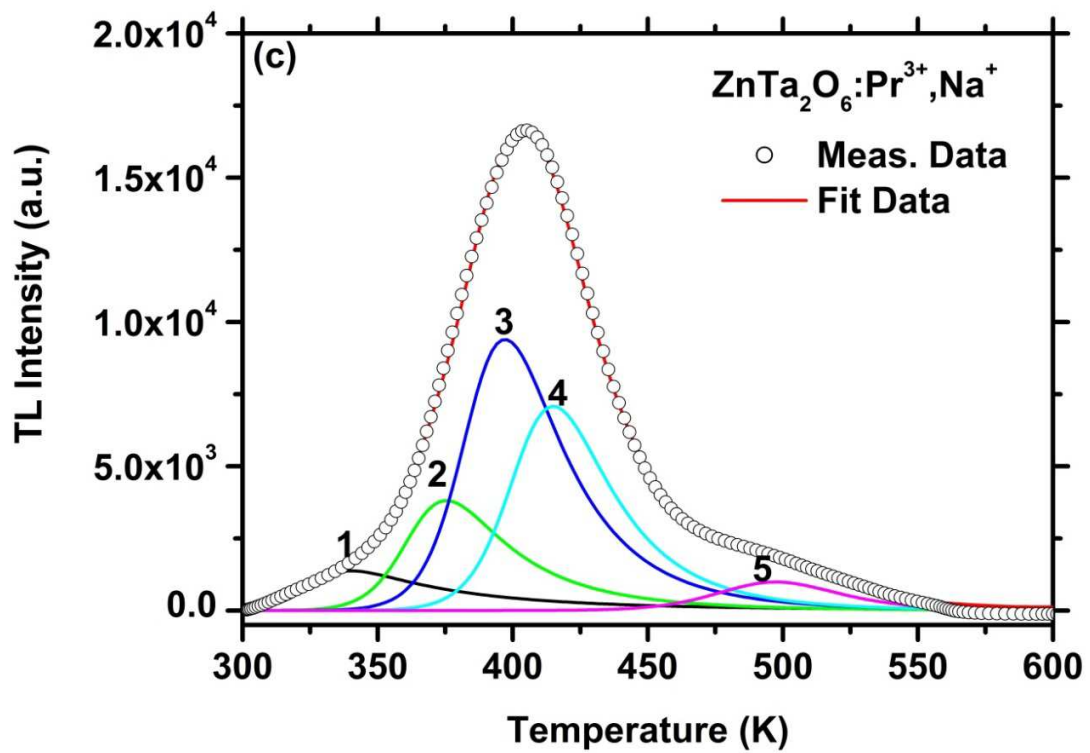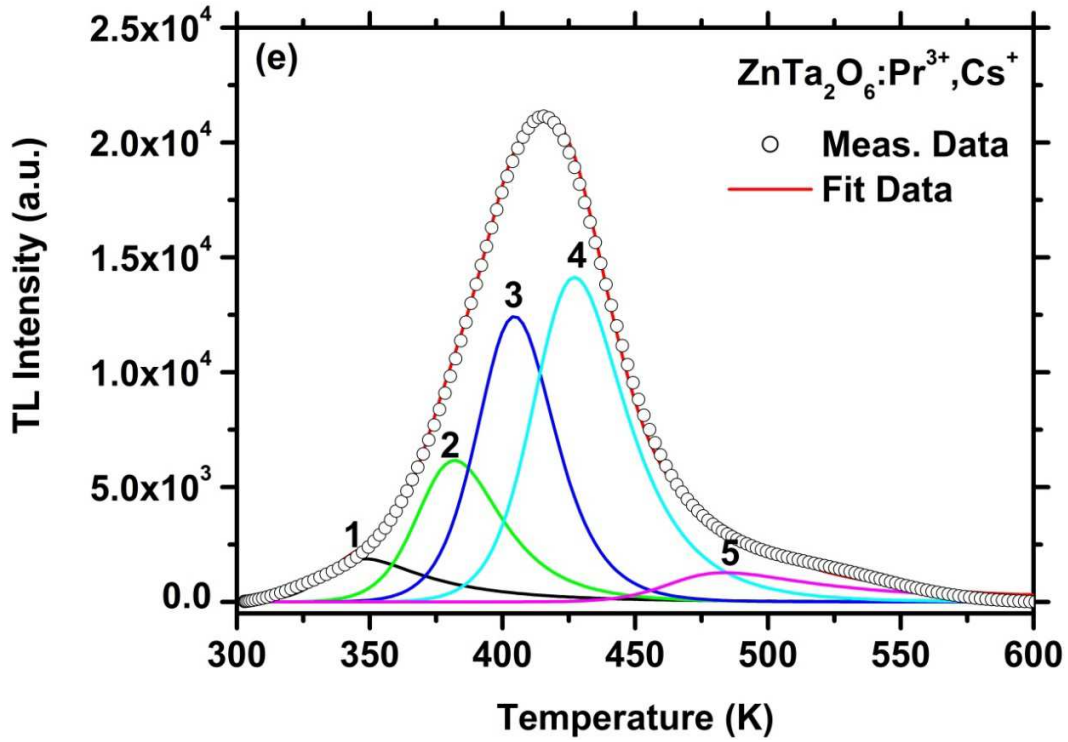
Figure 9: (a) TL glow curve of $ZnTa_2O_6$:Pr^{3+} and the samples co-doped with (b) Li^+, (c) Na^+, (d) K^+ and (e) Cs^+ ions.

$$I(T) = I_M b \frac{b}{b-1} exp\left(\frac{E}{kT}\right.$$

$$\times \frac{T - T_M}{T_M}\right)\left[1 + (b-1)\frac{2kT_M}{E} + (b-1)\left(1 - \frac{2kT_M}{E}\right)\right.$$

$$\times \left(\frac{T^2}{T_M^2}\right) exp\left(\frac{T - T_M}{T_M}\frac{E}{kT}\right)\right]^{\frac{-b}{b-1}} \qquad [6.3]$$

$$s = \frac{\beta E}{kT_M^2\left(1 + \frac{2kT_M(b-1)}{E}\right)} exp\left(\frac{E}{kT_M}\right) \qquad [6.4]$$

$$I(T) = sn_o exp\left(-\frac{E}{kT}\right)\left[1 + \frac{s(b-1)}{\beta}\int_{T_0}^{T} exp\left(-\frac{E}{kT}\right) dT\right]^{-\frac{b}{b-1}} \qquad [6.5]$$

where I_M and T_M are the TL intensity and temperature (K) at the glow peak maximum respectively, E is the activation energy (eV), k is the Boltzmann constant, β is the heating rate, n_o is the concentration of the trapped electrons and b is the kinetic parameter [13]. The corresponding kinetic parameters for all samples are listed in Tables 6.3, 6.4, 6.5 6.6 and 6.7. The data shows an increase in concentration of the trapped electrons with the increase in the ionic radius of the co-dopant ion. This is an indication of the material generating more oxygen vacancies as it undergoes more strain caused by the co-dopant ions.

Table 6.3: The kinetic parameters associated with $ZnTa_2O_6:Pr^{3+}$ glow curve, which were obtained using the CGCD procedure.

Trap	T_{max} (K)	Trap depth $E(eV)$	Concentration n_o (cm^{-3})	Frequency factor s (s^{-1})
1	341	1.13	3.71×10^4	6.77×10^{17}
2	373	1.36	5.64×10^4	5.67×10^{17}
3	399	1.40	1.48×10^5	7.81×10^{17}
4	415	1.48	9.34×10^4	9.99×10^{16}
5	594	1.71	3.92×10^4	5.94×10^{17}

Table 6.4: The kinetic parameters associated with the glow curve of $ZnTa_2O_6:Pr^{3+},Li^+$.

Trap	T_{max} (K)	Trap depth $E(eV)$	Concentration n_o (cm^{-3})	Frequency factor s (s^{-1})
1	334	0.98	2.91×10^4	1.37×10^{17}
2	375	1.34	6.70×10^4	1.58×10^{17}
3	397	1.41	6.52×10^5	1.06×10^{17}
4	415	1.49	7.90×10^4	1.19×10^{17}
5	490	1.70	2.81×10^4	1.37×10^{17}

Table 6.5: The kinetic parameters associated with the glow curve of $ZnTa_2O_6:Pr^{3+},Na^+$.

Trap	T_{max} (K)	Trap depth $E(eV)$	Concentration n_o (cm^{-3})	Frequency factor s (s^{-1})
1	329	0.96	3.93×10^4	1.58×10^{17}
2	363	1.22	6.84×10^4	1.09×10^{17}
3	386	1.39	2.98×10^5	1.00×10^{17}
4	409	1.43	8.45×10^4	1.32×10^{17}
5	490	1.72	3.22×10^4	1.16×10^{17}

Table 6.6: The kinetic parameters associated with the glow curve of $ZnTa_2O_6:Pr^{3+},K^+$.

Trap	T_{max} (K)	Trap depth $E(eV)$	Concentration n_o (cm^{-3})	Frequency factor s (s^{-1})
1	331	1.97	1.71×10^4	6.77×10^{17}
2	363	1.21	5.12×10^4	5.67×10^{17}
3	386	1.40	7.48×10^5	7.81×10^{17}
4	409	1.42	9.74×10^4	9.99×10^{16}
5	491	1.72	3.52×10^4	5.94×10^{17}

Table 6.7: The kinetic parameters associated with the glow curve of $ZnTa_2O_6:Pr^{3+},Cs^+$.

Trap	T_{max} (K)	Trap depth $E(eV)$	Concentration n_o (cm^{-3})	Frequency factor s (s^{-1})
1	347	1.14	4.71×10^4	6.77×10^{17}
2	382	1.36	8.64×10^4	5.67×10^{17}
3	404	1.42	6.48×10^5	7.81×10^{17}
4	427	1.51	7.14×10^5	9.99×10^{16}
5	485	1.67	3.92×10^4	5.94×10^{17}

6.4. Conclusion

The incorporation of the alkali metals (Li, Na, K and Cs) as co-doponts in $ZnTa_2O_6$:Pr^{3+} phosphor improved the lifetime of the persistent emission. The XRD showed pure phase formation, indicating successful synthesis of the phosphor by solid state route at 1200 ^{o}C for 4 hrs. The ToF-SIMS imaging further showed homogeneous distribution of all ions in the phosphor. Incorporation of the co-dopant ions further introduced the strain in $ZnTa_2O_6$:Pr^{3+}, which increased with the increase in the ionic radius. Similarly, the persistent emission and the quantity of the electron trapping centres increased with an increase in the ionic radius of the co-dopant ion. The trend was observed from the phosphorescent decay curves and the TL glow curve analysis, respectively.

6.5.   References

1.   Z. Pan, Y.Y. Lu , and F. Liu, Nat. Mater. **11** (2012) 58.

2.   J. Holsa, Persistent Luminescence Beats the Afterglow: 400 Years of Persistent Luminescence, The Electrochem. Soc. Interface 2009.

3.   J.R. Lakowics, Principles of fluorescence spectroscopy, 2006, 3rd Ed., Springer publishers, USA.

4.   L.L. Noto, S.S. Pitale, M.A. Gusowki, J.J. Terblans, O.M. Ntwaeaborwa and H.C. Swart, Powder Technol. **237** (2013) 141.

5.   H.C. Swart, J.J. Terblans, O.M. Ntwaeaborwa, E. Coetzee, B.M. Mothudi, M.S. Dhlamini, Nucl. Instrum. Methods Phys. Res. B, **267** (2009) 2630.

6.   Y. Lin, Z. Zhang, Z. Tang, J. Zhang, Z. Zheng, X. Lu, Mater. Chem. Phys. **70** (2001) 156.

7.   R.D. Shannon, Acta Cryst. **A32** (1976) 751.

8.   M. Waburg, H. Muller-Buschbaum, Zeitschrift fuer Anorganische und Allgemeine Chemie **508** (1984) 55.

9.   Bernard Dennis Cullity, Stuart R. Stock, ***Elements of X-ray diffraction 3rd Ed***, 2001, prentice hall, London.

10.   L.L. Noto, M.L. Chithambo, O.M. Ntwaeaborwa, H.C. Swart, J. Alloy Compd. **589** (2014) 88.

11.   K. Brandenburg & H. Putz, ***Diamond - Crystal and Molecular Structure Visualization, Crystal Impact GbR***, Postfach 1251, D-53002 Bonn.

12.   L.L. Noto, M.L. Chithambo, O.M. Ntwaeaborwa, H.C. Swart, Powder Technol. 247 (2013) 147.

13.   V. Pagonis, G. Kitis, C. Furetta, Numerical and practical exercises in thermoluminescence, 2006, Springer publishers, USA.

14.   L.L. Noto, S.S. Pitale, M.A. Gusowki, O.M. Ntwaeaborwa, J.J. Terblans, H.C. Swart, J. Lumin. **145** (2014) 907.

[15]   K.S. Chung, H.S. Choe, J.I. Lee, J.L. Kim, S.Y. Chang, Radiat. Prot. Dosim. **115** (2005) 1.

"When something is important enough, you do it even if the odds are not in your favor."

— Elon Musk

7

Enhancement of luminescent intensity and persistent emission of ZnTa$_2$O$_6$:Pr^{3+} phosphor by adding fluxing agents

7.1.   Introduction

Rare earth ions play a crucial role when they act as dopants in a luminescent material (phosphor). They enable cost effective production of phosphors [1] and save energy, because some are excitable by sunlight [2]. Pr^{3+} ions provide a possibility to generate a phosphor that glows with an emission similar to that of an ideal red light [3]. Pr^{3+} ions doped in CaTiO$_3$ result in a phosphor that glows with a red emission that has a colour index with coordinates (0.68,0.31) [3], which are very close to the coordinates (0.67, 0.33) of the ideal red emission [4], according to the Commission Internationale de l'Eclairage (CIE) colour indexing [5]. This unique single red emission is aided by the intervalence charge transfer between Pr^{3+} ions that reside within the inner octahedron of CaTiO$_3$ and the Ti^{4+} ions that reside within the oxygen cages of the CaTiO$_3$ [6,7]. The result is complete quenching of the blue emission from the ^{3}P$_0 \rightarrow$ ^{3}H$_4$ transition, leading to a single red emission from the ^{1}D$_2 \rightarrow$ ^{3}H$_4$ transition [7,8,9]. Even though the red emission of Pr^{3+} in a phosphor may be close to that of an ideal red colour, its luminescence intensity still requires to be improved considerably in order to be regarded suitable for the commercial sector, such as the blue and green emitting phosphors [1,2]. The subject of enhancing the luminescence intensity has been approached in several ways by various researchers. An enhanced down-converted green emission associated with the ^{5}D$_4 \rightarrow$ ^{7}F$_5$ transitions of Tb^{3+} ions was observed from ZnAl$_2$O$_4$:Ce^{3+},Tb^{3+} powders with different concentrations of Ce^{3+} and Tb^{3+}[10].   It was inferred from fluorescence decay data that the

enhancement was due to energy transfer from Ce^{3+} to Tb^{3+} by a down-conversion process. Noto et. al. [11] demonstrated how to increase the photoluminescence intensity of $CaTiO_3:Pr^{3+}$ phosphor by co-doping with In^{3+}. The In^{3+} ions acted as charge compensators that suppressed the formation of point defects that act as luminescence quenching centres. Ahmed et al [12] showed enhancement of luminescence efficiency of Tb^{3+} activator doped in LaF_3 by co-doping with Ce^{3+}, which acts as a sensitizer. The role of the sensitizer ion is to absorb energy from the excitation source and transfer it to the activator ion and thereby improving the luminescent intensity of the phosphor. Popovici et al [13] showed luminescence improvement by using a flux agent to prepare $YTaO_4:Tb^{3+}$ phosphor. The flux agent facilitates and increases the chemical reaction rate without reacting with the final product. During the reaction, the flux ensures complete reaction of the reagents at lower temperatures [13], and prevents the formation of point defects that may be created by the unreacted reagents [14]. The point defects may act as quenching centres that reduce the luminescence efficiency [10]. Eventually the energy transfer from the host material to the activator will be higher, and the luminescence intensity increases [14]. The present study aims to improve the luminescence intensity of $ZnTa_2O_6:Pr^{3+}$ phosphor by using Li_2SO_4 and Li_2CO_3 as flux agents. The effect of the flux on the ratio of the Pr^{3+} to Pr^{4+} in the phosphor was investigated by X-ray photo electron spectroscopy (XPS) and the influence of the flux on the electron trapping centres was studied by thermoluminescence (TL) spectroscopy.

7.2.   Experimental

$ZnTa_2O_6: Pr^{3+}$ (0.4 mol%) phosphor was prepared by solid state reaction in the presence of different concentrations of Li_2SO_4 and Li_2CO_3 acting as flux agents. The samples were prepared by mixing ZnO, Ta_2O_5, $PrCl_3$ and one of the flux materials in stoichiometric amounts. The reagents were mixed into a slurry using Ethanol. The slurry was preheated at 100 ^{o}C for 10 hrs and later sintered sintered at 1200 ^{o}C for 4 hrs. The product was allowed to cool down to room temperature and then grounded into a powder. The powder was washed with distilled water to remove the flux compounds from the phosphor. The samples were prepared using different concentrations of the flux, and the measurements of the X-ray diffraction (XRD) patterns, scanning electron microscopy (SEM) images, diffuse reflectance, XPS, TL and Decay curves were done for the samples that yielded the optimal photoluminescence (PL) intensity.

$ZnTa_2O_6:Pr^{3+}$, $ZnTa_2O_6:Pr^{3+}$ prepared with 9 wt% of Li_2SO_4 and 3 wt% of Li_2CO_3 gave the optimum PL intensities. The crystalline phase was identified by a Bruker AXS D8 Advance X-Ray diffractometer using Cu *Kα* radiation. The PL emission and excitation (PLE) properties of the phosphor were probed using a Varian Carry-Eclipse fluorescence spectrophotometer. The SEM images were obtained using a Shimadzu SSX-550 SEM. A PerkinElmer Lambda 950 UV/VIS spectrometer was used to record the diffuse reflectance spectra. The chemical state was probed using a PHI 5000 *Versa-probe* XPS spectrometer. The X-ray source was operated at 15 kV and 25 W. The Al monochromatic X-ray beam (*hv*=1486.6 eV) had a spot size of 100 µm. For higher resolution spectra, the hemispherical sector analyzer pass energy was maintained at 11.8 eV for the O 1s, C 1s, Zn 2p and Ta 4f peaks. It was changed to 58.7 eV for the analysis of the Pr 3d peak, because Pr is present within the phosphor in very small quantities compared to other ions. The instrument work function was calibrated to give a binding energy of 83.95 eV for the Au $4f_{7/2}$ line and the spectrometer dispersion was adjusted to 932.63 eV for the Cu $2p_{3/2}$ peak. The charge neutralizer was used on all specimens. Spectra have been charge corrected to the main line of the adventitious carbon 1s spectrum set to 284.5 eV. Detail spectra were analysed using the PHI MultiPak software (version 9). During the fitting procedure, Shirley background was used, the peak shapes were 100 % Gaussian and the full width at half maximum (FWHM) for Ta 4f, Zn 2p, Pr 3d and O 1s peaks were kept the same in all three samples. The phosphorescence decay curves to determine the persistent emission lifetime were measured after exciting the phosphor with an ultraviolet source for 5 minutes, then monitoring the time it takes for the emission to decay using a photomultiplier tube (PMT). The glow curves were obtained using a 254 nm ultraviolet source for excitation, and measuring the TL using a TL 10091, NUCLEONIX spectrometer.

7.3. Results and Discussion

The XRD patterns of $ZnTa_2O_6:Pr^{3+}$ (Figure 7.1), $ZnTa_2O_6:Pr^{3+}$ prepared with 9 wt% of Li_2SO_4 (Figure 7.2) and 3 wt% of Li_2CO_3 (Figure 7.3) along with those of the standard data from ICSD card No. 36289 [15] are presented. The patterns of the sample prepared without a flux match those of the standard file, and proving that a phase pure compound was synthesized.
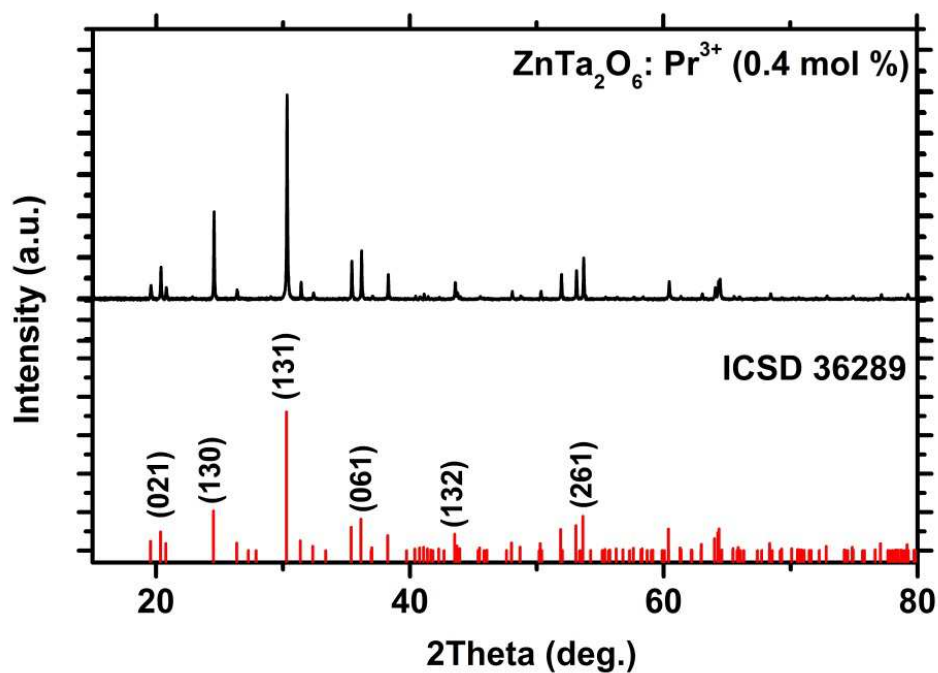
Figure 7.1: XRD patterns of $ZnTa_2O_6$: Pr^{3+} and the ICSD 36289 standard.

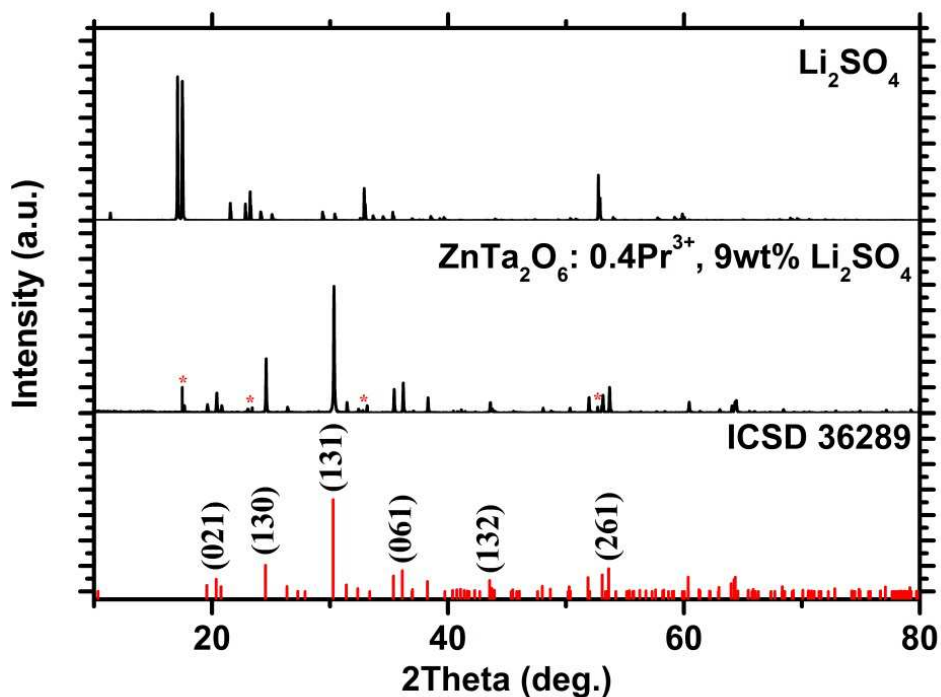Figure 7.2: XRD pattern $ZnTa_2O_6$:Pr^{3+} prepared with 9 wt% of Li_2SO_4, Li_2SO_4 and the ICSD 36289 standard.
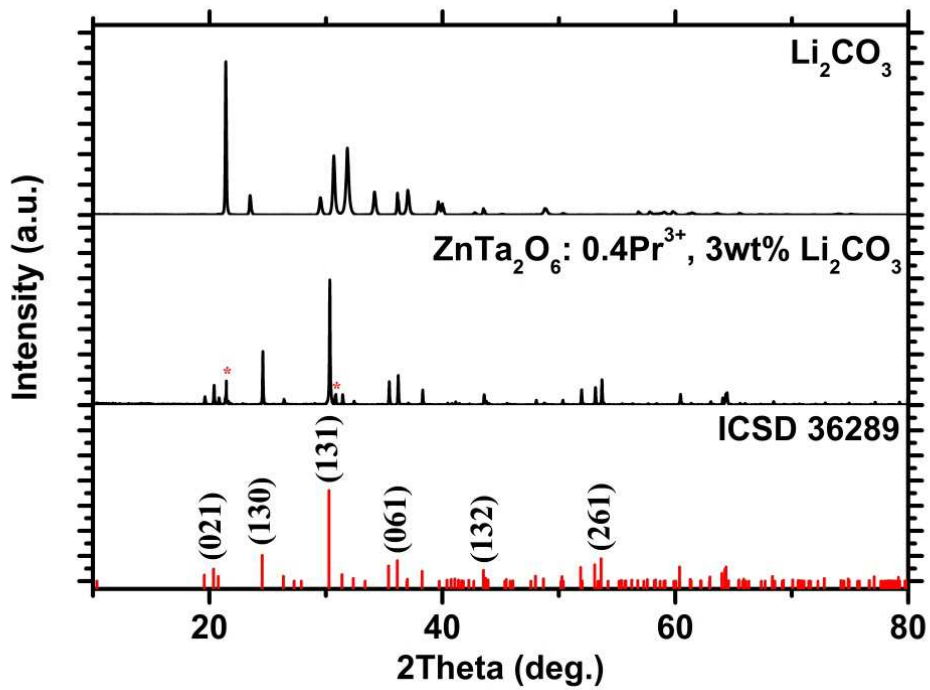
Figure 7.3: XRD pattern $ZnTa_2O_6$:Pr^{3+} prepared with 3 wt% of Li_2CO_3, Li_2CO_3 and the ICSD 36289 standard.
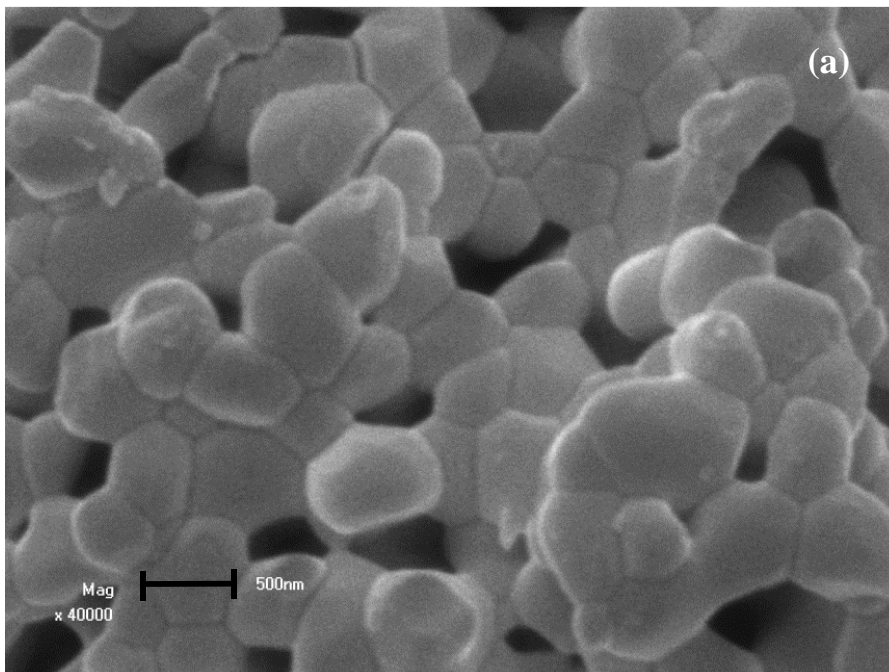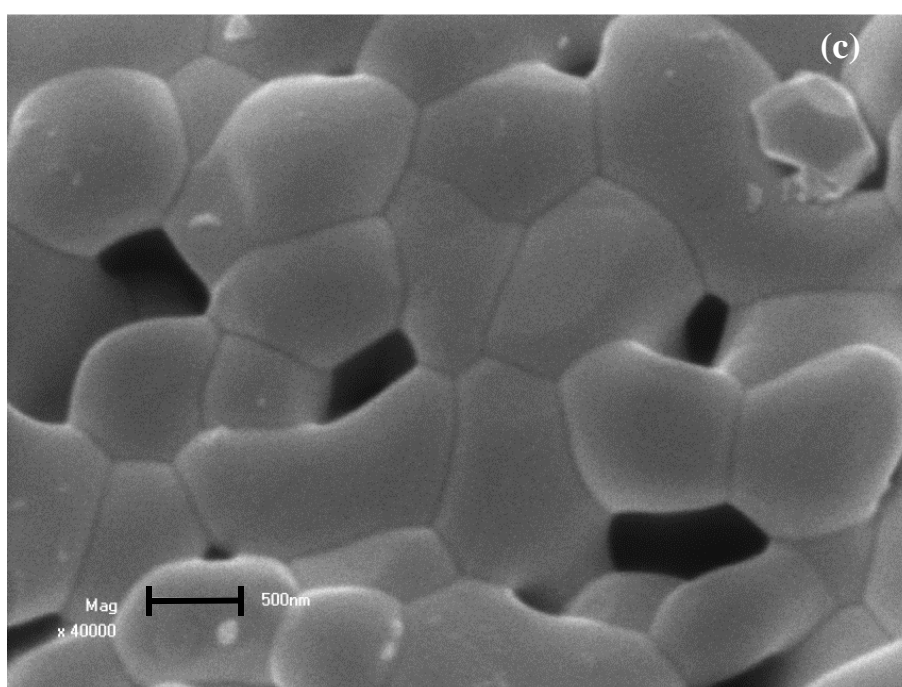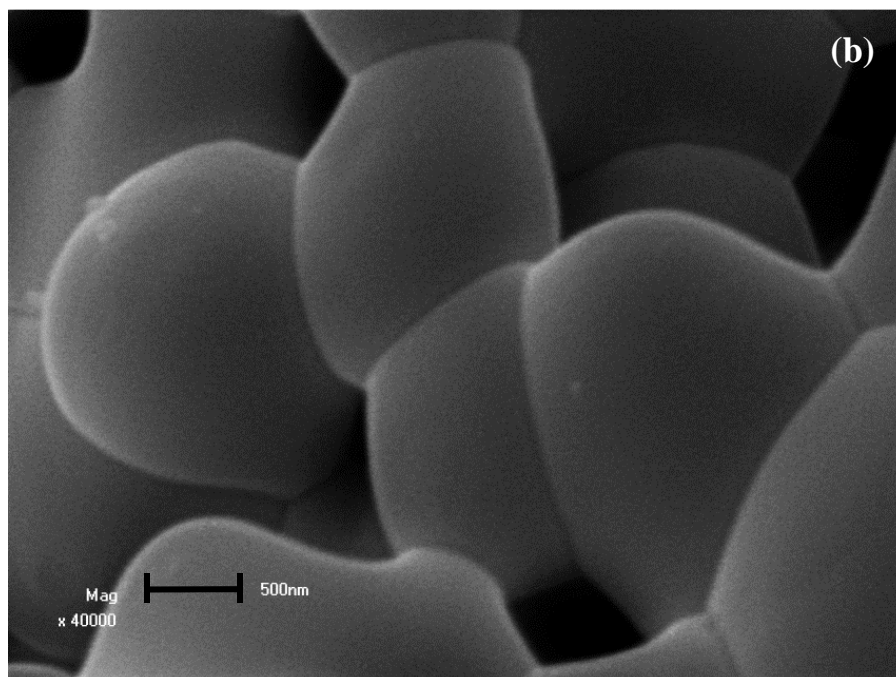
Figure 7.4: SEM images of (a) $ZnTa_2O_6:Pr^{3+}$, (b) $ZnTa_2O_6:Pr^{3+}$ prepared in the presence of Li_2SO_4 and (c) $ZnTa_2O_6:Pr^{3+}$ prepared in the presence of Li_2CO_3. (Measured at a $4.9 \times 3.6\ \mu m$ field of view).

The samples prepared using the flux agents resemble peaks that correspond to Li_2SO_4 and Li_2CO_3 species which were not washed away completely from the phosphor samples. Figure 7.4(a), (b) and (c) show SEM images, which are a representation of the images with the same trend taken at random positions on the sample. They show that the phosphors consisted of particles with different shapes and sizes, which are bound to each other.

The latter effect is correlated with the high temperatures involved in solid state reactions [16]. The three SEM images show that the particles of the samples grow with the incorporation of the flux. The average particle size was approximately 500 nm for the non-fluxed samples (Figure 7.4(a)), 1.4 µm for the sample prepared with Li_2SO_4 (Figure 7.4(b)), and 966 nm for the samples prepared using Li_2CO_3.

The PL emission spectrum (Figure 7.5(a) and (b)) of the $ZnTa_2O_6:Pr^{3+}$ phosphor shows red emission lines when it was excited with a 259 nm ultraviolet light source. The red emission lines are attributed to the $^1D_2 \rightarrow {}^3H_4$, $^3P_0 \rightarrow {}^3H_6$ and $^3P_0 \rightarrow {}^3F_2$ transitions at 608, 619 and 639 nm, respectively [17]. There are also two minor emission lines attributed to the $^1D_2 \rightarrow {}^3H_{5,6}$ transitions at 721 and 820 nm, respectively [17].

The PLE spectrum was acquired to evaluate the position of the excitation bands, and the most prominent absorption band is situated at 259 nm and was used to excite the phosphor. There is also an additional absorption band at 330 nm that may correspond to the intrinsic defect absorption or the virtual charge transfer reported by Boutinaud et al [18]. The spectra (Figure 7.5(a) and (b)) of the samples prepared in the presence of a flux (Li_2SO_4 and Li_2CO_3), show an occurrence of a blue emission at 505 nm that is attributed to the $^3P_0 \rightarrow {}^3H_4$ transition, and an enhancement of the red emission intensity from the $^3P_0 - {}^3H_6$ transition. Additionally, the luminescence intensity has almost doubled. These effects of the flux material on luminescent intensity are not unusual, Popovici et al [13], also reported great improvement of the luminescence intensity of $YTaO_4:Tb$ phosphor when it was prepared in the presence of 50 wt% of Li_2SO_4. Whilst Popovici investigated the effects of the flux, we investigate the actual chemical changes that take place during the reaction by probing for chemical changes using XPS as shown below.
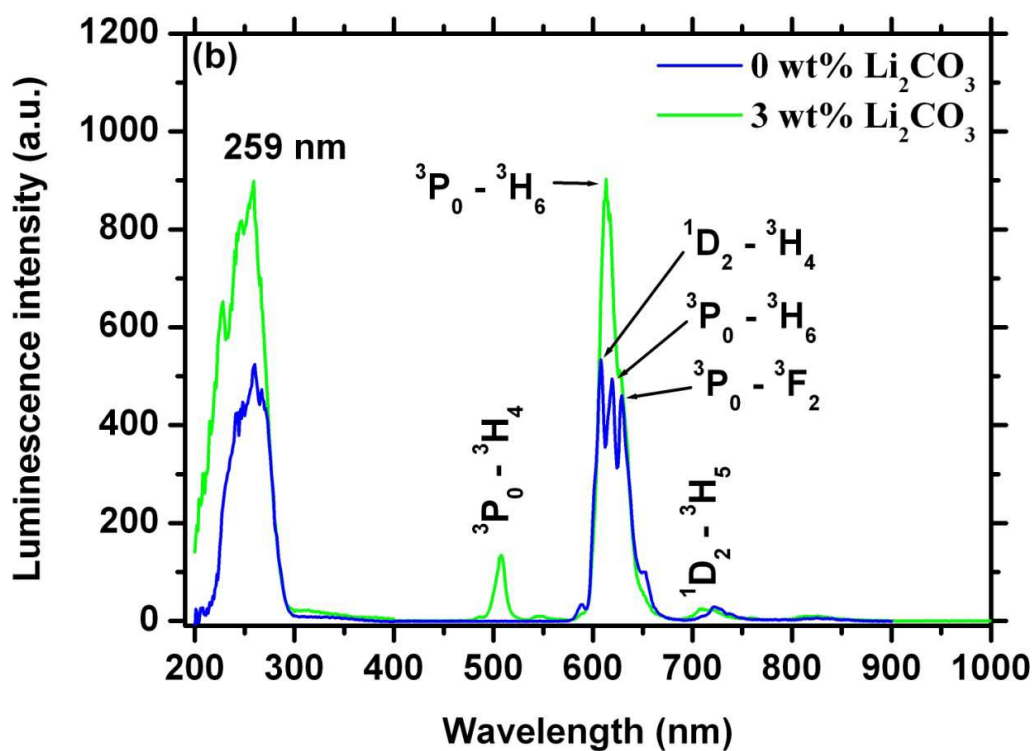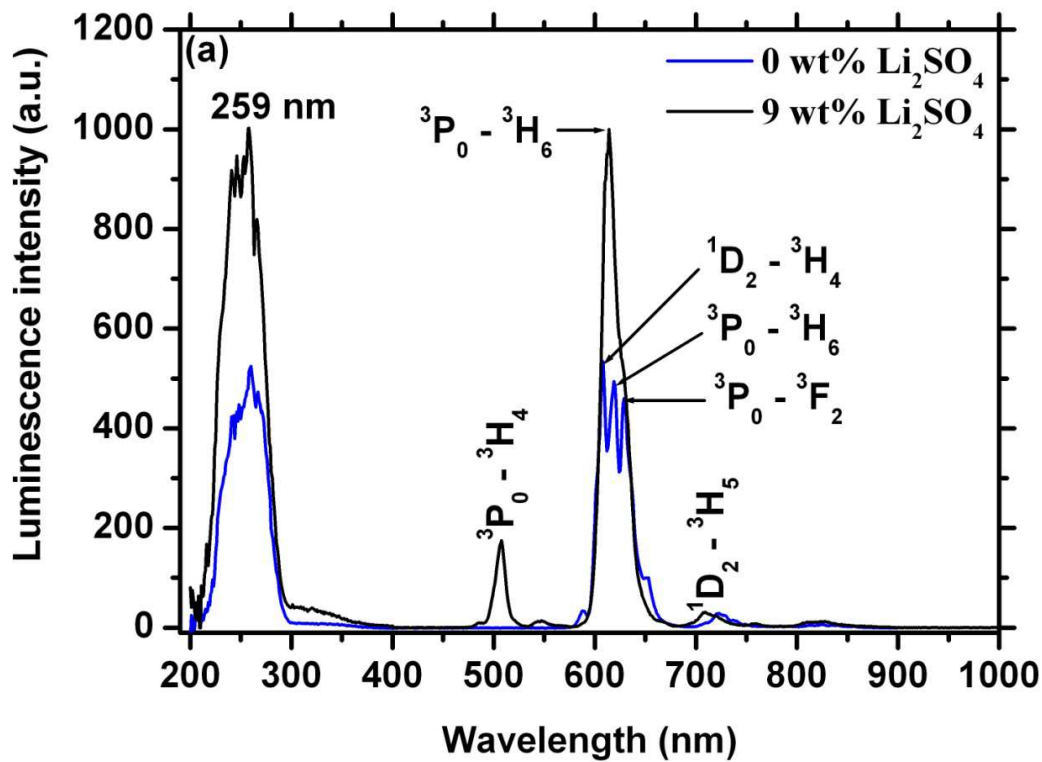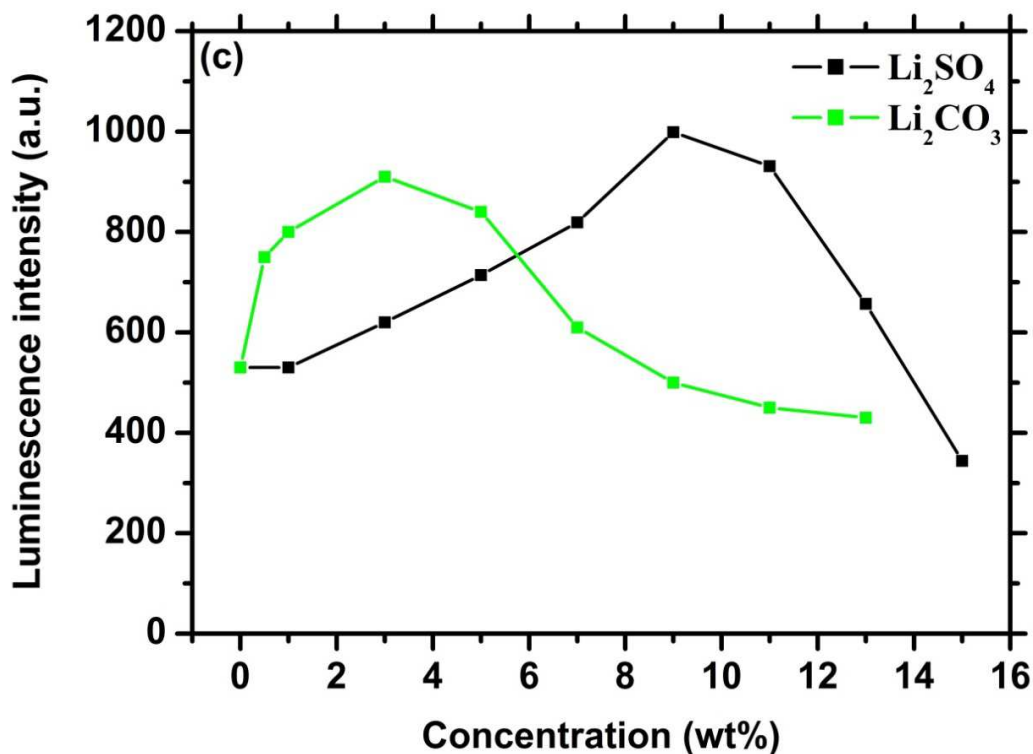
Figure 7.5: (a) Luminescence spectra of $ZnTa_2O_6:Pr^{3+}$ prepared using Li_2SO_4. (b) Luminescence spectra of $ZnTa_2O_6:Pr^{3+}$ prepared using Li_2CO_3. (c) Comparison of PL intensity prepared at the different flux concentrations.

Different concentrations of Li_2SO_4 and Li_2CO_3 flux, and the corresponding effects on the luminescence intensity are shown in Figure 7.5(c). The decrease in the luminescent intensity upon increasing the concentration of the flux, may be due to the fluxes reacting with the phosphor and thus generating additional phases that act as quenching centres. The XRD spectra (Figure 7.2 and 7.3) show evidence of the additional phases that formed during the reaction.

The diffuse reflectance spectrum (Figure 7.6) shows strong absorption at 259 nm, which is a region that corresponds to the band-to-band transition [19], and it is in agreement with the PLE spectrum (Figure 7.5(a) and (b)). The strong absorption at 330 nm may be due to intervalence charge transfer or charge transfer (CT) to the intrinsic defect levels in the material [19]. The charge transfer absorption is observed to be stronger for the samples prepared in the presence of the flux materials. No emission is observed in the region corresponding to the CT was present, and this may be an indication that the absorbed charge is transferred to the luminescent centre, to

reinforce the emission intensity. The additional bands observed at 420 to 500 nm correspond to f–f transitions of Pr^{3+} [10,19].

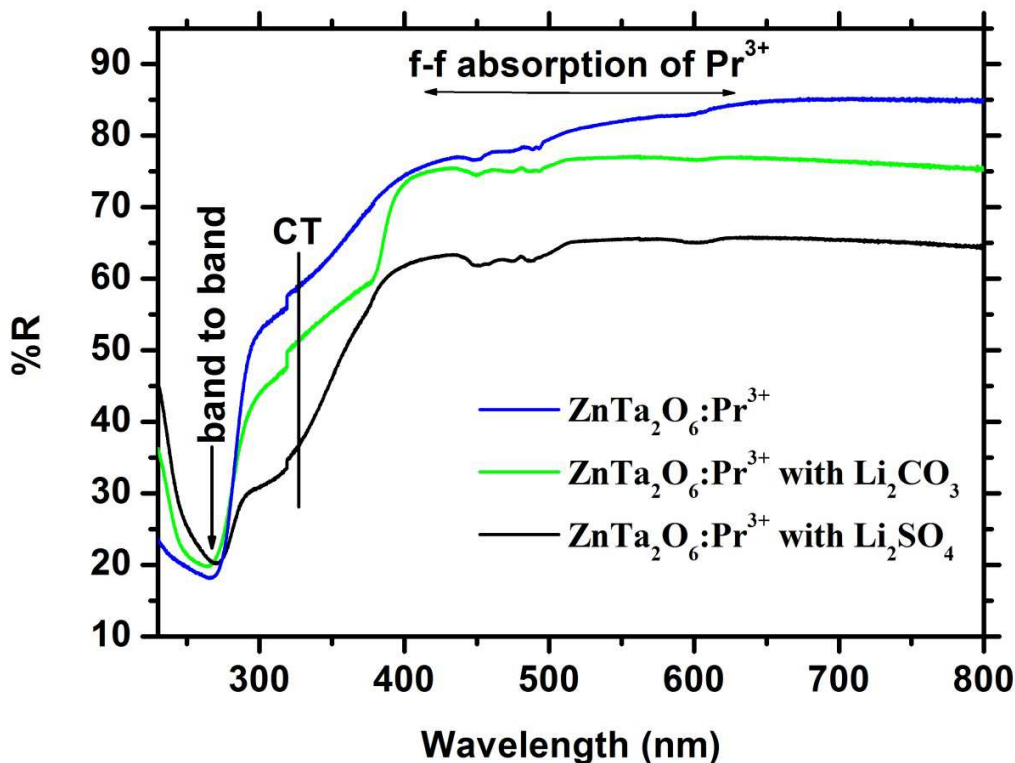Figure 7.6: Diffused Reflectance spectra of $ZnTa_2O_6:Pr^{3+}$, $ZnTa_2O_6:Pr^{3+}$ prepared in the presence of Li_2SO_4 and $ZnTa_2O_6$ Pr^{3+} prepared in the presence of Li_2CO_3.

XPS analysis was performed to investigate the chemical changes that occurred when $ZnTa_2O_6:Pr^{3+}$ was prepared in the presence of the flux materials, which may have caused the doubling of the luminescence intensity. Figure 7.7(a), (b) and (c) show the Zn 2p XPS peaks of $ZnTa_2O_6:Pr^{3+}$, $ZnTa_2O_6:Pr^{3+}$ prepared in the presence of Li_2CO_3 and $ZnTa_2O_6$ prepared in the presence of Li_2SO_4, respectively. The Zn 2p signal is split into two peaks ($2p_{1/2}$ at higher and $2p_{3/2}$ at lower binding energies) as a result of spin-orbit splitting [20,21]. The $2p_{1/2}$ and $2p_{3/2}$ were deconvoluted into two sets of peaks. The first set positioned at 1044.9 and 1021.8 eV (Figure 7.7(a)) that are less prominent, which correspond to Zn 2p contribution from ZnO [22,23]. The most prominent set at 1043.1 and 1020.9 eV (Figure 7.7(a)), is assigned to a contribution of Zn 2p from the main compound, $ZnTa_2O_6$. The peaks associated with Zn 2p from ZnO are enhanced

for the samples prepared with flux (Figure 7.7(b) and (c)), which may be an indication that less $ZnTa_2O_6$ was formed and that the ZnO and Ta_2O_5 reacted with the flux agents, or some did not react. Hence the intensity of the Zn 2p peaks associated with $ZnTa_2O_6$ peaks decreased and those associated with ZnO increased.

Figure 7.8(a), (b) and (c) show the Ta 4f XPS peaks of $ZnTa_2O_6:Pr^{3+}$, $ZnTa_2O_6:Pr^{3+}$ prepared in the presence of Li_2CO_3 and $ZnTa_2O_6$ prepared in the presence of Li_2SO_4, respectively. The Ta 4f signal is also split into two peaks; the $4f_{5/2}$ at higher binding energies and $4f_{7/2}$ at lower binding energies. The less prominent peaks (Figure 7.8(a)) at 28.8 eV and 26.8 eV correspond to Ta contribution from Ta_2O_5 [24,25], and we assign the most prominent peaks at 27.8 and 25.9 eV to the Ta contribution from $ZnTa_2O_6$. Figure 7.8 (b) shows that the Ta contribution from $ZnTa_2O_6$ reduces with an increase in Ta contribution from Ta_2O_5 and also a formation of a new compound at 25.7 and 24.2 eV, due to the reaction of Ta_2O_5 and Li_2CO_3. The new compound labelled as TaC_x has binding energies close to the two carbon deficient carbides, $TaC_{0.98}$ [26] and $TaC_{0.95}$ [27].
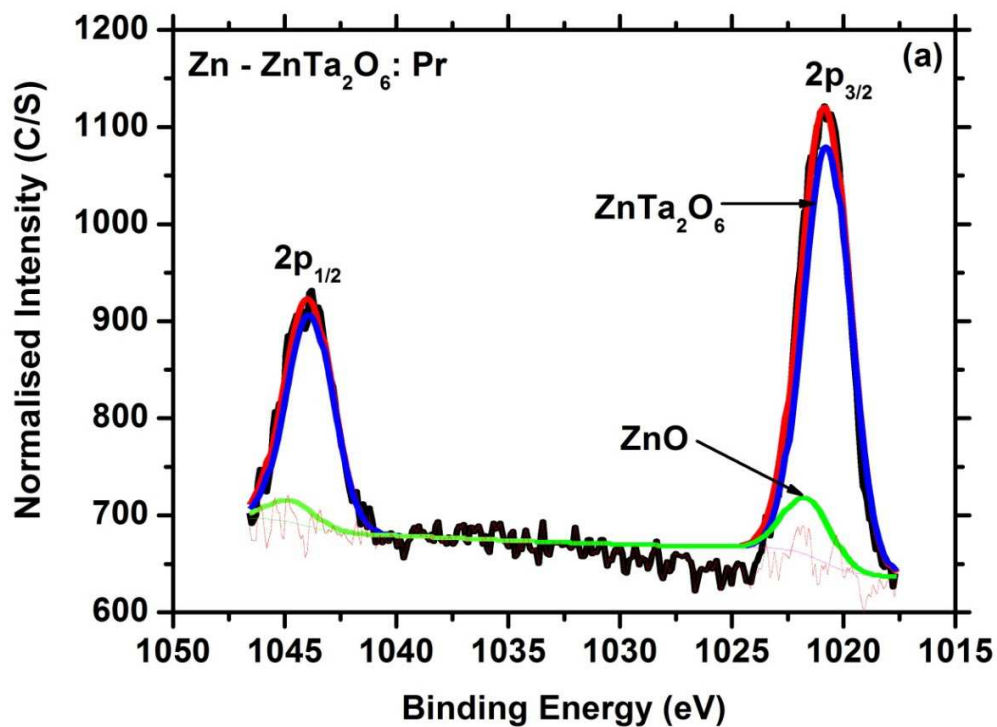
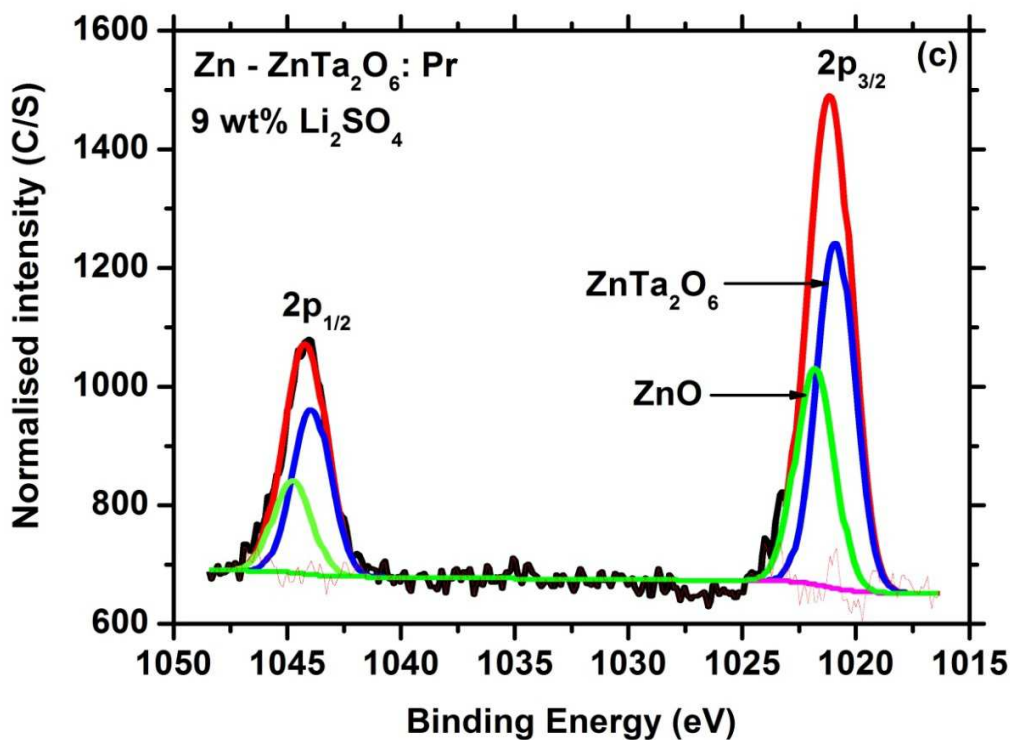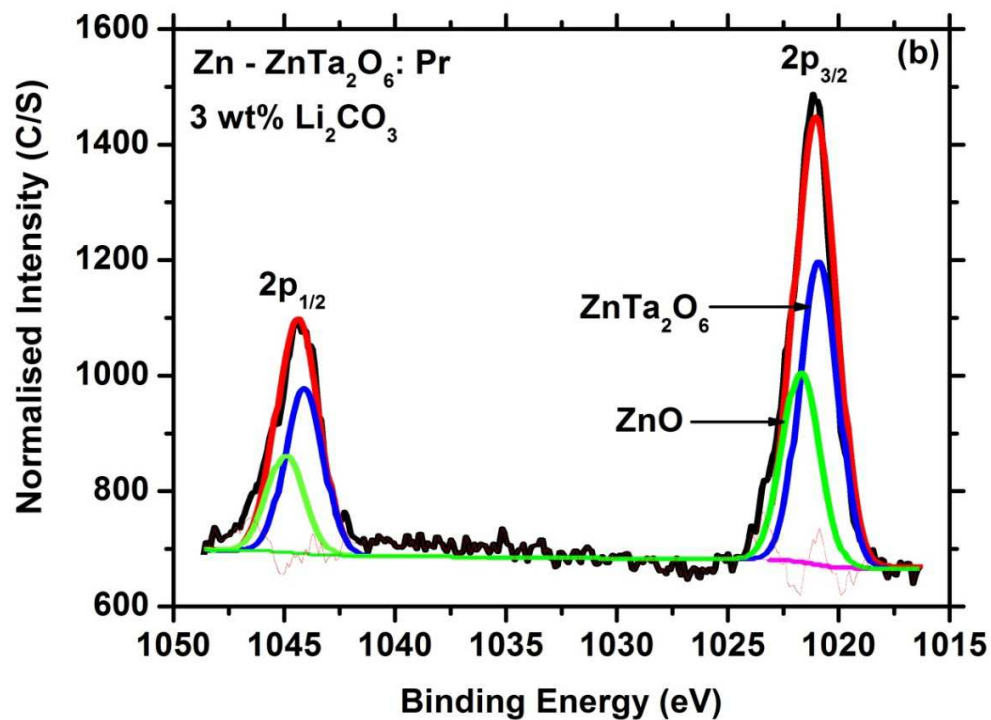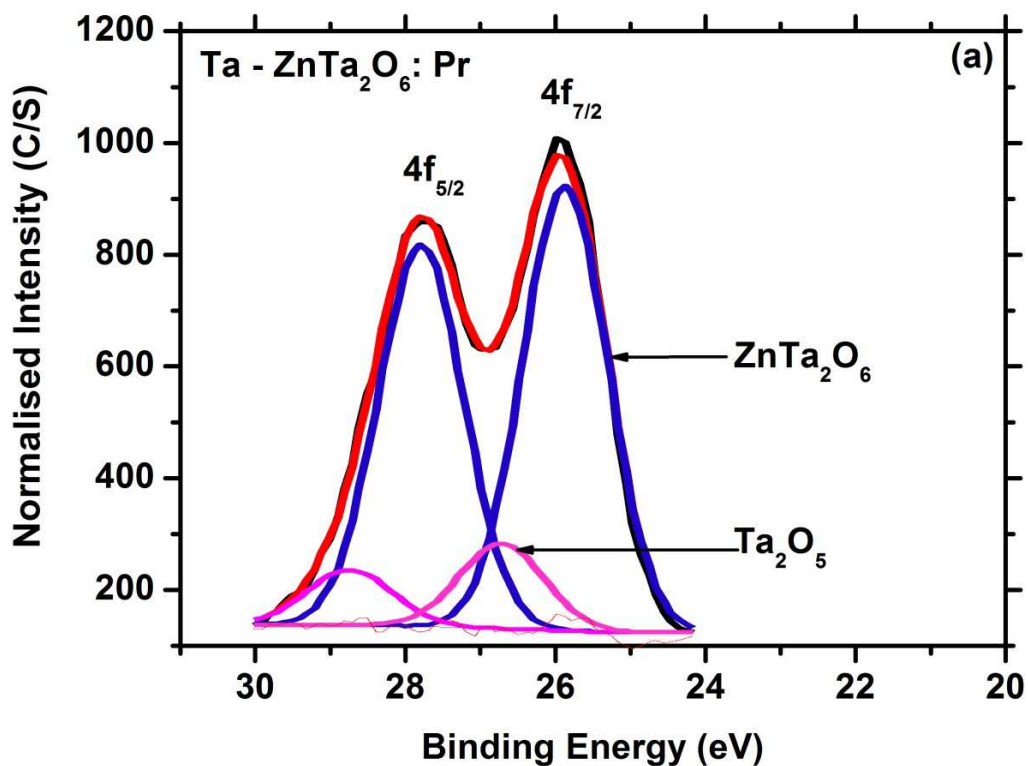Figure 7.7: The Zn $2p_{1/2}$ and $2p_{3/2}$ peaks for $ZnTa_2O_6$:Pr^{3+} (a) without flux, (b) with 3 wt% Li_2CO_3 and (c) with 9 wt% Li_2SO_4.

Similarly, the sample prepared in the presence of Li_2SO_4 (Figure 7.8 (c)) shows that the Ta contribution from $ZnTa_2O_6$ reduces with an increase in Ta contribution from Ta_2O_5. There are two additional peaks from pure Ta at 24.10 and 22.1 eV [28], and a contribution from an additional species at 25.1 and 23.6 eV, which corresponds to TaS_2 [29], due to the reaction of Ta_2O_5 and Li_2SO_4.

Figure 7.9 (a), (b) and (c) show the O 1s XPS peaks of $ZnTa_2O_6$:Pr^{3+}, $ZnTa_2O_6$:Pr^{3+} prepared in the presence of Li_2CO_3 and $ZnTa_2O_6$ prepared in the presence of Li_2SO_4, respectively. The oxygen peak of $ZnTa_2O_6$:Pr^{3+} (Fig 7.9(a)) is deconvoluted into three peaks positioned at 530.6, 530.2 and 529.3 eV, which are a contribution from Ta_2O_5 [30], ZnO [31] and $ZnTa_2O_6$, respectively. There are additional peaks at 531.5 and 532.1 eV for samples prepared in the presence of a flux (Fig 7.9(b) and (c)), coming from Li_2CO_3 [32] and Li_2SO_4 [33] species.

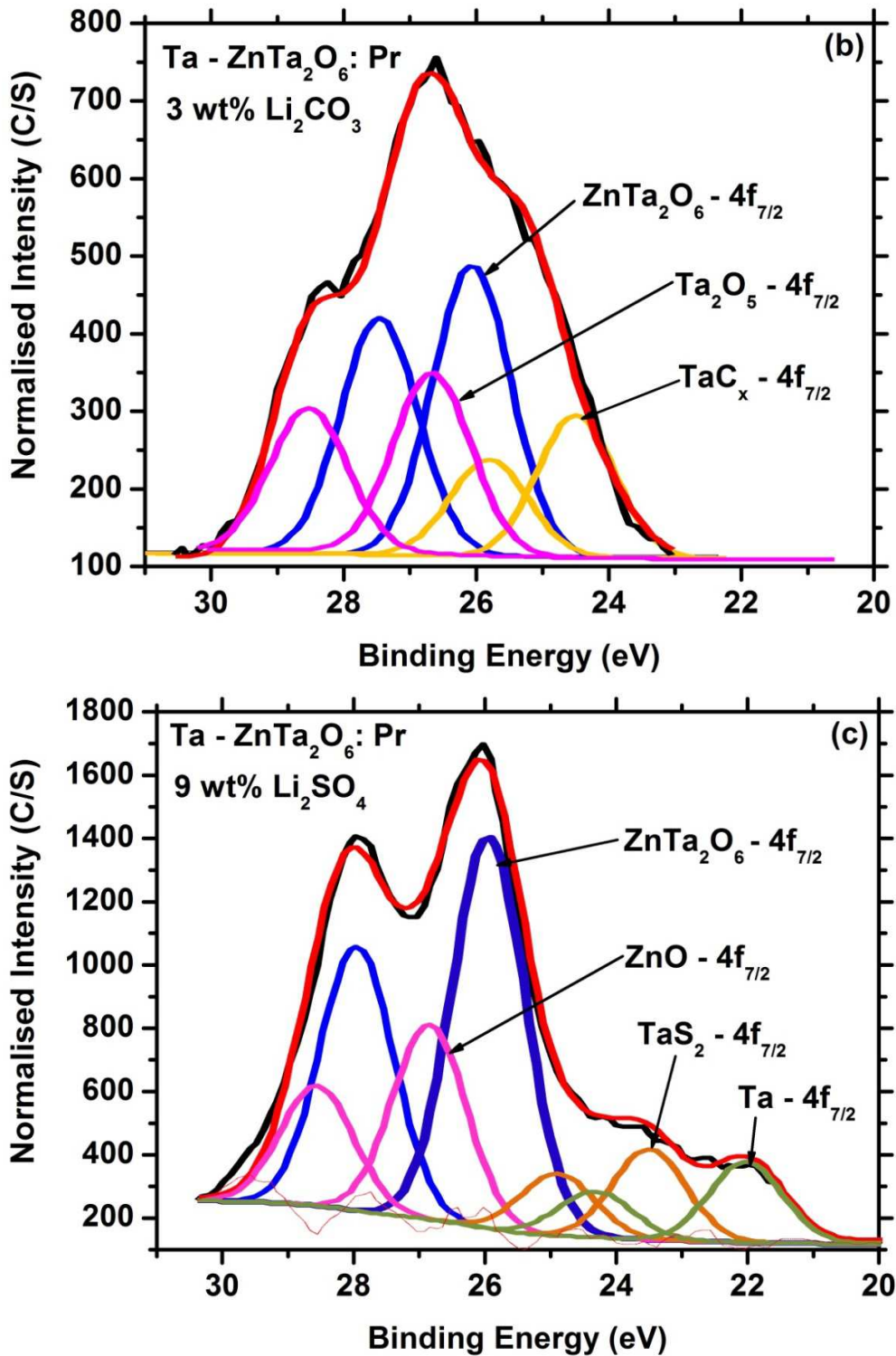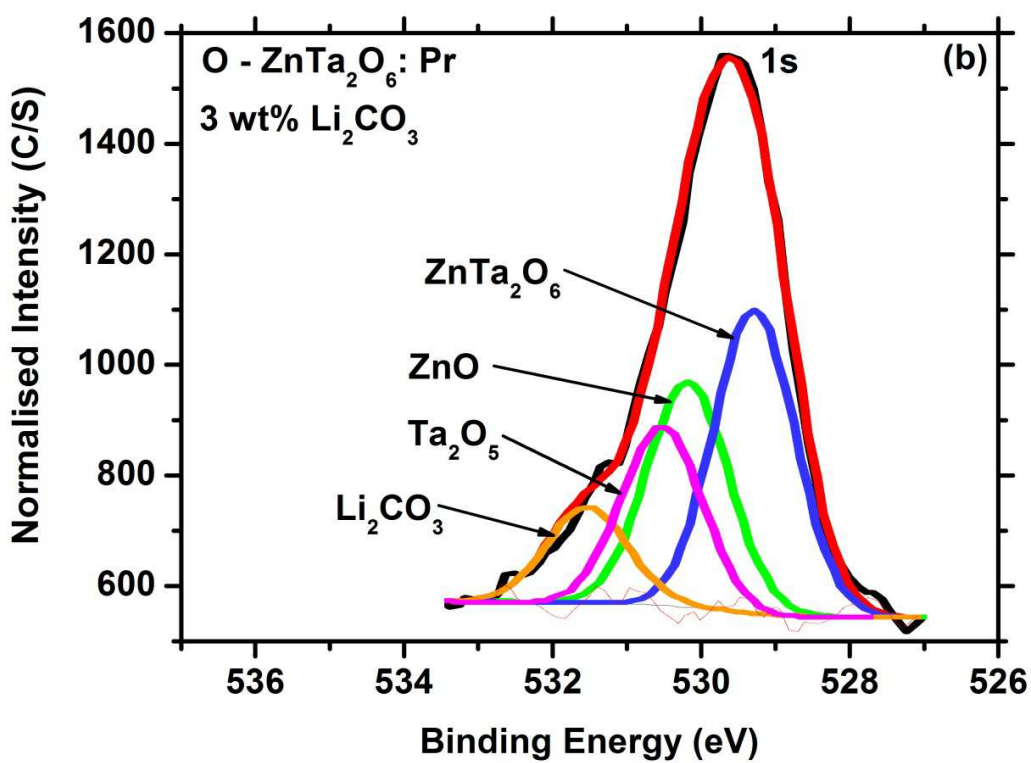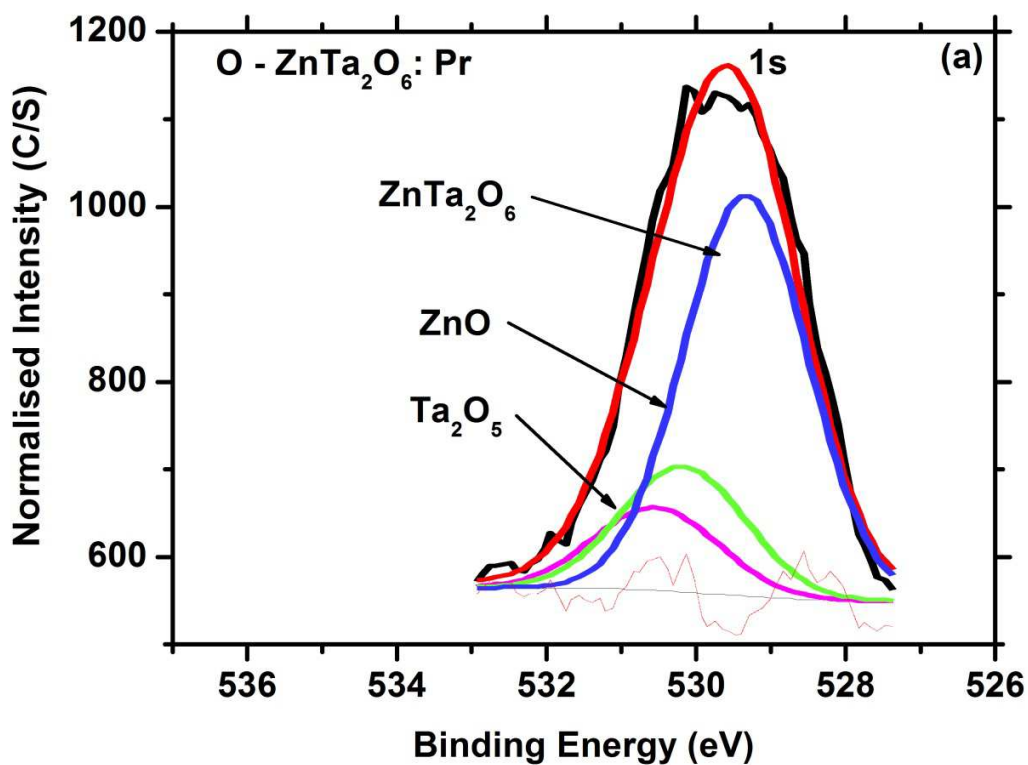Figure 7.8: The $4f_{5/2}$ and $4f_{7/2}$ Ta peaks of $ZnTa_2O_6$:Pr^{3+} (a) without flux, (b) with 3 wt% Li_2CO_3 and (c) with 9 wt% Li_2SO_4.
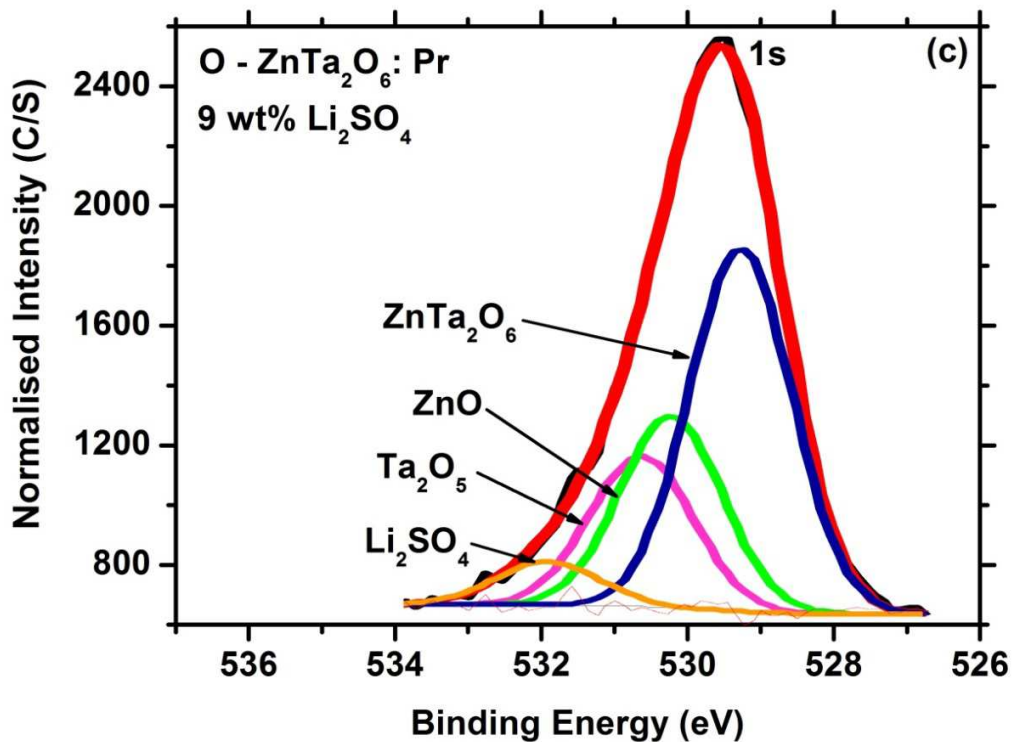
Figure 7.9: The O 1s peak of $ZnTa_2O_6$:Pr^{3+} (a) without flux, (b) with 3 wt% Li_2CO_3 and (c) with 9 wt% Li_2SO_4.

Figure 7.10(a), (b) and (c) show the Pr 3d XPS peaks of $ZnTa_2O_6$:Pr^{3+} and $ZnTa_2O_6$:Pr^{3+} prepared in the presence of Li_2CO_3 and $ZnTa_2O_6$:Pr^{3+} prepared in the presence of Li_2SO_4, respectively. The Pr 3d peak is also split into two peaks; the $3d_{3/2}$ at higher binding energies and $3d_{5/2}$ at lower binding energies. The peaks are deconvoluted into three peaks; from Pr^{4+} oxidation state at 952.0 and 935.1 eV [32,35], and two pairs of peaks from Pr^{3+} oxidation state at 953.0 and 932.5 eV [36,37] that is the most prominent and at 948.9 and 927.9 eV [36,37]. The doublet of the Pr^{3+} peak due to spin orbit coupling [35,36,37]. The Pr^{4+} peak decreases relative to the Pr^{3+} peaks for the samples prepared in the presence of a flux (Figure 7.10(b) and (c)). The decrease in the Pr^{4+}, which acts as a quenching centre in the material [6,8], may be the reason for the increase in the luminescence intensity (Figure 5(a) and (b)) for the fluxed samples.
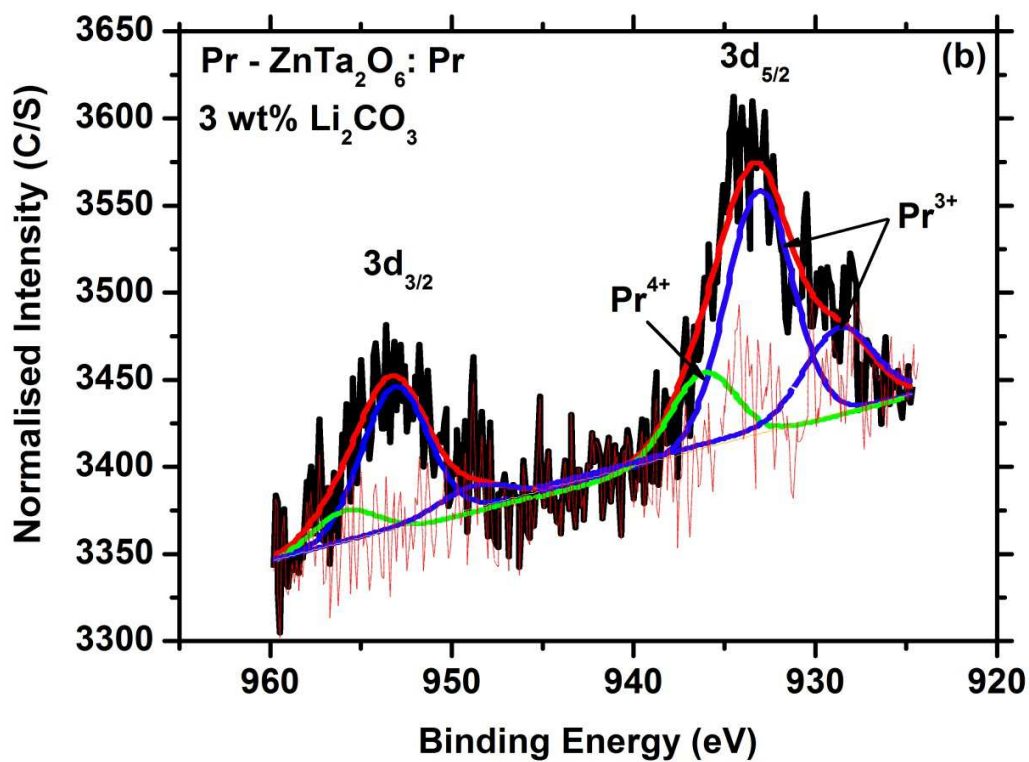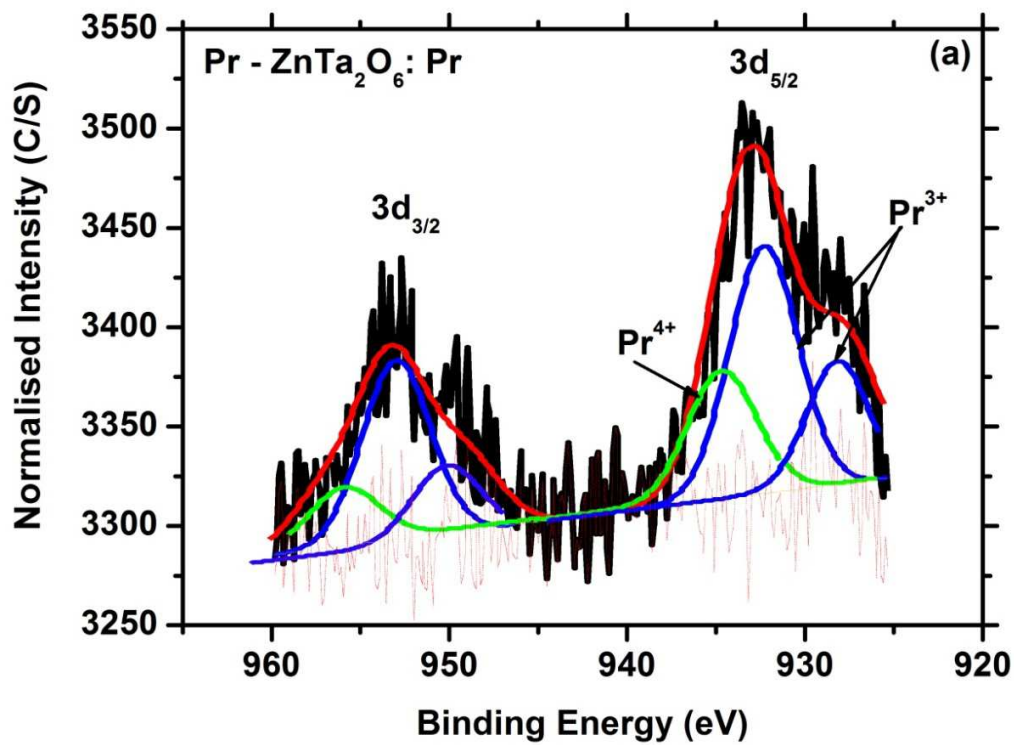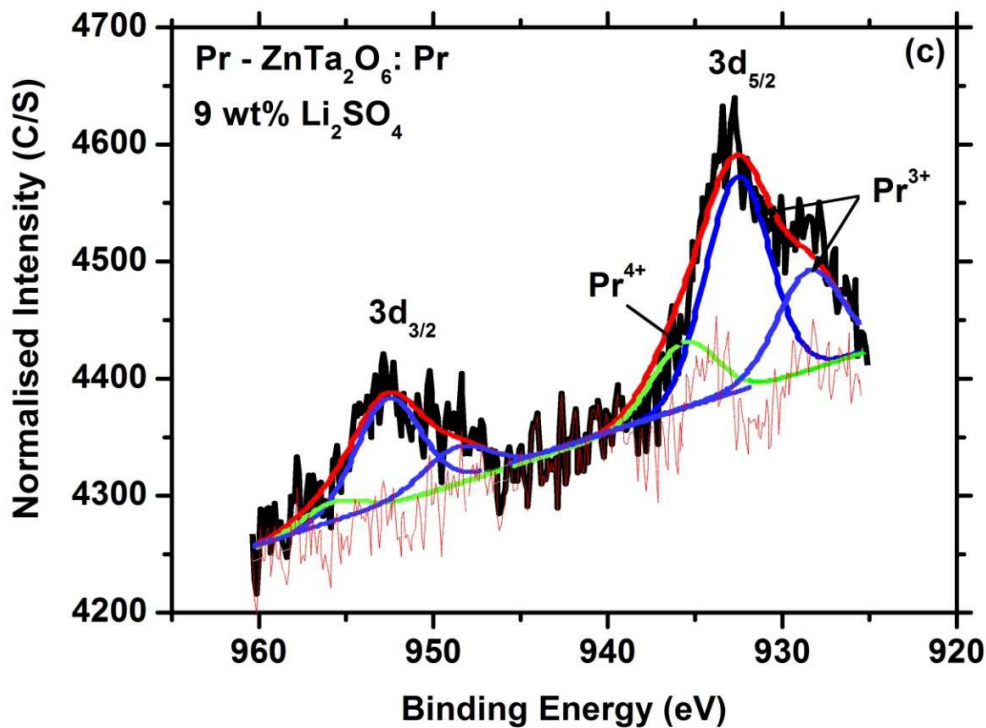
Figure 7.10: Pr $3d_{3/2}$ and $3d_{5/2}$ peaks of $ZnTa_2O_6$:Pr^{3+} (a) without flux, (b) with 3 wt% Li_2CO_3 and (c) with 9 wt% Li_2SO_4.

The electron trapping centres in the material were investigated using the TL spectroscopy. The trapping centres which originate from the formation of oxygen vacancies inside the material, may assume different depths within the energy gap [38]. The different depths are attributed to different orientations of the oxygen vacancies [39]. The $ZnTa_2O_6$:Pr^{3+} sample was exposed to different doses of the ultraviolet irradiation (Figure 7.11). The peaks are systematically shifting to higher temperatures as the dose increases, and this is an indication of kinetics which are neither first nor second order, but of general order [40]. The kinetics for the samples prepared in the presence of a flux were also treated as general order.

The broad nature of the acquired glow curves (Figure 7.11) is attributed to several other peaks that are overlapping coming from electron trapping centres with very close depth distribution. The underlying peaks can be resolved by deconvoluting the measured peak using computerised glow curve deconvolution (CGCD) [41, 43] as shown in Figure 7.13.

Figure 7.11: The dose response TL curves of the $ZnTa_2O_6:Pr^{3+}$ sample.
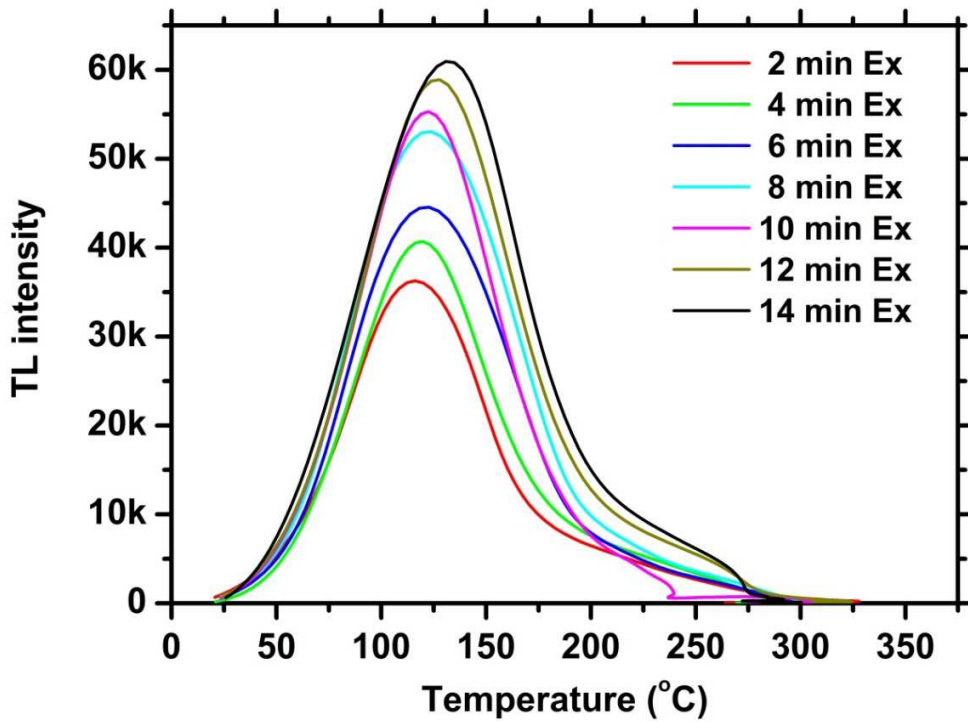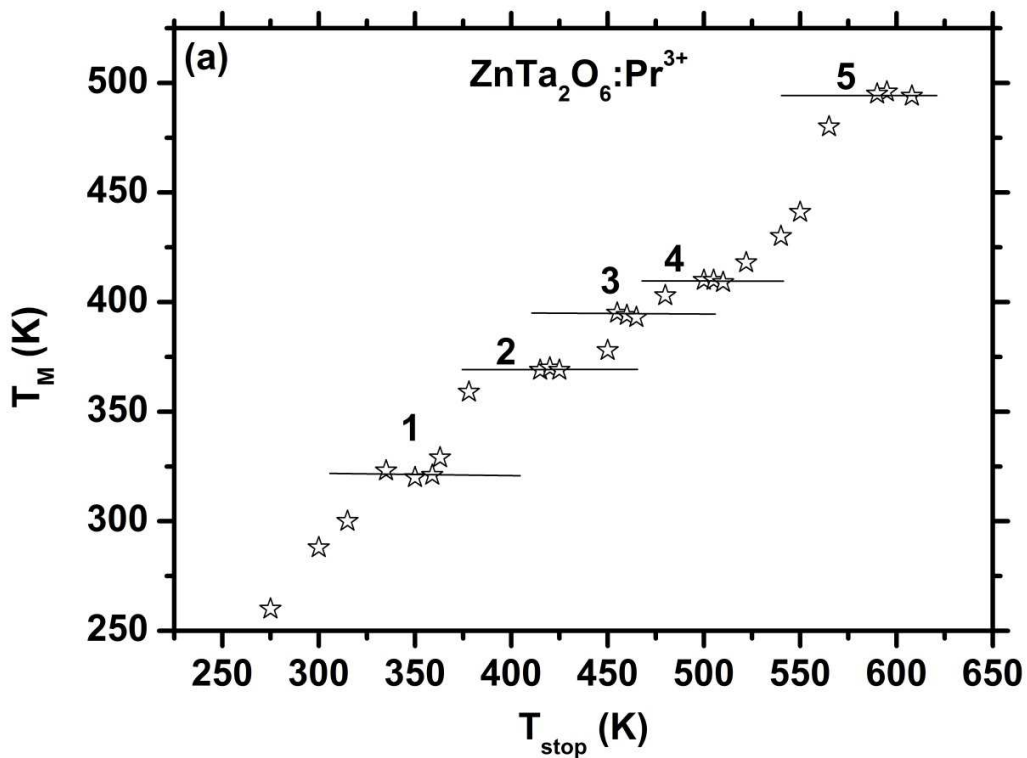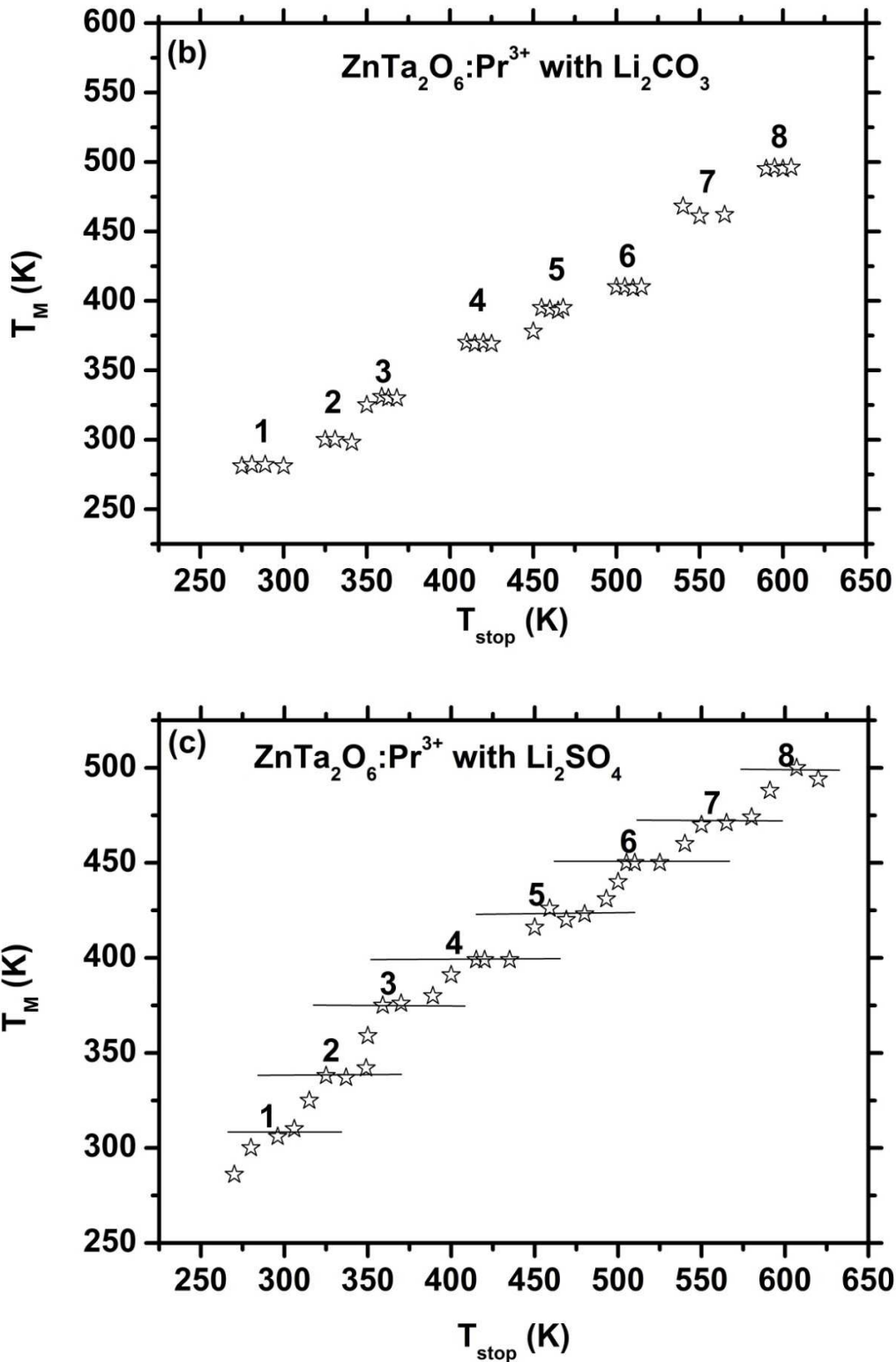
Figure 7.12: $T_m - T_{stop}$ plots of $ZnTa_2O_6:Pr^{3+}$ (a) without flux, (b) with 3 wt% Li_2CO_3 and (c) with 9 wt% Li_2SO_4

The deconvolution process is assisted by the $T_M - T_{stop}$ measurements to search for the possible number of thermal peaks [41]. The measurements were carried out for $ZnTa_2O_6:Pr^{3+}$, $ZnTa_2O_6:Pr^{3+}$ prepared in the presence of Li_2CO_3 and $ZnTa_2O_6:Pr^{3+}$ prepared in the presence of Li_2SO_4, respectively (Figure 7.12).The method involves heating a specimen that is pre-irradiated by UV radiation, to a specific temperature (T_{stop} 1) and then recording the temperature (T_M) corresponding to the maximum intensity of the corresponding glow curve.

The same sample is cooled down, and then re-irradiated and then followed by heating the sample to a specific temperature (T_{stop} 2 > T_{stop} 1), which is higher than the previous Temperature (T_{stop}), and then followed by recording T_M. The same measurements are repeated over until the whole glow curve is recorded, with each T_{stop} recorded at a higher temperature than the previous one. This is followed by plotting T_M as a function of T_{stop}, and each flat region in the plot is an indication of the prominent electron trapping centre. The number of the revealed trapping centres is then used to deconvolute the glow curves (Figure 7.13) [41]. The measurements showed 5 flat regions for $ZnTa_2O_6:Pr^{3+}$ (Figure 12 a), and 8 flat regions for $ZnTa_2O_6:Pr^{3+}$ in the presence of flux (Figure 7.12 b & c).

The TL glow curves were acquired for $ZnTa_2O_6:Pr^{3+}$ (Figure 13(a)), $ZnTa_2O_6:Pr^{3+}$ prepared in the presence of Li_2CO_3 (Figure 7.13(b)) and $ZnTa_2O_6$ prepared in the presence of Li_2SO_4 (Figure 7.13(c)). The heating rate for all samples was kept at 2 ^{o}K/sec, and the irradiation period was 2 minutes for each sample. The $ZnTa_2O_6:Pr^{3+}$ sample has a narrow glow curve, which is deconvoluted into 5 thermal peaks, which correspond to the distribution of electron trapping centres with close depth [39]. (Figure 7.13(a)). The glow curves of the samples prepared in the presence of flux show new additional traps at lower temperatures, which are induced by both Li_2CO_3 (Figure 7.13(b)) and Li_2SO_4 (Figure 7.13(c)). The glow curves of these samples were deconvoluted into 8 thermal peaks.

The glow curves were deconvoluted using the computerised glow curve deconvolution (CGCD) from a software package (TLAnal) developed by Chung et al [42]. The general order kinetics related functions were used to compute for the activation energy (Eq. 7.1), frequency factor (Eq. 7.2) and the concentration of the electrons trapped within electron trapping centres (Eq. 7.3).
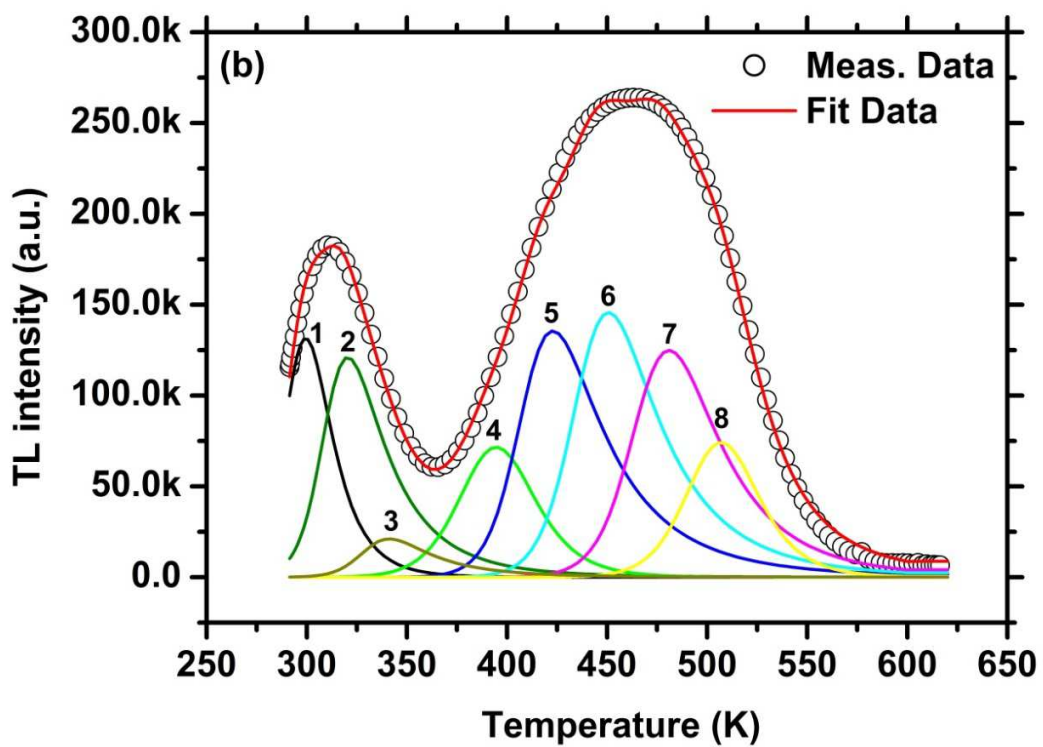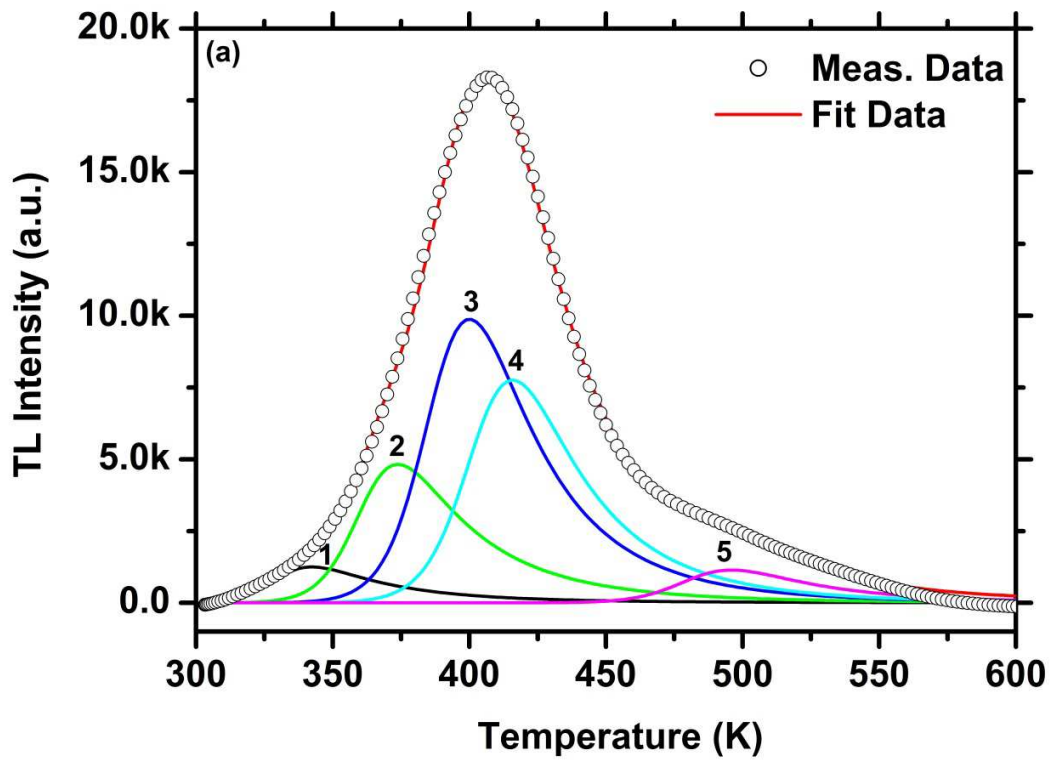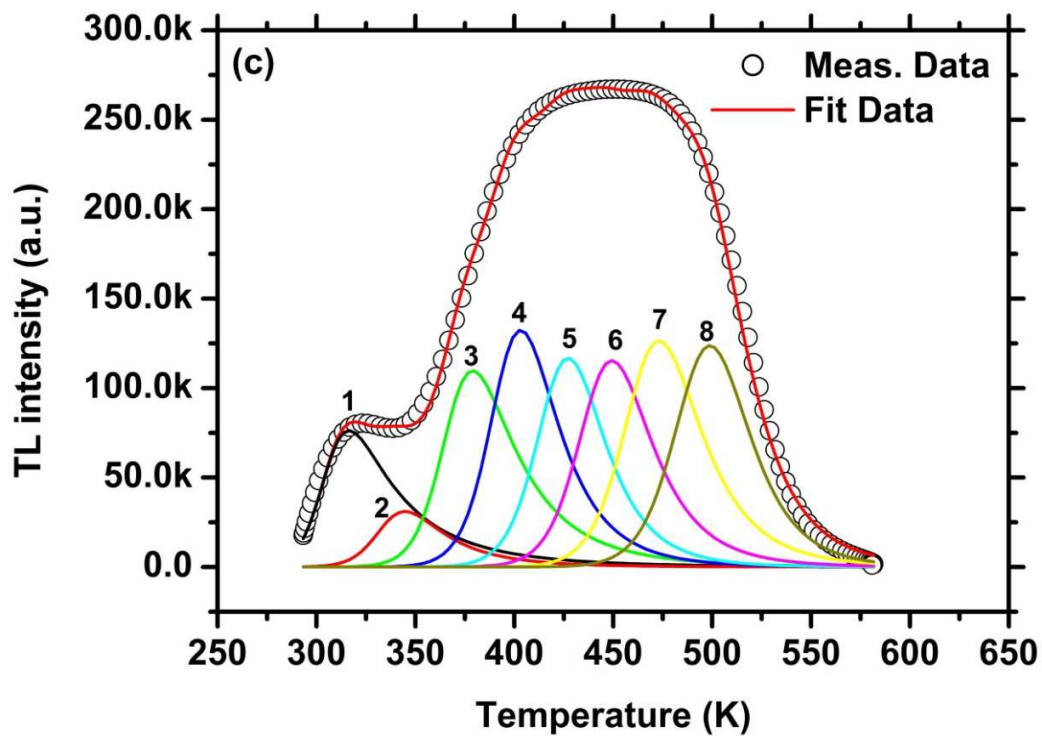
Figure 7.13: The TL glow curves for $ZnTa_2O_6:Pr^{3+}$ (a) without flux, (b) with 3 wt% Li_2CO_3 and (c) with 9 wt% Li_2SO_4.

Table 7.1: The kinetic parameters associated with $ZnTa_2O_6:Pr^{3+}$ glow curve, which were obtained using the CGCD procedure.

Trap	T_{max} (K)	Trap depth $E(eV)$	Concentration n_o (cm^{-3})	Frequency factor s (s^{-1})
1	341	1.13	3.71×10^4	6.77×10^{17}
2	373	1.36	5.64×10^4	5.67×10^{17}
3	399	1.40	1.48×10^5	7.81×10^{17}
4	415	1.48	6.34×10^4	9.99×10^{16}
5	594	1.71	3.92×10^4	5.94×10^{17}

Table 7.2: The kinetic parameters associated with the glow curve of $ZnTa_2O_6:Pr^{3+}$ prepared in the presence of Li_2CO_3, which were obtained using the CGCD procedure.

Trap	T_{max} (K)	Trap depth $E(eV)$	Concentration n_o (cm^{-3})	Frequency factor s (s^{-1})
1	299	0.98	1.91×10^6	1.37×10^{17}
2	321	1.06	2.70×10^6	1.58×10^{17}
3	340	1.13	5.40×10^5	2.10×10^{17}
4	393	1.20	1.81×10^6	3.87×10^{17}
5	423	1.40	4.20×10^6	1.03×10^{17}
6	450	1.60	4.52×10^6	1.06×10^{17}
7	481	1.70	3.90×10^6	1.19×10^{17}
8	508	1.79	1.81×10^6	1.37×10^{17}

Table 7.3: The kinetic parameters associated with the glow curve of $ZnTa_2O_6:Pr^{3+}$ prepared in the presence of Li_2SO_4, which were obtained using the CGCD procedure.

Trap	T_{max} (K)	Trap depth $E(eV)$	Concentration n_o (cm^{-3})	Frequency factor s (s^{-1})
1	315	1.12	2.19×10^6	1.58×10^{17}
2	343	1.20	7.84×10^5	1.09×10^{17}
3	378	1.33	2.98×10^6	1.00×10^{17}
4	403	1.41	3.44×10^6	1.19×10^{17}
5	427	1.50	2.80×10^6	1.02×10^{17}
6	449	1.58	2.93×10^6	2.20×10^{17}
7	473	1.68	3.45×10^6	1.32×10^{17}
8	500	1.76	3.22×10^6	1.16×10^{17}

$$I(T) = I_M b \frac{b}{b-1} exp \left(\frac{E}{kT} \right.$$

$$\times \left. \frac{T - T_M}{T_M} \right) \left[1 + (b-1) \frac{2kT_M}{E} + (b-1) \left(1 - \frac{2kT_M}{E} \right) \right.$$

$$\times \left. \left(\frac{T^2}{T_M^2} \right) exp \left(\frac{T - T_M}{T_M} \frac{E}{kT} \right) \right]^{\frac{-b}{b-1}} \qquad [7.1]$$

$$s = \frac{\beta E}{kT_M^2 \left(1 + \frac{2kT_M(b-1)}{E} \right)} exp \left(\frac{E}{kT_M} \right) \qquad [7.2]$$

$$I(T) = sn_o exp \left(-\frac{E}{kT} \right) \left[1 + \frac{s(b-1)}{\beta} \int_{T_0}^{T} exp \left(-\frac{E}{kT} \right) dT \right]^{-\frac{b}{b-1}} \qquad [7.3]$$

where I_M and T_M are the TL intensity and temperature (K) at the glow peak maximum respectively, E is the activation energy (eV), k is the Boltzmann constant, β is the heating rate, n_o is the concentration of the trapped electrons and b is the kinetic parameter [43]. The parameters of the traps are presented in tables 7.1, 7.2 and 7.3 for $ZnTa_2O_6:Pr^{3+}$, $ZnTa_2O_6:Pr^{3+}$ prepared in the presence of Li_2CO_3 and $ZnTa_2O_6$ prepared in the presence of Li_2SO_4.

The data are plotted in the log scale to show that the curves have two components; the fast and the slow component. The fast component can be attributed to the decay time of Pr^{3+} emission, and the slow component can be attributed to persistent emission as a result of trapping and detrapping of charge carriers [19,39]. The trap levels may be more than one in this system, and amongst them are the oxygen vacancies ($V_o^{\cdot}$ and $V_o^{\cdot\cdot}$) that are responsible for electron trapping [6,39]. The curves were fitted (as shown Figure 7.14 insert) with a second order exponential equation (Eq. 7.4):

$$I(t) = Ae^{-t/\tau1} + Be^{-t/\tau2} \qquad [7.4]$$
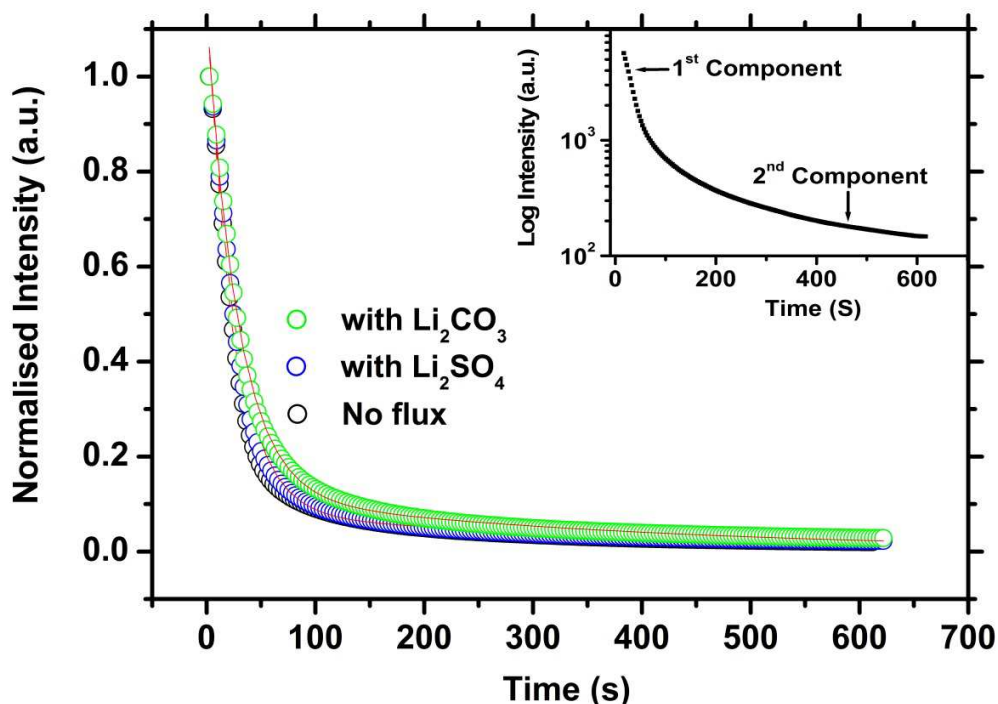
Figure 7.14: Phosphorescence decay curves of $ZnTa_2O_6:Pr^{3+}$ and the samples prepared in the presence of flux. The insert shows the fitted decay curve of $ZnTa_2O_6:Pr^{3+}$ sample.

Table 7.4: The decay times parameters; τ_1 and τ_2, for the $ZnTa_2O_6:Pr^{3+}$ sample, and the ones prepared in the presence of a flux.

sample	τ_1 (s)	τ_2 (s)
$ZnTa_2O_6:Pr^{3+}$	30.1 ± 0.6	550 ± 10
$ZnTa_2O_6:Pr^{3+}$ with Li_2SO_4	31.1 ± 0.6	620 ± 11
$ZnTa_2O_6:Pr^{3+}$ with Li_2CO_3	30.2 ± 0.6	690 ± 10

$I(t)$ is the luminescence intensity, A and B are constants and t is the time. The first term on the right side of the equation describes the decay of luminescence from the dopant ion, and whose lifetime is presented by τ_1. The second term describes the decay of the persistent emission and whose lifetime is presented by τ_2 (Table 7.1) [19,39]. The corresponding time parameters (τ_1 and τ_2) are presented in table 7.4. The second time parameter increases with the addition of the flux

in the material; this effect is attributed to the increased electron trapping centres (Figure 7.13) that are induced by preparing the samples in the presence of the flux.

Figure 7.15 is a luminescent mechanism proposed to explain the effects of a flux to $ZnTa_2O_6$:Pr^{3+} phosphors. According to this illustration, upon excitation; there is band to band excitation and charge transfer (CT) to the defect levels of $ZnTa_2O_6$ residing at the donor level. The electrons which are excited to these two states are eventually de-excited to the luminescent centres of Pr^{3+} non-radiatively. This is as revealed by the PLE (Figure 7.5(a) and (b)) and the diffused reflectance (Figure 7.6) spectra. Prior to the preparation in the presence of a flux, the luminescent emission intensity of $ZnTa_2O_6$:Pr^{3+} is limited to the red emitting transitions from $^1D_2 \rightarrow ^3H_4$, $^3P_0 \rightarrow ^3H_6$ and $^3P_0 \rightarrow ^3F_2$ at 608, 619 and 639 nm, respectively (Presented by the solid red arrows).
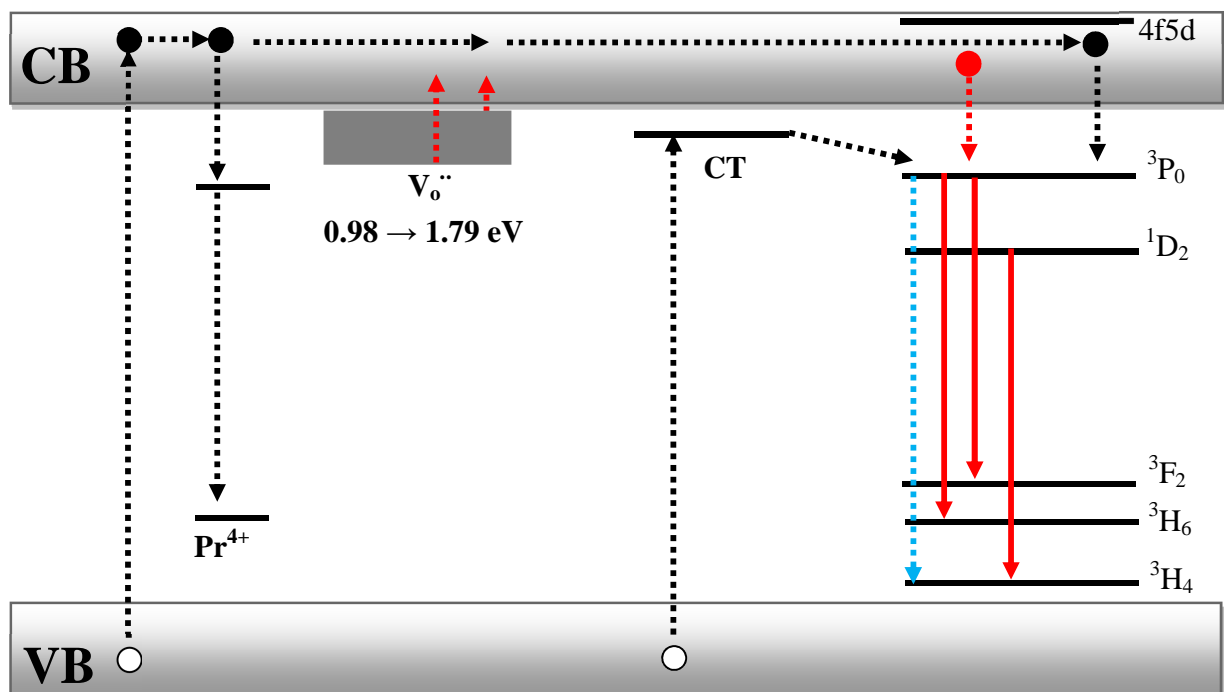
Figure 7.15: A schematic diagram to present the luminescent mechanism involved in the phosphors prepared in the presence of a flux.

Preparing with the flux introduced the blue emission (presented in a dashed arrow) at 505 nm that is attributed to the $^3P_0 \rightarrow ^3H_4$ transition, and strongly enhanced the red emission at 619 nm from $^3P_0 \rightarrow ^3H_6$ transition. This effect is introduced by the strongly improved charge transfer (Figure 7.6) to the donor levels, due to the flux, which reinforces charge transfer from these

levels to the luminescent centres of Pr^{3+}. The XPS data (Figure 7.10) reveals that the Pr exists as Pr^{3+} and Pr^{4+} oxidation states, with the latter state acting as a quenching centre from where non-radiative recombination is induced. For the samples prepared in the presence of a flux, the relative intensity Pr^{4+} peak is reduced compared to that of Pr^{3+}, which is an indication that there is less Pr^{4+}. The reduced quenching centre of Pr^{4+} reinforces the transfer of carriers to the luminescent centres of Pr^{3+}. This is an additional factor that contributes to the introduction of the blue emission and the strongly enhanced red emission.

The electrons trapped within the electron trapping centres follow neither first nor second, but general order kinetics when they are stimulated to the conduction band. The TL spectra (Figure 7.13) reveal additional trap centres at lower temperatures (marked with a horizontal dashed line) due to the preparation in the presence of a flux. The generation of additional trap centres has caused the persistent emission to increase from 550 to 690 seconds.

7.4.   Conclusion

$ZnTa_2O_6$:Pr^{3+} phosphor was prepared at 1200 ^{o}C via the solid state route, and two other samples were prepared in the presence of Li_2CO_3 and Li_2SO_4. The flux materials greatly improved the luminescence intensity of the phosphor. This was achieved by reinforcing energy transfer to the Pr^{3+} luminescence centres by strengthening the matrix absorption through the charge transfer state and by suppressing the Pr^{4+} quenching centres. This is as observed from the diffused reflectance and the XPS spectra. The persistent emission was also improved by the flux by promoting the formation of additional electron trapping centres as observed from the TL glow curves.

7.5. References.

1. C.J. Summers, H.M. Menkara, R.A. Gilstrap, M. Menkara, T. Morris, Mater. Sci. Forum **654-656** (2010) 1130.

2. Z. Pan, Y.Y. Lu, F. Liu, Nat. Mater. **11** (2012) 58.

3. Y. Pan, Q. Su, H. Xu, T. Chen, W. Ge, C. Yang, M. Wu, J. Solid Stat. Chem. **174** (2003) 69.

4. S. S. Chadha, D. W. Smith, A. Vecht. C. S. Gibbons, 94 SID Digest **51** (1994) 1.

5. C. Gheorghies, P. Boutinaud, M. Loic, V.O. Atanasiu, J. Optoelectron. Adv. Mater. **11** (5), (2009) 583.

6. P.T. Diallo, P. Boutinaud, R. Mahiou, J. Cousseins, Phys. Stat. Sol. (a) **160** (1997**)** 255.

7. P. Boutinaud, L. Sarakha, E. Cavalli, M. Bettinelli, P. Dorenbos, R. Mahiou, J. Phys. D: Appl. Phys. **42** (2009) 045106.

8. S. Li, X. Liang, J. Mater. Sci: Mater Electron **19** (2008) 1147.

9. W. Tang, D. Chen, Phys. Status Solidi A **206** (2), (2009) 229.

10. K.G. Tshabalala, So-Hye Cho, Jun Ku Park, Indrajit M. Nagpure, Hendrik C Swart and Martin O. Ntwaeaborwa, *J. Vac. Sci. and Technol. B,* **30**(3) (2012) 031401.

11. L.L. Noto, S.S. Pitale, M.A. Gusowki, J.J. Terblans, O.M. Ntwaeaborwa, H.C. Swart, Powder Technol. **237** (2013) 141.

12. H.A.A.S. Ahmed, O.M. Ntwaeaborwa, R.E. Kroon, Curr. Appl Phys. **13** (2013) 1264.

13. E.J. Popovici, M. Nazarov, L. Muresan, D.Y. Noh, L.B. Tudoran, E. Bica, E. Indrea, J. Alloys Compd. **497** (2010) 201.

14. T.P. Tang, M.R. Yang, K.S. Chen, Ceram. Int. **26** (2000) 341.

15. M. Waburg, H. Muller-Buschbaum, Zeitschrift fuer Anorganische und Allgemeine Chemie **508** (1984) 55.

16. X.C. Jiang, W.M. Chen, C.Y. Chen, S.X. Xiong, A.B. Yu, Nanoscale Res Lett **6** (2011) 32.

17. C. De Mello Donega, A Meijerink, G. Blasse, J. Phys. Chem. Solids **56** (5), (1995) 673.

18. P. Boutinaud, E. Pinel, M. Dubois, A.P. Vink, R. Mahiou, J. Lumin.*,* **111** (2005) 69.

19. L.L. Noto, M.L. Chithambo, O.M. Ntwaeaborwa, H.C. Swart, Powder Technol. **247** (2013) 147.

20. H. Virieux, M. Le Troedec, A. Cros-Gagneux, W.S. Ojo, F. Delpech, C. Nayral, H. Martinez, B. Chaudret, J. Am. Chem. Soc. **134** (2012) 19701.

21. C.D. Wagner, W.M. Riggs, L.E Davis, J.F. Moulder, Handbook of X-ray Photoelectron Spectroscopy, Perkin-Elmer Corp., 1979, Eden Prairie, MN, USA.

22. J.C. Klein, D.M. Hercules, J. Catal. **82** (1983) 424.

23. C.T. Campbell, K.A. Daube, J.M. White, Surf. Sci. **182** (1987) 455.

24. V.I. Nefedov, D. Gati, B.F. Dzhurinskii, N.P. Sergushin, Y.V. Salyn, Zh. Neorg. Khimii **20** (1975) 2307.

25. V.I. Nefedov, N.M. Firsov I.S. Shaplygin, J. Electron Spectrosc. Relat. Phenom. **26** (1982) 65.

26. O.Y. Khyzun, A.K. Sinelnichenko, V.A. Kolyagin, Dopovidi Natsionalnoi Academii nauk Ukraini **69** (1996).

27. T. Anazawa, S. Tokumitsu, R. Sekine, E. Miyazaki, K. Edamoto, H. Kato, S. Otani, Surf. Sci. **328** (1995) 263.

28. P. Prieto, L. Galan, J.M. Sanz, Appl. Surf. Sci. **70** (1993) 186.

29. A.R.H.F. Ettema, C. Haas, J. Phys. Cond. Matter **5** (1993) 3817.

30. J.H. Thomas 3rd. L.H. Hammer, J. Electrochem. Soc. **136** (1989) 2004.

31. E. Agostinelli, C. Battistoni, D. Fiorani, G. Mattogno, M. Nogues, J. Phys. Chem. Solids **50** (1989) 269.

32. J.P. Contour, A. Salesse, M. Froment, M. Garreau, J. Thevenin, D. Warin, J. Microsc. Spectrosc. Electron **4** (1979) 483.

33. S. Contarni, J.W. Rabalais, J. Electron Spectrosc. Relat. Phenom. **35** (1985) 191.

34. J. Gurgul, M.T. Rinke, I. Schellenberg, R. Pöttgen, Solid State Sci. **17** (2013) 122.

35. A.A. Yaremchenko, S.G. Patrício, J.R. Frade, J. Power Sources **245** (2014) 557.

36. F. Jin, Y. Shen, R. Wang, T. He, J. Power Sources **234** (2013) 244.

37. V.V. Atuchin, T.A.Gavrilova, J.C.Grivel, V.G.Kesler, I.B.Troitskaia, J. Solid State Chem. **195** (2012) 125.

38. W. Jia, D. Jia, T. Rodriguez, D.R. Evans, R.S. Meltzer, W.M. Yen, J. Lumin. **119 – 120** (2006) 13.

39. L.L. Noto, S.S. Pitale, M.A. Gusowki, O.M. Ntwaeaborwa, J.J. Terblans, H.C. Swart, J. Lumin. **145** (2014) 907.

40. L.L. Noto, M.L. Chithambo, O.M. Ntwaeaborwa, H.C. Swart, J. Alloys Compd. **589** (2014) 88.

41. S.W.S. Mckeever, M. Moscovitch, P.D. Townsend, *Thermoluminescnec Dosimetry materials: Properties and uses*, 1995, Nuclear Technology Publishing, England.

42. K.S. Chung, H.S. Choe, J.I. Lee, J.L. Kim, S.Y. Chang, Radiat. Prot. Dosim. **115** (2005) 1.

43. V. Pagonis, G. Kitis, C. Furetta, Numerical and practical exercises in thermoluminescence, 2006, Springer publishers, USA.

44. B.J. Nyman, M.E. Bjorketun, G. Wahnstrom, J. Sol. Stat. Ionics**189** (2011) 19.

"Your time is limited, so don't waste it living someone else's life. Don't be trapped by dogma - which is living with the results of other people's thinking. Don't let the noise of others' opinions drown out your own inner voice. And most important, have the courage to follow your heart and intuition."

― Steve Jobs

8

Persistent luminescence study of ZnTaGaO$_5$:Pr^{3+}

8.1.   Introduction

The persistent luminescence is recently receiving attention because of the demand in applications in the bio imaging for medical diagnostic, high energy radiation detection, thermal sensors, self-lit road lines and emergency signs [1,2,3]. Such luminescence is one that continues after the removal of the excitation source, due to the stored energy from absorption being gradually released as visible light [1,2]. Good persistent phosphors continue to glow for several hours in the absence of the excitation source [1]. Such phosphors include Zn$_3$Ga$_2$Ge$_2$O$_{10}$: Cr^{3+} with an emission lasting longer than 300 hours, which is attributed to electron tunnelling back and forth between the electron trapping centres and the chromium luminescence centre [1]. Persistent luminescence of SrAl$_2$O$_4$:Eu^{2+}, Dy^{3+} was reported to be attributed to the delay of electrons by electron trapping centres associated with oxygen vacancies, before they reach the 5d state of Eu^{2+}, from where luminescence emanates [3].

Our research is mostly directed in tantalite phosphors. The chemical stability and the persistent luminescence lasting more than ten minutes were reported for YTaO$_4$:Pr^{3+}, LaTaO$_4$:Pr^{3+} and GdTaO$_4$:Pr^{3+} phosphors having multiple electron trapping canters [4,5]. The chemical stability was investigated by prolonged electron beam irradiation on the sample at 1 $\times$ 10^{-6} Torr O$_2$ pressure [4]. A new red emitting phosphor ZnTa$_2$O$_6$:Pr^{3+} was reported with a persistent emission lasting longer than nine minutes after it was excited for five minutes using an ultraviolet lamp [6]. When 0.4 mol % doping of Pr^{3+} was used in ZnTa$_2$O$_6$ host, emission resulted in a pure red colour coming from the ^{1}D$_2 \to$ ^{3}H$_4$, ^{3}P$_0 \to$ ^{3}H$_6$ and ^{3}P$_0 \to$ ^{3}F$_2$ transitions at 608, 619 and 639 nm, respectively, according the CIE coordinate plots [7]. CaTa$_2$O$_6$:Pr^{3+}, with a greenish blue emission constituting of emission lines coming from the ^{3}P$_0 \to$ ^{3}H$_4$ transition at 487 and 498 nm in the blue region of the electromagnetic spectrum, and at 530,

543 and 556 nm from $^3P_0 \rightarrow {}^3H_5$ transition in the green region of the electromagnetic spectrum. Addtitionally, there were spectral lines in the red region of the electromagnetic spectrum at 597 and 610 nm from $^1D_2 \rightarrow {}^3H_4$ transition, at 620 and 627 nm from $^3P_0 \rightarrow {}^3H_6$ transition, and at 656 nm are attributed to $^3P_0 \rightarrow {}^3F_2$ transition. The phosphor had a persistent luminescence lasting longer than 26 minutes after an ultraviolet irradiation for five minutes [8]. In the search of developing new phosphors, we are presenting $ZnGaTaO_5$:Pr^{3+}, which is prepared by combining $ZnTa_2O_6$ and $ZnGa_2O_4$ structures into a new compound. $ZnGa_2O_4$ compound is spinel type of an oxide, which crystallizes either into a normal spinel or mixed spinel [9]. In the normal spinel the Zn ion occupies the tetrahedral site and the Ga ion occupies the octahedral site, whereas in a mixed spinel the Zn and Ga ions are randomly distributed between in the tetrahedral and the octahedral sites [9]. The compound exhibits strong blue emission attributed to the transition between the Ga and O defect levels, and has been reported to have applications in low voltage cathodoluminesce and liquid crystal displays [9]. In the current paper we are introducing $ZnGaTaO_5$:Pr^{3+}, the luminescence properties and the energy distribution of the electron trapping centres. Further characterization was done to investigate ion distribution and was investigated with the ToF–SIMS.

8.2.   Experimental

$ZnTaGaO_5$: Pr^{3+} (0.4 mol %) phosphor was prepared by solid state reaction by mixing ZnO, Ta_2O_5, Ga_2O_3 and $PrCl_3$ in stoichiometric amounts. The reagents were mixed into a slurry using Ethanol. The slurry was preheated at 100 ^{o}C for 10 hrs and later sintered at 1200 ^{o}C for 4 hrs. The product was allowed to cool down to room temperature and then grounded into a powder. The powder was washed with distilled water to remove the flux compounds from the phosphor. The crystalline phase was identified by a Bruker AXS D8 Advance X-Ray diffractometer using Cu $K\alpha$ radiation. The PL emission and excitation (PLE) properties of the phosphor were probed using a Varian Carry-Eclipse fluorescence spectrophotometer. The SEM images were obtained using a Shimadzu SSX-550 SEM. The surface maps showing the distribution of the ions, were obtained using the time of flight secondary ion mass spectroscopy (ToF – SIMS). The Bi^+ ion gun with 1 pA beam current was used to probe the surface of the phosphor, and was operated in the imaging mode. A PerkinElmer Lambda 950 UV/VIS spectrometer was used to record the diffuse reflectance spectra. The

phosphorescence decay curves to determine the persistent emission lifetime were measured after exciting the phosphor with an ultraviolet source for 5 minutes, then monitoring the time it takes for the emission to decay using a photomultiplier tube (PMT). The glow curves were obtained using a 245 nm ultraviolet source for excitation, and measuring the TL using a TL 10091, NUCLEONIX spectrometer.

8.3.   Results and Discussion

The ZnTaGaO$_5$:Pr^{3+} sample was prepared and the phase purity was checked using the XRD, and mixed phases were observed. The nature of the peaks confirms that the crystalline particles were formed at 1200 ^{o}C. The XRD pattern of ZnTaGaO$_5$:Pr^{3+} (Figure 8.1) matched with the patterns of ZnTa$_2$O$_6$ with a standard file indexed by ICSD 36289 and that of ZnGa$_2$O$_4$ with a standard file indexed by JCPDS 38-1240.
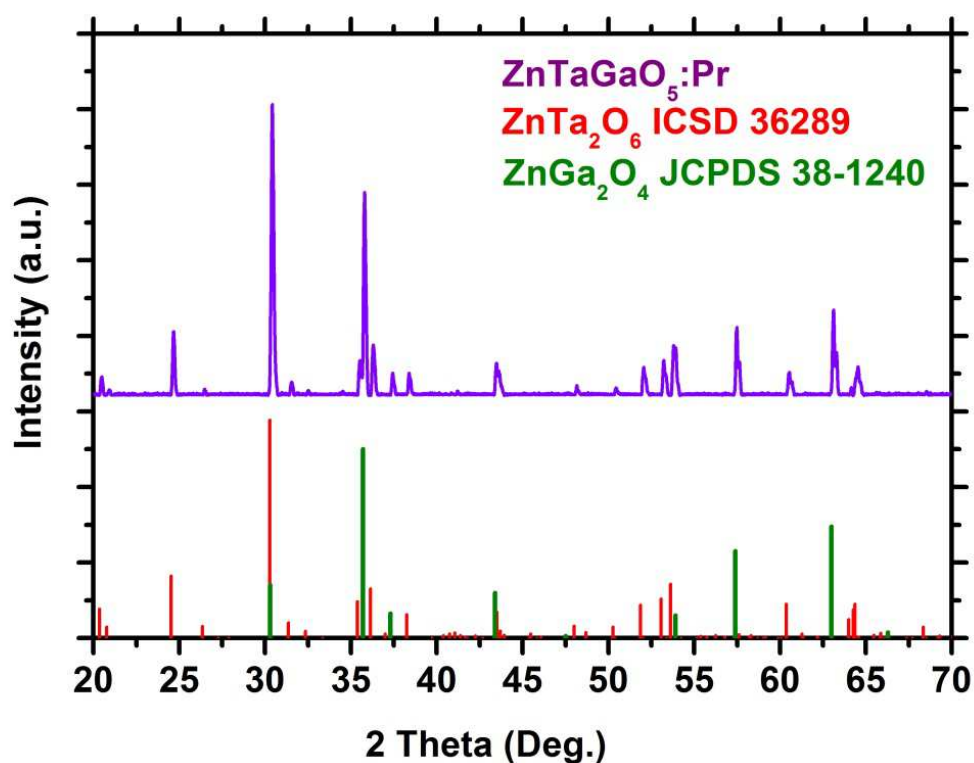
Figure 8.1: The XRD patterns of ZnTaGaO$_5$:Pr and the standard patterns of ZnTa$_2$O$_6$ and ZnGa$_2$O$_4$.

The SEM images of ZnTaGaO$_5$:Pr^{3+} which is a representative of the surface morphology measured over a 9.9 × 7.4 µm^2 field of view area are shown in figure 8.2. The image shows that the particle crystallized into three different shapes; rod, rhombus and round shapes with

different sizes. The round shaped particles are agglomerated to each other as a result high temperature used for the synthesis process [8]. The rhombus and rod shapes particles were not present in the $ZnTa_2O_6$:Pr^{3+} sample [6], and this may be an effect introduced by the Ga incorporation into the structure to form $ZnTaGaO_5$: Pr^{3+}.
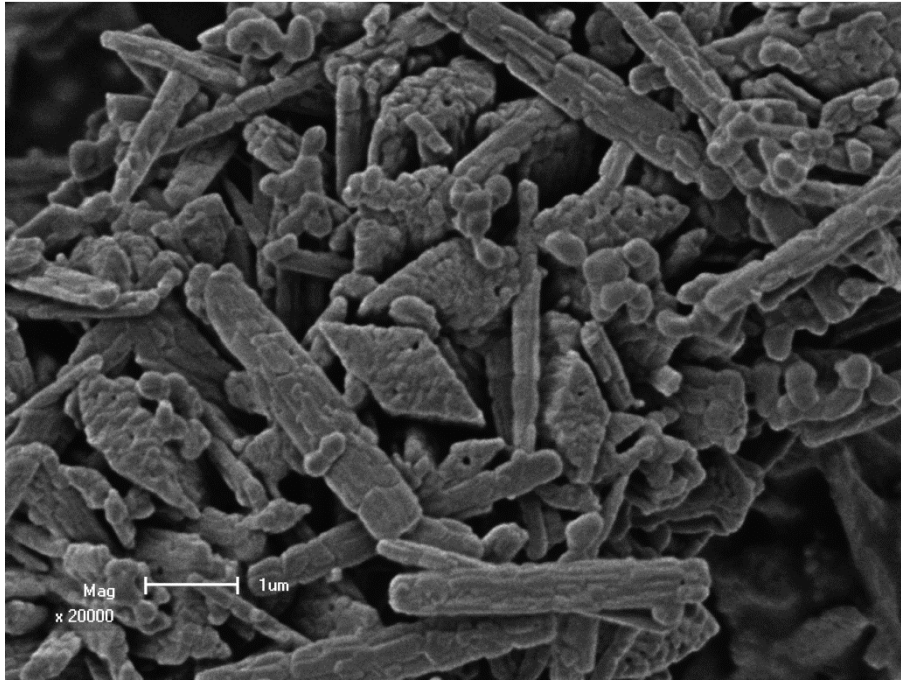
Figure 8.2: SEM image of $ZnTaGaO_5$:Pr^{3+} with a field of view of 9.9×7.4 μm^2

Figure 8.3 Shows the ToF-SIMS mapping that was obtained in order to investigate the distribution of the ions inside $ZnTaGaO_5$:Pr^{3+} over an area of 100×100 μm^2. Zn^+ (Red), GaO^+ (Green in Figure 3a), TaO^+ (Green in Figure 3b) and PrO^+ (blue) representing Zinc, Aluminium, Tantalum and Praseodymium ions in the phosphor, respectively. All the ions appear to be uniformly distributed, and this is an indication of its successful preparation and incorporation of the dopant in the host lattice.

The PLE and PL spectra of $ZnTaGaO_5$: Pr^{3+} are shown in figure 8.4. Upon exciting the materials with 259 nm ultraviolet source, there were emission lines that were observed from the $^1D_2 \rightarrow {}^3H_4$, $^3P_0 \rightarrow {}^3H_6$ and $^3P_0 \rightarrow {}^3F_2$ transitions at 608, 119 and 639 nm from the PL spectra, respectively, attributed to Pr^{3+} emission lines [6]. There is also a minor emission line attributed to $^1D_2 \rightarrow {}^3H_5$ transitions at 696 and 710 nm of Pr^{3+} [6]. The emission from the $^1D_2$

$\rightarrow$ $^3H_5$ transitions is much more intense than usual as reported in our previous work [4,5,6,7,8], and this effect may be induced by the incorporation of Ga ions into the matrix of the host. This shall further be investigated and will be discussed in our next paper. The PLE spectra shows prominent excitation states at 259 and 270 nm, which correspond to band to band (B–B) excitation as reported by Noto et al [6].
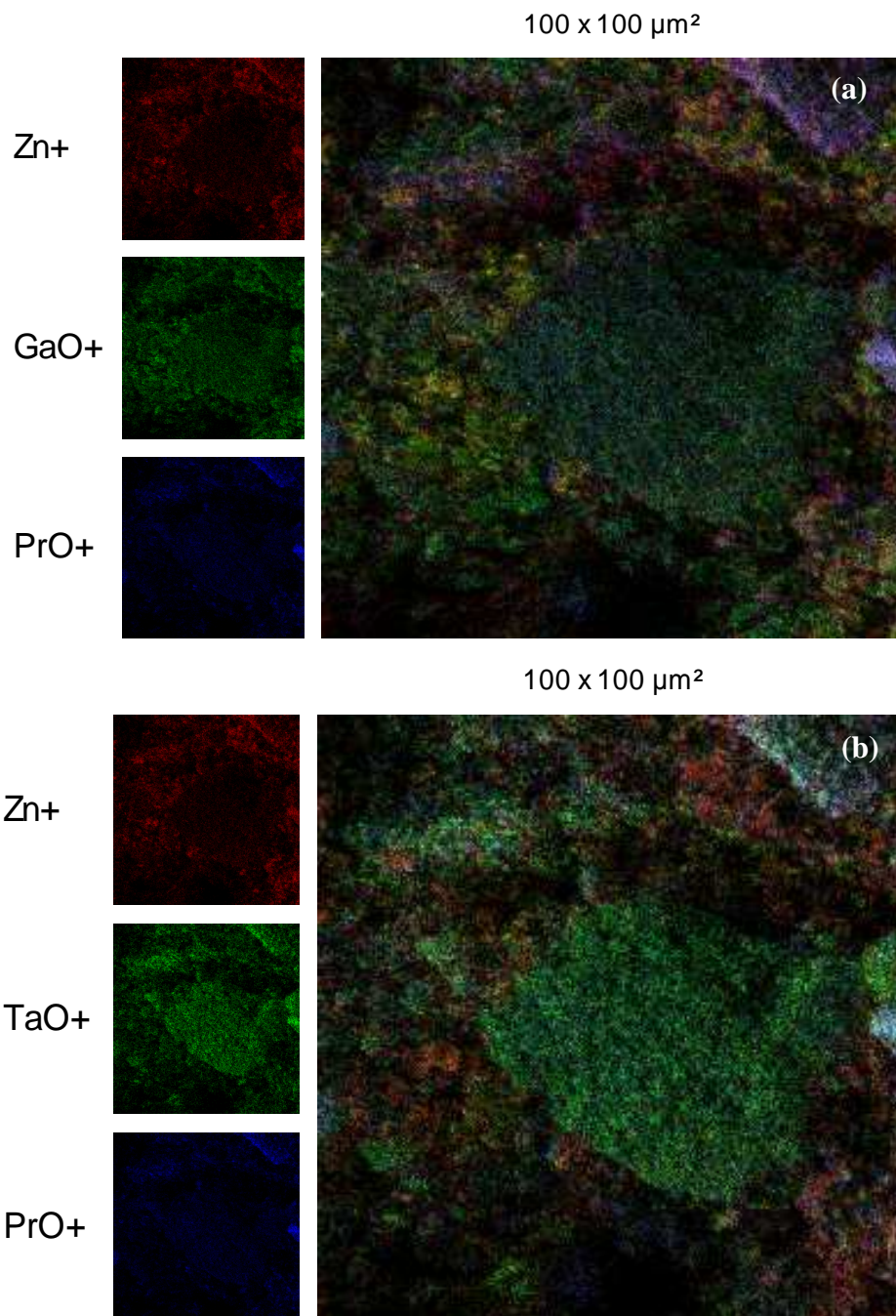

Figure 8.3: ToF–SIMS maps of ZnTaGaO$_5$:Pr^{3+} with a field of view of 100×100 µm^2

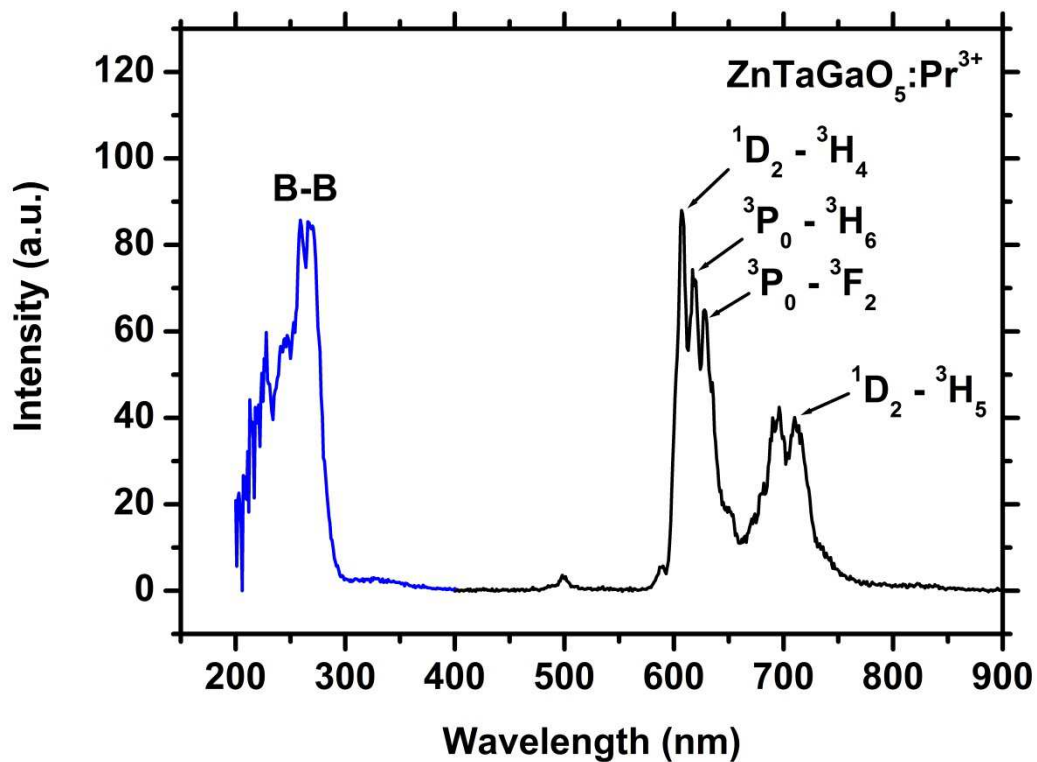Figure 8.4: The PLE and PL spectra of $ZnTaGaO_5$: Pr^{3+}.
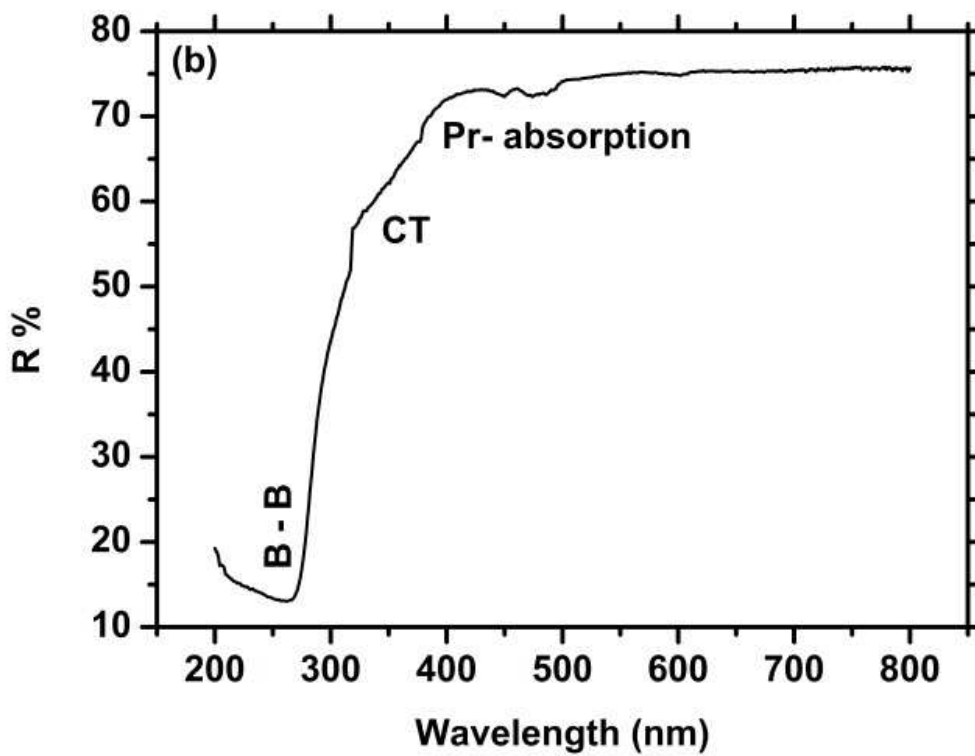

Figure 8.5: Diffused reflectance spectrum of $ZnTaGaO_5$: Pr^{3+} phosphor.

The same band is observable in the diffused reflectance spectrum (Figure 8.5) at 270 nm as the region where the major absorption occurs. This suggests that the incorporation of the Ga into the structure has an effect of lowering the energy position of the conduction band by approximate 0.3 eV. The rest of the transitions observed at 330 nm and at 450 – 500 nm region of the diffused reflectance spectrum (Figure 8.5) are attributed to the charge transfer and Pr^{3+} absorption [4,5,6,7].

The decay curve of $ZnTaGaO_5$: Pr^{3+} (Figure 8.6) was obtained by radiating the phosphor with an ultra violet source of 245 nm. This is followed by measuring the decay time of the persistent luminescence using a photomultiplier tube (PMT) at room temperature. The resulting persistence of the luminescence comes is attributed to the electrons that are trapped within the electron trapping centres and gradually released to the luminescence centre. The delay of the electron from the conduction band to the luminescence centre by the electron traps results the persistent luminescence [4,5,6]. The curve decay curve was additionally plotted in the log scale (Figure 8.6 inset) to extract the number of components involved in the persist luminescence. Two components are distinguished; the first component corresponding to the decay of the Pr^{3+} luminescence and the second component corresponding to the decay of the luminescence corresponding to the electrons delayed by the electron trapping centres before they reach the luminescence centre [5,6]. The curve was fitted (Figure 8.5) with a second order exponential decay equation (Eq. (8.1)) to extract the decay time parameters.

$$I(t) = A\,e^{-t/\tau 1} + B\,e^{-t/\tau 2} \qquad\qquad [8.1]$$

where $I(t)$ is the luminescence intensity, A and B are constants and t is the time. The first term on the right side of the equation describes the decay of luminescence from the dopant ion, and whose lifetime is presented by τ_1. The second term describes the decay of the persistent emission and whose lifetime is presented by τ_2 [5,6]. The persistent luminescence decay time resulting from the electron trapping centre was approximated to 374 ± 8 seconds, which was less compared to that of $ZnTa_2O_6$:Pr^{3+} phosphor [6].

Thermoluminescence measurements were done for $ZnTaGaO_5$: Pr^{3+} phosphor to evaluate the distribution of the electron trapping centres. Electron traps are generally attributed to oxygen vacancies in materials, which may assume different orientations and can therefore occupy different energy levels [5]. The measurements were carried out by exciting the sample with

an ultra violet source of 245 nm, then acquiring a glow curve by heating the sample from 300 to 600 K (27 to 327 $^{\circ}$C) at a heating rate of 2 K/sec.
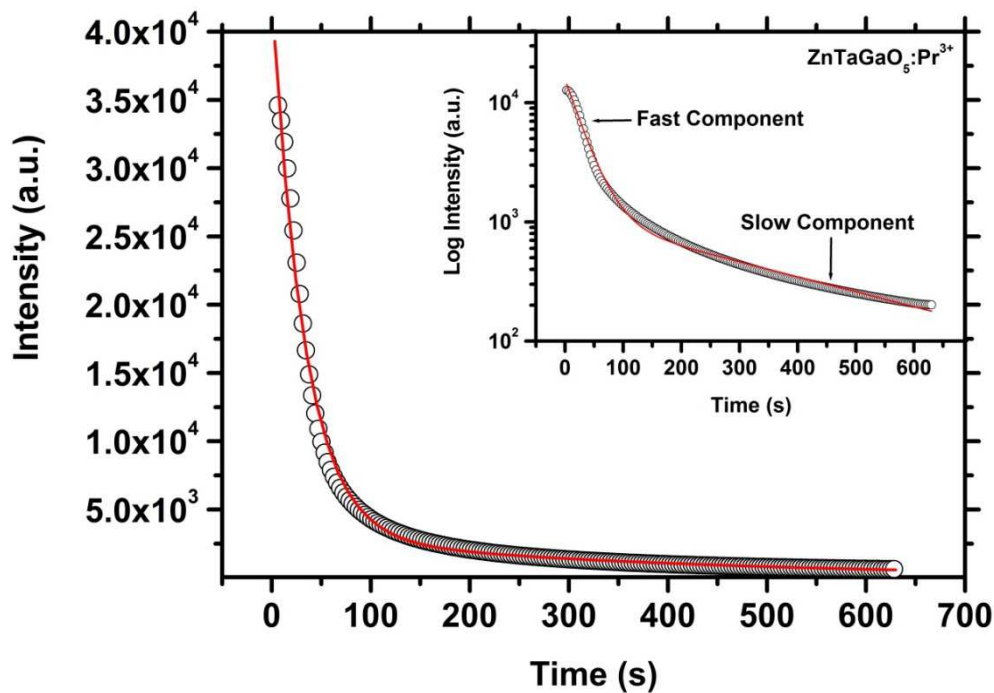

Figure 8.6: Phosphorescence decay curves of ZnTaGaO$_5$: Pr^{3+} phosphor.

The electron detrapping kinetics were evaluated by exposing the phosphor to different ultraviolet irradiation time (2, 5, 9, 12 or 15 min). The glow curves (Figure 8.7a) of the samples shift to higher temperatures with an increase in irradiation time, which is an indication of kinetics which are neither first nor second order, but general order [6,8]. The glow curves of the different phosphors appeared broad and this may be attributed to the overlapping thermal peaks from electron trapping centres that are close to each other [5]. In order to determine the number of prominent electron trapping centres, the T$_M$-T$_{stop}$ method was used. The method involves heating a sample that is pre-irradiated by UV radiation, to some temperature (T$_{stop}$ 1) and then recording the temperature (T$_M$) corresponding to the maximum intensity of the glow curve. The procedure is repeated by heating the sample to a higher temperature (T$_{stop}$ 2 > T$_{stop}$ 1), until the rest of the glow curve is recorded. The flat regions in the plot are an indication of a prominent electron trapping centre [10]. The measured T$_M$-T$_{stop}$ data for ZnTaGaO$_5$: Pr^{3+} phosphor suggested the existence of six electron trapping centres. This is followed by plotting T$_M$ as a function of T$_{stop}$, and each flat region in the plot is an indication of the prominent electron trapping centre.

Table 8.1: The kinetic parameters associated with the glow curve of ZnTaGaO$_5$:Pr^{3+}, which were obtained using the CGCD procedure.

Trap	T_{max} (K)	Trap depth $E(eV)$	Concentration n_o (cm^{-3})	Frequency factor s (s^{-1})
1	344	1.01	3.93×10^4	1.30×10^{17}
2	379	1.32	7.84×10^5	1.03×10^{17}
3	402	1.43	1.06×10^6	1.80×10^{17}
4	423	1.56	5.65×10^5	1.70×10^{17}
5	459	1.62	4.72×10^4	1.00×10^{17}
6	494	1.75	2.42×10^4	1.76×10^{17}

The glow curve corresponding to two minutes irradiation was deconvoluted using a computerised glow curve deconvolution (CGCD) model, as shown in equation 8.2 for the general order, from a software package 'TLAnal' developed by Chung et al [11]. The general order kinetics related functions were used to compute for the activation energy (Eq. 8.2), frequency factor (Eq. 8.3) and the concentration of the electrons trapped within electron trapping centres (Eq. 8.4).

$$I(T) = I_M b \frac{b}{b-1} exp\left(\frac{E}{kT}\right.$$

$$\times \left.\frac{T-T_M}{T_M}\right)\left[1 + (b-1)\frac{2kT_M}{E} + (b-1)\left(1 - \frac{2kT_M}{E}\right)\right.$$

$$\times \left.\left(\frac{T^2}{T_M^2}\right) exp\left(\frac{T-T_M}{T_M}\frac{E}{kT}\right)\right]^{\frac{-b}{b-1}} \qquad [8.2]$$

$$s = \frac{\beta E}{kT_M^2\left(1 + \frac{2kT_M(b-1)}{E}\right)} exp\left(\frac{E}{kT_M}\right) \qquad [8.3]$$

$$I(T) = s n_o exp\left(-\frac{E}{kT}\right)\left[1 + \frac{s(b-1)}{\beta}\int_{T_0}^{T} exp\left(-\frac{E}{kT}\right) dT\right]^{-\frac{b}{b-1}} \qquad [8.4]$$

where I_M and T_M are the TL intensity and temperature (K) at the glow peak maximum respectively, E is the activation energy (eV), k is the Boltzmann constant, *β is the heating rate*, n_o is the concentration of the trapped electrons and b is the kinetic parameter [11]. The corresponding kinetic parameters are presented in Table 8.1.
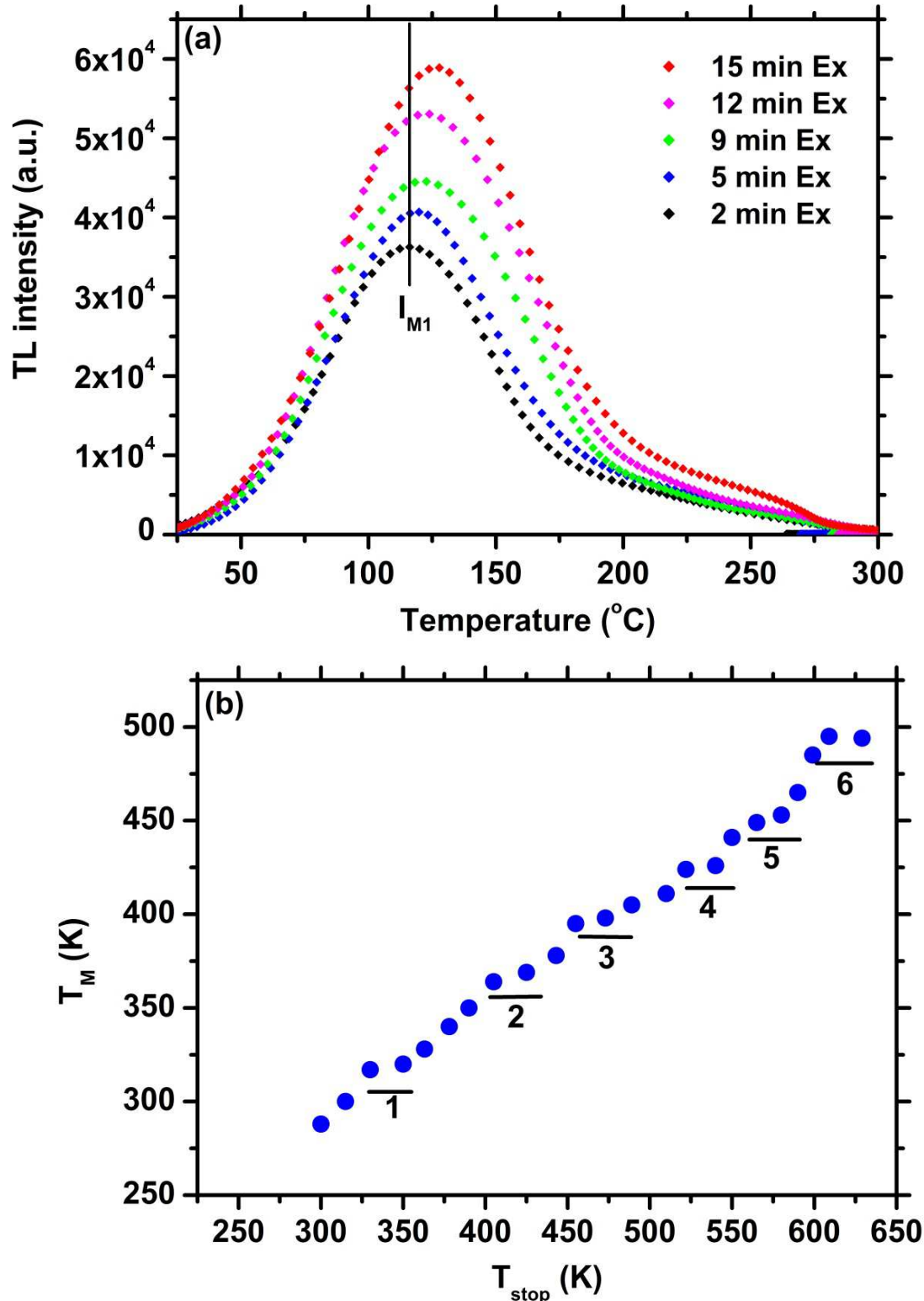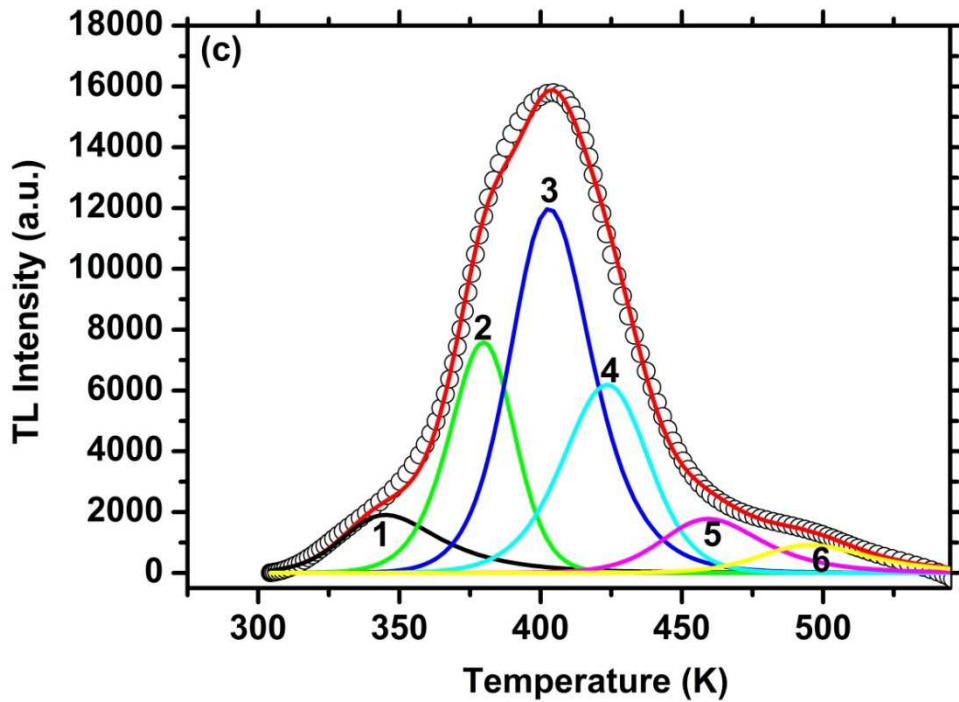
Figure 8.7: (a) Glow curves at different irradiation time, (b) T_M-T_{stop} plots and (c) the deconvoluted glow curve of ZnTaGaO$_5$: Pr^{3+} phosphor.

8.4. Conclusions

The persistent emitting ZnTaGa$_5$:Pr^{3+} phosphor was prepared at 1200 ^{o}C via the solid state route. Mixed phases were observed from the XRD corresponding to ZnGa$_2$O$_4$ and ZnTa$_2$O$_6$ phases. The material was found to have mixed particle shapes, which were rod, rhombus and irregular shapes. Prominent red emission lines were observed from the ^{1}D$_2 \rightarrow$ ^{3}H$_4$, ^{3}P$_0 \rightarrow$ ^{3}H$_6$, ^{3}P$_0 \rightarrow$ ^{3}F$_2$ and ^{1}D$_2 \rightarrow$ ^{3}H$_5$ transitions at 608, 119, 639, 696 and 710 nm from Pr^{3+}, respectively. Persistent luminescence lasting up to 374 $\pm$ 8 seconds was observed, and the corresponding electron trapping centres were investigated using TL spectroscopy.

8.5. References

1.   Z. Pan, Y.Y. Lu and F. Liu, Nature Mater. **11** (2012) 58.

2.   G. Ju, Y. Hu, L. Chen, X. Wang, Z. Mu, Opt. Mater. **36** (2014) 1183.

3.   H.C. Swart, J.J. Terblans, O.M. Ntwaeaborwa, E. Coetzee, B.M. Mothudi, M.S. Dhlamini, Nucl. Instrum. Methods Phys. Res. B, **267** (2009) 2630.

4.   L.L. Noto, S.S. Pitale, O.M. Ntwaeaborwa, J.J. Terblans, H.C. Swart, J. Lumin. **140** (2013) 14.

5.   L.L. Noto, S.S. Pitale, M.A. Gusowki, O.M. Ntwaeaborwa, J.J. Terblans, H.C. Swart, J. Lumin. **145** (2014) 907.

6.   L.L. Noto, M.L. Chithambo, O.M. Ntwaeaborwa, H.C. Swart, Powder Technol. **247** (2013) 147.

7.   L.L. Noto, O.M. Ntwaeaborwa, M.Y.A. Yagoub, H.C. Swart,
       http://dx.doi.org/10.1016/j.materresbull.2014.04.036

8.   L.L. Noto, M.L. Chithambo, O.M. Ntwaeaborwa, H.C. Swart, J. Alloys Compd. **589** (2014) 88.

9.   X. Duan, J. Liu, Y. Wu, F. Yu, X. Wang, J. Lumin. **153** (2014) 361.

10.   S.W.S. Mckeever, M. Moscovitch, P.D. Townsend, *Thermoluminescnec Dosimetry materials: Properties and uses*, 1995, Nuclear Technology Publishing, England.

11.   K.S. Chung, H.S. Choe, J.I. Lee, J.L. Kim, S.Y. Chang, Radiat. Prot. Dosim. **115** (2005) 1.

"If there is a good will, there is great way."

— William Shakespeare

9

The greenish-blue emission and thermoluminescent properties of CaTa$_2$O$_6$:Pr^{3+}

9.1.   Introduction

Calcium tantalite CaTa$_2$O$_6$ compound is considered an important material for the microwave applications because of its good dielectric properties in the microwave range which are attributed to its large quantity of oxygen vacancies [1]. The tantalite phosphors often require high temperatures to prepare, and are often phase impure [2], however Bleier et al [3] were successful in preparing a phase pure LaTaO$_4$:Eu using a hydrothermal route at 255 ^{o}C and further annealed at 900 ^{o}C. Karsu et al [4] also propose that a phase pure compound is achievable using Li$_2$SO$_4$ as a flux material. It is a perovskite and it can assume different symmetries depending on the preparation temperatures. It is cubic for temperatures that are below 800 ^{o}C, and is orthorhombic between 800 and 1558 ^{o}C [5]. The orthorhombic symmetry resembles a distorted perovskite [5], and the distortion is one of the crucial components leading to the formation of oxygen vacancies [6]. These oxygen vacancies have been reported to be a crucial component of the long afterglow phosphors [7,24], because they act as electron trapping centres [9]. They capture electrons and gradually release them to the luminescent centres [9], and upon electron-hole recombination long afterglow luminescence is observed [10,11]. Such materials can continue to emit light longer than several hours after the excitation source is removed. SrAl$_2$O$_4$:Eu, Dy and other phosphor [10] are well studied and they can glow with a green or other emission to over 30 hours. Dy is introduced in the system to generate more oxygen vacancies that further enhance the decay time from 60 minutes to 30 hours [12]. Phosphors with such characteristics are important for applications in self-lit road

signage, emergency route signs and medical diagnostics [13]. These electron trapping centres reside within the band gap of the material [24], and they can be analysed by thermoluminescence spectroscopy to approximate their energy distribution and quantification [15]. The analysis is based on thermally stimulating electrons coming from the trapping centres to the recombination centres, and the process is followed by luminescence [24]. The kinetics of the electrons from the trapping centres to the recombination centres are of a wide variety such as first order, second order or general order [24,24]. The first order kinetics assume no interaction between the trapping centres and the second order kinetics assume interaction of trapping centres, which leads to electron retrapping [24]. Pr^{3+} doped phosphors have been studied and orthorhombic perovskites are reported to have a single and narrow red emission peak. The single red emission peak is attributed to the intervalence charge transfer that supports complete quenching of the blue emission [16,18,19]. In this paper, we are reporting the luminescence properties of greenish-blue emission of Pr^{3+} by using $CaTa_2O_6$ as host material for our phosphor and the analysis of the energy distribution of the electron trapping centres.

9.2. Experimental

$CaTa_2O_6$: Pr^{3+} (0.5 mol %, which is not an optimal concentration of Pr in $CaTa_2O_6$) phosphor was prepared through solid state reaction by directly mixing stoichiometric amounts of Ta_2O_5 99.0 % (Sigma Aldrich) and $CaCO_3$ 99.0 % (Sigma Aldrich) and $PrCl_3$, and ethanol were used to make a slurry mixture, which was dried at 100 ^{o}C for 10 hrs, and finally calcined at 1200 ^{o}C for 4 h. The crystalline phase was identified with a Bruker, AXS D8 Advance X-Ray diffractometer using Cu *Kα* radiation at room temperature. The photoluminescence (PL) emission and excitation (PLE) properties of the phosphor were probed using the Varian Carry-Eclipse fluorescence spectrophotometer at room temperature. The diffuse reflectance spectra were measured using a PerkinElmer Lambda 950 UV/VIS spectrometer at room temperature. The distribution of the energy traps was approximated using the thermoluminescence spectroscopy (Riso TL/OSL reader – model TL/OSL-DA-20) after irradiating the phosphor using beta particles from ^{90}Sr beta radiation source at a dose rate of 0.1028 Gy/s. The luminescence detection for the TL/OSL system consists of a photomultiplier tube (PMT) with

a U340 Schott filter that is effective in the 340 – 380 nm wavelengths. The glow curve measured using a 254 nm ultraviolet source for excitation, was measured using a TL 10091, NUCLEONIX spectrometer for thermoluminescence (TL). The phosphorescence decay curves for the measurement of the persistent emission lifetime were done by exciting the phosphor with an ultraviolet source for 5 minutes, then measuring the time it takes for the emission to decay using a PMT

9.3.   Results and Discussion

The measured X-ray diffraction (XRD) patterns (Figure 9.1a) show that phase pure and crystalline particles of $CaTa_2O_6$:Pr^{3+} were prepared. These are consistent with the standard orthorhombic $CaTa_2O_6$ phase referenced in the JCPDS card number 39-1430 [20]. The microstrain experienced by the material and the particle sizes were approximated using the Hall–Williamsons' equation (Eq. 9.1):

$$\frac{\beta Cos(\theta)}{\lambda} = \frac{1}{D} + \frac{\varepsilon Sin(\theta)}{\lambda}$$
[9.1]

where β (Corrected as B in Figure 9.1b) is the Full width at half maximum, θ angle of the diffraction peak in degrees, λ (1.54 Å) is the wavelength of the corresponding X-ray wavelength, D is the crystalline size, and ε is the percentage of the strain in the material [17]. The corresponding strain, which is obtained as a slope of the fit in the data plotted in Figure 9.1b is 0.089 ± 0.004, and the crystallite sizes were approximated to 0.51 µm from the intercept value (0.003) of the fit. The SEM image of $CaTa_2O_6$:Pr^{3+} with 5 µm field of view (Figure 9.2) shows agglomerated small particles of irregular shapes and different sizes. The agglomeration of the particles is attributed to the very high temperatures or preparation associated with solid state reaction [21].

The photoluminescence excitation (PLE) spectrum (Figure 9.3) shows that the major absorbing band is at 257 nm, corresponding the 498 nm emission. A single red emission of $CaTiO_3$:Pr^{3+}, In^{3+} from the $^1D_2$ level has recently been reported by Noto et al [22].
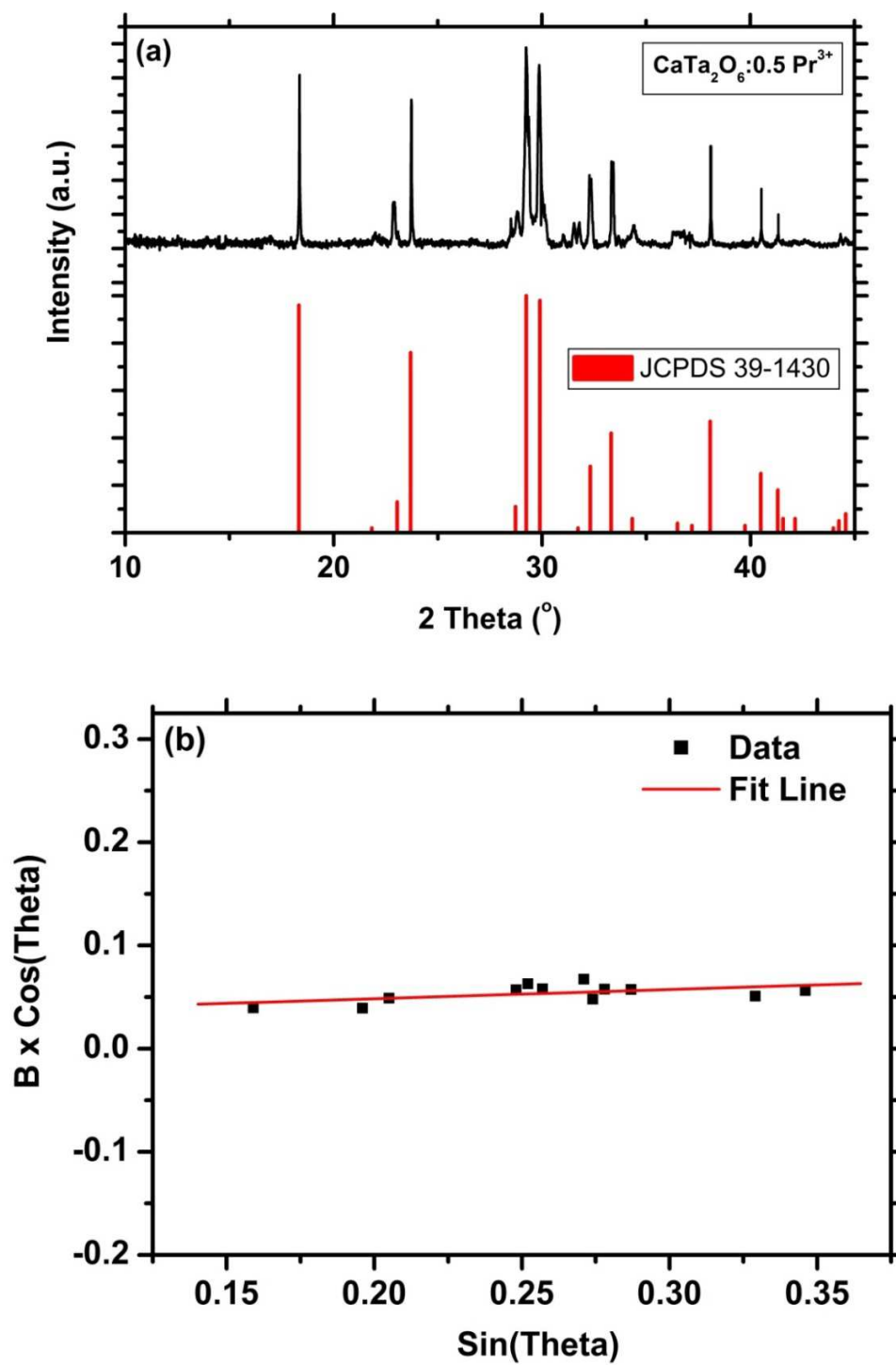
Figure 9.1: (a) The XRD patterns of CaTa$_2$O$_6$:Pr^{3+} , and (b) Hall-Williamson plot for microstrain analysis.

This is a consequence of total quenching of the $^3P_0$ level emission due to the strong coupling between the virtual intervalence charge transfer (IVCT) and the $^3P_0$ level at room temperature, which leads to the electrons non-radiatively crossing over to the $^1D_2$ level [23]. The photoluminescence (PL) spectrum presented in figure 9.3 shows both blue and red emissions from $CaTa_2O_6:Pr^{3+}$ phosphor. The blue spectral lines observed at 487 and 498 nm are attributed to two manifolds of $^3P_0 \rightarrow {}^3H_4$ level, and those at 530, 543 and 556 nm are attributed to three manifolds of $^3P_0 \rightarrow {}^3H_5$ level. The red spectral lines are observed at 597 and 610 nm that are attributed to the two manifolds of $^1D_2 \rightarrow {}^3H_4$ level those at 620 and 627 nm are attributed to two manifolds of $^3P_0 \rightarrow {}^3H_6$ level, and those at 656 nm are attributed to $^3P_0 \rightarrow {}^3F_2$ level [24]. The blue emission from the $^3P_0 \rightarrow {}^3H_4$ transition is glowing brighter than the red emission from $^1D_2 \rightarrow {}^3H_4$, $^3P_0 \rightarrow {}^3H_6$ and $^3P_0 \rightarrow {}^3F_2$ transitions. This is different from the observations in other oxide phosphors like: $Na_5Y(WO_4)_4:Pr^{3+}$, $Na_5Y(MoO_4)_4:Pr^{3+}$ and $YNbO_4:Pr^{3+}$, where the emissions due to $^3P_0 \rightarrow {}^3F_2$ transitions are much more intense than the emission due to $^3P_0 \rightarrow {}^3H_4$ [24].

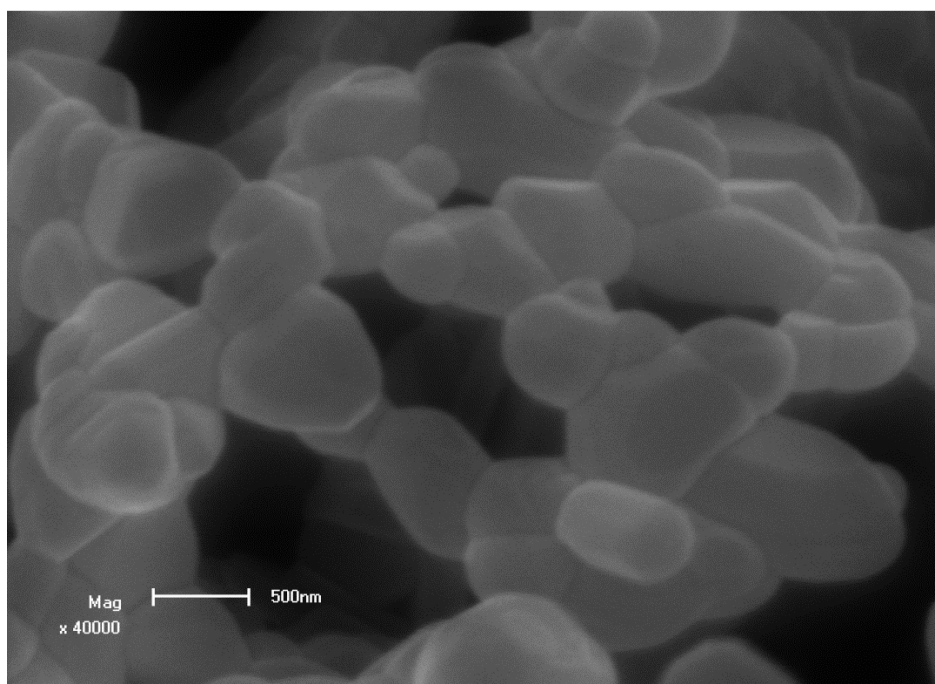Figure 9.2: SEM image of $CaTa_2O_6:Pr^{3+}$ with 5 µm field of view.

The presence of the emission due to transition from the $^3P_0$ to H and F levels may in this instance be an indication that the virtual charge transfer state is positioned in such a way that it

cannot completely quench this emission. The diffuse reflectance spectrum (Figure 9.4) shows a major absorption at 256 nm, which is at a position that is associated with band excitation [22], and the broad band absorption (charge transfer), which is believed to be the intervalence charge transfer state as reported for Pr^{3+} [23]. There are minor absorptions at 430 to 500 nm coming from the 4f–4f ($^3H_4 \rightarrow ^3P_0, ^1I_6, ^3P_1, ^3P_2$) transition of Pr^{3+} [22]. The position of the IVCT around 298 nm, which is shifted by 62 nm from 360 nm as observed in $CaTiO_3:Pr^{3+}$ [22,23], is a possible explanation for the IVCT not being able to completely quench the emission from the $^3P_0$ level.
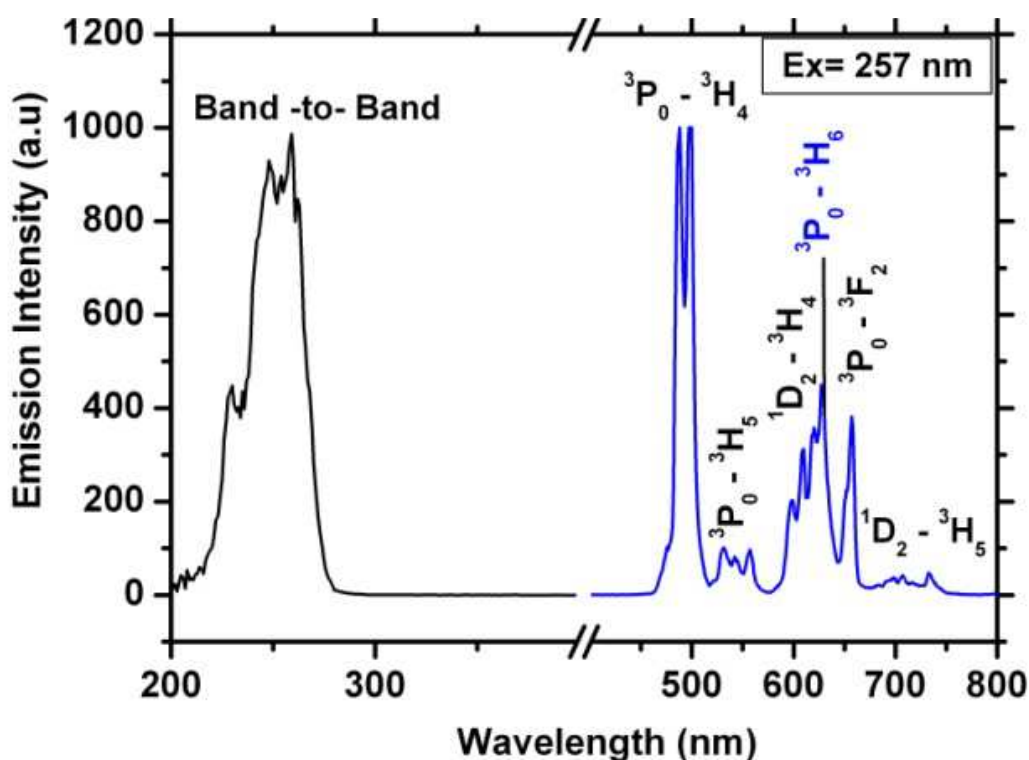
Figure 9.3: PLE and PL spectra of $CaTa_2O_6:Pr^{3+}$.

The energy distribution of the electron trapping centres that reside within the energy band gap of $CaTa_2O_6:Pr^{3+}$ phosphor was investigated. The glow curve of $CaTa_2O_6:Pr^{3+}$ (Figure 9.5) was measured by dosing the sample with 12 Gy up to 740 Gy and heating it at the rate of 5 ^{o}C/s (Figure 9.5). Upon increasing the dose, two more peaks appeared, suggesting that three types of electron traps exist, and the peaks of the glow curves shifted to higher temperatures. Glow peaks that do not shift in temperature positions upon exposing the material with different

doses, imply that the system follows first order kinetics [25,26,27]. Those peaks that shift systematically to lower temperatures imply that the system follows second order kinetics [26].
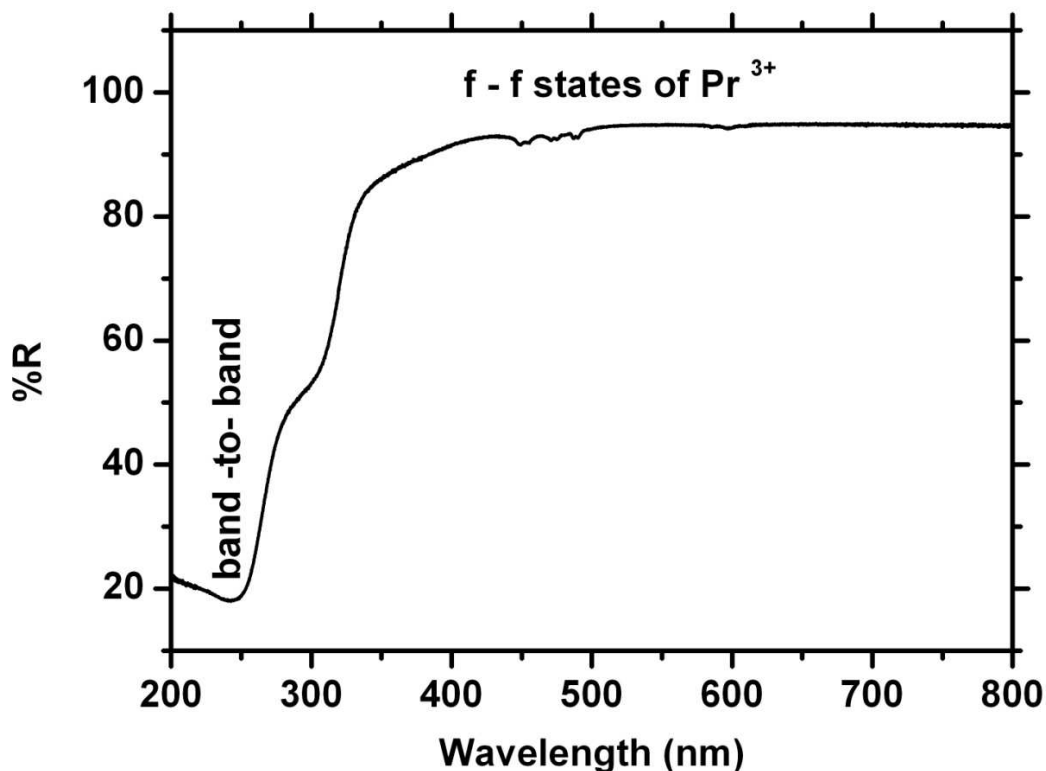

Figure 9.4: Diffuse reflectance spectrum of $CaTa_2O_6:Pr^{3+}$.

The peaks of the glow curve in figure 9.5 shifts systematically to higher temperatures as the dose is increased. This suggests that the system is neither following the first order nor the second order kinetics, but general order. Figure 9.6 shows the intensity response of the glow curve peaks (Figure 9.5) of the phosphor to different radiation doses (the line in between data points is a visual guide, not a model fit). Different materials respond differently to radiation dose, depending on their natural dosimetric behavior [28], and the TL intensity of such is dependent on the amount of the absorbed dose [29]. The nature of response can either be linear, sublinear or/and superlinear, depending on the linearity indexes [28]. The dose response of the three trap centres was investigated, and I_M (maximum intensity) is plotted as function of dose. The response of the three thermal peaks of the glow curves (Figure 9.5) seem to be linear for doses up to 740 Gy as presented in Figure 9.6. There seems to be

sublinearity at low doses for the second and third peak. However so, no full conclusion can be reached about sublinearity because at low doses the glow curves are noisy. According to Chen et al [30], the dose response curves reveal information about the trapping mechanism of the electron traps, and this can be used to investigate the competition that exists amongst different types of trap centres existing in a material.
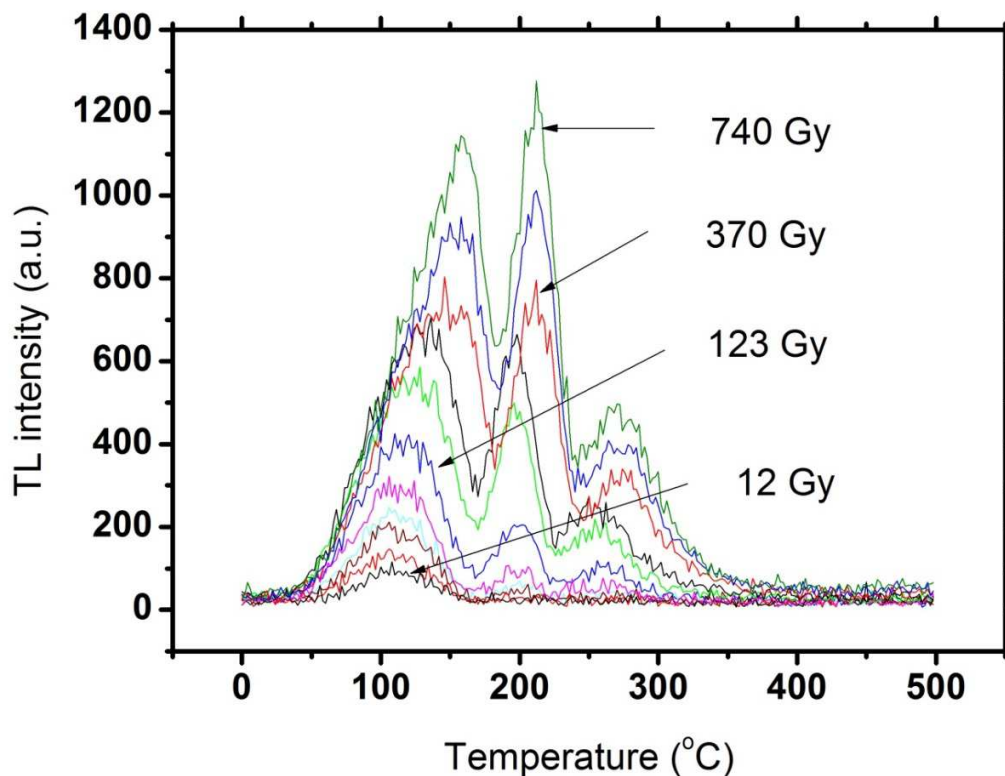
Figure 9.5: Different glow curves acquired by exposing $CaTa_2O_6:Pr^{3+}$ to different radiation doses.

The sublinearity of the dose response at low doses for the first peak and the third peak of $CaTa_2O_6:Pr^{3+}$ glow curves may in this regard suggest that the trapping of electrons at the centres represented by those peaks was slower, compared to that of the traps represented by response of the second peak. The linearity response of the traps represented by the second peak suggests that at low doses more charge carriers were trapped by these trap centres compared to two trap centres.

Figure 9.6: Dose response curve of the 3 peaks of the glow curve in figure 9.5.

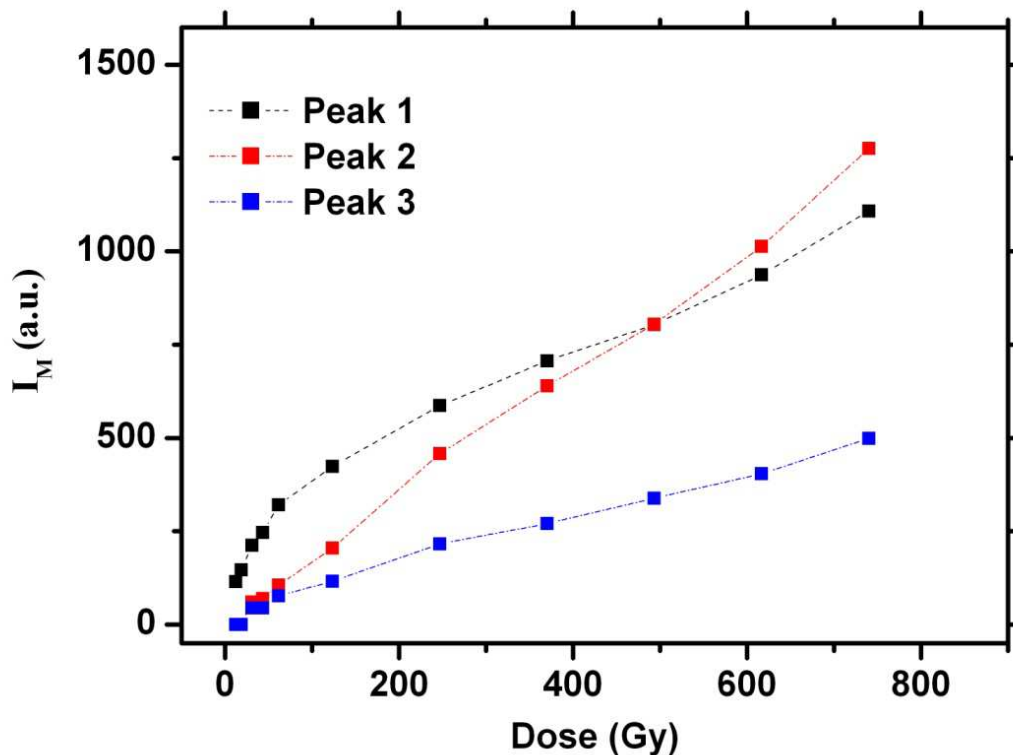An experiment to investigate the sensitivity of the trap centres to radiation was performed by dosing $CaTa_2O_6:Pr^{3+}$ with 370 Gy. The TL glow curves were acquired by heating the sample at the rate of 5 ^{o}C/s, and the same measurement was repeated six times on the same sample. The glow curves are presented in figure 9.7, and the last five glow curves (black spectra in Figure 9.7) have shifted from the firstly measured glow curve (peak 1 in Figure 9.7). The shift may be caused by the pre dose effect, which alters the position of the trap centres [31]. The deviation of the peaks from the expected position was calculated and presented in Table 9.1. From Figure 9.7, it is clear that the first glow curve has peaks (T_{M1}, T_{M2} and T_{M3}) positioned at higher temperatures, which shift to lower temperatures for the second to the fifth measurement. The peaks shifted from 135, 199 and 250 ^{o}C for T_{M1}, T_{M2} and T_{M3}, respectively, to a mean position of 117, 166 and 224 ^{o}C for T_{M1}, T_{M2} and T_{M3} (Table 9.1).

A sample can show radiation sensitivity depending on the nature of defect structures within a particular compound, and this is also known as the pre-dose effect [31,32].
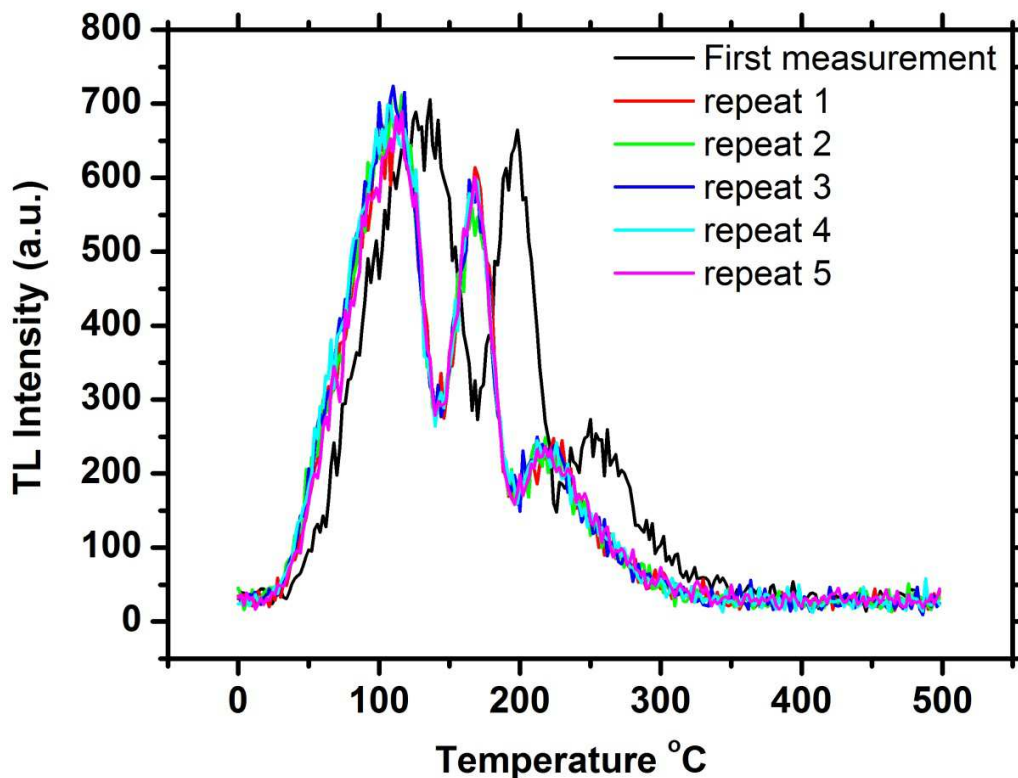
Figure 9.7: Repeatability measurements.

Such parameters can be competition between traps of different depths, radiation induced defect centres and also radiation damage to the defect structures [33]. To investigate this effect it is often customary to repeat the same measurement at least on one sample several times by keeping the experimental parameters the same, and observe any changes that may take place to the glow curves. If the signal remains the same, then that may be suggesting stable traps, but if the glow curve changes continuously upon irradiating the sample with the same dose repeatedly, then the traps in the system are not stable and may easily be changed by the radiation [31].

The glow curves of $CaTa_2O_6:Pr^{3+}$ (Figure 9.8) were acquired at different heating rates (0.5, 1, 2, 3, 4 and 5 ^{o}C/s) for a sample that was exposed to 370 Gy. The peaks (I_{M1}, I_{M2} and I_{M3}) of the glow curves show a decrease in intensity and a shift to higher temperatures, with an increase in the heating rate. The earlier effect is attributed to thermal quenching [34], and the latter is attributed to recombination that is slowing down [35]. When electrons are in the excited state they can absorb phonons and decay non-radiatively by losing their energy to the

phonons, and the efficiency of this mechanism may increase with an increase in temperature or the heating rate [36] When the variable heating rate method is used, the activation energy can be approximated using equation 9.2 [34]:

$$E = \ln\left(\frac{T_M^2}{\beta}\right) k T_M \qquad [9.2]$$

where E is the activation energy, T_M is temperature at the maximum intensity of the glow curve, β (Written as B in figure 9.9) is the heating rate, and k is Boltzmann's constant. The activation energy is extracted directly from the slope of $\ln\left(\frac{T_M^2}{\beta}\right)$ vs $1/k T_M$ [34] as shown for the first peak, second and third peak in Figure 9.9a, b & c. The slope obtained is the mean representation of the data points of the activation energy obtainable using equation 9.2. The activation energy for the first, second and third peak is 0.61 ± 0.02, 1.41 ± 0.06 and 1.6 ± 0.01 eV, respectively.
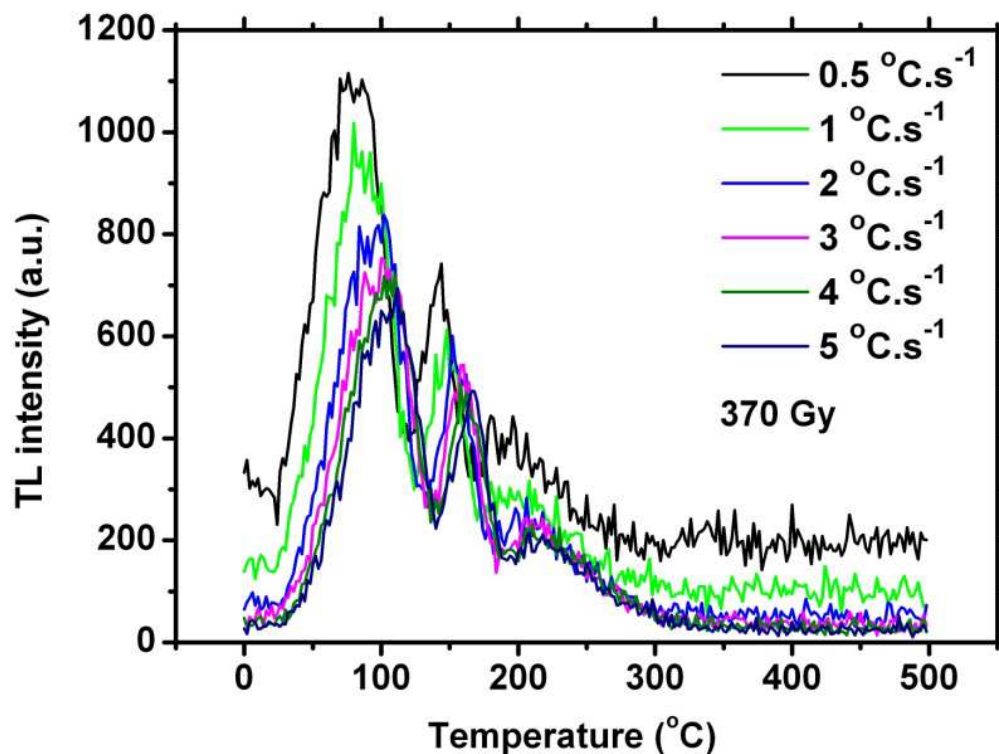
Figure 9.8: CaTa$_2$O$_6$:Pr^{3+} glow curves acquired using different heating rates.

Table 9.1: Peak positions of T_M at the maximum intensity.

	T_{M1}	T_{M2}	T_{M3}
	°C	°C	°C
Measurement 1	118	168	224
Measurement 2	116	166	222
Measurement 3	118	164	226
Measurement 4	118	168	226
Measurement 5	116	168	222
average	117	166	224
TD	1	1	2
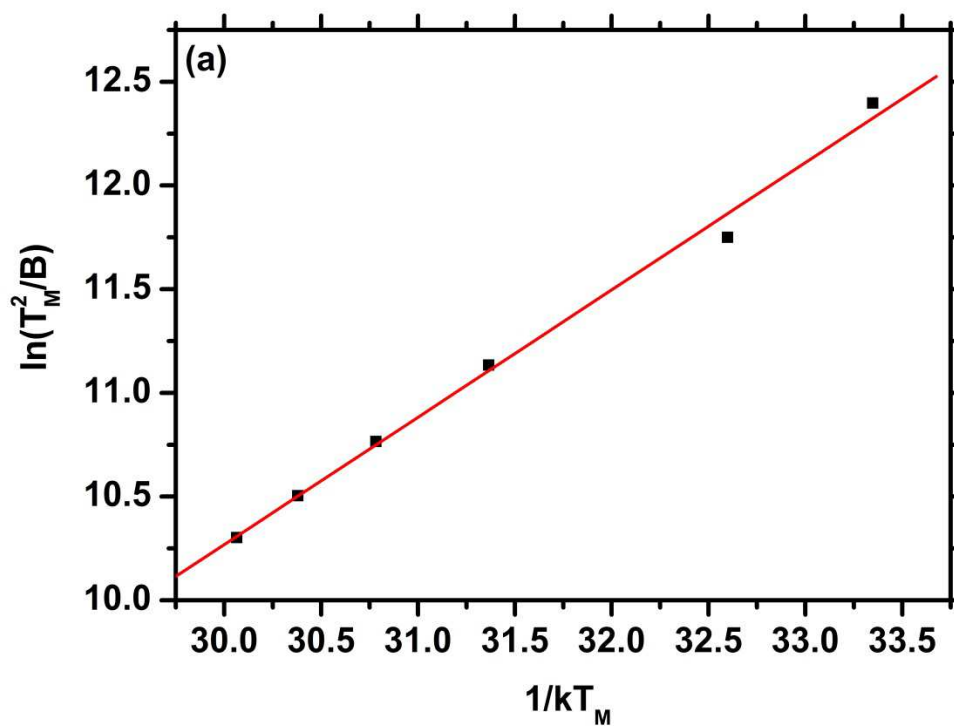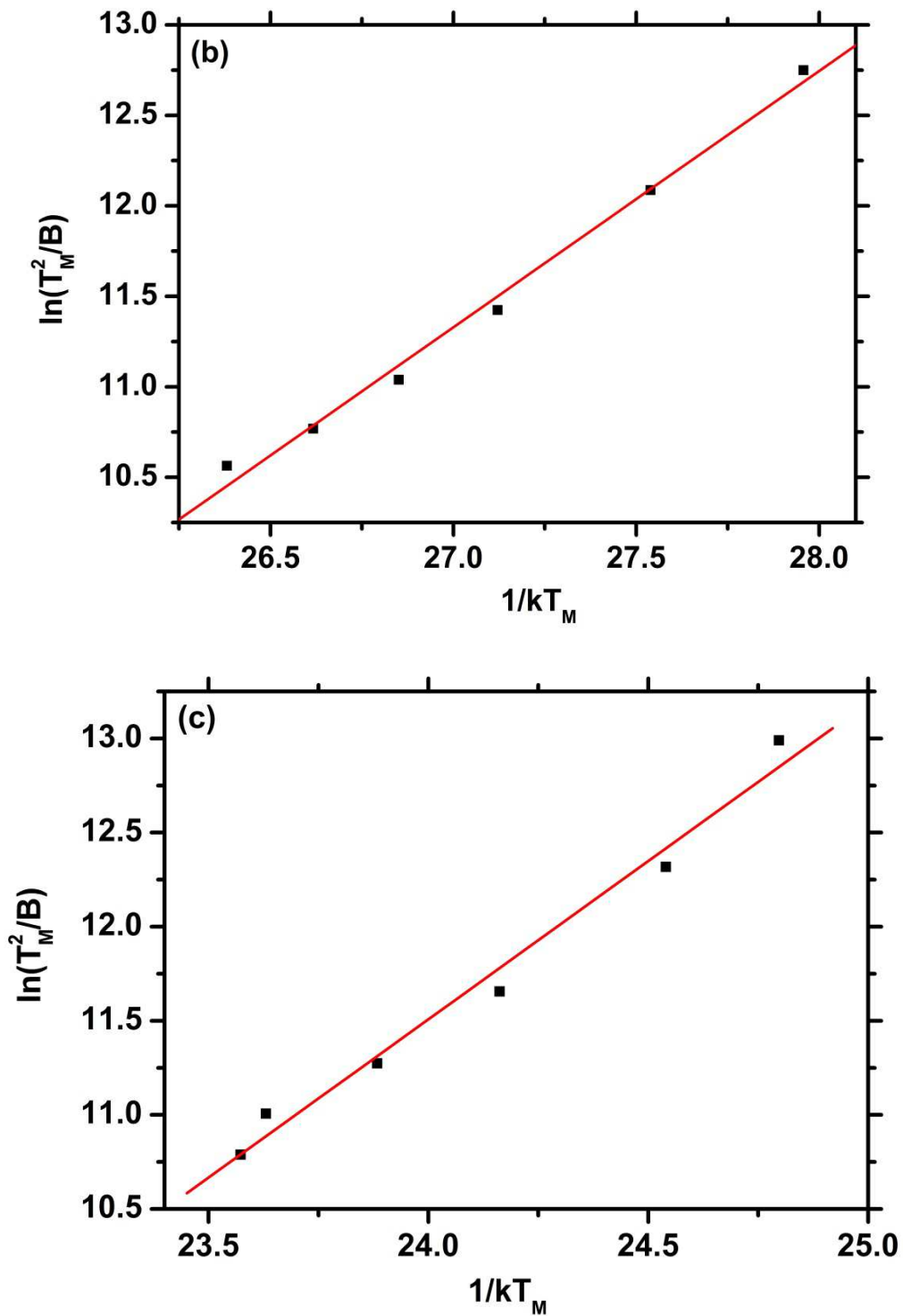
Figure 9.9: Linear fit from which the slope is an approximation of the activation energy of the traps. (a) is the approximation for the first peak, (b) for the second peak and (c) for the third peak.
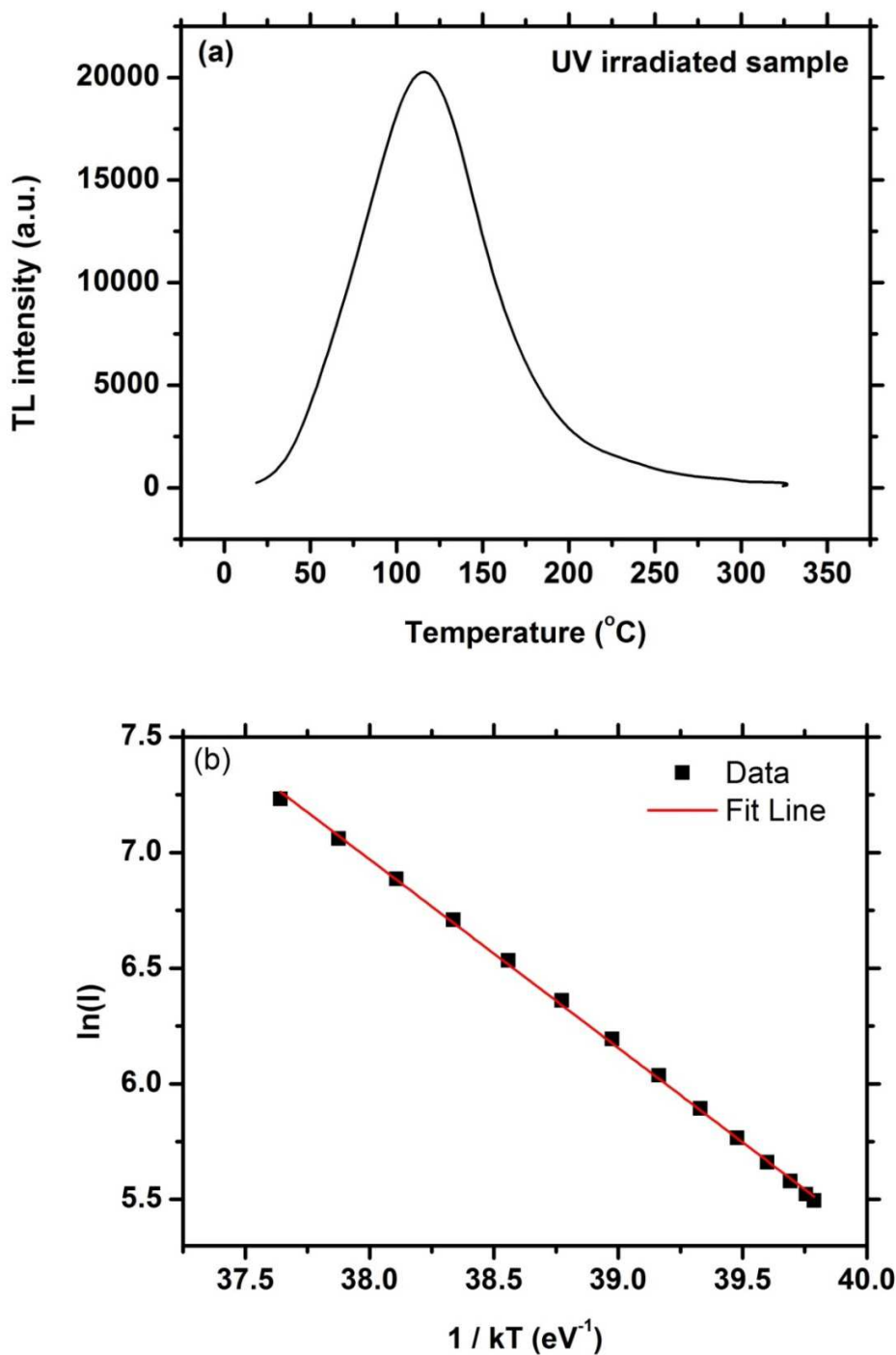
Figure 9.10: The activation energy calculation by initial rise method for a sample excited using Ultraviolet irradiation. (a) Shows the glow curve and (b) the fit of the first 15% of the glow curve from which the slope is an approximation of the activation energy.

Additionally, the sample was irradiated using an ultraviolet lamp to trace possible radiation damage or additional trap levels induced by the beta particles. The activation energy of the sample irradiated with an ultraviolet lamp was approximated using the initial rise method by Garlick and Gibson [26], which approximates the activation energy independent of the order of kinetics [28,33]. According to the model the thermoluminescence emission for the first low temperature interval of the glow curve can be expressed as (Eq. 9.3) :

$$I(t) = Ce^{-E/kT} \tag{9.3}$$

Where E is the activation energy of the electrons trapped within the electron trapping centres, k is Boltzmann constant, T is the temperature, and C a constant [26, 28, 33]. Figure 10a and 10b show the glow curve of the sample irradiated with ultraviolet and the corresponding linear fitted curve of the first low temperature interval of the glow curve, respectively.

The activation energy was approximated to 0.65 ± 0.07 eV, which is similar to that of the variable heating rate for the beta particle irradiation. The temperature position of the glow curve peak around at $100\ ^{\circ}C$ is common for the sample irradiated with an ultraviolet lamp (Figure 9.10a) and also for the sample irradiated using beta particles. The additional two peaks (Figure 9.5) revealed by exciting with the beta particles may be revealed due to the higher energies associated with beta particles and not necessarily an indication of beta induced trap centres due to radiation damage to the material.

The phosphorescence decay curve of $CaTa_2O_6$: Pr^{3+} phosphor (Figure 9.11) for the measurement of the persistent emission lifetime were done by exciting the phosphor with an ultraviolet source (254 nm) for 5 minutes, then measuring the time it takes for the emission to decay using a photomultiplier tube. The decay curve shows two components as observed in the log scale plot (Fig 9.10 insert) of the phosphorescence decay curve. The fast component is associated to the decaying of the Pr^{3+} emission that decays within microseconds [37] and the slow component that is associated to the delayed emission as a result of trapping and detrapping of charge carriers by the electron trapping centres [32, 38,40]. The corresponding time parameters were extracted by fitting the curve with second order exponential decay function (Eq. 9.4):

$$I(t) = Ae^{-t/\tau_1} + Be^{-t/\tau_2} \qquad \qquad [9.4]$$

where I is the luminescence intensity, A & B are constants, t is the phosphorescence time, τ_1 and τ_2 are the decay times of the first and the second components, respectively [38]. The phosphorescence decay times were determined to be $33.5 \pm 0.6\,\mu s$ and 1598 ± 336 s for τ_1 and τ_2, respectively.
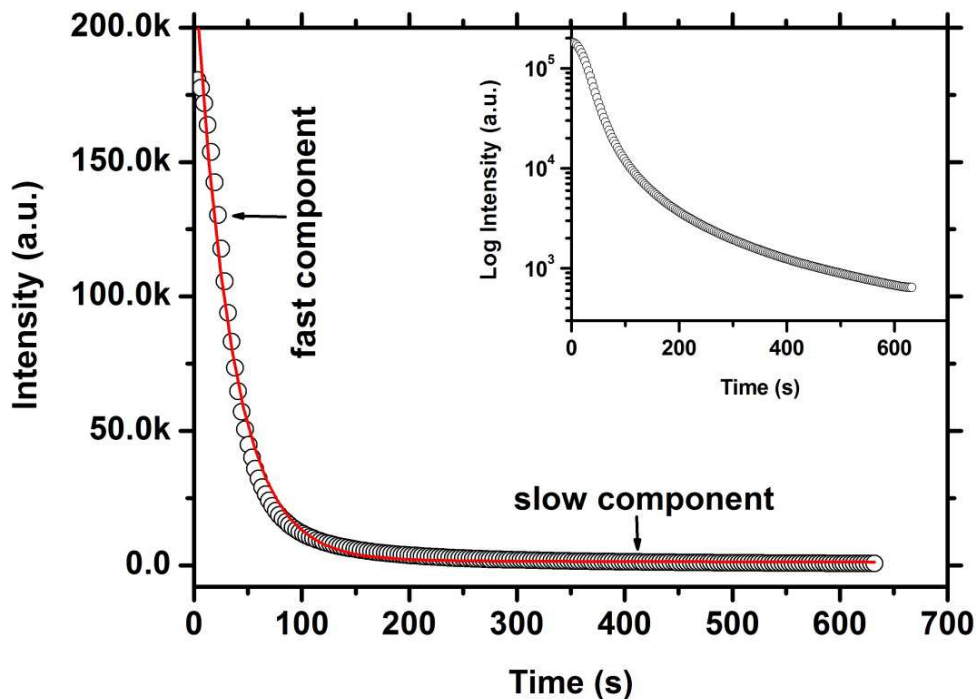
Figure 9.11: The phosphorescence decay curve of $CaTa_2O_6$:Pr^{3+}. The insert is the decay curve presented in the log scale.

9.4. Conclusion

A $CaTa_2O_6$: Pr^{3+} phosphor with greenish-blue emission was prepared by solid state reaction at 1200 ^{o}C for 4 hrs. An orthorhombic single phase was obtained, as identified by XRD. The scanning electron microscopy images showed that particles were of irregular shapes and had different crystallite sizes. Most f – f transitions from Pr^{3+} were observed, and greenish blue emission from $^3P_0 \rightarrow {}^3H_4$ was most dominant. The phosphor exhibits three different types of electron trapping centres and competition amongst them was detected. The depth of the

electron trapping centres was approximated to be 0.61 ± 0.02, 1.41 ± 0.06 and 1.6 ± 0.01 eV for the first, second, and third peaks, respectively. When the phosphor was excited using UV lamp only the peak at 0.6 eV volt was revealed and this may be caused by the low irradiation energy of the UV lamp which is not sufficient to pump more carriers to the deeper electron trapping centres, like the beta particles.

9.5.   References

1.   N.G. Teixeira and R.L. Moreira, R.P.S.M. Lobo, M.R.B. Andreeta, A.C. Hernandes A. Dias,   Cryst. Growth Des**. 11** (2011) 5567.

2.   L.L. Noto, S.S. Pitale, M.A. Gusowski, O.M. Ntwaeaborwa, J.J. Terblans, H.C. Swart, J. Lumin. **145** (2014) 907.

3.   G.C. Bleier, M Nyman, L.E.S. Rohwer, M.A. Rodriguez, J. Solid Stat. Chem. **184** (2011) 3221.

4.   E.C. Karsu, E.J.Popovici, A.Ege, M.Morar, E.Indrea, T.Karali, N.Can, J. Lumin. **131** (2011) 1052.

5.   A.P. Pivovarova, V.I. Strakhov, Y.N. Smirnov, Refract. Ind. Ceram. **41** (2000) 9.

6.   J. Milanez, A.T. de Figuciredo, S. de Lazaro, V.M. Longo, R. Erlo, V.R. Mastelaro, R.W.A. Franco, E. Longo, J.A. Varela, J. Appl. Phys. **106** (2009) 043526.

7.   J.S. Kim, H.L. Park, C.M. Chon, H.S. Moon, T.W. Kim, Solid. Stat. Com. **129** (2004) 163

8.   J. Milanez, A.T. de Figuciredo, S. de Lazaro, V.M. Longo, R. Erlo, V.R. Mastelaro, R.W.A. Franco, E. Longo, J.A. Varela, J. Appl. Phys. **106** (2009) 043526.

9.   H.F. Brito, J. Holsa, H. Jungner, T. Lamanen, M.H. Lastusaari, M. Malkanmaki, L.C.V. Rodriguess, Opt. Mater. Express, **2** (3), (2012) 287.

10.   S. Yin, D. Chen, W. Tang, J. Alloy and Compd., **441** (2007) 327.

11.   B.M Mothudi, O.M. Ntwaeaborwa, Shreyas S. Pitale and H.C. Swart, J Alloy and Compd.*,* **508** (2010) 262.

12.   B.M. Mothudi, O.M. Ntwaeaborwa, J.R. Botha, H.C. Swart, Physica B **404** (2009) 4440.

13.   K. Korthout, K. von den Eechout, J. Botterman, S. Nikitenko, D. Poelman, P.F. Smet, Phys. Rev. B **84** (2011) 085140.

14.   Z. Pan, Y.Y. Lu, F. Liu, Nat. Mater. **11** (2012) 58.

15.   W. Liwei, X Zheng, T. Feng, J. Weiwei. Z Fujun, M. Lijian, J. Rare Earths **23** (6), (2005) 672.

16.   M.A. Lephoto, O.M. Ntwaeaborwa, S.S.Pitale, H.C.Swart, J.R.Botha, B.M.Mothudi, Physica B **407** (2012) 1603.

17. Y. Pan, Q. Su, H. Xu, T. Chen, W. Ge, C. Yang, J. Sol. Stat. Chem. **174** (2003) 69.

18. S. Som S.K. Sharma, *J. Phys. D: Appl. Phys.* **45** (2012) 415102.

19. L.L. Noto, S.S. Pitale, J.J. Terblans, O.M. Ntwaeaborwa, H.C. Swart, Physica B **407** (2012) 1517.

20. G.H. Mhlongo, O.M. Ntwaeaborwa, M.S. Dhlamini, H.C. Swart and K.T. Hillie, J. Alloy. and Compd. **509** (2011) 2986.

21. W. Wong-Ng, H. McMurdie, B. Paretzkin, C. Hubbard, A. Dragoo, Powder Diffr. **3** (1988) 251.

22. X.C. Jiang, W.M. Chen, C.Y. Chen, S.X. Xiong, A.B. Yu, Nanoscale Res Lett **6** (2011) 32.

23. L.L. Noto, S.S. Pitale, M.A. Gusowki, J.J. Terblans, O.M. Ntwaeaborwa, H.C. Swart Powder Technol. **237** (2013) 141.

24. P. Boutinaud, E. Pinel, M. Dubois, A.P. Vink, R. Mahiou, *J. Lumin.* **111** (2005) 69 .

25. C. De Mello Donega, A. Meijerink, G. Blasse, J. Phys. Chem. Solids. **56** (5), (1995) 673.

26. H.F. Brito, J. Hassinen, J. Holsa, H. Jungner, T. Lamanen, M.H. Lastusaari, M. Malkanmaki, J. Niittykoski, P. Novak, L.C.V. Rodriguess, J. Therm. Anal. Calorim. **105** (2), (2011) 657.

27. V. Pagonis, G. Kitis, C. Furetta, Numerical and practical exercises in thermoluminescence, 2006, Springer and business Media Inc. USA.

28. A.J.J. Bos, Radiation Measurement **41** (2007) S45.

29. C. Furetta, Handbook of Thermoluminescence, 2003, world scientific publishing, Singapore.

30. S.W.S. McKeever, M. Moscovitch, P.D. Townsend, Thermoluminescence Dosimetry Materials: Properties and uses, 1995, Nuclear Technology Publishing, England.

31. R. Chen, V. Pagonis, Thermally and optically stimulated luminescence, a simulated approach, 2011, John Wiley and Sons Ltd. UK.

32. N.A. Larsen, Dosimetry based on thermally and optically stimulated luminescence [Thesis], Niels Bohr Institute University of Copenhagen.

33. A.G. Kozakiewicz, A.T. Davidson, D.J. Wilkinson, Nucl. Instr. and Meth. In Phys. Res. B **166-167** (2000) 577.

34. S.W.S McKeever, Thermoluminescence of Solids, 1985, Cambridge University Press, New York.

35. P.R. Gonzales, C. Furetta, E. Cruz-Zaragoza, J. Azorin, Mod. Phys. Lett. B, **4** (8), (2010) 717.

36. I. Veronese, The thermoluminescence peaks of quarts at intermediate temperatures and their use in dating and dose reconstruction [Thesis], 2005, UniversitaDegliStudi Milano.

37. L. Bøtter-Jensen, S.W.S. McKeever, A.G. Wintle, Optically Stimulated Luminescence Dosimetry, 2003, Elsevier, Amsterdam.

38. P. Boutinaud, E. Cavalli, M. Bettinelli, J. Phys.: Condens. Matter, 19 (2007) 386230.

39. L.L. Noto, M.L. Chitambo, O.M. Ntwaeaborwa and H.C. Swart, Powder Technol. **247** (2013) 147.

40. J. Zhi, A. Chen, L.K. Ju, Opt. Mater. **31** (2009) 1667.

"If you hear a voice within you saying: "you cannot paint," then by all means paint and that voice will be silenced."

— Vincent Van Gogh

10
Photoluminescence and persistent emission of SrTa$_2$O$_6$:Pr^{3+}

10.1. Introduction

The SrTa$_2$O$_6$ compound has shown interesting evolution, in that it was initially known to completely crystallize at 1800 ^{o}C to a tetragonal symmetry, which belongs to the tungsten bronzes, as reported by Whiston et. al. [1]. SrO – Ta$_2$O$_5$ systems have the capacity to crystallize into a broad range of products with different phases, such as SrTa$_2$O$_6$, Sr$_5$Ta$_4$O$_{15}$, Sr$_6$Ta$_2$O$_{11}$, Sr$_2$Ta$_2$O$_7$ [1] and Sr$_3$Ta$_5$O$_{15}$ [2], which are all preparable using the solid state chemical reaction [1,2]. Later it was discovered that the SrTa$_2$O$_6$ crystallizes into different polymorphs. A high temperature tetragonal modification β'–SrTa$_2$O$_6$, which requires temperatures above 1500 ^{o}C to prepare [3], a β–SrTa$_2$O$_6$ that crystallizes at temperatures between 1200 and 1500 ^{o}C [3], and the α–SrTa$_2$O$_6$ that crystallizes at temperatures below 1100 ^{o}C [4]. A recent study by Lee et al [5] revealed that the three polymorphs do not only crystallize at different temperatures, but they also have different X-ray diffraction (XRD) patterns, and the XRD patterns of the α–SrTa$_2$O$_6$ correspond to the pattern that was reported by Sirotinkinet et. al. [6], whilst the others deviate from this pattern. The polymorphs resemble different symmetry with the β and the β' being tetragonal tungsten bronzes and the α polymorph being orthorhombic [5]. Additionally, the work reveals that the α, β and β' polymorphs have different energy band gaps, ranging from 4.4, 4.0 to 3.8 eV, respectively [5]. The wide band gap nature of the materials makes them to be of interest in producing rare earth doped phosphors with an efficient emission [7]. The SrTa$_2$O$_6$ compound is currently playing an important role in the field of photocatalysis, where it is used to decompose water molecules into H$_2$ and O$_2$ molecules [8]. It is also used for applications in radio frequency circuits [9]. In the field of phosphors, the oxide compounds are of interest in developing phosphors with persistent emission, as reported for MAl$_2$O$_4$:Eu,Dy (M = Ca, Sr, B)

[10], $CaTiO_3$:Pr [11] and $Zn_3Ga_2Ge_2O_{10}$:Cr [12]. The persistent emission is attributed to the trapping and gradual release of the electrons by the electron trapping centres to the luminescence centres [13], from where the observable emission originates [14]. The existence of the electron trapping centres in these materials is attributed to the existence of the positively charged oxygen vacancies with an energy that resides within the bandgap (E_g) of the electronic structure of the phosphor [15]. They are formed within the material as defects [15,16]. In this work we show that $SrTa_2O_6$ is usable as a host for Pr^{3+} ion doped phosphor. Pr^{3+} ions are very important in the sense that the Pr:Tm co-doped phosphor has commercial applications in optical fibres as a possible amplifier [17]. They are also reported to have a single red emission when it is doped in $CaTiO_3$ that is almost pure, according to the Commission Internationale de l'Eclairage (CIE) coordinate plots [13]. The single red emission coming from the $^1D_2 \rightarrow \,^3H_4$ transition is due to the complete depopulation of the $^3P_0$ state, by the virtual charge transfer between the $^3P_0$ and $^1D_2$ states, via the intervalence charge transfer (IVCT) [18]. This leads to complete quenching of the blue emission [18]. Additionally, in this work the luminescence properties of Pr^{3+} and the absorbance were obtained from where the energy width of the band gap was calculated. We approximated the lifetime of the persistent emission from the phosphorescent decay curves, and determined the activation energy of the electrons trapped within electron trapping centres.

10.2. Experimental

$SrTa_2O_6$: Pr^{3+} phosphor was prepared at different temperatures by solid state reaction, at 1200 ^{o}C for 10 hrs, 1400 ^{o}C for 20 hrs, and at 1500 ^{o}C for 32 hrs. The temperatures and time were chosen in order to obtain the α, β and β' polymorphs phases. The phases were identified by a Bruker AXS D8 Advance X-Ray diffractometer using Cu *Kα* radiation. The scanning electron microscopy (SEM) images were captured using the Shimadzu SSX-550 SEM from Kyoto, Japan. The surface maps showing the distribution of the ions, were obtained using the time of flight secondary ion mass spectroscopy (ToF – SIMS 5). The Bi^+ ion gun with 1 pA beam current was used to probe the surface of the phosphor, and was operated in the imaging mode. The photoluminescence (PL) emission and excitation (PLE) properties of the phosphor were probed using the Varian Carry-Eclipse fluorescence spectrophotometer. The phosphorescence decay curves were obtained by exciting the samples for 2 min with an Ultraviolet (UV) lamp of 254 nm wavelength, and then followed by measuring the intensity decay curves with a photomultiplier

tube (PMT) at 25 $^{\circ}$C. A TL 10091, NUCLEONIX spectrometer was used to acquire the thermoluminescence (TL) glow curves at 25 °C for the samples excited using a 245 nm ultraviolet source.

10.3. Results and Discussion

The XRD patterns of the $SrTa_2O_6$:Pr^{3+} (0.4 mol %) phosphor that were synthesized at different temperatures along with the standard data for $SrTa_2O_6$ with ICSD card No. 39706 [6] are shown in figure 10.1. The patterns show that the phase of the sample prepared at 1200 $^{\circ}$C is only starting to form and with the temperature increasing to 1400 and 1500 $^{\circ}$C better phase development took place. This differs from the reports in the literature [3,4,5], which proposes the occurrence of α, β and β' polymorphs at these temperatures. Instead we only find one phase, which corresponds to the $SrTa_2O_6$ original phase proposed by Sirotinkin et. al. [6].
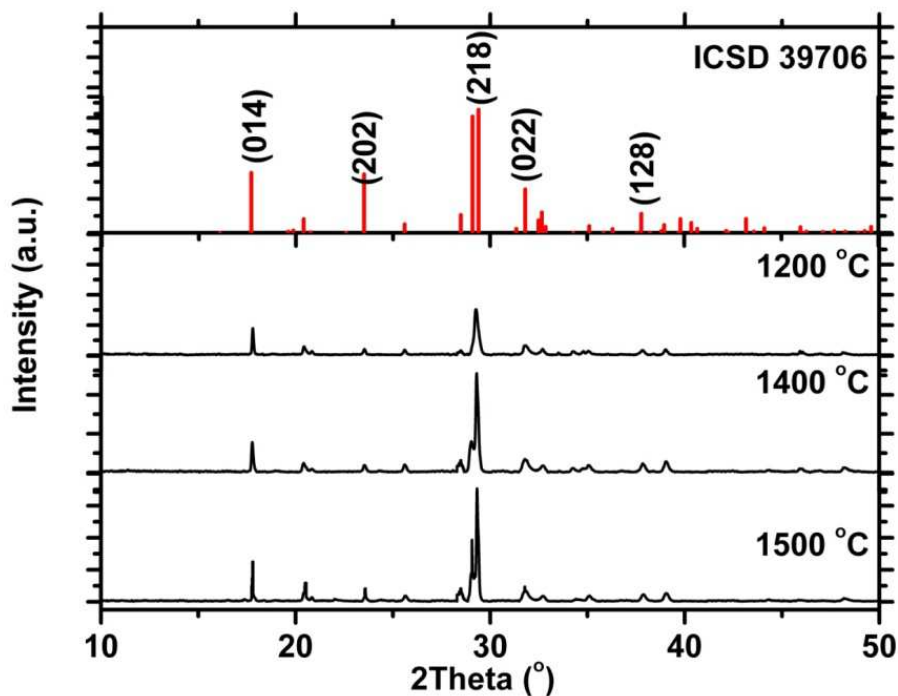

Figure 10.1: XRD patterns of $SrTa_2O_6$:Pr^{3+} matched with that of the standard data.

The SEM images (Figure 10.2) of the three samples prepared at 1200, 1400 and 1500 $^{\circ}$C are shown for a 4.8 µm, 19.2 µm, and 19.2 µm field of view, respectively. The samples exhibit particles of irregular shapes and different sizes, which are agglomerated. The particle

agglomeration increased with temperature, such that co-melting of the particles is visible. The agglomeration of the particles is attributed to very high temperatures or preparation associated with the solid state reaction [19].

Figure 10.3 (a), (b) and (c) show the surface mapping of $SrTa_2O_6:Pr^{3+}$ mapping using the ToF-SIMS, operated in the imaging mode for the samples prepared at 1200, 1400 and 1500 ^{o}C. The ion distribution on the surface of the sample is shown using false colour surface mapping over an area of 100 µm $\times$ 100 µm.
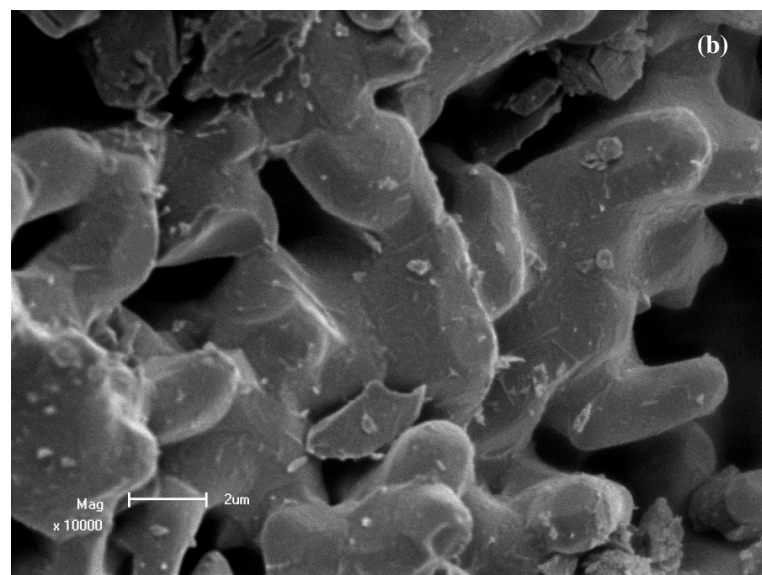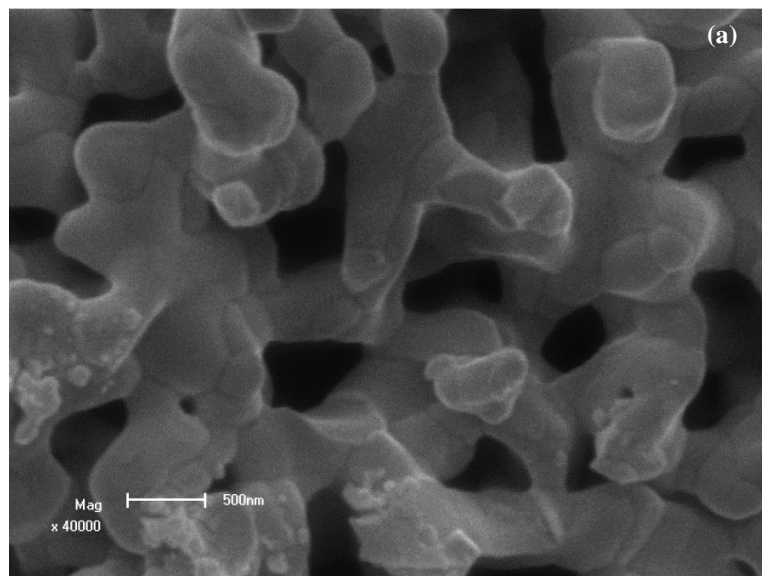
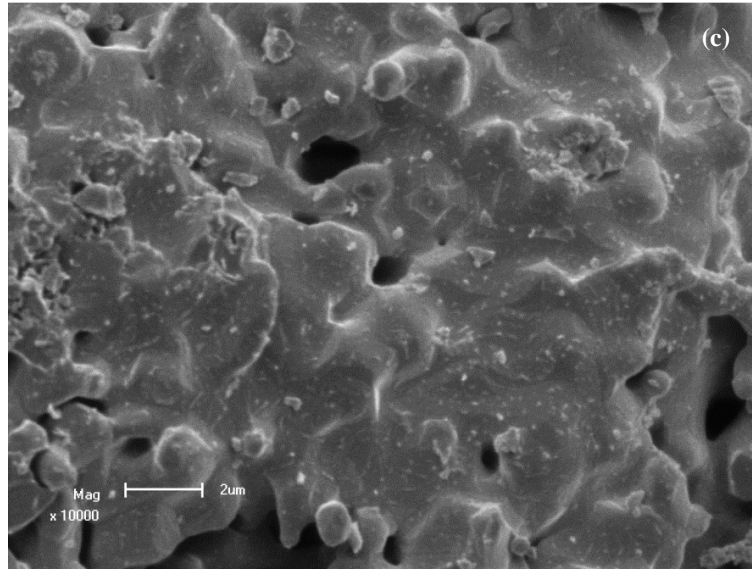Figure 10.2: SEM images of the samples prepared at 1200 (a), 1400 (b) and 1500 $^{\circ}$C (c).

The SrH^+, TaO^+, (PrH^+ or PrO^+) ions obtained upon probing the sample are used to reflect the distribution of the corresponding Strontium, Tantalum, Oxygen, and Praseodymium ions inside the phosphors. The scale on each map shows the concentration of the image ranging from 0 counts to a certain value which is supposedly the maximum concentration.
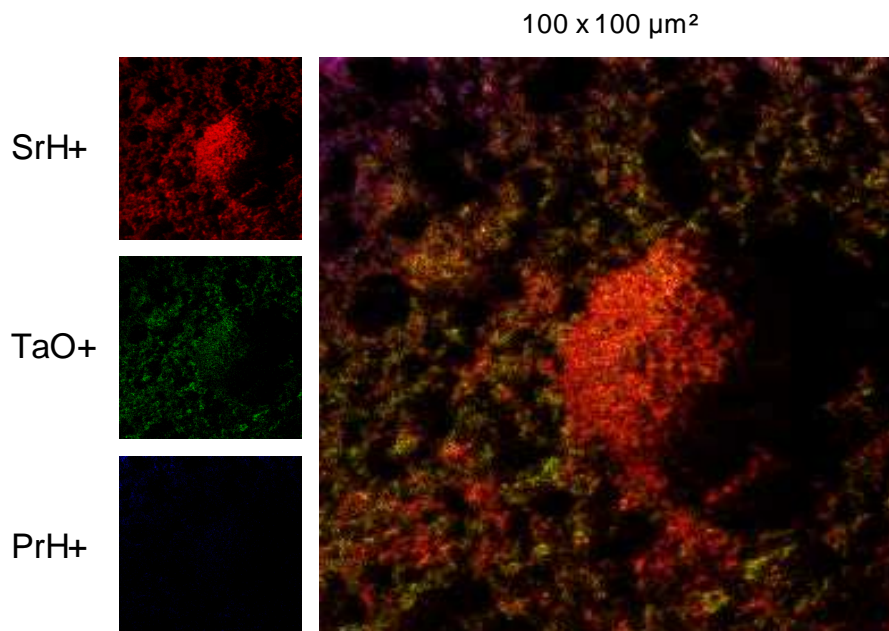
100 x 100 µm²

Figure 10.3 (a): ToF – SIMS surface mapping of $SrTa_2O_6$:Pr^{3+} prepared at 1200 $^{\circ}$C.
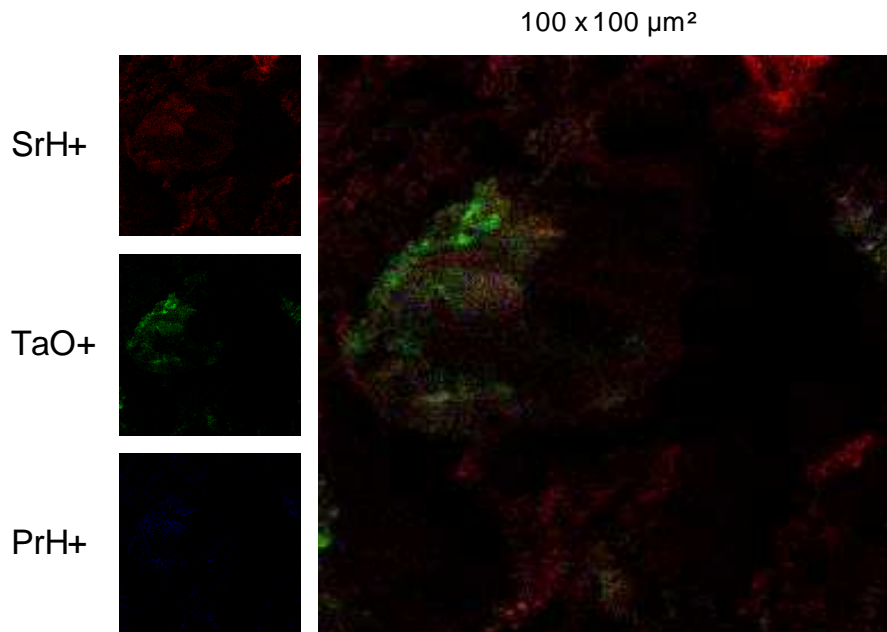
Figure 10.3 (b): ToF – SIMS surface mapping of $SrTa_2O_6:Pr^{3+}$ prepared at 1400 ^{o}C.
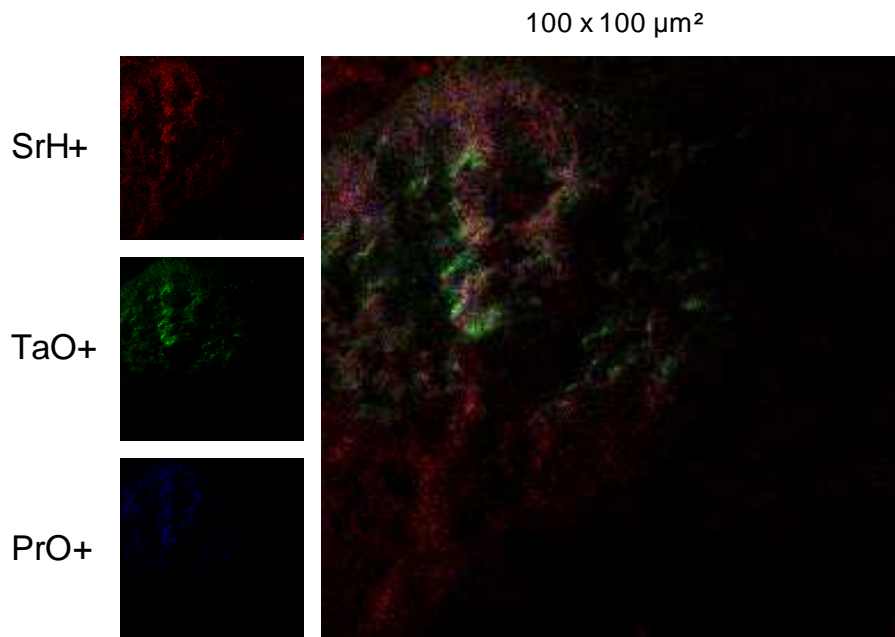
Figure 10.3 (c): ToF – SIMS surface mapping of $SrTa_2O_6:Pr^{3+}$ prepared at 1500 ^{o}C.

The images of all samples show that the SrH^+ overshadow all the other ions and maybe an indication that the surface of the $SrTa_2O_6:Pr^{3+}$ is enriched with Sr and oxygen and that the Ta present in the $SrTa_2O_6:Pr^{3+}$ is covered. The overlay mapping shows uniform distribution of all

ions throughout all the three phosphor samples. The SrH$^+$, TaO$^+$ and (PrH$^+$ or PrO$^+$) ions are presented as red, green and blue (Figure 10.3 (a), (b) and(c)), respectively, for the overlay mapping to allow comparison of all ions at once. The Pr ions in all samples appear to be homogeneously distributed, which is an indication of successful incorporation.
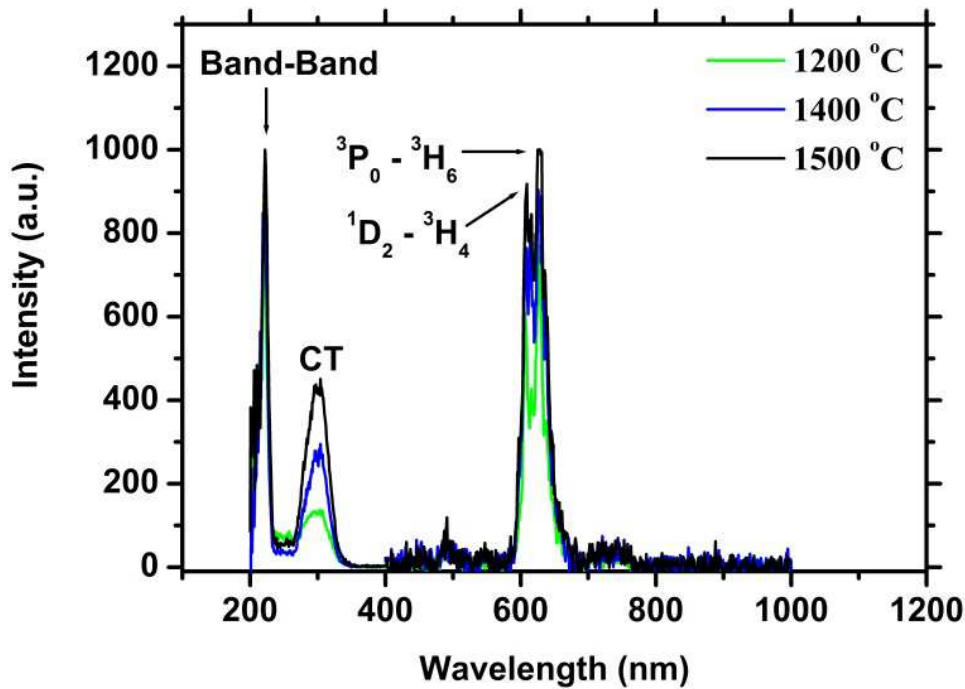

Figure 10.4: PLE and PL spectra of SrTa$_2$O$_6$:Pr^{3+}.

Figure 10.4 shows the PLE and the PL spectra of the SrTiO$_3$:Pr^{3+} phosphor for the sample prepared at 1200, 1400 and 1500 ^{o}C. The PLE spectra show that the major absorbing band is at 225 nm, and it is accompanied by a broader absorbing band at 300 nm. The band at 225 nm corresponds to band to band absorption as it is verified from the band gap calculations below. The broad band at 300 nm that occurs within the band gap is associated with charge transfer, which probably emanates from the intrinsic defect absorption [20]. The PL spectra show an emission in the red region coming from two peaks positioned at 610 nm and 627 nm. These two spectral lines correspond to the f–f emission of Pr^{3+} coming from the ^{1}D$_2$→^{3}H$_4$ and the ^{3}P$_0$ →^{3}H$_6$ transitions, respectively [21]. The presence of the red emission from the ^{3}P$_0$ state corrupts the explanation of the single red emission observable for Pr^{3+} in CaTiO$_3$ due to the intervalence charge transfer as reported previously [11]. This can be due to the absence of the intervalence

charge transfer in the present system or that it is situated above the $^3P_0$ state, such that it populates both the $^3P_0$ and the $^1D_2$ states.
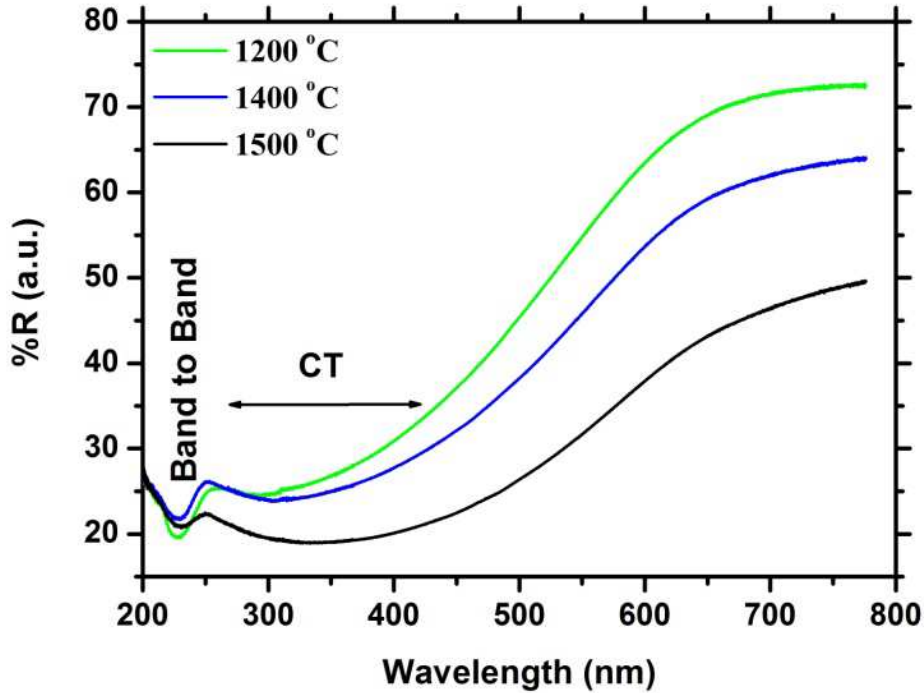

Figure 10.5: Diffused reflectance spectra of $SrTa_2O_6:Pr^{3+}$.

The diffused reflectance spectra (Figure 10.5) of the three samples show major absorption bands at 225 nm and a broad band around 300 nm. The absorbing centres of the material correspond very well with the bands observed from the PLE spectra, as reported above. The peak observable at 225 nm as shown in the PLE spectrum (Figure 10.3) is proven to be from band to band excitation by calculating the width of the energy band gap as demonstrated below for all three samples. Figure 10.6 shows Kubelka–Munk functions that were transformed from the diffused reflectance spectra (Figure 10.5) of the three $SrTa_2O_6:Pr^{3+}$ phosphor samples using Eq. 10.1:

$$F(R) = \frac{(1-R)^2}{2R} \qquad [10.1]$$

where $F(R)$ is the reflectance factor that is transformed according to the Kubelka – Munk from the reflectance R. the value of R is obtained by subtracting the system's background obtained using Ba_2SO_4 standard, from the reflectance of the sample [22]. The Tauc's relation is then

reconstructed using the Kubelka – Munk relation to obtain (Eq. 10.2) from which the energy band gap (E_g) of the material was obtained [22]:

$$(F(R) \, h\nu \,)^2 = C\big(h\nu - E_g\big) \qquad [10.2]$$

where the $h\nu$ is the photon energy and C is a proportionality constant [22]. From the relation given by Eq. 10.2, a curve of $(F(R) \, h\nu \,)^2$ *vs* $h\nu$ is then constructed, from which a tangent line is fitted at its point of inflection. The point at which the tangent line intersects with the $h\nu$ is equivalent to the energy band gap of the material for $(F(R) \, h\nu \,)^2 = 0$ [23]. The energy band gaps of the three samples were approximated to be 5.54 ± 0.4, 5.52 ± 0.3 and 5.50 ± 0.1 eV (225 nm) for the sample prepared at 1200, 1400 and 1500 $^{\circ}$C, respectively. The calculated value is equivalent to the band observed at 225 nm (5.5 eV) using both the PLE and UV/Vis absorption spectroscopies.

Figure 10.7 shows the phosphorescent decay curves of the three samples of $SrTa_2O_6$:Pr^{3+}. The decay curves have two components (Fig 10.7 insert)that are responsible for the luminescence; the fast component that is attributed to phosphorescence Pr^{3+} and the slow component from the persistent emission due to electron trapping centres [11,24–28].
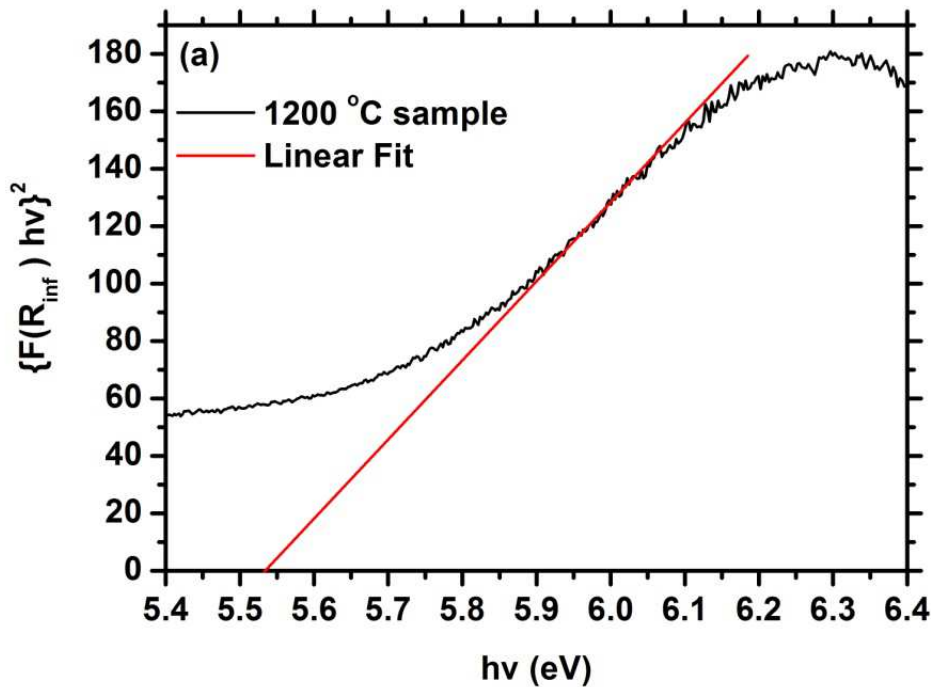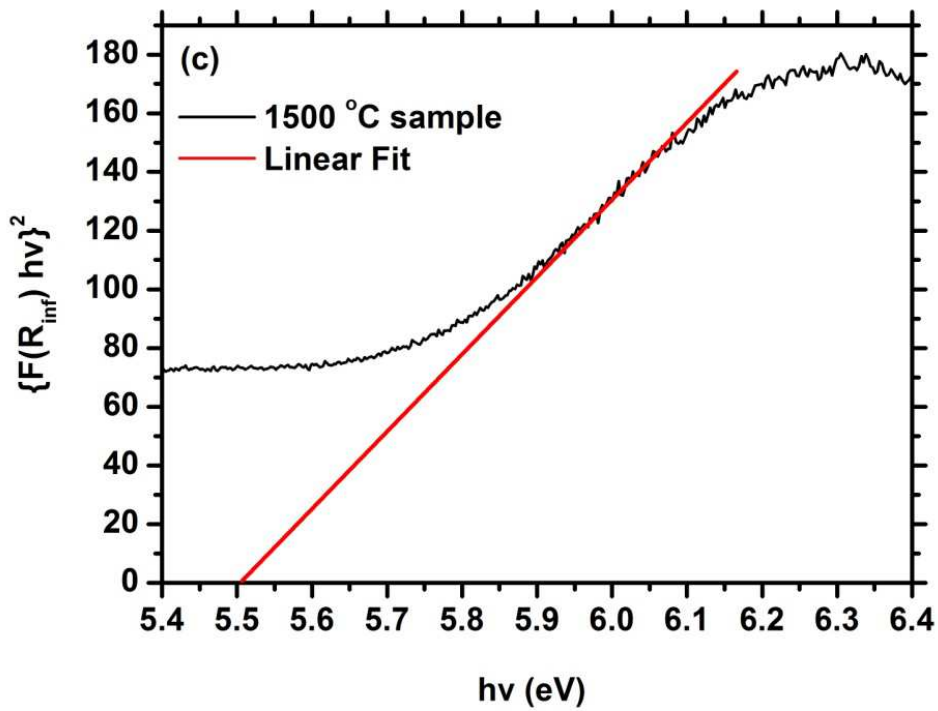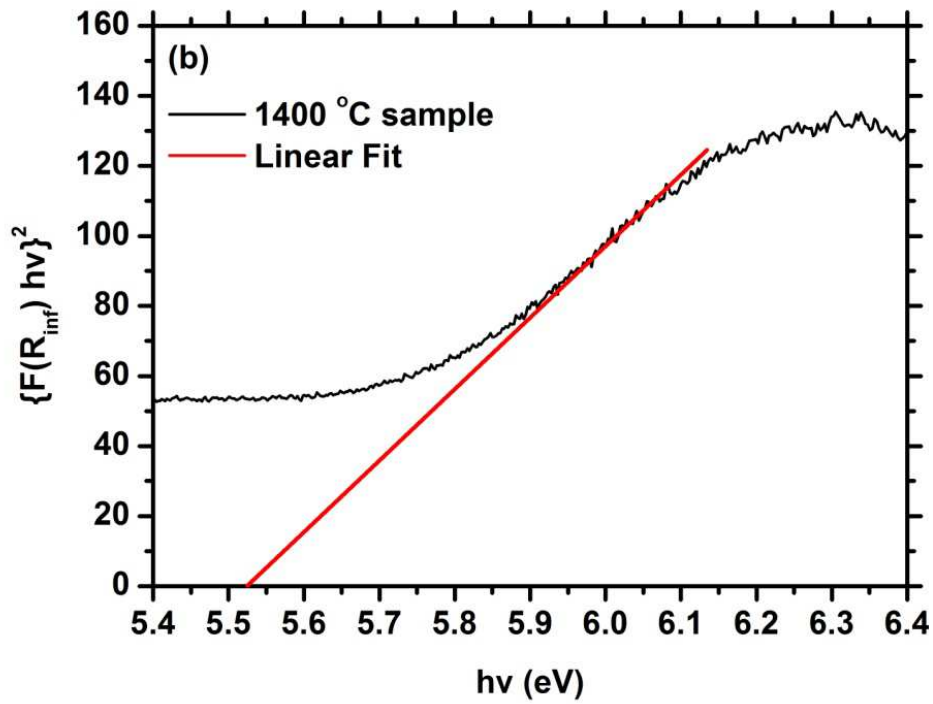
Figure 10.6: Energy band estimation from the Kubelka-Munk function.

The persistent emission time parameters were extracted from the decay curve by fitting with the second order decaying exponential curve (Eq. 10.3):

$$I(t) = Ae^{-t/\tau 1} + Be^{-t/\tau 2} \qquad [10.3]$$

where $I(t)$ is the luminescence intensity, A and B are constants and t is the time. The first term on the right side of the equation describes the decay of luminescence from the dopant ion, and whose lifetime is presented by τ_1. The second term describes the decay of the persistent emission and whose lifetime is presented by τ_2 [11,27,28].
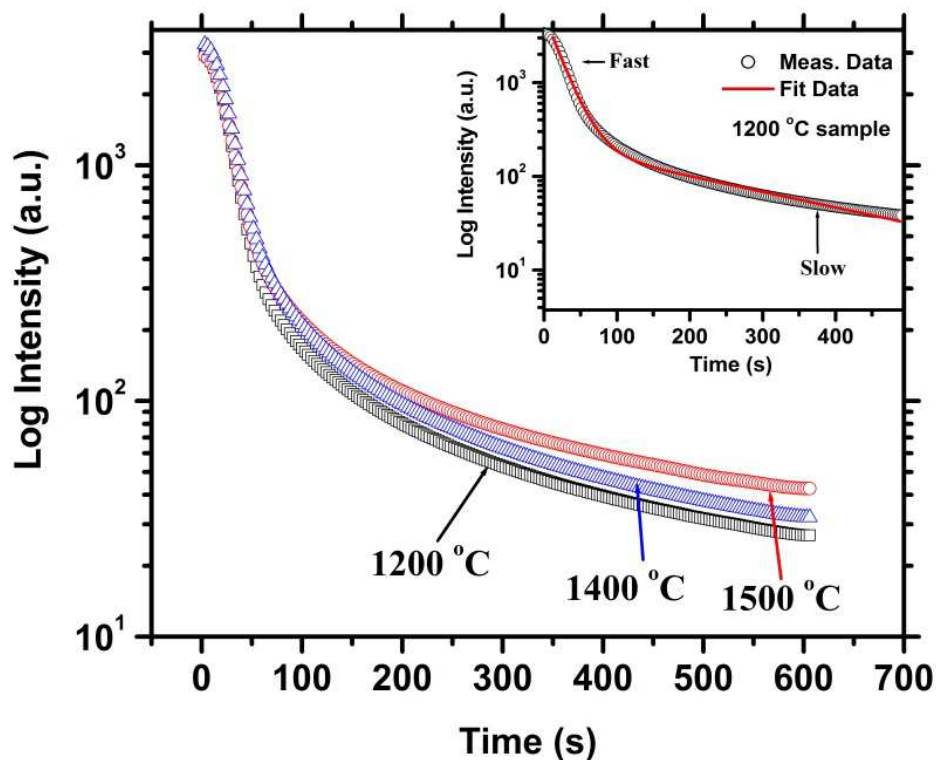
Figure 10.7: Phosphorescence decay curves of $SrTa_2O_6$ phosphor samples prepared at different temperatures. The insert shows decay curve measured data of the sample prepared 1200 ^{o}C with a fitted line.

The extracted persistent emission times were approximated to be 260 ± 19, 276 ± 25 and 296 ± 19 seconds for the samples prepared at 1200, 1400 and 1500 ^{o}C, respectively. The increase in the

persistent lifetime of the phosphors with an increase in preparation temperature reflects an increase in the density of the electron trapping centres [11,24]. The energy distribution of the electron trapping centres in these materials is investigated below.
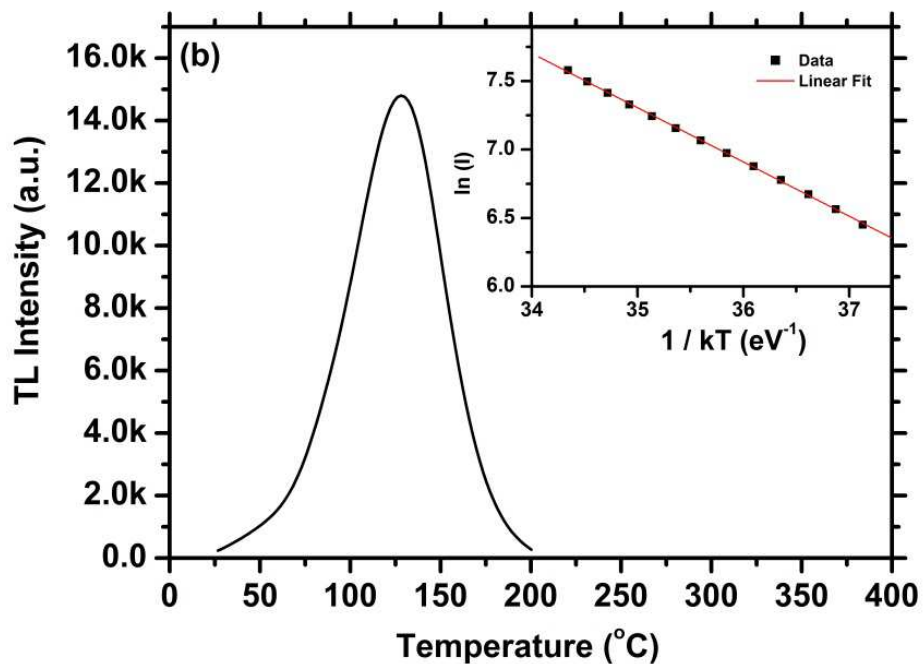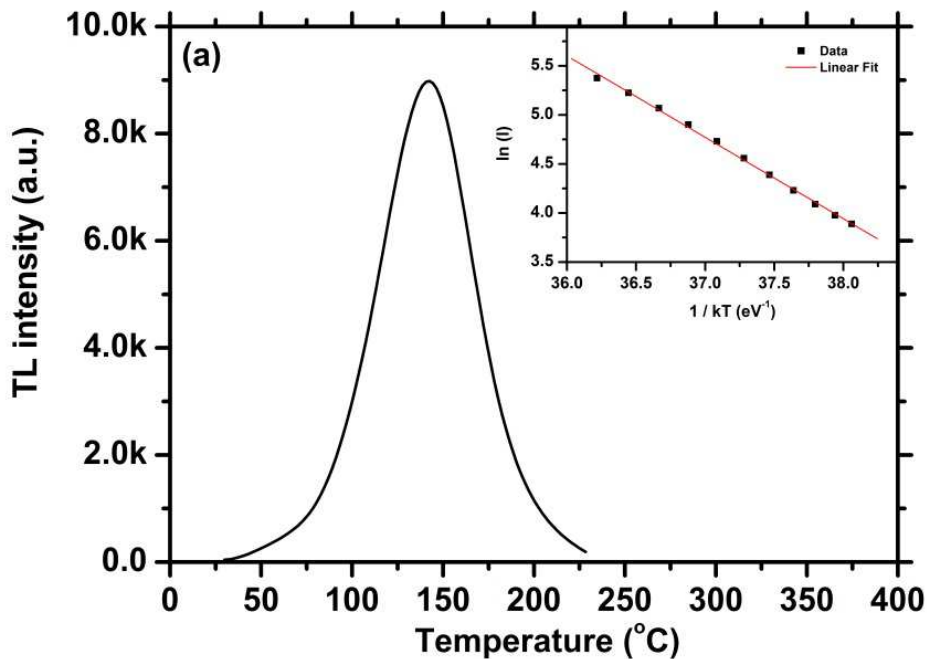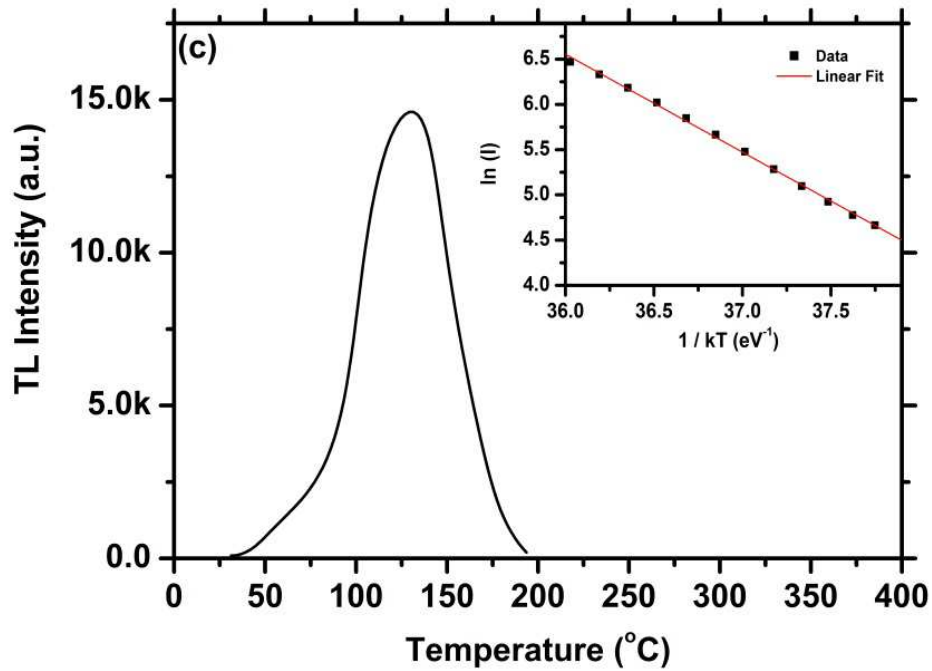
Figure 10.8: TL glow curves for the samples prepared at 1200, 1400 and 1500 ^{o}C. The insert is the initial rise model curve to determine the activation energy.

The glow curves, presented in figure 10.8 (a), (b) and (c), are for the samples prepared at 1200, 1400 and 1500 ^{o}C, respectively. These were measured using the TL spectroscopy to determine the activation energy of the electrons trapped within the electron trapping centres. The inserts in the three figures show the linear fitted curves according to the initial rise method, which is independent of the order of kinetics [29,30]. According to the method, the TL emission for the first low temperature interval of the glow curve can be expressed as (Eq. 10.4):

$$I(t) = Ce^{-\frac{E}{kT}} \qquad [10.4]$$

Where $I(t)$ is the luminescence intensity, E is the activation energy of the electrons trapped within the electron trapping centres, k is Boltzmann constant, T is the temperature, and C a constant [29,30]. The activation energies were approximated to be 0.85 ± 0.01, 1.03 ± 0.02 and 1.08 ± 0.01 eV for the samples prepared at 1200, 1400 and 1500 ^{o}C, respectively.

10.4. Conclusion

The new red emitting $SrTa_2O_6:Pr^{3+}$ phosphor with persistent emission properties was prepared by solid state reaction at 1200, 1400 and 1500 ^{o}C. Orthorhmbic phases were obtained as evidenced from XRD patterns. The particles of the samples showed co-melted structures because of the high temperatures that were involved during the synthesis process. Uniformity of the ion distribution is shown by the ToF – SIMS images. The phosphor only showed red emission from the $^1D_2 \rightarrow ^3H_4$ and the $^3P_0 \rightarrow ^3H_6$ transitions at 608 and 619 nm, respectively. The main absorption that occurs at 225 nm (5.5 eV), was proven to be from band to band excitation as indicated by the band gap (E_g) calculations. The persistent emission times were 260 ± 19, 276 ± 25 and 296 ± 19 seconds for the samples prepared at 1200, 1400 and 1500 ^{o}C, respectively. The activation energy for the electrons trapped within electron trapping centres were approximated to be 0.85 ± 0.01, 1.03 ± 0.02 eV and 1.08 ± 0.01 eV for the samples prepared at 1200, 1400 and 1500 ^{o}C, respectively, using the initial rise method.

10.5.   References

1.   CD Whiston and AJ Smith, ActaCryst. **23** (1967) 82.

2.   T Siegrist, RJ Cava and JJ krajewski, Mater. Res. Bull **32** (7) (1997) 887.

3.   A Deschanvres, G Desgardin and B Raveau, Mater. Res. Bull. **7** (9) (1972) 921.

4.   Y Repelin, E Husson, NQ Dao and H Brusset, Mater. Res. Bull **15** (7) (1980) 985.

5.   E Lee, CH Park, DP Shoemaker, M Avdeev and YI kim, J. Solid Stat. Chem. **191** (2012) 232.

6.   VP Sirotinkin and SP Sirotinkin, Russ. J. Inorg. Chem. **38** (6) (1993) 992.

7.   YF Lin, YH Chang, YS Chang, BS Tsai and YC Li, J. Alloys. Compd. **421** (2006) 268.

8.   K Yoshioka, V Petrykin, M Kakihana, H Kato and AKudo, J. Catal. **232** (2005) 102.

9.   L Lu, T Nishida, M Echizeu, K Uchiyama and Y Uraoka, Thin Solid Films **520** (2012) 3620.

10.   Y Lin, Z Zhang, Z Tang, J Zhang, Z Zheng, X Lu, Mater. Chem. and Phys. **70** (2001) 156–159.

11.   LL Noto, SS Pitale, MA Gusowki, JJ Terblans, O.M. Ntwaeaborwa, H.C. Swart, Powder Technol. **237** (2013) 141.

12.   Z Pan, YY Lu, F Liu Nat. Mater. **11** (2012) 58.

13.   S Yin, D Chen, W Tang, J.Alloys and Compd., **441** (2007) 32.

14.   BM Mothudi, OM Ntwaeaborwa , JR Botha, HC Swart, Physica B **404** (2009) 4440.

15.   S Yang, LE Halliburton, A Manivannan, PH Bunton, DB Baker, M Klemm, S Horn, A Fujishima, Appl. Phys. Lett. **94** (2009) 162114.

16.   I Tanaka, F Oba, K Tatsumi, M Kunisu, M Nakano, H Adachi, Mater Trans **43** (7) (2002) 1426.

17.   YG Choi, JH Baik, J Heo, Chem. Phys. Lett. **406** (2005) 436.

18.   P Boutinaud, E Pinel, M Dubois, AP Vink, R Mahiou, J. Lumin., **111** (2005) 69.

19.   XC Jiang, WM Chen, CY Chen, SX Xiong, AB Yu, Nanoscale Res Lett **6** (2011) 32.

20.   G Blasse, A Bril, J. Lumin **1970**, *3*, 109.

21.   C De Mello Donega, A Meijerink, G Blasse, J. Phys. Chem. Solids. **56** (5), (1998) 673.

22.   AE Morales, ES Mora, U Pal, Rev. Mex. Fis. S **53** (5) (2007) 18.

23.   EA Davis and NF Mott, Philos. Mag., **22** (1970) 903.

24. EJ Popovici, M Nazarov, L Muresan, DY Noh, E Bica, M Morar, I Arellano, E Indrea, Phys. Proc. **2** (2009) 185.

25. BJ Nyman, ME Bjorketun, GJ Wahnstrom, Sol. Stat. Ionics **189** (2011) 19.

26. PJ Deren, R Pazik, W Strek, P Bautinaud, RJ Mahiou, J. Alloy Compd. **451** (2008) 595.

27. PT Diallo, P Boutinaud, R Mahiou, JC Cousseins, Phys. Stat. Sol. (a) **160** (1997) 255.

28. LL Noto, ML Chitambo, OM Ntwaeaborwa, HC Swart, Powder Technol. **247** (2013) 147.

29. Pagonis V, Kitis G, Furetta C, ***Numerical and practical exercises in thermoluminescence***, 2006, Springer and business Media Inc. USA.

30. McKeever SWS, ***Thermoluminescence of Solids***, 1985, Cambridge University Press, New York.

"Learning does not make one learned: there are those who have knowledge and those who have understanding. The first requires memory and the second philosophy"

— Alexandre Dumas

11

Summary and Future work.

11.1 Summary

The thesis reports the persistent luminescence of $ZnTa_2O_6$, $ZnTaGaO_5$, $CaTa_2O_6$ and $SrTa_2O_6$ doped with Pr^{3+}. The basis of the study was to study the mechanism of persistent luminescence involved in the materials and also to enhance the luminescence intensity and the lifetime of the persistent luminescence emission.

$ZnTa_2O_6$:Pr^{3+} phosphor was prepared by solid state chemical reaction at 1200 ^oC for 4 hours. It displayed weak blue and prominent red emission, with the blue emission spectral line observed at 448 nm from $^3P_0 \rightarrow {}^3H_4$ transition, and the red spectral lines observed at 608, 619 and 639 nm from $^1D_2 \rightarrow {}^3H_4$, $^3P_0 \rightarrow {}^3H_6$ and $^3P_0 \rightarrow {}^3F_2$ transitions, respectively. When the concentration of Pr^{3+} was varied, 0.4 mol% Pr^{3+} displayed only red emission with the Commission Internationale de l'Eclairage coordinates (CIE) coordinates matching those of an ideal red color. The phosphor mostly absorbs the ionizing radiation by band to band excitation, as confirmed by calculations of the energy band gap.

Enhancement of the luminescence intensity of $ZnTa_2O_6$:Pr^{3+} phosphor was achieved by preparing it in the presence of Li_2SO_4 and Li_2CO_3, which acted as flux agents. The strong absorption by the defect levels due to the flux was observed from the diffused reflectance spectra. Pr was found to exist in both Pr^{3+} and Pr^{4+} oxidation states by the X-ray photoelectron spectroscopy data. The presence of Pr^{3+} increased, while Pr^{4+} decreased in the samples prepared in the presence of a flux. The increased absorption by the defect levels and the reduction of Pr^{4+} in the samples prepared using a flux resulted in the enhancement of the luminescence intensity as observed from the photoluminescence spectra.

The lifetime of the persistent luminescence of $ZnTa_2O_6$:Pr^{3+} prepared in a flux was calculated using a second order exponential decay curve from the measured phosphorescence decay curves. This showed an enhancement in the lifetime of the persistent luminescence of the fluxed sample, which is attributed to the additional electron trapping centres induced by the flux as observed from the thermoluminescence glow curves. The lifetime of the persistent luminescence were additionally enhanced by co-doping $ZnTa_2O_6$:Pr^{3+} with Li^+, Na^+, K^+ or Cs^+ ions, and by also incorporating gallium ions to form a new host $ZnTaGa_5$:Pr^{3+}.

The $ZnTa_2O_6$:Pr^{3+} resembled an orthorhombic single phase was obtained, as identified by X-ray diffraction (XRD). The scanning electron microscopy (SEM) images showed that particles were of irregular shape and with different sizes. Preparing the samples in the presence of the fluxing material resulted in increased particle sizes. The SEM images of $ZnTaGa_5$:Pr^{3+} showed a surface morphology that is composed of particles with different shapes, the irregular, rhombus and rod shapes. The distribution of the ions in the material was investigated using the Time of Flight Secondary Ion Mass Spectroscopy (ToF SIMS) surface maps, which showed that the ions were uniformly distributed throughout the matrix. This showed successful incorporation of the ions.

A $CaTa_2O_6$: Pr^{3+}phosphor with greenish-blue emission was prepared by solid state reaction at 1200 ^{o}C for 4 hrs. An orthorhombic single phase was obtained, as identified by XRD. The scanning electron microscopy images showed that particles were of irregular shapes and had different crystallite sizes. Most f – f transitions from Pr^{3+} were observed, and greenish blue emission from $^3P_0 \rightarrow {}^3H_4$ was most dominant. The phosphor exhibits three different types of electron trapping centres and competition amongst them was detected. The depth of the electron trapping centres was approximated to be 0.61 ± 0.02, 1.41 ± 0.06 and 1.60 ± 0.01 eV for the first, second, and third peaks, respectively. When the phosphor was excited using UV lamp only the peak at 0.6 eV was revealed and this may be caused by the low irradiation energy of the UV lamp which is not sufficient pump more carriers to the deeper electron trapping centres, like the beta particles.

The new red emitting $SrTa_2O_6$:Pr^{3+} persistent luminescence phosphor was prepared by solid state reaction at 1200, 1400 and 1500 ^{o}C. Orthorhombic phases were obtained as evidenced from XRD patterns. The particles of the samples showed co-melted structures because of the high

temperatures that were involved during the synthesis process. Uniformity of the ion distribution is shown by the ToF – SIMS images. The phosphor only showed red emission from the $^1D_2 \rightarrow {}^3H_4$ and the $^3P_0 \rightarrow {}^3H_6$ transitions at 608 and 619 nm, respectively. The main absorption that occurs at 225 nm (5.5 eV), was proven to be from band to band excitation as indicated by the band gap (E_g) calculations. The persistent emission times were 260 ± 19, 276 ± 25 and 296 ± 19 seconds for the samples prepared at 1200, 1400 and 1500 ^{o}C, respectively. The activation energy for the electrons trapped within electron trapping centres were approximated to be 0.85 ± 0.01, 1.03 ± 0.02 eV and 1.08 ± 0.01 eV for the samples prepared at 1200, 1400 and 1500 ^{o}C, respectively, using the initial rise method.

11.2. Future work

Intervalence charge transfer has been accepted as the main reason behind the single red emission of Pr^{3+} at room temperatures in $CaTiO_3$, which has an effect of completely depopulating the $^3P_0$ state by feeding the $^1D_2$ state. The Intervalence Charge transfer state for $CaTiO_3:Pr^{3+}$ was reported to be around 360 nm, which is approximately at the same position where the charge transfer band of $ZnTa_2O_6:Pr^{3+}$ is observed in this study. Further studies at low temperatures can be done at lower temperatures up to 77K to investigate the changes in position of the this band, to confirm whether it comes from intrinsic defect levels or the Intervalence Charge transfer state.

The cross electron spin state for the $^3P_0 \rightarrow {}^3H_4$ transition is lower than that of $^3P_0 \rightarrow {}^3H_4$ and $^3P_0 \rightarrow {}^3H_4$ transitions, which suggest that the emission coming from the $^3P_0 \rightarrow {}^3H_4$ is most likely to be more intense than the two later transitions. However in $ZnTa_2O_6:Pr^{3+}$ it was observed to be lower. This opens up and opportunity to further investigate the exact mechanism that may be leading to the luminescence intensity of $^3P_0 \rightarrow {}^3H_4$ being lower than that of $^3P_0 \rightarrow {}^3H_4$ and $^3P_0 \rightarrow {}^3H_4$ transition.

The rare earth doping in all other phosphors which were studied were doped with 0.4 mol% of Pr^{3+}, which was the concentration that yield the optimal luminescence intensity in $ZnTa_2O_6$ compound. In this study it was kept the same for the sake of comparison. The future approach can be to vary the concentration of Pr^{3+} in $CaTa_2O_6$, $SrTa_2O_6$, $ZnTaAlO_5$, $ZnTaGaO_5$, $ZnTa_2SiO_8$ and search for the optimal luminescence intensity.

The persistent luminescence strong depends on oxygen vacancies in the material. Nano-particles are reported to exhibit more surface defects than bigger particles. This opens up a research opportunity for the future research to investigate the persistence luminescence nano particles with different particle shapes. To prepare such particles solvothermal synthesis route may be a better route to use.

11.3. List of publications

11.3.1   Pitale SS, Noto LL, Nagpure IM, Ntwaeaborwa OM, Terblans JJ, Swart HC, *Promising Zn3Ta$_2$O$_8$:Pr^{3+} red phosphor for low voltage cathodoluminescence applications*, AMR2011 Emerging Focus on Advanced Materials – Advance Materials Research, 306-307 (2011) 251-254.

11.3.2   Noto LL, Pitale SS, Terblans JJ, Ntwaeaborwa OM, Swart HC, *Surface chemical changes of CaTiO$_3$:Pr^{3+} upon electron beam irradiation*, Physica B: Physics of Condensed Matter, 407 (2012), 1517.

11.3.3   Noto LL, Pitale SS, Gusowski MA, Terblans JJ, Ntwaeaborwa OM, Swart HC, *Afterglow enhancement with In^{3+} codoping in CaTiO$_3$:Pr^{3+} red phosphor,* Powder Tech. 237 (2013) 141.

11.3.4   Luyanda L. Noto, Shreyas S. Pitale, Marek A. Gusowki, O. Martin Ntwaeaborwa, Jacobus J Terblans, Hendrik C Swart, *Luminescent dynamics of Pr^{3+} in MTaO$_4$ host (M=Y, La or Gd)*, J. Lumin. 145 (2014) 907.

11.3.5   Noto LL, Pitale SS, Ntwaeaborwa OM, Terblans JJ, Swart HC*, Cathodoluminescent stability of rare earth tantalate phosphors,* J. Lumin. 140 (2013) 14.

11.3.6   Noto LL, Chithambo MK, Ntwaeaborwa OM and Swart HC, *Photoluminescence and thermoluminescence properties of Pr^{3+} doped ZnTa$_2$O$_6$ phosphor,* Powder Technol. 247 (2013) 147.

11.3.7   Noto LL, Chithambo MK, Ntwaeaborwa OM and Swart HC, *The greenish-blue emission and thermoluminescent properties of CaTa$_2$O$_6$:Pr^{3+}*, J. Alloys. Compd. *589 (2014) 88.*

11.3.8   Noto LL, Ntwaeaborwa OM, Yagoub MYA and Swart HC, *Luminescence Intensity Enhancement of ZnTa₂O₆ :Pr³⁺*, Mater. Res. Bul. **55** (2014) 150.

11.3.9   Noto LL, Ntwaeaborwa OM, Terblans JJ and Swart HC, *Dependence of luminescence properties of CaTiO₃:Pr³⁺ on different TiO₂ polymorphs*, Powder Technol. **256** (2014) 477.

11.3.10   L.L. Noto, W.D. Roos, O.M. Ntwaeaborwa, M. Gohain, M.Y.A. Yagoub, E. Coetsee and H.C. Swart. *Enhancement of luminescent intensity and persistent emission of ZnTa₂O₆:Pr³⁺ phosphor by adding fluxing agents*. Sci. Adv. Mater. **7** (2015) 1.

11.3.11   L.L. Noto, M.Y.A. Yagoub, O.M. Ntwaeaborwa and H.C. Swart. *Enhancement of persistent luminescence of ZnTa₂O₆:Pr³⁺ by addition of Li⁺, Na⁺, K⁺ and Cs⁺ ions*. J. Lumin. March 2014, **submitted**.

11.3.12   MYA Yagoub, HC Swart, LL Noto and E Coetsee, *The effects of Eu-concentrations on the luminescent properties of SrF₂:Eu nanophosphor*, J. Lumin. **156** (2014)150. **Accepted**.

11.3.13   Noto LL, Ntwaeaborwa OM, Yagoub MYA and Swart HC, *Photoluminescence and persistent emission of SrTa₂O₆:Pr³⁺*, J. Solid Stat Sci. 2014, **Submitted.**

11.3.14   Yousif A, Seed Ahmed H, Som S, Kumar V, Noto LL, Swart HC, *Effect of Ga³⁺ doping on the photoluminescence properties of Y₃Al₅₋ₓGaₓO₁₂:Bi³⁺ phosphor*, ECS J. Solid Stat. Sci. Technol. **3** (11) (2014) R222.

11.3.15   Noto LL, Shaat S, Yagoub MYA, Ntwaeaborwa OM, Swart HC, *Luminescence Study of ZnTaGaO₅:Pr³⁺*, 2014, **Due for submission**.

11.3.16.   Noto LL, Shaat S, Yagoub MYA, Ntwaeaborwa OM, Swart HC, *Persistent luminescence of ZnTaAlO₅:Pr³⁺ and ZnTa₂SiO₈:Pr³⁺⁺*, 2014, **Due for submission**.

11.3.17.   Yagoub MYA, Swart HC, Noto LL, Coetzee E, *Concentration quenching, surface and spectral analysis of SrF$_2$:Pr^{3+} prepared by different synthesis techniques*, J. Lumin. 2014, **Submitted.**

11.3.18.   Yagoub MYA, Swart HC, Noto LL, Coetzee E, *Efficient energy transfer and fluorescence emission of Ce3+ co-doped SrF$_2$:Eu^{3+} nanophosphor,* 2014, **Due for sumission.**

11.4. List of conference proceedings

11.4.1. Noto LL, Pitale SS, Gusowki MM, Terblans JJ, Ntwaeaborwa OM, Swart HC, *Enhancement of Pr^{3+} red emission by adding In^{3+} as co-dopant in $CaTiO_3$:Pr^{3+} phosphor*, SAIP'2011 Proceedings, the 56th Annual Conference of the South African Institute of Physics, edited by I. Basson and A.E. Botha (University of South Africa, Pretoria, 2011), p 254-257. ISBN: 978-1-86888-688-3.

11.4.2. LL Noto, SS Pitale, OM Ntwaeaborwa and HC Swart, *Pr^{3+} luminescence in a $GdTaO_4$ host,* 2012 SAIP proceeding.

11.4.3. MYA Yagoub, HC Swart, LL Noto and E Coetsee, *Luminescent properties of Pr^{3+} doped SrF_2 prepared by different synthesis techniques,* SAIP 2013 proceeding.

11.4.4. Noto LL, Pitale SS, Ntwaeaborwa OM, Terblans JJ, Yagoub MYA and Swart HC, *Effects of different TiO_2 phases on the luminescence of $CaTiO_3$:Pr^{3+}*, SAIP 2013 proceeding.

11.4.5. MYA Yagoub, HC Swart, L L. Noto, E Coetsee, *Energy transfer in SrF_2:Eu^{2+},Pr^{3+} for solar cell applications*, 2nd South African Solar Energy Conference, 2014.

11.5. Research presentations

11.5.1 Noto LL, Pitale SS, Terblans JJ, Swart HC, *Optimization of Pr^{3+} concentration in $CaTiO_3$ host*, South African Institute of Physics, Pretoria, South Africa, 2010 (Local Conference)

11.5.2. Noto LL, Pitale SS, Terblans JJ, Ntwaeaborwa OM, Swart HC, *Surface chemical changes of $CaTiO_3:Pr^{3+}$ upon electron beam irradiation*, 4th South African Conference on Photonic Materials ,Kariega, South Africa, 2011 (International Conference).

11.5.3. Noto LL, Pitale SS, Gusowski MA, Terblans JJ, Ntwaeaborwa OM, Swart HC, *The Enhancement of Pr^{3+} red emission by adding In^{3+} as a co-dopant in $CaTiO_3:Pr^{3+}$ phosphor*, South African Institute of Physics, Pretoria, South Africa, 2011 (Local Conference)

11.5.4. Noto LL, Pitale SS, Gusowski MA, Terblans JJ, Ntwaeaborwa OM, Swart HC, *Red Emssion of Pr^{3+} ions*, Workshop for photonics students, Stellenbosch, 2011 (Workshop).

11.5.5. LL Noto, SS Pitale, OM Ntwaeaborwa and HC Swart, *Pr^{3+} luminescence in a $GdTaO_4$ host*, South African Institute of Physics, Pretoria, South Africa, 2012 (Local Conference).

11.5.6. Noto LL, Pitale SS, Ntwaeaborwa OM, Terblans JJ, Yagoub MYA and Swart HC, *Effects of different TiO_2 phases on the luminescence of $CaTiO_3:Pr^{3+}$*, SAIP 2013 proceeding (Local Conference).

11.5.7. Noto LL, Ntwaeborwa OM, Terblans JJ, Swart HC, *Optimization of the luminescent intensity of $ZnTa_2O_6:Pr^{3+}$ phosphor*, 5th South African Conference on photonic materials, South Africa, 2013 (International Conference).